Novel fabrication method for a hot gas supersonic micro-thruster

H.S.E. Versteeg

Technische Universiteit Delft

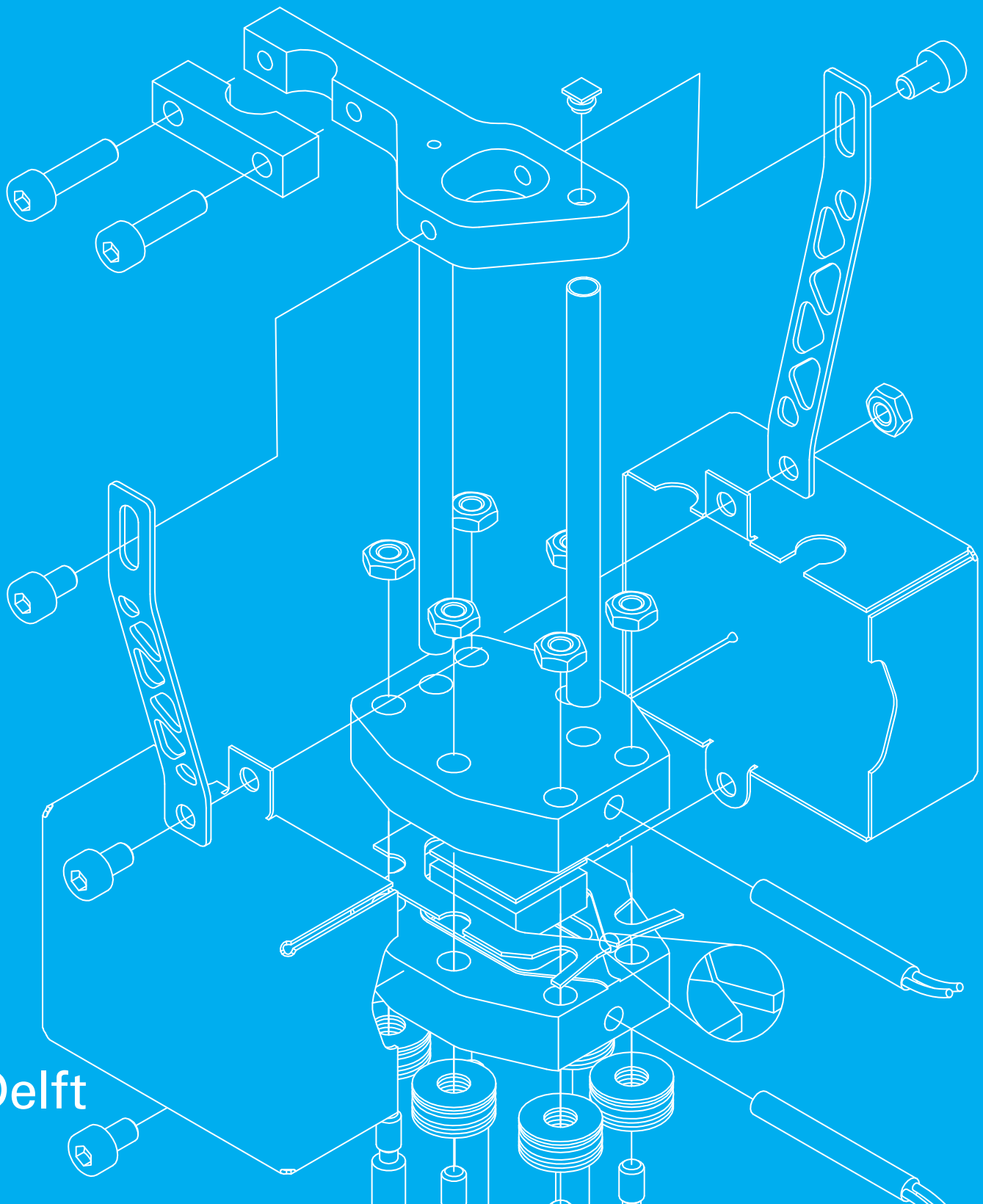

TU Delft

Novel fabrication method for a hot gas supersonic micro-thruster

by

H.S.E. Versteeg

to obtain the degree of Master of Science
at the Delft University of Technology,
to be defended publicly on Wednesday May 6, 2020 at 14:00.

Student number:	4302257	
Project duration:	July 16, 2019 – May 6, 2020	
Thesis committee:	Prof.dr. E.K.A. Gill	TU Delft, Chair
	ir. R. Noomen	TU Delft
	ir. B.T.C. Zandbergen	TU Delft, Supervisor

An electronic version of this thesis is available at https://repository.tudelft.nl/.

TU Delft

Preface

When I started my Bachelor of Science in mechanical engineering at TU Delft, it would have been difficult for me to predict the path that would eventually lead to this thesis. Firstly, working on a hydrogen race car for a year before starting my Master was not something I had expected, but provided invaluable experience and friendships. Switching from mechanical to space engineering was somewhat less surprising though, considering my interests. When later choosing a topic for my thesis, I tried to find something where I could apply my love for mechanical engineering design and prototyping work with space applications. I can safely say this has been a success, and a thoroughly enjoyable experience.

This success is in no small part due to the aid of others, whose contributions I would like to acknowledge here. First, I would like to thank my supervisor Barry Zandbergen for his unwavering enthusiasm and support, as well his valuable insights and comments. This project was also made possible in its current form by Frank Overes and Daan Treurniet, who lent their expertise and time by CNC machining several key components of the thruster, for which I am most grateful. My gratitude also goes to Leon Roessen and Rob van der List for their help regarding manufacturing, together with Durga Mainali for his aid with microscope imaging and polishing. Furthermore, my thanks go to Şevket Uludağ for electronics and soldering support, and Vidhya Pallichadath for helping with component acquisition. Lastly, I would like to extend my thanks to my fellow students in the 8th floor master room for the many coffee breaks and their technical insight, and to my friends and family for their non-technical support.

Huib Versteeg
Delft, April 2020

Abstract

A propulsion system provides satellites with the ability to perform attitude control, station keeping, and orbital manoeuvres. This in turn allows them to extend their mission duration and follow more complex flight paths. With the emergence of ever smaller satellites in the past few decades, the need has arisen for propulsion systems to shrink in size, so that they may be used on such satellites as well.

At the chair of Space Systems Engineering of Delft University of Technology, one such system is currently being developed: a vaporizing liquid micro-thruster. This operates by resistively heating a stream of liquid to a superheated vapour and expanding this vapour through a nozzle to supersonic speeds for thrust generation. Its current design is fabricated out of silicon using Deep Reactive Ion Etching (DRIE), a common MEMS production method also used for similar thrusters elsewhere. Unfortunately this fabrication method suffers from long lead times for new designs and a high total cost due to the use of highly specialized equipment. This impedes design iteration and thrust model validation.

To alleviate these issues, wire electric discharge machining was identified as a possible cheaper and faster alternative for creating the prismatic geometry of the supersonic nozzle and heating chamber. To investigate this, a conceptual design for a breadboard micro-resistojet was made around this fabrication method. This was then refined into a detailed design using analytical models to predict thrust, heating and mechanical behaviour. Main points of the design include the use of commercial off-the-shelf cartridge heaters, soft copper sealing surfaces for the nozzle geometry that also function as heat spreaders, and laser-cut metal foam for exchanging heat with the propellant.

The design was subsequently fabricated, after which the geometry of the created nozzle and the leak-tightness of the design were verified. Vacuum thrust tests were then performed with nitrogen as propellant, from room temperature up to 400 °C. For this range of temperatures, throat Reynolds numbers decreased from 3800 down to 1700, with thrust varying between 11.8 and 13.5 mN. Meanwhile, specific impulse increased from 63 to 88 s, though specific impulse efficiency decreased from 87 to 81 %. Thrust performance measurements were in agreement with those found by others for a comparable DRIE-based micro-thruster, verifying the breadboard micro-resistojet and its fabrication method.

Contents

List of Figures

List of Tables

Nomenclature

Acronyms

CAD	Computer-Aided Design
COG	Centre Of Gravity
COTS	Commercial Off-The-Shelf
DASML	Delft Aerospace Structures and Materials Laboratory
DEMO	Dienst Elektronische en Mechanische Ontwikkeling / *Department for Electronic and Mechanical Development*
DRIE	Deep Reactive Ion Etching
EDM	Electric Discharge Machining
IRT	Ideal Rocket Theory
LPM	Low Pressure Micro-resistojet
MEMS	Micro-Electro-Mechanical Systems
RID	Reactor Institute Delft
sccm	standard cubic centimetres per minute
SpE	Space Engineering
SSE	Space Systems Engineering
TB	Thrust Bench
TTC	Thrust Test Cold
TTH	Thrust Test Hot
TU Delft	Delft University of Technology
VLM	Vaporizing Liquid Micro-thruster
WBS	Work Breakdown Structure

Symbols

A	Area	[m^2]
a	Slope of actuator current to force relation	[$mN\,A^{-1}$]
a_{sf}	Foam specific surface area	[m^{-1}]
c^*	Characteristic velocity	[$m\,s^{-1}$]
C_D	Discharge coefficient	[–]
$C_{F,loss}$	Thrust coefficient loss factor	[–]
C_F°	Characteristic thrust coefficient	[–]

C_{F}	Thrust coefficient	[–]
c_p	Specific heat at constant pressure	[J kg^{-1} K^{-1}]
C_θ	Divergence loss factor	[–]
d	Diameter	[m]
d_{c}	Foam diameter of a cubic representative unit	[m]
d_{f}	Foam mean fibre diameter	[m]
D_{h}	Hydraulic diameter	[m]
d_{p}	Foam mean pore diameter	[m]
E	Elastic modulus	[Pa]
F	Foam inertial coefficient	[–]
F	Force	[N]
f	Frequency	[Hz]
F_{ij}	Radiation heat transfer factor	[–]
g_0	Standard gravitational acceleration	[m s^{-2}]
h	Height	[m]
h	Specific enthalpy	[J kg^{-1}]
h_{sf}	Foam convective heat transfer coefficient	[W m^{-2} K^{-1}]
I	Electric current	[A]
I	Second moment of area	[m^4]
I_{sp}	Specific impulse	[s]
J	Radiosity	[W K^{-4}]
K	Foam permeability	[m^2]
k	Thermal conductivity	[W m^{-1} K^{-1}]
L	Length	[m]
$\dot{m}$	Mass flow	[kg s^{-1}]
M	Mean molar mass	[kg mol^{-1}]
M	Moment	[N m]
m	Mass	[kg]
n	Number of	[–]
Nu	Nusselt number	[–]
$\dot{p}$	Pressure rate of change	[Pa s^{-1}]
$\mathscr{P}$	Perimeter length	[m]
P	Power	[W]
p	Pressure	[Pa]

PPI	Foam pores per linear inch	[inch^{-1}]
Pr	Prandtl number	[–]
$\dot{Q}$	Heat flow	[W]
$r_{\mathrm{t,c}}$	Nozzle throat radius of curvature	[m]
R	Tube mean wall radius	[m]
R	Universal gas constant	[J mol^{-1} K^{-1}]
Re	Reynolds number	[–]
R_{ij}	Radiative thermal resistance between surfaces i and j	[m^{-2}]
SEE	Standard Error of Estimate	[–]
T	Temperature	[K]
t	Time	[s]
t	Tube wall thickness	[m]
V	Voltage	[V]
V	Volume	[m^3]
v	Velocity	[m s^{-1}]
W	Weight	[N]
w	Width	[m]
x	Distance	[m]
α	Thermal expansion coefficient	[K^{-1}]
γ	Specific heat ratio	[–]
ϵ	Foam porosity	[–]
ϵ	Grey body emittance	[–]
ϵ	Nozzle expansion area ratio	[–]
ε	Heater effectiveness	[–]
η_{heat}	Heating efficiency	[–]
θ	Nozzle divergent half angle	[°]
κ	Stiffness	[N m^{-1}]
λ	Force conversion factor	[–]
μ	Viscosity	[Pa s]
ξ_{F}	Specific impulse or thrust coefficient efficiency	[–]
ρ	Density	[kg m^{-3}]
σ	Material stress	[Pa]
σ	Standard deviation	[–]
σ	Stefan-Boltzmann constant	[W m^{-1} K^{-4}]

ϕ	Thrust misalignment error	[°]
χ	Foam tortuosity	[–]
ψ	Nozzle convergent half angle	[°]

Subscripts

a	Ambient conditions
act	Electro-magnetic calibration actuator
as	Assembled
c	Thrust chamber / stagnation conditions
da	Disassembled
exp	Experimental results
e	At the nozzle exit
el	Electrical
end	After end of thrust
f	Fluid
ideal	Calculated with IRT
mid	During thrust
p	Propellant
start	Before start of thrust
t	At the nozzle throat
tb	Thruster body
w	Wall

1 Introduction

A propulsion system provides satellites with the ability to perform attitude control, station keeping, and orbital manoeuvres. This in turn allows them to extend their mission duration and follow more complex flight paths. With the emergence of ever smaller satellites in the past few decades, the need has arisen for propulsion systems to shrink in size, so that they may be used on such spacecraft as well.

At the chair of Space Systems Engineering (SSE) at the Delft University of Technology (TU Delft), two concepts for such a micro-propulsion system are currently being developed: a Vaporizing Liquid Micro-thruster (VLM) and a Low Pressure Micro-resistojet (LPM), the first of which is of interest here. This thruster operates by resistively heating a stream of liquid to a superheated vapour and expanding this vapour through a nozzle to supersonic speeds for thrust generation.

The current design of the VLM stems from 2014 [54], and has since undergone several iterations and improvements [14, 41, 67]. This design is based around the use of semiconductor fabrication techniques as also used for other Micro-Electro-Mechanical Systems (MEMS), specifically the use of a silicon wafer as a base for subtractive and additive manufacturing. The process used to create the fluid channels, Deep Reactive Ion Etching (DRIE), can produce small features with high accuracy and low surface roughness [4], which are desirable qualities for a micro-thruster.

This process does have some drawbacks though, primarily the high batch cost per silicon wafer, which is currently estimated at roughly $€7 \cdot 10^3$. Each wafer can contain up to 40 individual thrusters, bringing down the price per unit to a more manageable $€2 \cdot 10^2$, though still requiring a large up-front investment. The production steps are also unfortunately relatively complex, with long lead times for the production of new designs. The process additionally puts constraints on the material and geometry that can be used, as DRIE can only easily create 2D extrusions in silicon. Furthermore, the etch rate for DRIE depends on the aspect ratio of the channel: the ratio of channel width to depth. As a result, the cross section of very narrow channels can become trapezoidal instead of rectangular. This affects the nozzle throat in particular, illustrated by a 10 to 15 µm deviation over a 100 µm deep trench that was recently observed [19].

Besides production cost, high temperature operation is also a point of interest as this can increase the specific impulse of the thruster [70]. The temperature at which the Delft VLM can operate is currently limited by its interface due to the use of low melting point materials [14, 41]. Connected to this issue is the need for additional thermal insulation to limit heat loss to the environment. The latest tests of the current design showed power efficiencies of only 25 % at 200 °C [14].

With this in mind, the following main objective is formulated for this project:

To realize lower production costs and higher temperature operation of the Delft VLM by *designing a version using alternative fabrication techniques, creating a prototype, and performing basic functional verification of said prototype.*

The following sub-goals are defined to achieve this:

1. To design and build a prototype micro-resistojet by using alternative fabrication techniques.

2. To verify the functionality of the prototype by testing it with the SSE micro-thruster measurement equipment and comparing its thrust performance to data from a reference thruster by Bayt [4].
3. To find out how the new thruster compares to the current VLM design in terms of production cost, production time, and high temperature operation.

Alternative fabrication techniques for this project are defined to be those that are not based around the etching of silicon wafers. Thrust testing of the created design will only be performed with gaseous N_2, in the interest of simplicity and time, as equipment for this is most readily available [68]. As a result, the term micro-resistojet is often used instead of VLM in this report, as it covers the same function, though with more possible propellants (such as N_2).

The choice to verify the design by comparison with a reference design other than the Delft VLM was mainly made because of initial size limitations for the chosen fabrication method and the absence of validated thrust models at this scale. The absence of hot gas thrust data for the Delft VLM was also a factor, which Bayt did provide for temperatures up to 400 °C. These reasons are further discussed at the start of chapter 3.

Besides thruster production, efforts have also been made in previous thesis projects [27, 41] and by others [15] to find simple analytical models to predict the thrust performance of supersonic micro-nozzles. The small scale of these devices results in operation at low Reynolds numbers, where losses from viscous effects become increasingly dominant. The limited experimental data available shows these losses ranging anywhere from 10 to 85 % of ideal performance. The quantity and quality of this experimental data is unfortunately not yet sufficient for model validation [68]. Numerical flow simulations have also been used [15, 19, 36], but these are currently considered to be too time consuming for initial design phases. With this in mind and in light of successes encountered during this project with production and testing of the thruster prototype, a fourth goal was added regarding analytical thrust modelling:

4. To find out to what degree the analytical thrust model suggested by Makhan [41] can predict the behaviour of the prototype, by comparing modelled and measured thrust results.

Four main research questions for the project are then formulated as follows:

1. How can a micro-resistojet be created using alternative fabrication techniques?
2. How does the measured thrust performance of the prototype compare to data from the reference thruster design by Bayt?
3. How do the production cost, production time, and high temperature operation of the prototype compare to that of the current VLM?
4. How does the measured thrust performance of the prototype compare to predictions from the analytical model suggested by Makhan?

To achieve the given objective and answer the research questions, first a literature study [68] was performed to find a suitable nozzle fabrication method and gain inspiration from other micro-thruster designs. Following this, a basic thruster design was made, focusing on production cost and high temperature operation. The design was made so that it could first be tested as a cold gas system, and later as a resistively heated hot gas system after some minor upgrades. This two-stage approach to fabrication and testing was used to have a testable system early on, leaving enough time to fix potential issues. Both the cold and hot gas version of the system were tested for leaks and the geometry of the created nozzles was measured. Vacuum thrust measurements were made with nitrogen as propellant, which were compared to modelled values and experimental results from the reference thruster. Heat loss from the hot gas system was also measured and compared to modelled values.

In this report, first the main findings from the abovementioned literature study are given in chapter 2. Next, concept generation and selection for key parts of the system is discussed in chapter 3. In chapter 4, the selected concepts are worked out further to create a detailed design. Chapter 5 then shows the fabrication process for the cold gas system from this design, for which the thrust test are discussed in chapter 6. The fabrication steps to upgrade the system for hot gas operation are then laid out in chapter 7, with the hot gas thrust tests in chapter 8. Lastly, conclusions for the project are given in chapter 9, and recommendations in chapter 10.

2

Thruster fabrication background

This chapter serves to provide a background for the design process and choices by going over the designs and fabrication techniques of similar thrusters, as well as possible other applicable fabrication methods for supersonic micro-nozzles. Here, a supersonic micro-nozzle is defined to be a converging-diverging nozzle, with throat dimensions $< 1\,\text{mm}$, wherein gas is accelerated from subsonic to supersonic speeds.

The information contained in this chapter summarizes parts of an earlier literature study by the current author [68]. First, the different iterations of the two types of resistojet developed at the TU Delft Space Engineering department (SpE) are laid out in section 2.1, looking at their fabrication and design. Several further fabrication methods are then discussed which have previously been used to create similar micro-thrusters. Following this in section 2.3, several more possible fabrication techniques are laid out for which no example micro-thrusters were found. Next, in the interest of limiting heat loss for the prototype, insulation strategies found on earlier resistojets are discussed in section 2.4. Lastly a comparison is made between possibly applicable fabrication techniques and a general conclusion to the chapter is given in section 2.5.

2.1. Previous TU Delft micro-resistojets

There have been a decent number of projects at the SpE department to develop small or micro-resistojets in the past, which are briefly discussed here, to provide a background for the current project. Two separate approaches can be identified in recent years: projects that use traditional machining and Commercial Off-The-Shelf (COTS) components, and ones that rely primarily on silicon-based MEMS techniques. These systems and their main points of interest are discussed below.

2.1.1. Traditional manufacturing

Early efforts to create a small resistojet at the SpE department were made by Rycek [57] in 2005, followed by Ferreira [18] in 2008. Both used helically wound tube with a high current running through it to resistively heat propellant inside of it. These were quite large and produced a thrust of around 1 N, several orders of magnitude more than desired here. The heating efficiency for the latter was quite high though, at around 85 %.

Almost a decade later in 2015, Krusharev [32] attempted to create a VLM with COTS heaters and machined aluminium parts, but was not able to measure any thrust during tests. Following this, Stohr [59] used one of the heaters from the previous project for a design with a new, simplified enclosure, but was also unsuccessful due to a leak that could not be remedied. The designs from these two projects can be seen in Figure 2.1.

In all cases the nozzles were axisymmetric and machined with very small drill bits. Because of this the shape of the convergent and divergent nozzle sections was fixed to the drill geometry, resulting in $\geq 30°$ convergent and divergent half angles. Very small throat diameters down to 0.06 mm have been made though [33].

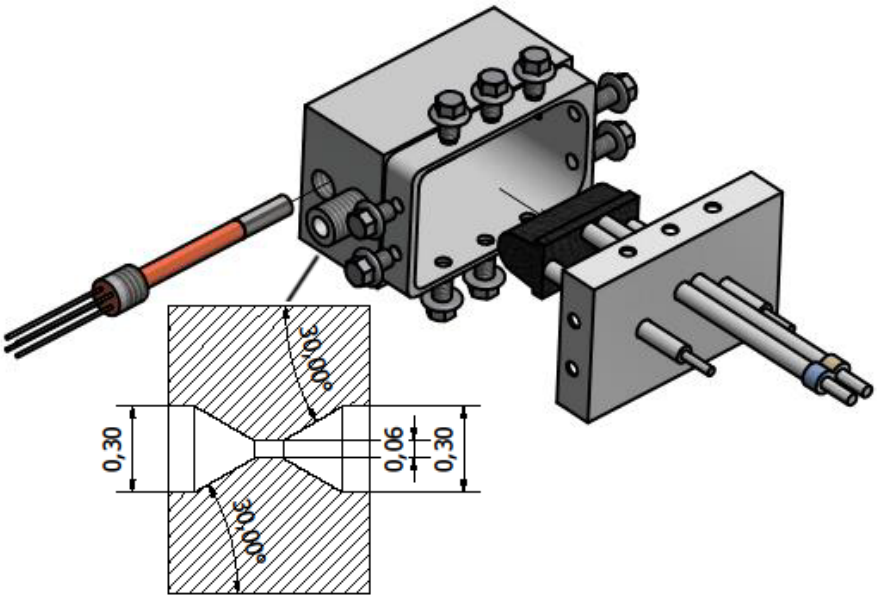

(a) Design by Krusharev [32].

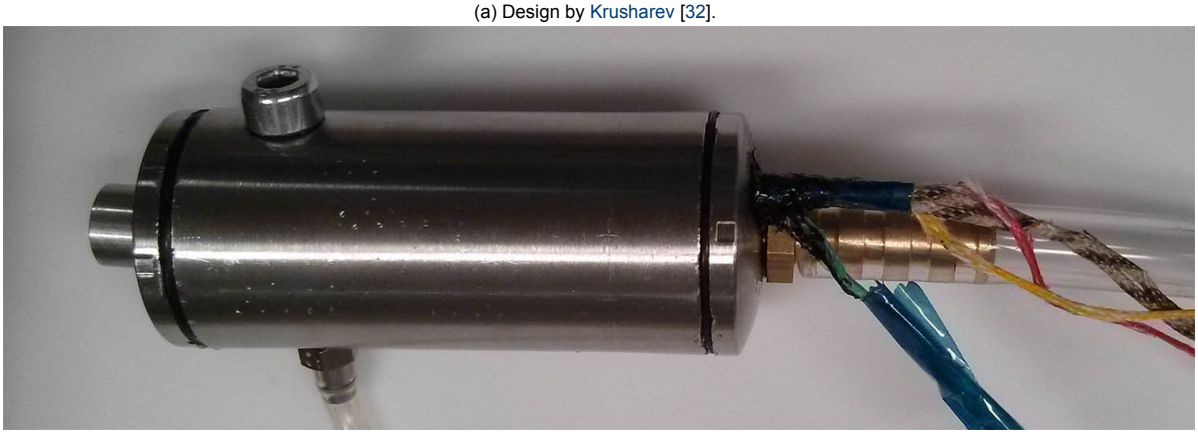

(b) Engineering model by Stohr [59].

Figure 2.1: Example design and engineering model of TU Delft VLMs from previous projects [32, 59].

2.1.2. Silicon etching

Parallel to the traditionally machined thrusters, several other projects looked into the use of silicon MEMS based thruster designs, with channels created using DRIE. The first to do this at TU Delft was Mathew [44] in 2011, with assistance from electrical engineering faculty staff. The resulting design can be seen in Figure 2.2, which is much smaller than the clasically machined alternatives and has an integrated thin film heater on top. It also has a planar 2D instead of an axisymmetric nozzle geometry, due to the limitations of DRIE.

Several later projects were dedicated to improving this design and measuring its thrust performance [14, 41, 54, 67], though so far only with nitrogen propellant. During this process, the concept of using immersed thin-wire heaters was rejected due to their fragility, and the use of two etched silicon halves for creating the nozzle geometry was also discarded based on alignment issues [67]. The eventual design is much like the initial one by Mathew, though with a wider heating section and meandering propellant channels for maximizing heat transfer and minimizing the chance of liquid droplets getting to the nozzle [54]. One side is now covered with glass, giving visual access to propellant channels. The heater is also once again a thin film version on the exterior of the silicon half, though now made from molybdenum instead of aluminium for higher temperature operation. A different interface was also created by using Teflon as a sealing material for propellant delivery and spring-loaded pins instead of wire-bonds for electrical power [13]. This can be seen together with the channel design in Figure 2.3.

There are still several issues with this design though, as mentioned in the introduction. Batch

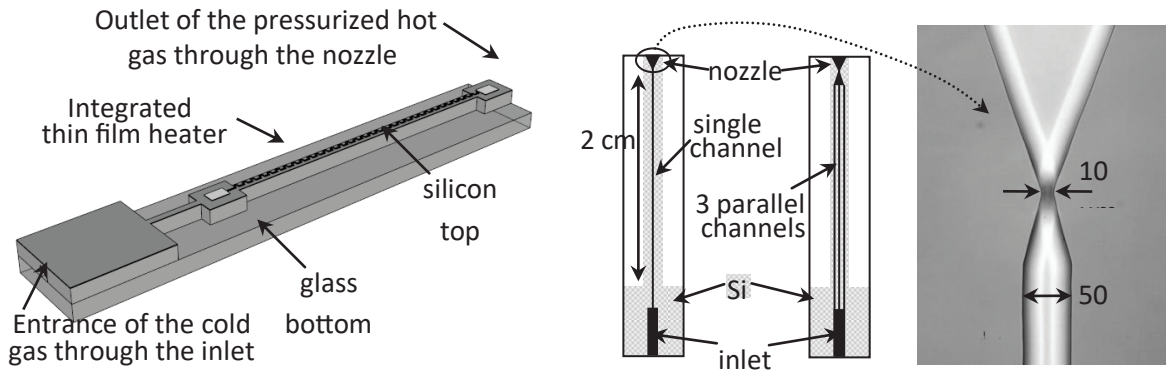

Figure 2.2: Micro-thruster design by Mathew [44].

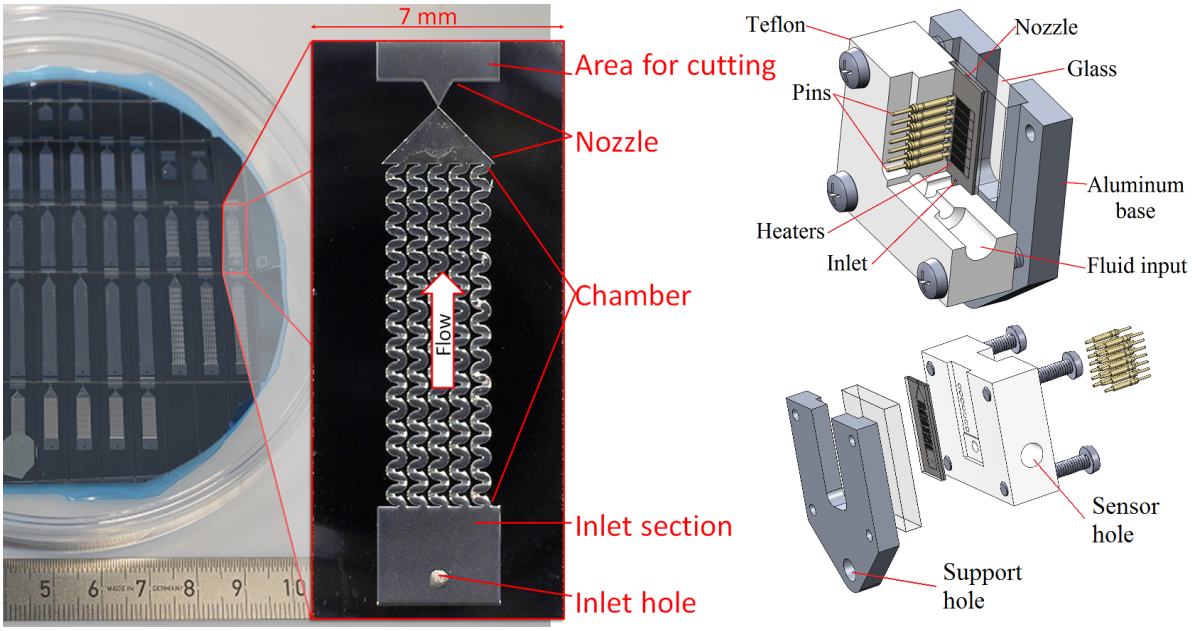

Figure 2.3: Image of a silicon wafer with one of the current thruster designs (left) and the interface for using it (right) [14].

fabrication cost and lead time for new designs are high due to the specialized equipment and clean room work involved. The propellant and power delivery to the chip has also become a bottleneck, as it was designed without a clear interface in mind. This has resulted in the current version not being able to go above roughly 150 °C without warping and leaking due to the reliance on Teflon for sealing. Earlier issues with dimensional accuracy of small features [67] fortunately seem to have been fixed in the latest batch of thruster chips [19].

On the other hand, silicon etching can create accurate features several times smaller than what is possible with traditional machining, all while maintaining an excellent surface finish. Integrated thin film heaters are also nigh impossible to make without chemical etching methods as used here. Furthermore, the process is very well suited for larger production quantities with a constant design, as several dozen chips can be made in parallel.

2.2. Similar micro-thrusters and their fabrication

To see what kind of fabrication techniques and thruster designs are already in use elsewhere, and as inspiration for the current design, part of the aforementioned literature study was dedicated to finding similar thrusters. The similarity definition used was: "*Thrusters using a sonic nozzle to accelerate a propellant gas to supersonic speeds, with throat dimensions in the order of 100 µm or a thrust magnitude in the order of 10 mN.*" Ones that were found with a fabrication method specified are discussed below,

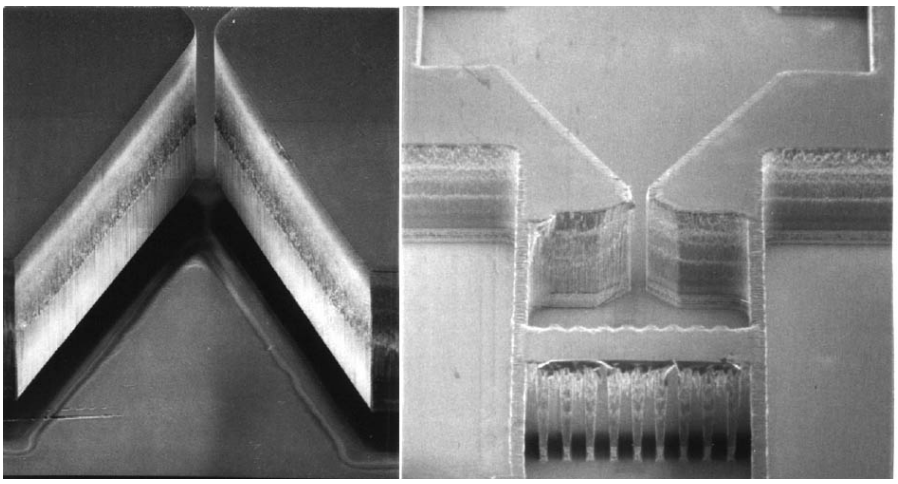

Figure 2.4: Nozzle divergent of the thruster by Bayt [4] as seen from the exit plane (left) and heating fins with nozzle from the opposite side (right).

grouped by fabrication method.

2.2.1. Silicon etching

DRI-Etching of silicon has also widely been used outside of TU Delft, first by Bayt [4] in 1999. They managed to create several different nozzle shapes and measure their thrust using N_2 as propellant, while resistively heating the device to temperatures up to $\sim$ 700 K. The nozzle they created can be seen in Figure 2.4.

Further developments include for example the use of DRIE to create a monopropellant micro-thruster by Hitt et al. [24] and later by Yuan and Li [69]. Cen and Xu [12] used the technique to create a VLM, focusing on measuring boiling behaviour and instability when using water as propellant, and also included some limited thrust measurements. Further developments include the use of the aspect dependent etch rate of DRIE to create a nearly axisymmetric nozzle by Palmer et al. [52]. More recently, a more standard planar nozzle was applied in a MicroSpace commercial cold gas system by Manzoni and Brama [42].

2.2.2. Chemical etching

Besides chemical etching of silicon as in the previous section, other materials were also found to be used with similar processes. First is a micro-thruster made of glass by Huh and Kwon [25], using H_2O_2 and ethanol as propellant. The planar geometry of the design is etched out of UV-sensitive glass using hydrofluoric acid which can create relatively small geometries, though also with slightly rounded edges, see Figure 2.5. Second is a thruster by Carroll et al. [11] which uses microcavity discharge heating with a 100 µm diameter nozzle throat that was etched into metal, though more specifics on the fabrication are not given.

Chemical etching in general can produce components at small enough scales for the current project and should be economical for small batch sizes, though issues with channel wall straightness and exact control of the dimensions may arise [20, 55]. The author currently has no knowledge of facilities for such a process at TU Delft, other than the ones for silicon chip production, thus an external company such as VECO[1] may have to be used.

2.2.3. Co-fired ceramics

A completely different method for micro-thruster fabrication can be found in the use of co-fired ceramics. These start as malleable thin sheets/tapes of ceramic granules, bound together by plastic. The desired shape is created in this malleable form, after which several layers can be stacked, with screen printed metal circuits in between if desired, before being compressed and sintered to create a full component.

Several examples of using this method were found, starting with a thruster made by Lekholm

[1] https://www.vecoprecision.com/technologies/chemical-etching

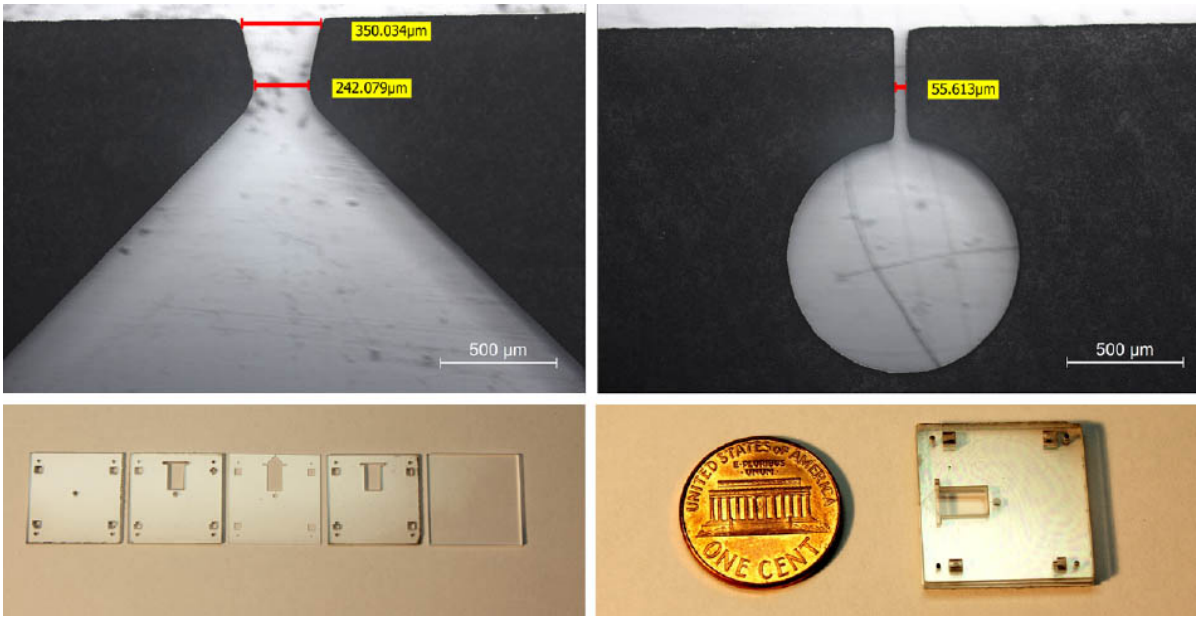

Figure 2.5: Micro-thruster etched out of UV-sensitive glass by Huh and Kwon [25]

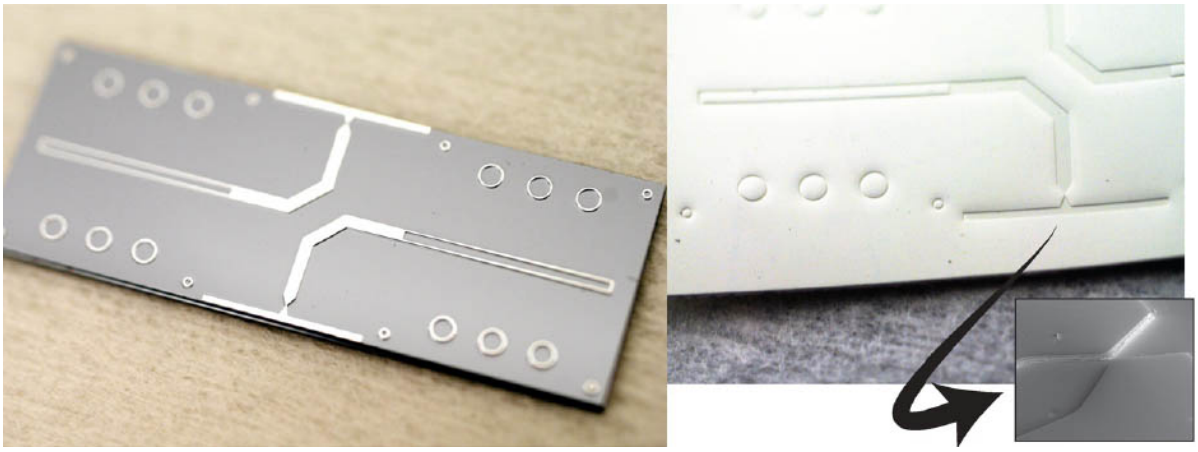

Figure 2.6: DRI-Etched mould (left) and corresponding embossed ceramic tape (right) by Lekholm et al. [38].

et al. [38], who used a DRI-Etched silicon mould to emboss a planar nozzle shape into the ceramic tape, see Figure 2.6. The component was heated to 1000 °C before a crack formed through it from thermal stresses. Later, Khaji et al. [31] created a monopropellant thruster with co-fired ceramics, citing high corrosion resistance and low thermal conductivity as reasons for choosing the material. They used a micro end-mill to create the thruster geometry, and were able to reach around 300 °C before the thruster cracked. Following this, Åkerfeldt [1] looked into ways to minimize the probability of thermal stress induced cracking as seen in the previous two thrusters. To this end they created a simple version that could be rapidly heated to 1461 °C without cracking, but were limited in the temperature they could sustain due to melting of their electrical interface. Lastly, Sturesson et al. [60] used many layers to create an out-of-plane axisymmetric nozzle with three different types of heaters: thin film resistive, suspended wire resistive and plasma resonator. They also measured the thrust and specific impulse, which was not done for the other three devices.

In general, co-fired ceramics can provide high temperature and corrosion resistance with reasonable feature accuracy, but may suffer from thermal stress cracking if not well designed. Equipment for this process is also not readily available at TU Delft.

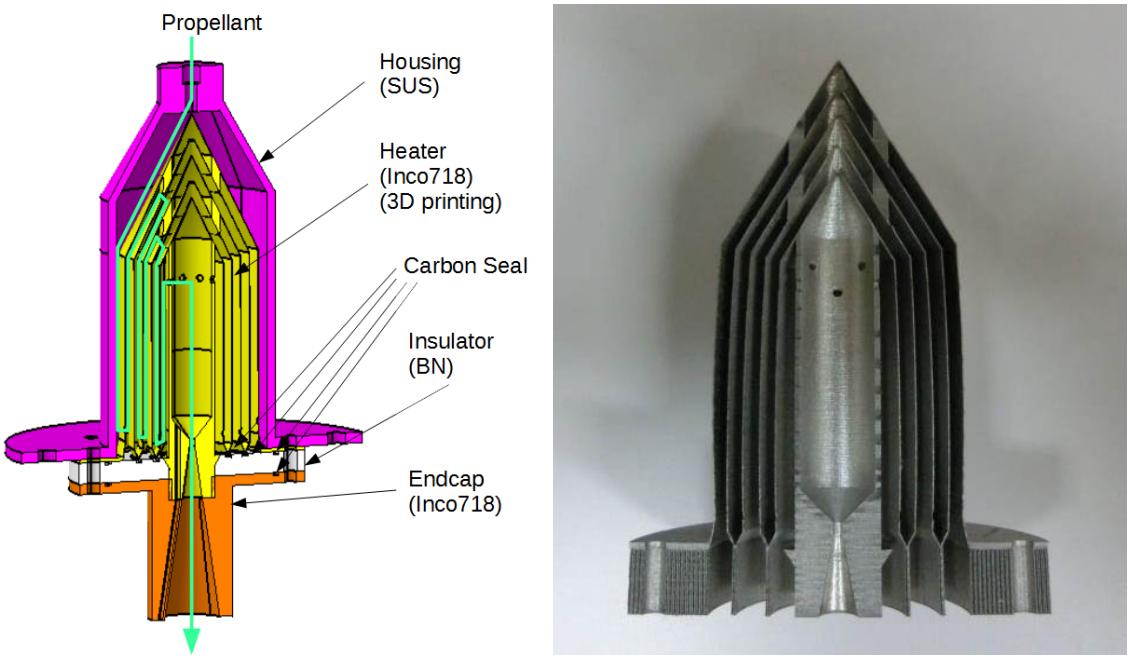

Figure 2.7: Metal 3D printed resistojet by Nakata and Kinefuchi [50]: design (left) and printed component cut in half (right).

2.2.4. Metal 3D printing

Plastic 3D printing has been used on several occasions to create cold gas thrusters and even full systems with propellant storage, tubing and valve connections [2, 23]. These methods are unfortunately unsuited for a VLM due to the high temperatures involved. Metal 3D printing is still an option though, which is discussed here.

Two nearly identical examples were found of this method being employed for small / micro-thrusters [50, 56], the latter of which can be seen in Figure 2.7 These also showed many design similarities to the much older macro-resistojet by Donovan et al. [17] (Figure 2.10c). All of these use an axially symmetric design with thin-walled channels guiding the propellant back and forth towards the nozzle in the centre. The channel walls then also act as high-current resistive heaters. 3D printing allows for making complex geometries such as these with relative ease, but most commercially available options have relatively high surface roughness and low resolution for the application here, placing a lower limit on component size. This is exemplified by both thrusters in this section having a one to two orders of magnitude larger throat area than desired here. For slightly larger thrusters, this could definitely be an option though, for example using micro laser sintering by Precipart[2].

2.2.5. Powder blasting

A previous cooperation between Dutch universities and research agencies, including TU Delft, produced T^3µPS: a cold gas micro-propulsion system that was used on-board the 3-unit CubeSat Delfi-n3Xt. The nozzle that was created for this made use of a specially developed powder blasting process to create an axially symmetric divergent in a thin sheet of Pyrex. The nozzle throat was subsequently rounded off and the other walls smoothed out by annealing the component at high temperature [39, 47]. These techniques could produce a nozzle of appropriate size and quality for this project, but it is unclear if the necessary equipment is still available. The nozzle geometry is also mostly fixed, resulting in a very narrow design space.

2.3. Other possible fabrication methods

Not all methods that could be applied for this project have necessarily been used for previous micro-thrusters / resistojets. To find other fabrication options, the processes database in [20] was combed

[2] https://www.precipart.com/products-capabilities/custom-mechanical-components/micro-3d-printing/

Figure 2.8: Component created with micro water-jet cutting by FinePart, ball-point pen for scale.

through, and a conversation was had with employees of the TU Delft mechanical production department DEMO[3]. This resulted in the list of methods found in this section. Methods not seen below, such as casting or deformation methods, were excluded based on e.g. achievable accuracy, minimum feature size, surface roughness or the need for moulds / extra process steps.

2.3.1. Micro water-jet cutting

As a first of three reasonably accessible sheet cutting methods, water-jet cutting can be used to create planar nozzle geometries, though with two open sides. A commercial example of a micro scale version of such a process are machines by FinePart[4], with slit widths of only 200 to 300 µm (experimentally down to 50 µm), taper-free cuts, and positional accuracy down to 2.5 µm. An example of a component made in this way can be seen in Figure 2.8 The process is also usually quite fast, has practically no material limitations, introduces no thermal stresses into the material, and requires no separate holes to be drilled for closed internal cuts.

The main downside is that only lower precision water jet cutters are available at TU Delft, requiring the production to be outsourced. The geometry limitation of prismatic cuts also means that two fluid channel sides have to be sealed off after fabrication, and that the integrated heater and heat exchanger concept from the current VLM can no longer be used. Lastly, the minimum slit width also results in a wider nozzle throat than what has been made with etched silicon (down to $\sim$ 20 µm [4, 41]).

2.3.2. Micro laser cutting

Laser cutting is the second possible sheet-cutting method, where material is ablated thermally instead of mechanically. Achievable manufacturing quality with this once again highly depends on the machine that is used. Known available equipment at TU Delft at the 3ME faculty is unfortunately only suited more for larger scale sheet-metal work. Commercial micro-scale options are available though, for instance by Vuichard SAS[5], who can cut slits down to 27 µm with surface roughness values of $R_a = 0.2$ µm. Pros and cons for this are essentially the same as for water-jet cutting, though regions around the cut may also be thermally affected by the process.

2.3.3. Wire-electric discharge machining

As the last of the three prismatic cutting processes, precision wire Electric Discharge Machining (wire-EDM) is actually available at TU Delft. This is also known as spark-erosion as the material is evaporated

[3]Dienst Elektronische en Mechanische Ontwikkeling / *Department for Electronic and Mechanical Development*
[4]https://www.finepart.com/about-awj-our-technology/waterjet-basics/
[5]https://vuichard.com/micromachining-expertise/high-precision-laser-micro-cutting/

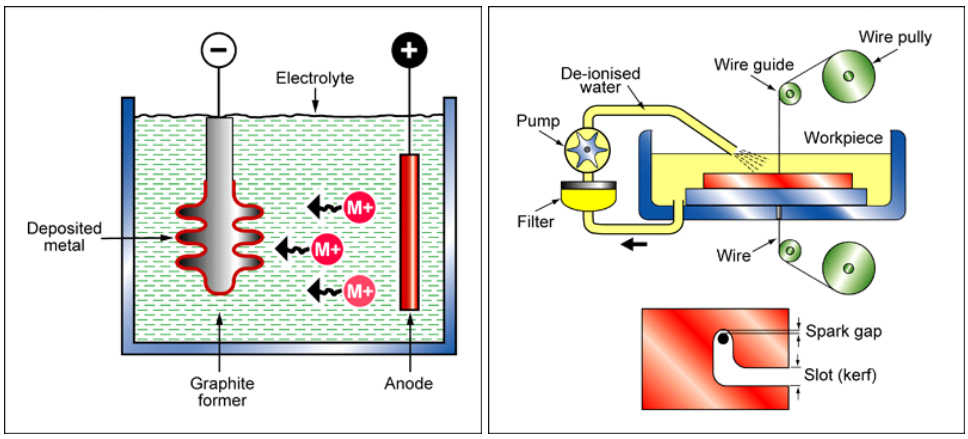

(a) Electroforming (b) Wire-EDM

Figure 2.9: Schematic representation of electroforming and wire-EDM [20].

through numerous tiny sparks between a cutting electrode and workpiece, see Figure 2.9b. The cutting electrode in the case of wire-EDM is a thin metal wire that is continuously refreshed to maintain its integrity and shape. Surface roughness of the finished cut is comparable to the previous two cutting methods, though the process is somewhat slower [20]. Slit widths can go down to roughly 130 µm for the machines available, which is limited by the wire thickness of 100 µm. Due to the nature of the process, only conductive materials can be cut, mostly limiting the material choice to metals. Because of the use of a wire, very high aspect ratio cuts can be made though, with the available machines being able to cut through 25 cm thick material. This would be at a much slower pace though, as cutting speed is inversely related to material thickness and desired surface roughness for this process [29].

2.3.4. Micro-electric discharge milling

EDM can also be used for microscopic milling operations by having an end-mill-like cutting electrode. Devices that perform such operations are for instance made by Sarix[6] and several of these are available at DEMO. The electrode is a short, thin, spinning piece of metal that is ground down to a desired size using wire-EDM before each milling operation. Because the electrode is not continuously refreshed like with wire-EDM, it suffers from similar erosion as the workpiece and must be re-ground intermittently, making this process slower and and more expensive. As an advantage over the cutting methods, EDM milling is not limited to prismatic cuts, but can create most geometries that would also be possible on a 3-axis end-mill.

2.3.5. Electroforming

Lastly, electroforming might be used to create the desired thruster nozzles. In this process, a shape negative mould / mandrel is submersed in liquid salt or a salt solution, after which it is electrochemically plated with the metal ions from the liquid, see Figure 2.9a. The mandrel is then removed to arrive at a component. This process has been used on larger thrusters (> 1 N) by [45] for instance, who created combined combustion chambers and nozzles out of iridium and rhenium. Refractory metals for extreme temperature applications can thus be used with this, though the equipment needed is highly specialized and unavailable at TU Delft. A mandrel of sufficient quality must also be made beforehand, requiring an extra fabrication step.

2.4. Resistojet insulation

Only a few of the micro-thrusters investigated here were designed with thermal insulation in mind. The insulation for a final thruster design is primarily in the interest of electrical power efficiency. For a breadboard prototype this is not a major concern, but the thruster should be able to reach its design temperature, which may be limited by its thermal losses and maximum heating power. For more inspiration on thermal insulation, larger resistojet designs were looked into.

[6] https://www.sarix.com/en/sx80-hpm-pulsar-en/

Several older designs were found, dating from 1965 to 1986, which all employed similar strategies to achieve low heat losses [17, 49, 51, 58]. Near the centre of the resistojet, just outside the resistive heater where the temperature is highest, several designs used multi-layered thermal radiation shields in a vacuum, usually made of refractory metals such as rhenium. For lower temperature regions further towards the exterior, layers of low thermal conductivity material such as granular zirconia were used. As a final measure, the propellant is made to go through regenerative cooling/heating channels before entering the main heating chamber. Example schematics from the work of Donovan et al. [17], Spisz et al. [58] and Page et al. [51] can be seen in Figure 2.10. As an example of how effective all these measures were, the thruster by [17] could reach 70 to 80 % heating power efficiency at temperatures up to 1950 K.

2.5. Conclusion

A number of possible fabrication techniques for supersonic micro-nozzles were identified. A summary of their advantages and disadvantages can be seen in Table 2.1 [68]. Based on this information, wire-EDM is currently seen as the most promising fabrication method for creating a planar micro-nozzle due to its relatively low cost, availability at TU Delft and good feature size and surface roughness. As a back-up, similar sheet cutting methods such as micro laser and water-jet cutting may also be used if the necessary equipment can be found and used elsewhere. These methods can only create prismatic cuts though, resulting in fluid channels with two open sides. In addition, the minimum channel width for wire-EDM (130 µm) is larger than what is possible with silicon etching. Combining these with an integrated heat exchanger and thin film heater, as used for the current silicon VLM, is also not possible. These issues will be dealt with during the design phase in the following two chapters.

In the interest of power efficiency and attainable thruster temperature, three main methods for limiting heat loss were also identified. These were the use of low thermal conductivity materials such as porous / fibrous ceramics or glasses, radiation shielding in high temperature areas, and using propellant for regenerative cooling when possible.

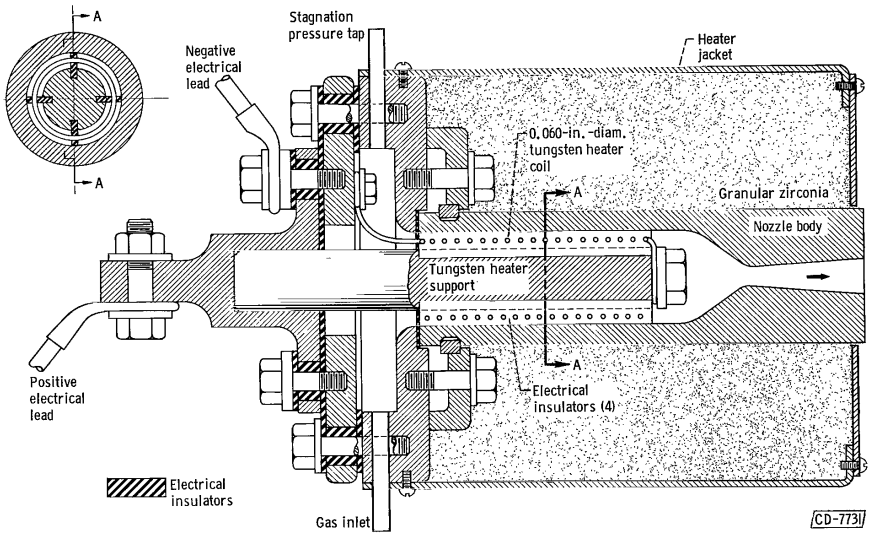

(a) Technical drawing of resistojet used by Spisz et al. [58].

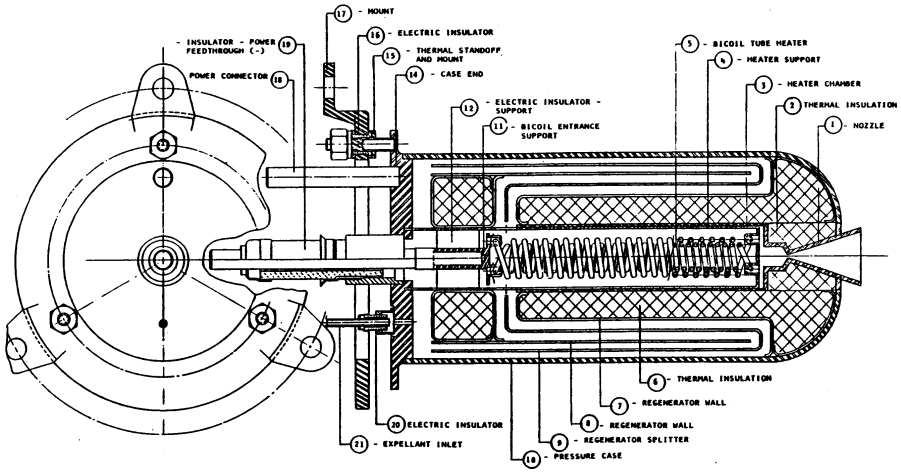

(b) Technical drawing of resistojet concept 3 (of 6) by Page et al. [51].

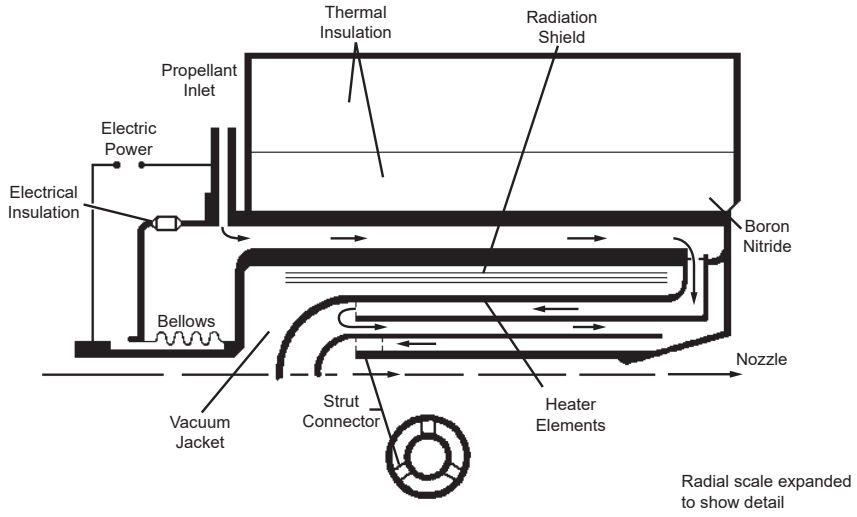

(c) Schematic drawing of resistojet used by Donovan et al. [17].

Figure 2.10: Schematic and technical drawings of older, larger resistojets [17, 51, 58].

Method	Feature size	Roughness	Equipment available?	Cost	Pros	Cons
DRI-Etched silicon	++	++	yes	−−	dozens at a time, integrated heater possible	very expensive per batch, slow design iteration
Co-fired ceramic tapes	+	+	no	?	High temperature & corrosion resistance	completely new process for TU Delft, thermal stress cracking
3D-printing	−	−−	no	?	Much design freedom for shape	limited selection of materials
Chemical etching	++	+	no	?	Parallelizable	Possible non-straight walls
Micro laser cutting	++	++	no	?	Relatively fast, many materials possible	only prismatic cuts
Micro milling	−	−	yes?	?	Simple	burr formation, geometry & size limitations
Wire EDM	+	++	yes	+	Parallelizable, very high aspect ratio cuts	Only for electrically conductive materials, prismatic cuts
Micro-EDM milling	++	++	yes	−	3D features possible	Slow
Electroforming	+	++	no	?	Parallelizable, geometric freedom	limited materials, mould required
Micro water-jet cutting	+	++	no	?	Relatively fast, many materials possible	only prismatic cuts

Table 2.1: Overview of possibly applicable methods for fabricating the nozzle geometry of a planar microthruster. Table from [68, p. 66]: "*A basic ordinal scale ranging from −− to ++ is used, as actual quantitative information is not always available.* [···] *For geometry, −− and − indicate that the property is unsuited for this project and to what degree. + and ++ is used wherever a similar outcome would be possible to the current thruster, with the first being for slightly less than desired performance and the second for the same results as with DRIE. For cost, this scale ranges logarithmically from very expensive (>€$5 \cdot 10^3$) per manufacturing run at −− to very affordable (<€$5 \cdot 10^1$) at ++.*"

3

Conceptual design

In this chapter the process of concept generation and selection for the design of the micro-thruster is discussed, in order to create a complete concept that can be worked out in detail in the next chapter. First, design guidelines are given in section 3.1, followed by an overview of which components are considered here in section 3.2. Next, concepts for each of the components are generated and selected in sections 3.3 to 3.7. A conclusion to the chapter is then given in section 3.8.

3.1. Design guidelines

Normally when creating a system, a set of requirements is laid out beforehand with which the end product shall comply. For this project, the end product will only be a proof-of-concept / breadboard prototype, not a component that could immediately be used as part of a larger system. Instead of strict requirements, somewhat more relaxed guidelines are therefore used, so as to not unnecessarily restrict the design while still guiding it towards the general desired outcome.

The first thing for which guidelines are laid out is regarding the size and shape of the thruster nozzle. For functional verification of the thruster, comparison of the thrust performance with a reference design was seen as the best option, due to a lack of validated analytical models which could otherwise have been used [68]. To reduce risk of faults during manufacturing, it would also be beneficial to not try to use a new fabrication technique near its functional limits, but instead choose a safer option regarding e.g. size and tolerances.

These two considerations, combined with the fact that little experimental thrust data has been published on planar micro-nozzles[68], resulted in only one suitable similar design: that of Bayt [4], specifically their hot gas version (see also section 2.2.1 and Figure 2.4). The nozzle in question has a throat width of 65 µm, a throat height of 491 µm, and a classic conical divergent section with an area ratio of 8.25. Its specifications are discussed in further detail in the next chapter, section 4.1, and its performance figures are given in Appendix A.

This is the only known planar nozzle resistojet with (extensive) published thrust performance results that uses the same propellant as intended here (N_2) *and* is heated resistively to a relatively high temperature (400 °C) *and* has a reasonable size for wire-electric discharge machining. This design also produced a thrust force that could still be measured on the available Thrust Bench TB-5m, simplifying testing. Other options were either unheated, too small, and/or did not use nitrogen as a propellant [9, 12, 41]. Here similar is taken to mean that measurement results from the prototype can be compared directly to those from the reference thruster, with few to no scaling conversions having to be applied. This results in the following guidelines:

1. The created thruster nozzle shall be similar to the heated design by Bayt:
    1. It shall have a similar throat size / throat Reynolds number.
    2. It shall have a similar in-plane shape (throat radius, divergent angle).
    3. It shall feature electrical heating of the thruster walls.
    4. It shall use nitrogen as a propellant.

Besides the physical design, the range of inputs to be used also has to be selected. The two main inputs are the pressure and temperature of the propellant just before entering the convergent part of the nozzle. Together with the nozzle geometry, these will determine the mass flow and thrust produced, and thus also which sensors/thrust bench can be used to measure these outputs. To keep similar throat Reynolds numbers as Bayt, the same range of temperatures will be used and the combination of pressure and throat size will be adjusted.

This temperature range (20 °C to 400 °C) also already introduces engineering problems regarding seals and material use (polymers and glues would melt or decompose), thermal insulation (high radiative losses) and thermal expansion. As a result, the design space will already be restricted to solutions that may also work if even higher temperatures are desired for future work. Furthermore, the highest temperature is above the critical temperature of water, so that operation as a VLM (the intended application) should be possible for most input pressures in future work without major design changes.

The geometry selected above was also designed for vacuum operation, as it uses a relatively high expansion ratio with low input pressure. This does mean that testing will have to be performed in vacuum, for which facilities are available. This also helps with negating thermal losses due to convection, simplifying the thermal insulation design, and lowering the needed heating power, as well as being more representative of the future intended application (spacecraft propulsion). In total, these guidelines are then as follows:

2. The range of inputs to the thruster shall be as follows:
    1. It shall be possible to heat the propellant up to 400 °C, starting at room temperature.
    2. The thrust chamber pressure shall result in a similar throat Reynolds number ($1 \cdot 10^3$–$3 \cdot 10^3$) as the heated design by Bayt.
    3. It shall be possible to test the thruster in a vacuum.

Thirdly, several outputs will have to be measured/computed for verification and comparison, thus the design will have to include several sensors or interface with compatible sensing systems. Of primary interest are the thrust related parameters as discussed in the next chapter, section 4.2, the same values as reported by Bayt, resulting in the following guidelines:

3. It shall be possible to measure or compute the following dynamic aspects of the thruster:
    1. The thrust force generated.
    2. The propellant mass flow through the nozzle.
    3. The propellant temperature at the nozzle entrance.
    4. The propellant pressure at the nozzle entrance.
    5. The specific impulse efficiency.
    6. The discharge factor.
    7. The throat Reynolds number.

The last three of these are derived quantities which rely on values from the first four as well as the nozzle geometry to be able to compute them.

Lastly there is also one hard requirement, in that there is a limited amount of funding available per thesis project at the department. This should also help to guide the project to the eventual goal of generating a more affordable VLM design than the silicon MEMS version:

4. Funding for the project from the SpE department shall be limited to €500.

Besides needing to comply with the design guidelines, concepts will be judged on the following four criteria, keeping in mind the limited time available for a thesis project and general engineering practice:

- Cost
- Difficulty / time to acquire / fabricate
- Chance of failure / risk
- Relevant physical performance (thrust generated, pressure drop, heat loss, etc.)

Concepts will be compared through qualitative reasoning, not through more rigorous means such as trade-off tables and / or quantitative calculations, primarily in an effort to save time so as to start detailed design and manufacturing early. This does mean that the possibility of not choosing the “best” concept is somewhat higher, but this is seen as less important than the time savings achieved.

3.2. Components considered

A number of concepts were made for the different components that are needed to make a functioning micro-resistojet. The choice of using wire-EDM to cut the nozzle profile out of a metal sheet is considered to be fixed and already restricts the design space substantially.

The system considered here then consists of the nozzle, thruster body, electrical propellant heater, propellant interface and sensors, and thermal insulation. Only the *interfaces* to sensors for thrust and mass flow measurements are considered as part of the system, as devices for these are already available at the department for the measurement ranges of interest, see chapter 6. The system boundary is thus set at the electrical connections to the data acquisition and power systems, the propellant connection to plastic tubing from the N_2 feed system, and the physical connection to the thrust test bench for transferring the thrust force.

In the following sections, first the nozzle profile and associated functions are discussed in section 3.3. Next, the heating source and solid to fluid heat exchanger are looked into in section 3.4, followed by the interface for the propellant in section 3.5. Lastly, propellant pressure and temperature sensing is discussed in section 3.6 and additional means of thermal insulation are outlined in section 3.7.

3.3. Nozzle profile

With the choice of wire-EDM for fabrication of the nozzle geometry, several design issues have to be addressed. Firstly, there is a certain minimum slit size that can be created due to the finite size of the wire used, which places a lower limit on the throat width and thus informs which nozzle geometry can be used. Secondly, only prismatic cuts can be made, so that two sides of the created geometry have to be created separately with a seal that can withstand 400 °C. Thirdly, as the nozzle now consists of 3 individual parts, a method for aligning these layers is needed. The concepts for solutions to these issues are discussed in this section in the order above. The term nozzle profile is used here to indicate the open-sided wire-EDM cut component containing the nozzle geometry.

3.3.1. Nozzle geometry

The throat height has practically no limit for the purposes of creating a micro-nozzle as this can go up to around $2.5 \cdot 10^5$ µm. For the machines present at TU-Delft, the minimum cutting width on the other hand is roughly 130 µm (for a single pass), two times larger than the throat width of the reference thruster. For this prototype however, this may not yet be an issue, as the design by Bayt featured a 65 µm wide by 491 µm high throat. The new thruster can then also be made to have similar Re_t (based on w_t) by scaling up the throat width by a factor 2 and simultaneously reducing the pressure by the same factor. This results in a chamber pressure of 1.34 to 1.52 bar (19.5 to 22 psi), which should be attainable for the existing feed system.

For future projects it may be beneficial or even necessary to be able to make nozzles with even smaller throat widths. To address this issue, the nozzle throat width may be adjusted *after* fabrication. Some inspiration was taken from the nozzle by Pedreira et al. [53]. who made an adjustable planar micro-nozzle by using two separately cut pieces for each contour side and sliding them more towards each other or further apart. One issue with this method would be keeping both sides parallel and keeping the edges of the throat aligned. This also creates another opening at the rear which has to be properly sealed and increases the possibility of leakage.

To (partially) avoid these two issues, here the the full nozzle contour with heating chamber and closed off rear is cut out of a single piece of metal. The nozzle contour sections of the cut-out would then simply be pushed together (or pulled apart) with a fine adjustment mechanism. The side walls of the chamber profile (or cut-out sections) can then be used as compliant joints, to allow for width adjustment without introducing additional holes, see Figure 3.1 for an example. The adjustment is then locked in place after sealing the nozzle profile in with the method chosen in the next section. Further working out of this adjustable throat width concept is left for future work.

3.3.2. Nozzle profile seal

For the silicon micro-thruster design, only the top of the thruster contour was open, instead of both sides for wire-EDM. This was sealed with a relatively standard MEMS fabrication method: either by anodically bonding a sheet of borosilicate glass on top or by fusion bonding it to another silicon wafer.

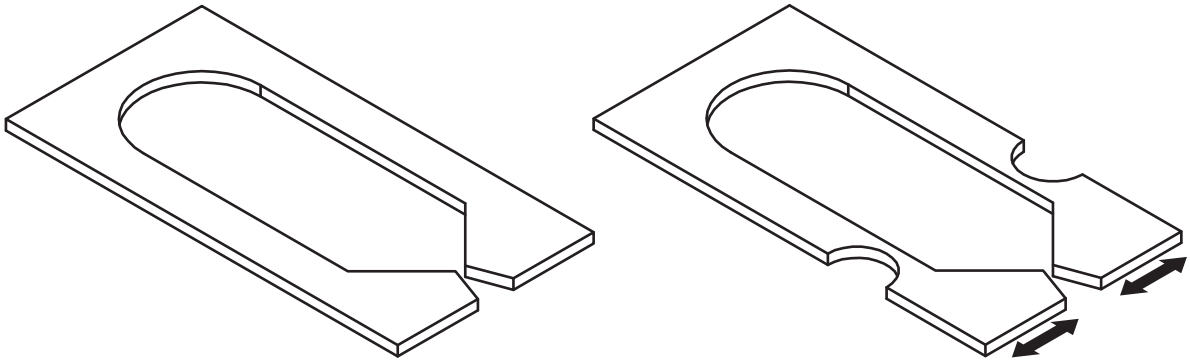

Figure 3.1: Wire-EDM cut nozzle concept, with a basic version (left) and one with explicit compliant joints for throat width adjustment (right).

Both these processes result in the material of the two layers fusing together and forming a leak-tight seal.

Anodic bonding is not an option for the metal profile used here, as this depend on glass and silicon having a similar coefficient of thermal expansion and the glass having a specific composition. It may be possible to use this method with a Kovar metal alloy, which has the same coefficient of expansion as silicon / glass, but this still requires the use of silicon MEMS lab facilities which is to be avoided for this project.

Fusion bonding of metals is possible, though this is usually called diffusion welding or bonding. In this process the metals to be joined are heated to 0.5 to 0.7 times their melting point and pressed together, so that small scale surface roughness will start to deform and flow together at the material interface [30]. The process is not instantaneous, but takes several (dozen) minutes to complete. This can be used to join (dissimilar) metals on an atomic level without melting or deforming them, including refractory metals for extremely high temperature operation. The joint strength achieved is normally on par with the base material strength. It does require specialized equipment though in order to create a non-oxidizing, high temperature environment, with a high force clamping device in place.

It is currently unknown if a diffusion welding oven is available at TU Delft, or where one could look for one. A search for companies offering diffusion welding services has so far also yielded no results. The process is also permanent, requiring a new nozzle profile and top and bottom sealing surface for each new thruster design created, increasing (future) costs.

Several other bonding and welding techniques were looked into, but all had one or more issues preventing their use here:

1. Glue: breaks down at high temperatures (polymer) and requires adding material that would interfere with nozzle geometry
2. Soldering/brazing: requires adding material that would interfere with nozzle geometry
3. Beam or arc welding: melts both base metals, resulting in deformation of nozzle geometry
4. Mechanical welding: introduces (large) deformations of base materials

As an alternative to the above methods, a mechanical clamping seal using bolts for compression and a type of gasket for sealing is considered. The gasket used cannot be a standard polymer version as these would not withstand the temperature reached in the thruster body. A relatively soft metal such as pure or low alloy copper or aluminium may be used, though this requires a higher clamping force than would be needed for a polymer version. These metals do have the advantage of having some of the highest thermal conductivity values of any material and can thus also serve to spread the heat emanating from the electrical heater to the propellant heat exchanger. If the stress in the interface is made to stay below the elastic limit, the thruster can also be disassembled and its nozzle contour swapped for a different one, though plastic deformation may be necessary to create a leak-tight seal. Lastly, such a mechanical seal requires no specialized equipment and can be assembled by hand, with components made on a standard CNC milling machine, with some additional polishing afterwards. This is thus seen as the best option at the moment. A drawing of the diffusion welding and clamping seal concepts can be seen in Figure 3.2.

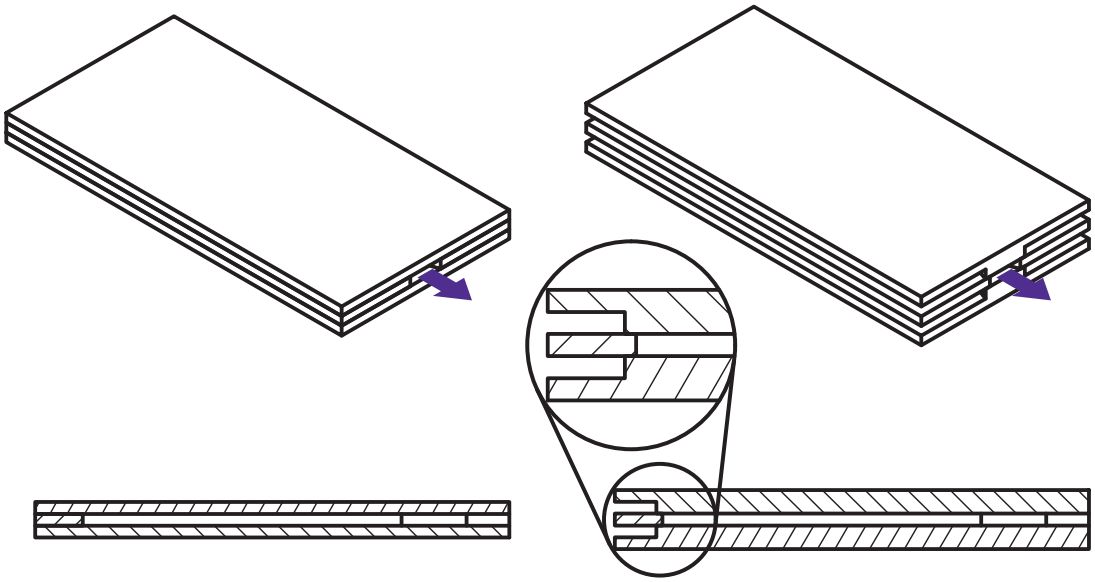

Figure 3.2: Two primary nozzle profile sealing concepts: diffusion welding (left) and soft metal clamping (right). Nozzle exit flows are indicated with purple arrows.

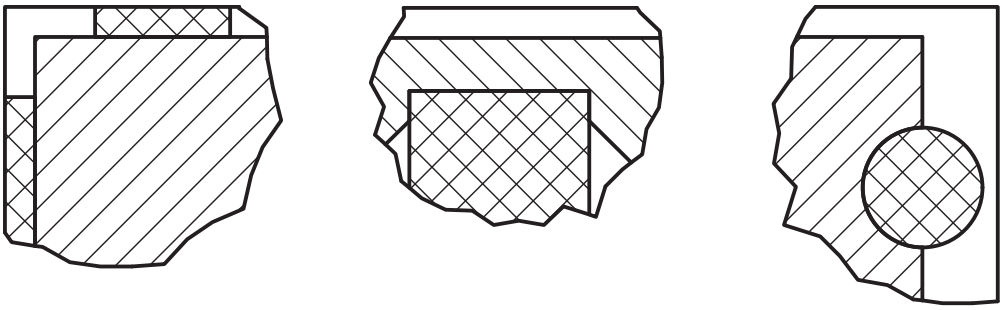

Figure 3.3: Concepts for nozzle layer alignment: machined edges on sides (left), around the internal heat exchanger geometry (middle) and by using dowel pins / shoulder bolts (right). Cross hatched sections indicate the aligning bodies, and single hatched sections the nozzle profile.

3.3.3. Nozzle layers alignment

A last issue that needs to be addressed regarding the nozzle fabrication is the alignment of the multiple layers it consists of. The nozzle direction should preferably be parallel to the whole thruster body, so that it can be properly aligned with the thrust bench and possible features on the sealing blocks such as the heat exchanger and seals. Manual alignment with e.g. micrometer XYZ-stages was considered to be too cumbersome and time consuming, thus some kind of mechanical alignment was needed, for which the following options were identified, see also Figure 3.3:

1. Adding a ridge to the sealing blocks around the edge of the nozzle profile
2. Adding slip-fit dowel pins through the assembly with (partial) holes in the nozzle profile
3. Using shoulder bolts to combine the functionality of dowels and clamping bolts
4. Using the internal heat exchanger geometry as alignment block

The first option would have a piece of the sealing block stick out above the sealing surface, which would make it difficult to polish this surface after machining. The last option is also not seen as viable because the heat exchanger may be quite a delicate component (e.g. thin fins, compliant metal foam), which makes it unsuitable to handle possible misalignment loads. Of the two other options, the shoulder

bolts require the least additional milling and don't need the extra space that extra dowels would need. Small size shoulder bolts are also simple COTS components, available in many sizes with specified close tolerances. These can be bought for just a few Euros each, making them the preferred choice.

3.4. Heater

The micro-thruster being designed here requires an external heating power input to attain the desired propellant temperatures of 400 °C. In this section, the concepts for the heat source are discussed first, followed by concepts for a heat exchanger to transfer this heat to the propellant.

3.4.1. Heating source

For this project, basic resistive heating will be used, which is used for the current silicon thruster design and the reference thruster. Two alternatives are outlined below, with a small explanation why they were disregarded.

Firstly, solar thermal heating is an option currently already under investigation by another MSc student at the SpE department. It unfortunately requires a specialized radiation heat exchanger and an intense light source such as a laser, which cannot be used in the SpE vacuum facilities.

Secondly, induction heating may be an option for electrical heating without physical contact between the heater wires and thruster body, where the heater itself can thus be at a lower temperature than the thruster body. This unfortunately requires somewhat specialized alternating current power supplies, may run into issues of electro-magnetic interference due to the high frequency alternating magnetic fields involved, and could heat up surrounding metals. The additional equipment needed, limited electrical engineering experience of the author and stray magnetic fields issues made this unsuitable for this project.

Regarding concepts for resistive heating methods, the current silicon thruster design uses thin molybdenum wires deposited on top of the thruster wafer. This is not seen as a viable option here because it would require using the expensive silicon MEMS fabrication facilities. If the base material is metal, another intermediate layer would then also have to be used to electrically insulate the heater. Only making the heaters on a silicon wafer without any channels would also still be expensive and require creating an additional heater electrical interface which can function at high temperatures.

Another resistive heating method is to use conductive heat exchanger fins or walls as electrical resistors and heating these directly by driving a current through them. This has been used before by e.g. [4, 50, 56] but comes with the major disadvantage that the materials used for the fins have so far always been good electrical conductors. This results in a very low resistance over the heating element, requiring a very high current to generate a reasonable amount of power. This in turn necessitates the use of thick electrical power leads, which result in large thermal conduction losses [4]. In one case it also required using special liquid gallium electrical connections to use on a thrust bench because the thick electrical leads would otherwise influence thrust measurements due to being too stiff when they expand under heating [56]. In all, this is not seen as an appropriate solution here.

As a simpler heating method, COTS heaters are investigated. Such devices have been used in previous TU Delft micro-thruster development, first by Krusharev [32], later by Stohr [59]. From the devices investigated by previous authors and from a recent search by the current author, the most appropriate COTS heaters seem to be Watlow FIREROD cartridge heaters. Other heaters found were either too large, too expensive or did not reach the desired temperature of 400 °C. This, together with the other resistive heater concepts can be seen in Figure 3.4.

Three $^1/_8$ inch diameter, $1^1/_2$ inch long versions with integrated thermocouple, a 30 W power rating and 760 °C maximum temperature should already be present at the department. These were ordered for the project by Krusharev, though these may be tied up in other MSc projects currently. When these were acquired several years ago, they were sold in a minimum batch of three units, with a cost of around €37 each for the standard version and double that for ones with an integrated thermocouple.

In the previous two projects, these heaters were used as immersion heaters with direct fluid contact, even though they are specified as cartridge *insertion* heaters. These would normally be inserted into a hole made in solid material instead. The solid material around the insertion heater can then be used to transfer this heat to fluids, without creating difficult to seal holes. The specific model available has no threaded end or other means of providing a leak-tight seal, though versions with threading

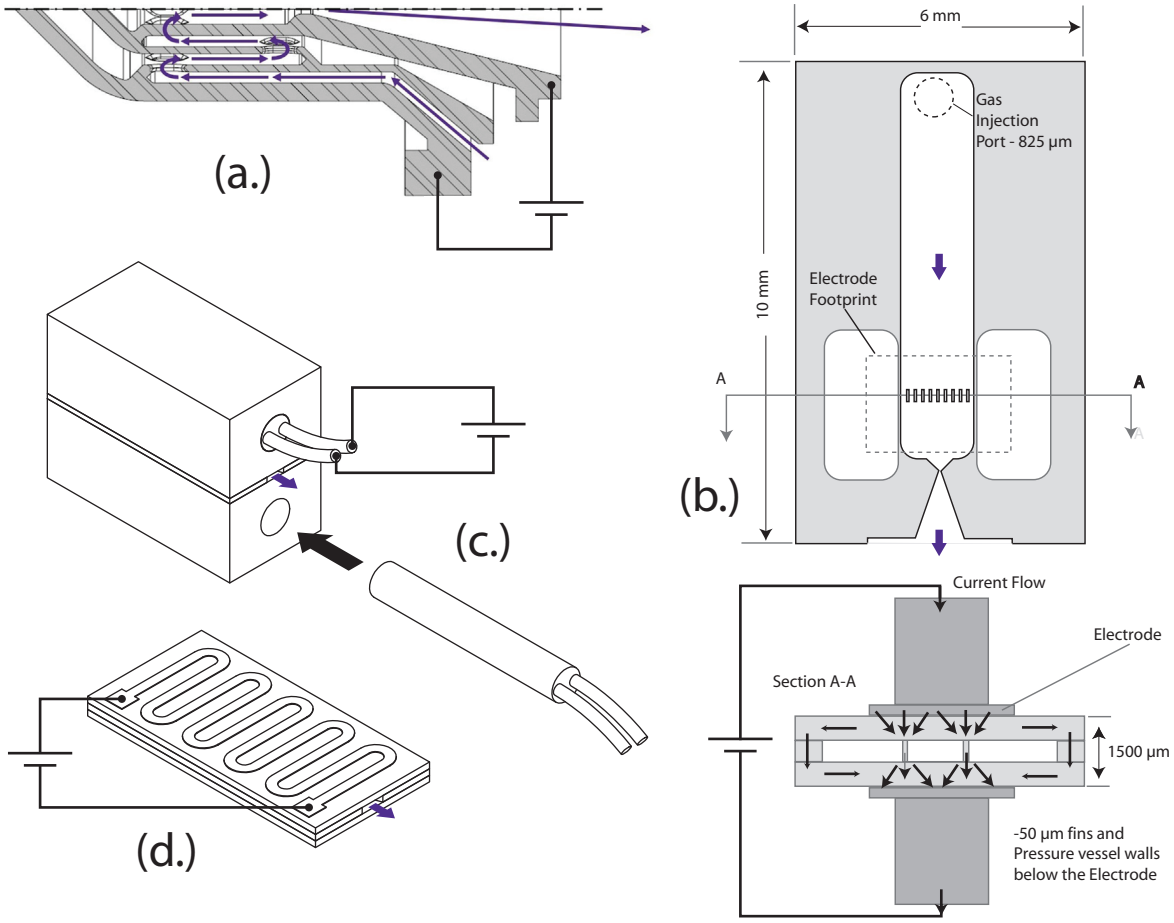

Figure 3.4: Concepts for resistive heaters: a.) current through low resistance 3D-printed metal walls [56], b.) current through low resistance etched silicon micro-fins [4], c.) COTS cartridge insertion heaters, d.) Current through high resistance wires etched on top of silicon [14]. Propellant flows are indicated with purple arrows.

for immersion use are available (only with low temperature NPT-thread though). Krusharev made the heater connection leak-tight by generous application of high temperature silicone (glue). Stohr on the other hand suffered from leakage around the electrical wires coming from the heater as they passed through the heating chamber walls, and was not able to fix this issue.

A concept using these insertion heaters was thus looked into, taking inspiration from the paper by Cen and Xu [12]. They used a cartridge heater inserted into a block of copper to indirectly heat up their silicon micro-thruster chip. Here, the copper block acted as an effective heat spreader due to its very high thermal conductivity. For the thruster being designed here, such a copper heat spreader block with cartridge heater could be combined with the need for a (copper) sealing surface on either side of the nozzle geometry. This minimizes the number of parts needed for heating and sealing, thus also limiting production cost and complexity. It does result in a relatively bulky thruster body though, with an increased surface area for radiative heat loss. Limiting such heat loss is discussed in section 3.7.

A further important point that needs to be addressed is that of the number of heaters to be used, in particular if heating should only occur on one side of the nozzle profile or on both sides. Using single sided heating has the advantage of requiring one fewer heater and may result in a thinner overall construction. However, this also possibly introduces thermal gradients over the height of the thruster if the temperature is ramped up quickly and conduction to the other side of the thruster is slow. This could result in thermal deformation, warping the thruster body and introducing leakage possibilities. Using two heaters on the other hand allows for a symmetrical temperature distribution and doubles the available power. To stay on the safe side of thermal deformation and power availability, the symmetrical dual heater concept is thus preferred.

3.4.2. Heat exchanger geometry

An important point for the heater as a whole is how the power from the electrical heater can be efficiently transferred to the propellant, i.e. what internal structure the fluid will flow past. Several heating chamber internal designs have been made in the past. The first TU Delft resistojets simply used a coiled tube without additional internal structure which was resistively heated by feeding a high current through it. This is too large an option for the thruster design here unfortunately.

Looking at geometries that others have used in the past, the first MEMS thruster by Mathew [44] at TU Delft used a very simple long rectangular design with three parallel rectangular channels. The MEMS thruster design by [12] was similar, though with more parallel channels. Another recent foray into heater design at the Electrical Engineering faculty of TU Delft also used this design, with varying numbers of parallel channels and different lengths and heights [35]. All of these designs featured very small fins though ($\sim$ 100 µm width), which will be hard to replicate with non-MEMS fabrication. Other MEMS designs by Poyck [54] featured microscopic arrays of diamond fins or serpentine channels which would be even harder to replicate.

A different approach was taken by [32] and [59] who used open cell metal foam as a simple to fabricate heat exchanger with a very high surface to volume ratio for high convective heat transfer. They were unfortunately unable to test the effectiveness of their designs due to leakage issues.

Based on these previous heater geometries, looking at other heater or radiator designs and with available fabrication methods in mind, several concept (categories) were created, which are laid out in Table 3.1 and visualised in Figure 3.5. The Table also summarizes the main advantages and disadvantages of each concept, which are further elaborated on next.

Concept	Advantages/Disadvantages	Sub-type	Figure
Machined channels	+ thermal contact ensured − more machining time needed − polishing issues	Using an end-mill Using a slit saw Interlocking	3.5a 3.5b 3.5c
Metal foam	+ material freely available + high surface per volume − may be difficult to cut	–	3.5d
Stacked plates	− many pieces needed (expensive) − thermal contact issues	Milled grooves Cut holes	3.5e 3.5f
Radiator core fins	− not easily available off-the-shelf − unknown home fabrication method	–	3.5g
Packed bed	+ high surface per volume − thermal contact issues	Cylindrical tubes Spheres	3.5h
Nozzle profile fins	− longer EDM cutting length (expensive)	–	3.5i

Table 3.1: Heat exchanger geometry concepts, with their main advantages and disadvantages.

The stacked plates concept was disregarded because it requires fabrication of a large number of (identical) components at a very small size (likely expensive). It may also run into issues of how to create an adequate thermal connection between the plates and the copper heat spreader without resorting to excessive clamping forces. Radiator core fins are not (easily) available off the shelf and have no known home-fabrication method. Cutting fins in the nozzle profile results in a large increase in the cutting length that would have to be performed by wire-EDM which would be too expensive.

Packed beds may be more appropriate as they have a high surface area to volume ratio, which is beneficial for convective heat transfer, but either require sintering or large clamping forces to form effective thermal connections. Pre-sintered sheets seem to be commercially available, but would still require large clamping forces for a thermal connection to the copper heat spreader. These sheets consist of solid spheres packed together instead of open bubbles for metal foam, resulting in much lower porosity and likely higher pressure drop for the same size. These also seem to be more commonly used as filters, rather than heat exchangers.

This leaves open cell metal foam and milled grooves as options. Milled grooves require more time

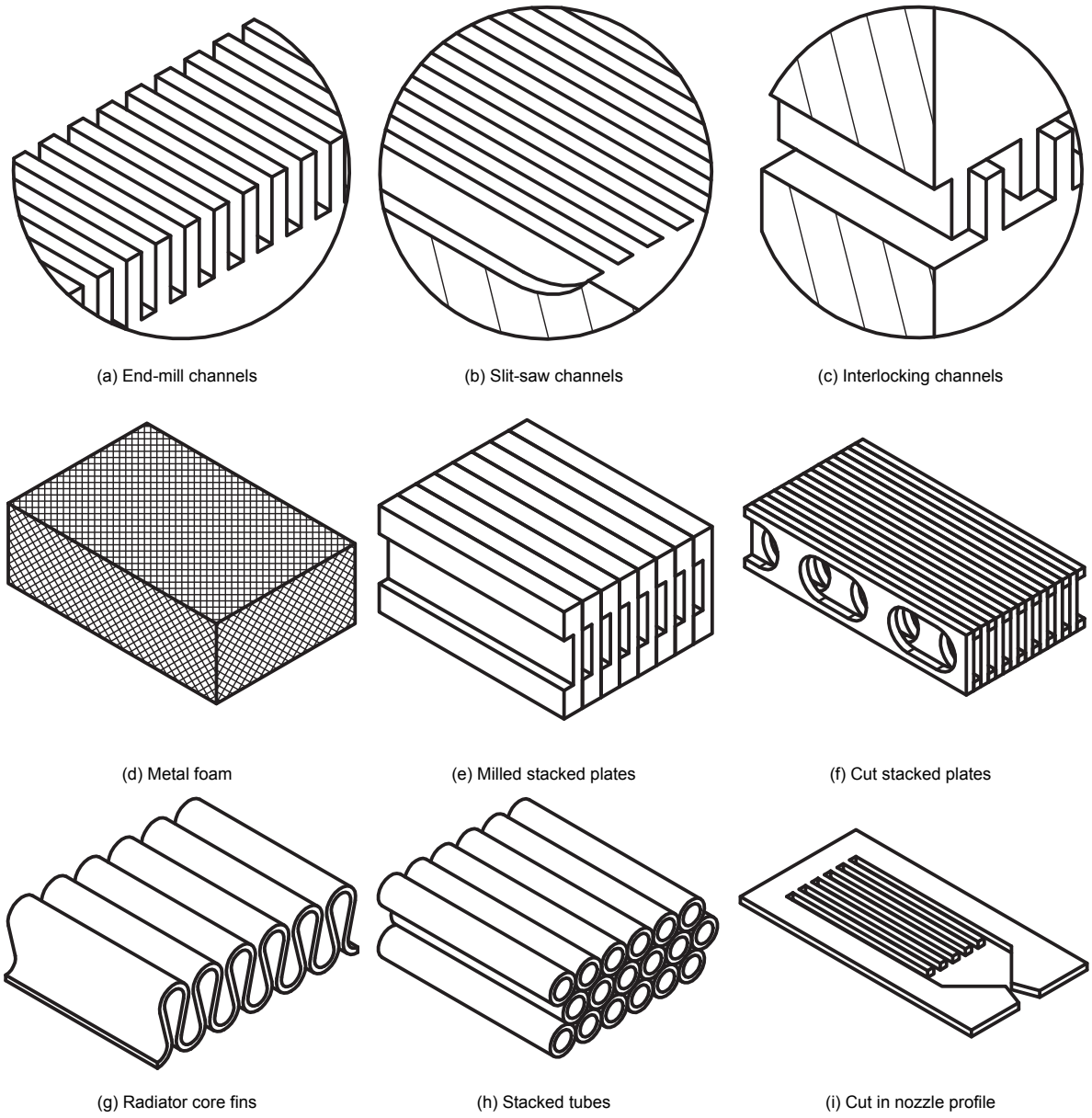

(a) End-mill channels (b) Slit-saw channels (c) Interlocking channels

(d) Metal foam (e) Milled stacked plates (f) Cut stacked plates

(g) Radiator core fins (h) Stacked tubes (i) Cut in nozzle profile

Figure 3.5: Heat exchanger geometry concepts, with propellant flow always from top left to bottom right.

spent on CNC machining, but also have a direct physical connection to the heat spreader block, thus do not require clamping forces for reasonable heat transfer. With the interlocking channels concept, the width of the grooves that needs to be cut can also be increased by a factor of ~3 compared to the single channel concept, making narrower and higher surface area channels possible with larger, more convenient end-mills. The interlocking concept furthermore allows for even heating from both sides without having to introduce clamping forces or spacers. It also unfortunately requires fins to stick out from the sealing surface, which would make polishing after the machining step more difficult.

Open cell metal foam also has a high surface area to volume ratio, and simplifies fabrication of the top and bottom blocks, only requiring a cavity to fit the piece of foam into. The foam itself may prove more difficult to manipulate though, as its flexibility makes it hard to cut into the desired shape, which Stohr [59] already noted. This may necessitate the use of laser or water jet cutting, possibly requiring an external company. Two sample pieces of foam were acquired several years back at the department, with some of it having been used already, but enough still remains for this project. Proper thermal contact also requires either compression of the material into the heater block or brazing / welding. Due to the size and high compliance of the material, a compression contact should be a reasonable option here.

Both of these last two options seem reasonable so far, with each having different positives and negatives. The main points that make the milled option less favourable are that it requires more difficult machining than the metal foam, and that—to achieve the smallest channel width—the fins will stick out above the sealing surface, which impedes surface polishing. This is why the metal foam option is preferred at this point.

3.5. Propellant interface

During operation, the (very) hot thruster must be supplied with propellant from an exterior feed system which is at a much lower temperature. This means that a leak-tight connection must be made between the two that can withstand such high temperatures while also limiting thermal losses through it. This last point is also important because the propellant feed system utilizes plastic hoses and connectors which should not be exposed to high temperatures. In this section, first the tubing for between the cold and hot parts of the system is discussed. After this, concepts for leak-tight high temperature connections between tubing and thruster/environment are looked into.

3.5.1. Propellant tubing

For the tubing, the main point to address is that of thermal conductivity. For the tubing through which the propellant will have to flow, a continuous spectrum of solutions is available. On one side of this is the option to limit conductivity through geometry, on the other to limit it through the use of inherently low conductivity materials.

Inherently low thermal conductivity materials ($\sim 1\,\mathrm{W\,m^{-1}\,K^{-1}}$) are unfortunately restricted to some specialty ceramics, polymers and foams. These materials are either difficult and expensive to shape in the case of ceramics; will melt or decompose below the desired temperature of 400 °C in the case of plastics; or are porous and cannot contain a fluid in the case of foams and cloths.

To limit heat loss through the propellant connections, the geometry option is thus preferred. The most basic option here is to have propellant connections that are long and have a small cross sectional area. For this purpose, thin stainless steel tubing should be well suited. Besides being widely available, this also has a relatively low thermal conductivity (15 to $20\,\mathrm{W\,m^{-1}\,K^{-1}}$ [20]). Some basic numerical experiments showed that conduction with this type of design should be low enough for the purposes of this prototype.

To prevent any additional thermal losses through conduction from occurring, the propellant tubing connections can also serve as the only physical links between the thruster and the cold interface. One thing to keep an eye on with this setup is that the tubing connection then becomes a trade-off between low heat loss and a high strength/stiffness connection. Both increasing length and decreasing diameter of the tubing lowers the conductive thermal losses but also makes the tubing less rigid and increases stresses on the tubing wall when a load acts on the thruster body. Too low a stiffness may also result in issues with resonance on a thrust bench. This trade-off is left for the detailed design stage (section 4.5). For a simple visualisation of the concept, see Figure 3.6.

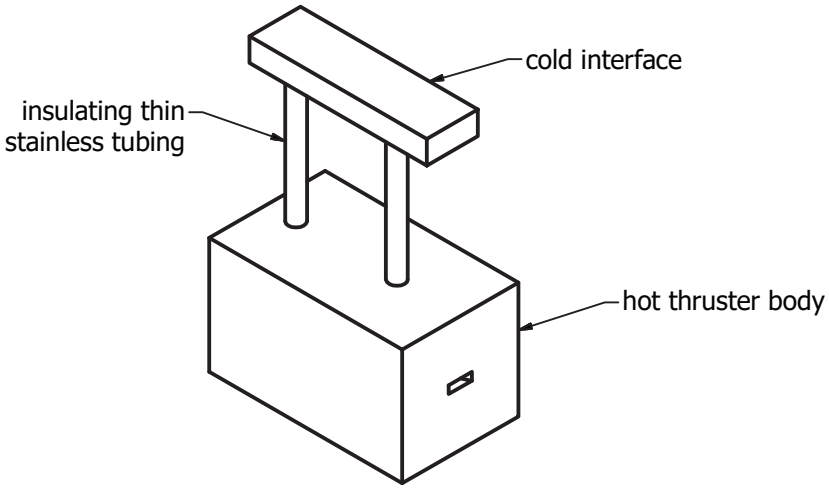

Figure 3.6: Propellant tubing and connection concept, using thin stainless steel tubes for thermal insulation: one as propellant inlet, one for pressure sensing.

3.5.2. Tube connections

Creating leak-tight fittings between the tubes and the thruster body is also a point of concern. Due to the high temperatures involved, regular polymer O-ring seals or thread sealant are not an option. This is a similar kind of issue as with the nozzle profile sealing, though with somewhat more standard geometry: a round tube in a round hole, without an opening in its circumference. Maintaining internal geometry is also far less important here, contrary to the nozzle section. Several options were thought of that could be used in two main categories, compression metal-metal seals or metal fusion:

1. Custom compression fitting (similar to nozzle profile seal or knife-edge like vacuum seals)
2. Threaded fittings with a metal-metal seal (Figure 3.7)
   (a) Normal parallel thread with copper crush washers
   (b) Conical surface seal (e.g. AN thread)
   (c) BSP thread tapered male to parallel female
3. Brazing/soldering of plain tubes
4. Welding of plain tubes

Of these, the first is too complex to machine compared to the others and also requires a method of holding on to the tube to clamp it down. Standard welding methods are not an option for dissimilar metals such as used here with the copper block and stainless steel tubing. Welding methods that could achieve such a connection are more specialized and not as easily available (i.e. laser, electron beam, or diffusion welding).

The second option is somewhat easier, though requiring specific taps to thread the holes. The fittings to go between such a threaded hole and tubing are standard commercially available components though. The three fitting options can be seen in Figure 3.7.

Brazing or soldering is like welding, but a connection is made by melting a different type of metal / solder onto the joint, without melting the base metals. This is for instance used with plumbing installations. The difference between brazing and soldering lies only in the temperature at which the joining piece of metal melts. For soldering, this is usually tin or lead based, with a melting point up to around 400 °C to 500 °C. Brazing works upwards from these temperatures using e.g. silver based compounds.

Compared to threaded fittings, brazing the tubing to the thruster body requires considerably less space due to the absence of threaded sections and an intermediate piece. It also provides a simpler kind of inspection for leak-tightness as the seal extends to a visible section of the thruster body and can more readily be assumed to keep functioning at high temperatures. Thermal expansion should not be able to loosen or tighten it, only deform or break it, at which point the leak would also be detectable at room temperature when leak-tests are possible. Unlike fittings however, it does require someone else to perform the brazing, which is possible at the faculty. Lastly, it does requires heating up the

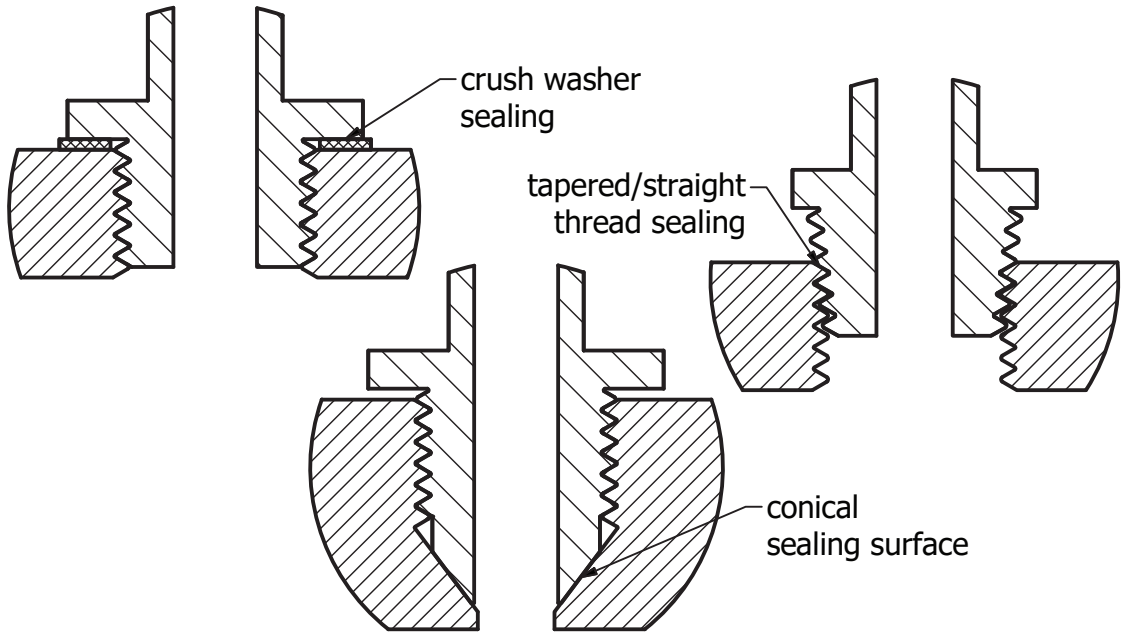

Figure 3.7: The three types of metal-metal seal threaded fitting options.

tube and thruster block to above the melting point of the brazing compound for assembly and possible disassembly, which may have unwanted side-effects.

With these positives and negatives in mind, brazing is seen as the most favourable option at the moment. On the cold side of the tubing the use of glue is seen as the simplest option.

3.6. Propellant sensors

For measuring the pressure and temperature of the propellant as it enters the nozzle, two sensors have to be integrated into the system. These are dealt with here, mainly looking at sensor placement for both, and sensor type for the temperature measurement.

3.6.1. Pressure sensor

To start off with, no pressure sensors could be found that were rated to operate at the thruster body temperature of 400 °C. Previous TU-Delft micro-thruster designs simply did not have a pressure sensor at the nozzle entrance and operated at much lower temperatures. Nozzle chamber pressure measurement was done by measuring pressure further upstream in the feed system and subtracting an estimated pressure drop over the tubing and heat exchanger channels in between. This unfortunately introduces an unwanted measurement uncertainty. Efforts to use MEMS sensors for local pressure measurements are ongoing at the electrical engineering faculty, but the sensors used are not rated for temperatures over $\sim$ 150 °C, require delicate wire bonds for electrical connections, and are attached using glue, making them unsuitable here.

Fortunately, the pressure sensor does not have to be at the same location as where the pressure must be measured. As the pressure dynamics are not important for this project, only the steady state values, the pressure sensor can simply be connected to the measurement location with a piece of fluid tubing to physically transmit the pressure from a hot location to a cold sensor. As long as there is no fluid movement in the tube (no open ends, no pressure variations over time), the fluid pressure along the tube should be constant, resulting in a measurement of the local pressure of interest without any offsets. This method was also seen to be employed in some commercial high temperature pressure sensors through the use of thin spiralling tubing between the sensor and its target. At the SpE department it has also been used by Leenders [37], and is currently in use by fellow MSc student A. Takken, in both cases for the creation of a solar-thermal thruster.

The tubing for connecting a cold sensor to the hot thruster faces the same considerations as for the

propellant feed tubing in the previous two sections, so that the same solution can be used for it (thin, long, stainless steel tubes). This also means that the type of sensor used can be chosen without much consideration for its maximum operating temperature, as it should remain relatively cool. Compared to the current silicon VLM, the placement of the pressure sensor removes the uncertainty of having to estimate the pressure drop over the heating chamber to the nozzle entrance, increasing measurement accuracy. As no viable alternatives could be found, this pressure sensing concept will be used.

3.6.2. Temperature sensor

Unlike the previously considered pressure sensor or the already available mass flow sensors, temperature sensing requires either a local physical device or the use of thermal imaging.

A thermal imaging camera is available, though this would be difficult to use as no vacuum pass-through for its ethernet cable is currently installed. Thermal imaging may also suffer from inaccuracies due to the high reflectivity of metal surfaces used here. It would however give far more insight into the overall thermal behaviour of the design as it would also show the temperature of the insulation and surrounding parts. For future work this could give a wealth of information for input to thermal insulation design though, without needing any physical connections to the thruster. Here it will not be used however, due to the issues mentioned.

This leaves physically connected temperature sensors, for which placement boils down to essentially three options:

1. Measuring the temperature of the propellant directly within the chamber.
2. Measuring the temperature of the heating element (via resistance or embedded thermocouple)
3. Measuring the temperature of the heat-spreading blocks / thruster body

The first is the most direct and thus suffers from the least uncertainty / possible measurement offset, as the propellant will be nearly directly in contact with the sensor. The second and third method however essentially rely on the propellant reaching thermal equilibrium with the thruster body / chamber walls. If this is the case, then the measurement can be quite close to the actual temperature of the propellant. However if this is not the case, these sensor will overestimate the propellant temperature, without a simple way to determine how large the offset could be. To combat this, these two methods should only be used in combination with a decently over-sized heat exchanger, so that one can be nearly certain there is little to no offset.

The direct chamber sensor is not guaranteed to be without an offset either though. The small scale of the device means that thermal conduction from the thruster body into the sensor may be relatively high compared to heat flux due to convection from the propellant. This may skew the measurement towards the wall temperature, so that the true temperature of the propellant remains unknown. No basic calculations were performed to check this, as this was not seen as the main reason to not choose this concept. There may be a possibility to use such an immersed probe with state estimation techniques to produce a temperature measurement, even in non-equilibrium situations. This would require more involved modelling though and is considered to be outside of the scope of this project.

Either of the other two placement options (sensor embedded somewhere in the heat spreader block) is seen as preferable here, as these don't introduce possible leakage points. These also require limited to no extra machining time to be able to install them. A National Instruments USB DAQ was already available for use with four thermocouples inside the vacuum chamber, making that type of sensor the preferred choice here, in the interest of simplicity. Which of the two placement options is used will be determined during detailed design.

3.7. Thermal insulation

To tackle thermal insulation, the three types of heat transfer have to be accounted for: conduction, convection and radiation. Because heated tests will only be performed in a vacuum, convection can be neglected. Conduction cannot become lower than with just the two (required) stainless steel tubing connections for the propellant inlet and pressure sensor, doubling as structural connections, and is thus already taken care of. This only leaves radiation, which can become a sizeable problem at high temperatures due to black body radiation scaling with T^4.

The following general strategies were devised to limit radiative heat losses:

1. Increase the thermal resistance from the thruster body to the outermost radiation emitting surface:
    1. Using low conductance insulation such as glass or ceramic fibre blankets
    2. Using (layered) radiation shielding, that is not directly connected to the thruster body
2. Decrease the emittance of radiation emitting surfaces by using highly reflective/polished materials

One of the simplest options here would be to wrap the thruster in high temperature fibrous insulation such as done by Ferreira [18]. A second simple option would be to use a single layer sheet metal radiation heat shield, cut with e.g. a laser cutter and folded by hand. The earlier mentioned strategies can also be used together as was seen in other high temperature resistojets. For example Ferreira used fibre insulation covered in reflective aluminium foil, Donovan et al. [17] used multi-layer rhenium radiation shields covered by porous ceramic/glass, and Tijsterman [65] used two layers of radiation shielding and solid insulation. For now, preference is given to the sheet metal radiation shield as the material for it is very inexpensive and readily available, fabrication with laser cutting and hand bending is free, with all aspects being on campus. The question if any additional insulation strategies have to be employed on top of this is left for the detailed design stage based on modelled heat losses.

3.8. Conclusion

In this chapter, a set of guidelines was set up for steering the design in the desired direction. The primary issues that needed to be addressed with this design were then looked into. None of the issues presented fundamental problems that could not be resolved. With the limited time and information available, one or more satisfactory solutions were found for each of these, which fit within the guidelines. The chosen concepts can thus move forward to the detailed design stage, which is described in the following chapter.

Several concepts were identified which were unsuited for the current project, but which could prove to be valuable for future iterations. The first of these is the use of diffusion welding to seal in the wire-EDM cut nozzle profile. This should be able to create a leak-tight seal without issue and can also be used with refractory metals for extremely high temperature operation. It is also unfortunately a permanent solution and requires special equipment which could not be located. The use of thermal imaging to measure thruster temperature and evaluate insulation design would also be recommended. A camera for this purpose is available, but not yet ready for use within the vacuum chamber. In addition, future designs may explore means to adjust the nozzle throat width *after* manufacturing, by using compliant joints cut into the nozzle profile. Lastly, inductive heating of the thruster may be looked into, for which there was simply a lack of time and experience on part of the author to evaluate its potential here.

4

Detailed design

In this chapter the concepts selected previously are used together with simple models to arrive at a fully finished design, and a selection of the components needed. As the intended outcome is akin to a breadboard model, use of more advanced computer design tools such as computational fluid dynamics and finite element analysis will be kept to a minimum. The design does not have to fall within exact specifications, so the possible higher accuracy of such tools is not seen as a benefit compared to simpler, less time consuming analytical models [68]. Margins will be set high to ensure that the design will still be able to safely fulfil its intended function.

Many of the choices made here are a result of small iterations in a Computer-Aided Design (CAD) model of the thruster, as most component sizing was dependent on the size and packaging of other components. The order of the sections in this chapter is more or less the order in which the components were designed, but their final size and layout only became clear once everything was put together. Models for estimating performance were used throughout the design process, to make sure that components were not severely under or over performing. In most cases however, only the performance for the final version is given for each in the interest of brevity and clarity.

As alluded to above, the non-novel components of the design are sized to have a relatively high factor of safety. This is done to not have the success of the project depend on components that are not critical in determining if the main nozzle fabrication concept works, i.e. the use of wire-EDM. The limits of strength, stiffness, mass and thermal losses can be looked into for a possible future iteration, for now they must simply be good enough to be able to test the device, even if some of the calculations were somewhat inaccurate. Thermal efficiency is also not yet seen a concern, though it can not entirely be ignored as the device must be able to reach and maintain the desired temperature with the heating power available.

With this in mind, the chapter is structured as follows: First, the exact nozzle geometry and size is laid out in section 4.1. After this, a model for calculating ideal and non-ideal thrust behaviour is discussed in section 4.2, together with thrust efficiency figures that will be used for comparison with the reference thruster. Next, the heater component selection and heat exchanger sizing is outlined in section 4.3. Sizing and design of the thruster body and the soft metal compression seal is then dealt with in section 4.4, followed by thermal insulation and propellant tubing in section 4.5. Next, the selection of specific sensors and the incorporation of these and other components into an interface is discussed in section 4.6. Finally, the complete design is outlined in section 4.7, followed by a conclusion to the chapter in section 4.8 and recommendations for future work in section 4.9.

4.1. Nozzle geometry

For the nozzle geometry, the design of the chosen reference thruster by Bayt [4] is used as a basis (see Table 4.1). To accommodate the use of wire-EDM, the throat width w_t [m] is doubled to 130 µm, and the thrust chamber pressure is halved to still achieve similar throat Reynolds numbers. The throat height h_t is rounded up slightly from 491 µm to 500 µm, as this is a standard thickness for the sheet metal to be used.

Several more values are needed to define the shape of the nozzle. First of these is the longitudinal

Parameter	Unit	Symbol	New design	Bayt [4] reference	Silicon VLM	
					Design	Measured [41]
Throat height	µm	h_t	500	491	100	81 ± 5
Throat width	µm	w_t	130	65	45	17.4 ± 1.2
Throat area	µm^2	A_t	65000	31915	4500	1400 ± 130
Throat aspect ratio	–	h_t/w_t	3.85	7.55	2.22	4.66 ± 0.43
Throat radius of curvature	µm	$r_{t,c}$	260	130	∼0	1.0
Expansion area ratio	–	ϵ	8.25	8.25	11.1	30 ± 3
Nozzle exit width	µm	w_e	1072.5	536.25	500	471.4 ± 4.1
Nozzle exit aspect ratio	–	h_t/w_e	0.466	0.916	0.200	0.172 ± 0.011
Divergent half angle	°	θ	20	20	29.6	29.8
Convergent half angle	°	ψ	35	?	19.4	20.5

Table 4.1: Dimensions and parameters defining the shape and size of the nozzle of the new design, the reference design [4], and that of the current TU Delft silicon VLM [41].

throat radius, which was specified to be “at least twice the throat width” [5] motivating the choice by citing [43]. The latter indeed looked at 2-D / planar nozzles, though with a larger size, higher Reynolds numbers and lower expansion areas, which were mainly intended for atmospheric operation on aircraft. This is contrary to research from La Torre [36] who, through simulations of axisymmetric nozzles, found that a sharp throat would result in higher thrust efficiency. Regardless of which of these may be true, the reference thruster design is followed by using the minimum value of $r_{t,c} = 2 \times w_t = 260\,\mu m$.

The divergent half angle was specified at $\theta = 20°$, which is maintained, while the convergent half angle ψ [°] is never mentioned. Previous works at TU-Delft used or suggested values of 15° [36] for (weakly) optimal performance, 20° for manufacturing ease [33] and 45° to minimize thruster length when using a relatively wide heating chamber [54]. Any value within this range of 15° to 45° is thus seen as acceptable. Due to the heating chamber size, electrical heater length, and placement of clamping bolts—while also keeping the thruster body size at a minimum to counter radiative losses—a convergent half angle of 35° was used. Further research would be needed to determine the actual effect of ψ on performance and its optimal value for a planar micro-nozzle such as this one.

The last value that is needed to fully define the geometry of this planar nozzle is the expansion area ratio ϵ [-], which was specified at 8.25 by Bayt. Using this same value results in a nozzle exit width w_e of 1072.5 µm. The design of the nozzle using all of these parameters can be seen in Figure 4.1 and an overview of the parameter values can be found in Table 4.1, together with those from the reference design and the current silicon VLM.

The main thing to note when comparing the new design to the current silicon VLM is that the throat area A_t [m^2] is now an order of magnitude larger, which largely determines thrust and mass flow magnitude. If desired, this area can be reduced for future projects by using a thinner base material for wire-EDM to reduce h_t(see section 5.2), or by looking into the compliant nozzle adjustment method mentioned previously in section 3.3 to lower w_t. The thicker base material used here does help to make the nozzle profile more robust for safer handling.

4.2. Modelled thrust performance

Besides direct comparison of thrust test results to those from the reference design (Appendix A), the results will also be compared to an analytical thrust model to determine to what degree this model can be used to predict thrust and mass flow for this design. The model is based on using ideal rocket theory (IRT) [70] with some correction factors for non-ideal behaviour. It was first suggested by Jansen [27] for axisymmetric micro-nozzles and later used by Makhan [41] for a planar micro-nozzle. IRT is also used to calculate efficiency figures from experimental thrust and mass flow measurements, again for comparison with both the reference thruster and the non-ideal model.

For this project, predictions within 10 % of experimental values will be considered to be sufficient for initial design, (keeping experimental uncertainty in mind). From an engineering perspective, this is mainly important for designing a thruster for use on an actual spacecraft. A more accurate thrust and specific impulse model can then for example result in lower margins on propellant mass, or fewer de-

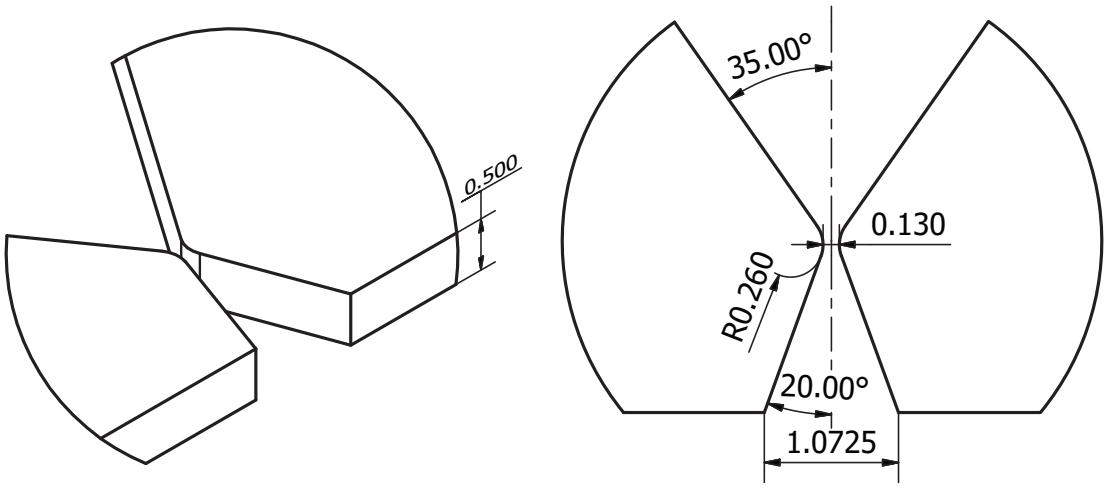

Figure 4.1: Isometric (left) and top view (right) of the final nozzle design with dimensions indicated in mm.

sign iterations. Micro and nano-satellites—the eventual intended application for this type of thruster—usually have relatively low propellant fractions and Δv requirements. The resulting propellant mass margins should then be similar to the 10 % accuracy for I_{sp}, and sufficient for initial design. For more accurate modelling in later design phases, the use of more complex numerical flow analysis would be recommended.

4.2.1. Ideal performance

Here the equations for IRT are discussed, with the correction factors being shown in the next subsection. IRT assumes that the propellant gasses flowing through the nozzle are homogeneous, have a constant composition and heat capacity, and obey the ideal gas law. Furthermore, the equations only consider steady-state, one dimensional, and isentropic flow. Using IRT (subscript ideal), the mass flow through the nozzle $\dot{m}$ [kg s^{-1}], the velocity of the propellant when it leaves the nozzle v_{e} [m s^{-1}] and the total thrust force generated F [N] are then given by the following equations [70]:

$$\dot{m}_{\mathrm{ideal}} = p_{\mathrm{c}} A_{\mathrm{t}} \sqrt{\frac{M}{R T_{\mathrm{c}}} \gamma \left(\frac{2}{\gamma+1}\right)^{\frac{\gamma+1}{\gamma-1}}} \tag{4.1}$$

$$v_{\mathrm{e,ideal}} = \sqrt{\frac{R T_{\mathrm{c}}}{M} \frac{2\gamma}{\gamma-1} \left[1 - \left(\frac{p_{\mathrm{e}}}{p_{\mathrm{c}}}\right)^{\frac{\gamma-1}{\gamma}}\right]} \tag{4.2}$$

$$F_{\mathrm{ideal}} = \dot{m}_{\mathrm{ideal}} v_{\mathrm{e,ideal}} + (p_{\mathrm{e}} - p_{\mathrm{a}}) A_{\mathrm{e}} \tag{4.3}$$

$$= p_{\mathrm{c}} A_{\mathrm{t}} \sqrt{\frac{2\gamma^2}{\gamma-1} \left[1 - \left(\frac{p_{\mathrm{e}}}{p_{\mathrm{c}}}\right)^{\frac{\gamma-1}{\gamma}}\right] \left(\frac{2}{\gamma+1}\right)^{\frac{\gamma+1}{\gamma-1}}} + (p_{\mathrm{e}} - p_{\mathrm{a}}) A_{\mathrm{e}} \tag{4.4}$$

Here p [Pa], T [K] and A [m^2] are the propellant pressure, temperature, and nozzle cross sectional area at specific locations along the nozzle. Subscript c denotes thrust chamber / stagnation conditions (upstream location where $v_{\mathrm{c,ideal}} \approx 0$), t is at the nozzle throat (smallest A where v_{t} equals the local speed of sound), and e is at the nozzle exit plane. Furthermore, $R = 8.314\,462$ J mol^{-1} K^{-1} is the universal gas constant, and M [kg mol^{-1}] and γ [-] are the mean molar mass and specific heat ratio of the propellant respectively. Lastly, p_{a} is the ambient pressure of the gas surrounding the thruster.

The two main values of interest, $\dot{m}_{\mathrm{ideal}}$ and F_{ideal}, can then be calculated based on the geometry of the nozzle, the thermophysical properties of the propellant, and the measurable values p_{c} and T_{c}.

For this, the value of p_e also needs to be known, which can be computed by numerically solving the following equation, as unfortunately no closed form expression exists:

$$\frac{A_e}{A_t} = \frac{\sqrt{\gamma \left(\frac{2}{\gamma+1}\right)^{\frac{\gamma+1}{\gamma-1}}}}{\sqrt{\frac{2\gamma}{\gamma-1}\left(\frac{p_e}{p_c}\right)^{\frac{2}{\gamma}}\left[1-\left(\frac{p_e}{p_c}\right)^{\frac{\gamma-1}{\gamma}}\right]}} \tag{4.5}$$

The specific impulse I_{sp} [s]—how efficient an engine is at converting stored mass into thrust—is finally given by the following equation, using the standard gravitational acceleration $g_0 = 9.806\,65\,\mathrm{m\,s^{-2}}$:

$$I_{sp} = \frac{F}{\dot{m} g_0} \tag{4.6}$$

4.2.2. Throat Reynolds number

Besides the variables introduced in the previous subsection, all the correction factor expressions are also defined in terms of the throat Reynolds number Re_t [-]. In addition, Bayt [4, p. 120] found this to be the governing similarity parameter for comparing nozzle performance. This dimensionless quantity is a ratio of momentum to viscous forces in a fluid and is defined as:

$$\mathrm{Re}_t = \frac{\rho_t v_t d_t}{\mu_t} = \frac{\dot{m} d_t}{\mu_t A_t} \tag{4.7}$$

Where d_t [m] is the diameter of the throat cross section and μ_t [Pa s], ρ_t [kg m^{-3}] and v_t [m s^{-1}], are the viscosity, density, and mean velocity of the fluid at the throat. When using exact values for calculation of Re_t, the above two definitions are equivalent. However, taking into account which values can be measured directly and their associated uncertainty, the second definition will give more accurate results in this case and is used for the rest of this report. This definition was also used by e.g. [4, 41].

Due to the rectangular cross section of the throat, d_t is not uniquely defined, as it would be for a circle. Two comparable values may be used here instead, namely the throat width w_t [4] and the throat hydraulic diameter $D_{h,t}$ [41]. The hydraulic diameter is normally used for calculating losses in subsonic flow through non-circular pipes. It is defined in terms of the perimeter length $\mathscr{P}$ [m] and cross sectional area A [m^2] of the channel, and is equal to the diameter for circular cross sections:

$$D_h = \frac{4A}{\mathscr{P}} \tag{4.8}$$

$$D_{h,t} = \frac{2 w_t h_t}{(w_t + h_t)} \tag{4.9}$$

The main difference between the two length scales lies in the fact that $D_{h,t}$ already incorporates the throat aspect ratio—the throat height relative to its width—in some form, while w_t does not. $D_{h,t}$ is equal to w_t and h_t for a square throat cross section, and tends to $2w_t$ for $h_t \gg w_t$ or $2h_t$ for $w_t \gg h_t$. For a single nozzle geometry, or similar ones with $h_t \gg w_t$, choosing one or the other then corresponds to simply scaling Re_t by a constant factor. More fundamental differences in parameters scaling with Re_t may become apparent when for instance comparing equal throat area nozzles nozzle with $h_t = 2w_t$ and $h_t = w_t/2$. Using w_t in that case would suggest a factor two difference between Re_t of each geometry, while $D_{h,t}$ would result in the same value for both, as the size and shape of the throat is the same, just rotated by 90°.

Then again, neither of these values takes into account that the nozzle aspect ratio for a planar nozzle changes continuously along its length due to the constant channel height, which could also affect thrust performance. In all, determining which approach is more valid or if both are incorrect will require further experimental research, and investigating nozzles with a greater variety of throat aspect ratios (most experimental data so far is for ones with $h_t \gg w_t$). Here, both values will be looked into, to see if either one provides better predictions with existing relations out of the gate.

For the used definition of Re_t, the value of μ_t must be known, which is a function of throat temperature T_t [K] and pressure p_t [Pa]. Here, these two values are always calculated from T_c and p_c using IRT according to the equations below. After this, μ_t is evaluated at these conditions using the thermophysical properties database CoolProp [6].

$$p_\mathrm{t} = p_\mathrm{c}\left(\frac{2}{\gamma+1}\right)^{\frac{\gamma}{\gamma-1}} \tag{4.10}$$

$$T_\mathrm{t} = T_\mathrm{c}\left(\frac{2}{\gamma+1}\right) \tag{4.11}$$

4.2.3. Discharge coefficient

To relate the mass flow through a sonic nozzle that is found from IRT and the value that is found from experimental data (subscript exp), the discharge coefficient C_D [-] is used, see equation (4.12). Quite a number of analytical expressions exist for modelling C_D of axisymmetric nozzles, though none were found for the rectangular throat that is used here. Three of these expressions were looked into for giving an estimate of the expected reduction in mass flow compared to IRT due to e.g. boundary layer formation, by again replacing the circular nozzle diameter with w_t or $D_\mathrm{h,t}$.

$$C_\mathrm{D} = \frac{\dot{m}_\mathrm{exp}}{\dot{m}_\mathrm{ideal}} \tag{4.12}$$

The first, chronologically, is the semi-empirical relation by Kuluva and Hosack [34] (subscript KH), derived from experiments with conical axisymmetric nozzles. This was used recently by [15] to model the nozzle of another rectangular channel micro-thruster, though unfortunately without direct comparison to experimental results independent of thrust.

$$C_\mathrm{D,KH} = \left(\frac{r_\mathrm{t,c}+0.05r_\mathrm{t}}{r_\mathrm{t,c}+0.75r_\mathrm{t}}\right)^{0.019} \times \left[1-\left(\frac{r_\mathrm{t,c}+0.10r_\mathrm{t}}{r_\mathrm{t}}\right)^{0.21}\frac{1}{\sqrt{\mathrm{Re}_\mathrm{t,ideal}}}(0.97+0.86\gamma)\right] \tag{4.13}$$

Here r_t [m] is the throat cross sectional radius, $r_\mathrm{t,c}$ [m] is the throat radius of curvature, and $\mathrm{Re}_\mathrm{t,ideal}$ is Re_t calculated using $\dot{m}_\mathrm{ideal}$ from IRT. Defining r_t for a rectangular throat faces the same challenge as defining d_t for the Reynolds number earlier. The same substitutions are applied, with $r_\mathrm{t} = w_\mathrm{t}/2$ if w_t is used for calculating Re_t, and $r_\mathrm{t} = D_\mathrm{h,t}/2$ if $D_\mathrm{h,t}$ is used. The validity region of the original correlation is reported as $50 < \mathrm{Re}_\mathrm{t} < 10^5$ and $0 < r_\mathrm{t,c}/r_\mathrm{t} < 40$.

The second relation was devised by Tang and Fenn [61] (subscript TF), which was used by previous students at the department to model micro nozzles [27, 41], though without validation of its accuracy. This is an analytically derived relation for an idealized case of an infinitely long conical nozzle—the only case for which an analytical solution could be found—with the note that the results were "very insensitive" to the expansion length. It was originally validated for $10^2 < \mathrm{Re}_\mathrm{t} < 10^4$ and internally uses a slightly modified Reynolds number, see the equations below:

$$\mathrm{Re}_\mathrm{t,TF} = \mathrm{Re}_\mathrm{t,ideal}\sqrt{\frac{r_\mathrm{t}}{r_\mathrm{t,c}}} \tag{4.14}$$

$$C_\mathrm{D,TF} = 1-\left(\frac{\gamma+1}{2}\right)^{\frac{3}{4}}\left(\frac{4\sqrt{6}}{3}+\frac{8\cdot(9-4\sqrt{6})}{3(\gamma+1)}\right)\frac{1}{\sqrt{\mathrm{Re}_\mathrm{t,TF}}}+\frac{2\sqrt{2}}{3}\frac{(\gamma-1)(\gamma+2)}{\sqrt{\gamma+1}}\frac{1}{\mathrm{Re}_\mathrm{t,TF}} \tag{4.15}$$

Lastly there is a simple empirical relation by Johnson et al. [28] (subscript JS). The dependence on Re_t of the equation is quite similar to the previous two. It uses only two coefficients α and β that were fitted from experimental data though, as well as using the chamber/stagnation conditions for evaluating μ:

$$\mathrm{Re}_\mathrm{t,JS} = \frac{\dot{m}_\mathrm{ideal}d_\mathrm{t}}{\mu_\mathrm{c}A_\mathrm{t}} \tag{4.16}$$

$$C_\mathrm{D,TF} = \alpha - \frac{\beta}{\sqrt{\mathrm{Re}_\mathrm{t,JS}}} \tag{4.17}$$

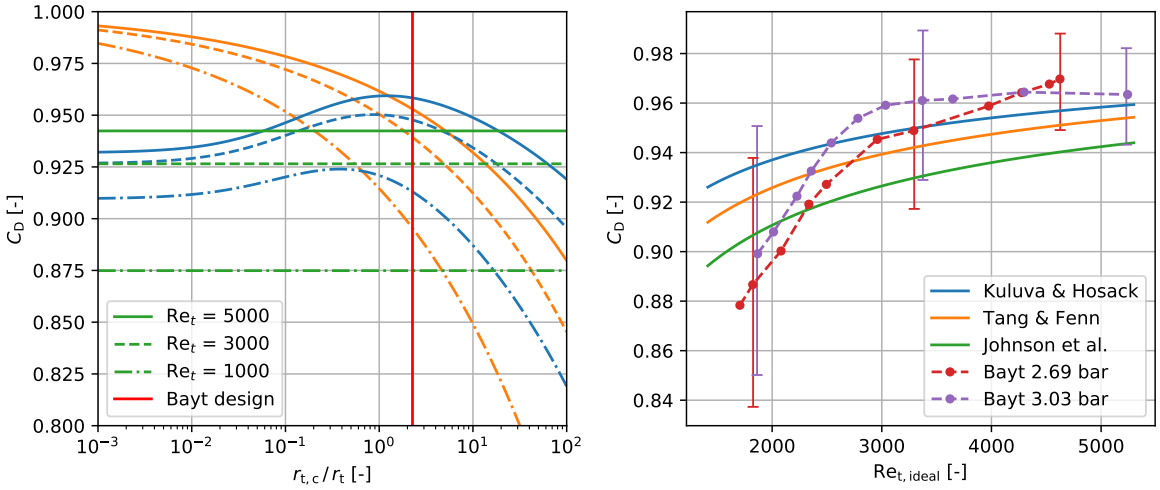

Figure 4.2: C_D variation with $\mathrm{Re}_{t,ideal}$ and $r_{t,c}/r_t$ for three different models [28, 34, 61] (colours match in both figures). The figure on the right is essentially a cross section of the one on the left (location indicated by vertical red line), and corresponds to the nozzle design by Bayt [4] with $r_t = D_{h,t}/2 = 2.26$ and $\gamma = 1.4$. Experimental data from hot thrust testing of the similar nozzle by Bayt is also indicated, with their Re_t scaled up by $D_{h,t}/w_t = 1.766$.

Johnson et al. used CO_2, N_2, H_2 and Ar as propellants and an axisymmetric nozzle with $r_{t,c} = 2d_t$, which gave $\alpha = 0.997$ and $\beta = 3.618$ for N_2 and $2000 < \mathrm{Re}_{t,JS} < 22000$. Expressions for application with different fluids and geometries can be found in e.g. [26]. Considering though that a difference of roughly 10 % between model and experimental values would be seen as sufficient and the nozzle geometry is quite different, the three equations discussed so far are seen as sufficient.

For comparison of the different relations, it is useful to only have the nozzle geometry and the same Reynolds number, $\mathrm{Re}_{t,ideal}$, as inputs. Due to T_c/T_t only depending on γ (equation (4.11)) and viscosity scaling with approximately $T^{0.727}$ in the temperature range of interest [68], conversion for this last relation is relatively straightforward with $\mathrm{Re}_{t,JS} \approx 0.878 \times \mathrm{Re}_{t,ideal}$.

For comparison, the modelled value of C_D according to the three models can be seen in Figure 4.2. Values for the reference nozzle design by Bayt over a range of expected Re_t are also shown, together with corresponding experimental data (see Appendix A). In the graph, only $d_t = D_{h,t}$ is used for Re_t and the C_D relations, as using w_t resulted in a consistent underestimation of C_D for the higher Reynolds numbers. This gives $r_t = 57.4\,\mu m$ and $r_{t,c}/r_t = 2.26$.

From this it can be seen that the difference between the models for the chosen geometry is at most around 2 %, with all three having similar graph shapes versus Re_t. The models all lie within the confidence bounds of the experimental data when using $D_{h,t}$ as the nozzle length scale, as shown in the figure. The model by Tang and Fenn is then used from this point on—with the mentioned assumptions—as it best matches the experimental data visually over the full range of Reynolds numbers. Comparison of the model with data from other planar micro-thrusters, e.g. from Makhan [41], is left for future work.

4.2.4. Specific impulse efficiency

To model losses in thrust from non-ideal behaviour, one other parameter is needed: the specific impulse efficiency ξ_F. In this case, and for micro-thrusters in general, this is a combined measure of heat and momentum losses. Due to this, It can be defined both in terms of specific impulse and in terms of the thrust coefficient C_F, as it is equal to the thrust coefficient efficiency in this case [70]:

$$\xi_F = \frac{I_{sp,exp}}{I_{sp,ideal}} = \frac{C_{F,exp}}{C_{F,ideal}} \tag{4.18}$$

For modelling, the second definition will be used, as the two types of losses considered are more easily incorporated into C_F. The definition for the thrust coefficient, and the related characteristic thrust coefficient C_F°, are shown in equations (4.19) and (4.20) below [70]. The relation between the two is

that $C_F = C_F^\circ$ if $p_e = p_a$, thus C_F° only accounts for momentum thrust.

$$C_F = \frac{F}{p_c A_t} = C_F^\circ + \left(\frac{p_e}{p_c} - \frac{p_a}{p_c}\right)\frac{A_e}{A_t} \tag{4.19}$$

$$C_F^\circ = \frac{\dot{m}_{ideal} v_{e,ideal}}{p_c A_t} \tag{4.20}$$

The first type of loss considered is due to flow divergence, as some component of the velocity of the propellant leaving the nozzle will not be along the nozzle centreline, reducing momentum thrust. This can be accounted for by multiplying the momentum term C_F° of C_F with the correction factor C_θ, which was analytically derived in [7] for a planar nozzle to be the following (with θ in radians):

$$C_\theta = \frac{\sin(\theta)}{\theta} \tag{4.21}$$

The rest of the losses are modelled using an empirical relation from Spisz et al. [58] to calculate a loss factor $C_{F,loss}$ [-], with an accuracy of $\pm 5\,\%$, that is subtracted from $C_{F,ideal}$. The relation was fitted to experimental data from seven different axisymmetric nozzles with moderate throat curvature, $\theta = 20°$, and $25 < \epsilon < 150$. Hot and cold hydrogen was used as propellant, with a Re_t range from 425 to 18000. The form of the relation was derived from an analytical equation for $C_{F,loss}$, which was based on boundary layer growth over a flat plate.

The relation uses a throat Reynolds number that is adjusted for the propellant temperature at the wall, see equations (4.22) and (4.23). This is responsible for the power of $1 + 0.727$ in the equation below, which accounts for density scaling with T^{-1} and viscosity of N_2 scaling with roughly $T^{0.727}$ [68]. Spisz et al. used H_2 and a factor of $^2/_3$ instead of 0.727. Furthermore, Re_t in this case is based on the measured mass flow, and is thus corrected with C_D compared to the IRT value.

$$\mathrm{Re}_{t,wall} = \left(C_{D,TF}\mathrm{Re}_{t,ideal}\right)\left(\frac{T_t}{T_{t,wall}}\right)^{(1+0.727)} \tag{4.22}$$

$$C_{F,loss} = 17.6\frac{\exp\left(0.0032\frac{A_e}{A_t}\right)}{\sqrt{\mathrm{Re}_{t,wall}}} \tag{4.23}$$

The original publication used an estimated recovery factor of 0.84 to arrive at a value of $T_t/T_{t,wall} = 0.857$. This was only used for cold data due to the wall temperature of the nozzle no longer being equal to the propellant stagnation temperatures for heated flow. Due to the small size of the thruster used here, the wall and propellant stagnation temperature are expected to be equal, so that the value of 0.857 can continue to be used for heated flow. The modelled values for the thrust coefficient with losses and ξ_F then follow from the two equations below:

$$C_{F,model} = C_\theta C_F^\circ + \left(\frac{p_e}{p_c} - \frac{p_a}{p_c}\right)\frac{A_e}{A_t} - C_{F,loss} \tag{4.24}$$

$$\xi_{F,model} = \frac{C_{F,model}}{C_{F,ideal}} \tag{4.25}$$

With this, the total thrust with losses from analytical models is as follows:

$$F_{model} = g_0\left(C_{D,TF}\dot{m}_{ideal}\right)\left(\xi_{F,model} I_{sp,ideal}\right) = C_{D,TF}\xi_{F,model}F_{ideal} \tag{4.26}$$

Next, the specific impulse efficiency and the full model are compared with the hot data from the reference nozzle by Bayt.

4.2.5. Comparison with experimental data

Figure 4.3 shows modelled and experimental values—with data from the reference thruster by Bayt (Appendix A)—for I_{sp} efficiency ξ_F versus Re_t, and for I_{sp} versus thrust. The reference thruster data is from two different operating chamber pressures (2.69 bar and 3.03 bar), both for a range of temperatures from 300 K to 677 K and 692 K respectively. $D_{h,t}$ was used as characteristic throat length for all modelled

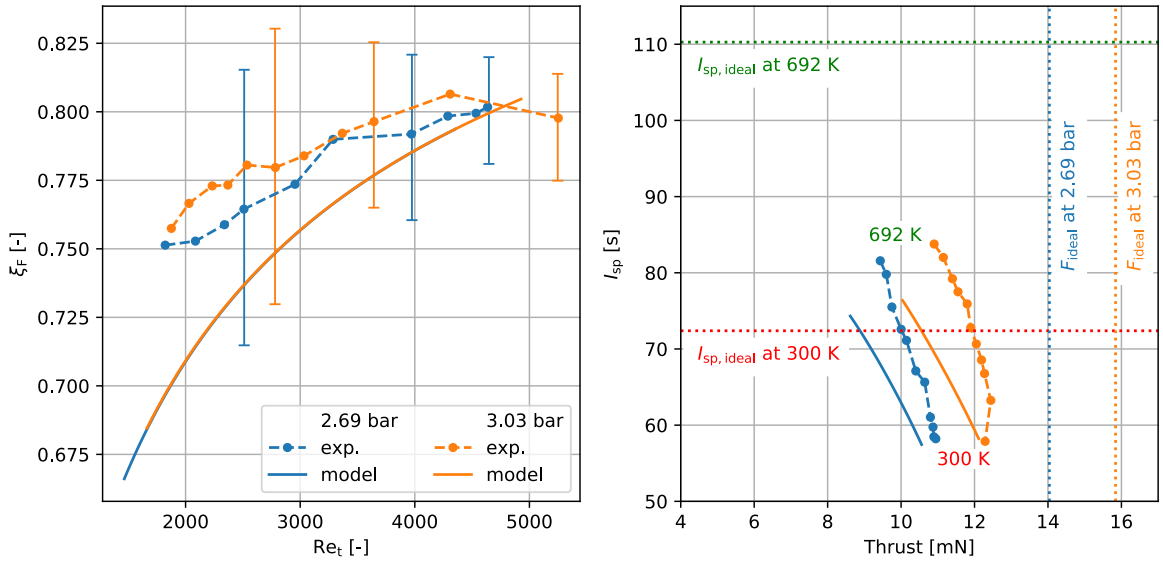

Figure 4.3: I_{sp} efficiency versus Re_t and I_{sp} versus thrust for experimental hot gas data by [4], with corresponding modelled values.

values, as using w_t resulted in a larger difference with experimental values. Use of w_t effectively reduces Re_t by a factor of 0.566, thus increasing $C_{F,loss}$ by a factor 1.33 for all inputs, resulting in even lower thrust and I_{sp}. For ξ_F, I_{sp} *and* thrust, the model is only off by 5 to 10 % at the highest temperatures / lowest Reynolds numbers, and even less at lower temperatures. It also lies well within the confidence bounds of the ξ_F data, especially considering the ± 5 % accuracy of the $C_{F,loss}$ relation. It is somewhat conservative though, as it consistently underestimates thrust and I_{sp}. Model predictions are also much closer to experimental values than the results from IRT (also indicated in the figure), which are off by roughly 30 % for the highest temperatures, and 20 to 25 % for room temperature. This highlights the substantial losses in the nozzle. For this case, the model is thus seen as sufficient for initial design, and a better method than using IRT alone.

Interestingly, for a different planar micro-thruster at TU Delft, the model using w_t actually matched experimental cold gas results from Makhan [41] better than with $D_{h,t}$. Using w_t even *over*estimated the thrust and specific impulse by $\sim$ 12 % at $Re_{t,w_t} \approx 1300$ and $\sim$ 60 % at $Re_{t,w_t} \approx 500$ [68, Fig. 2.2] instead of underestimating it (which is the case here). At this point it is unknown what is behind this difference in performance, though the thruster design tested by Makhan did have several geometric differences, such as a much larger expansion ratio and a sharp throat, see Table 4.1. The chosen reference thruster is thus still kept as a baseline for comparison, including the use of the model with $D_{h,t}$.

Finally, the modelled thrust, mass flow, specific impulse and efficiencies C_D and ξ_F, based on the chosen nozzle design and $p_c = 1.345$ bar, are shown for the desired range of operating temperature in Figure 4.4. This also shows the ideal values from IRT for comparison.

4.3. Heating chamber

This section primarily deals with the sizing of the heat exchanger, regarding its pressure drop and heat transfer to the propellant. To this end, first models for these effects are derived, which are then combined in a simple 1D steady-state simulation to estimate the effectiveness of heat exchanger designs for a given mass flow and wall temperature. A secondary point is the selection of a specific cartridge heater, which is briefly discussed first.

4.3.1. Heater component selection

As alluded to before, three identical cartridge heaters had been acquired for previous projects at the SpE department in the past [32, 59]. Two of these were still installed on their previous project and could

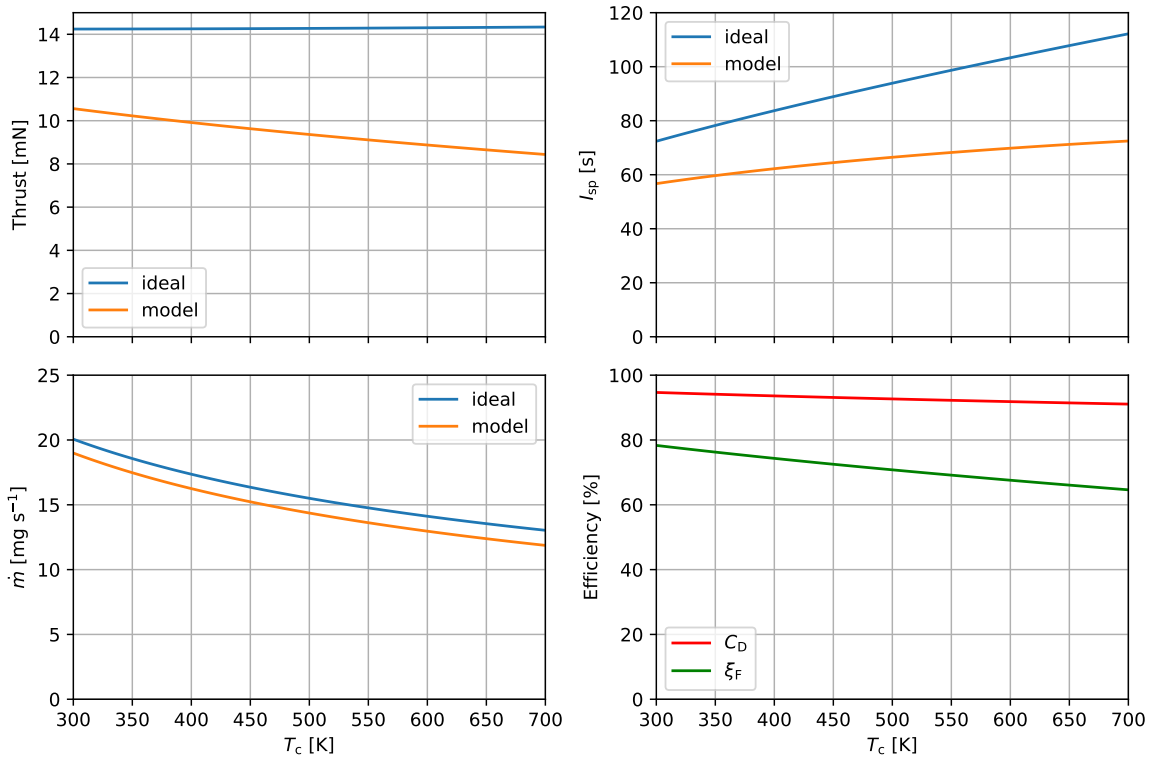

Figure 4.4: Variation of various modelled thrust performance values with thrust chamber temperature, for the chosen nozzle design with $p_c = 1.345$ bar.

not be removed, the third was available for use but was relatively long at 1.5 inch or 3.81 cm. These heaters are actually available down to a length og 1 inch, which would help make the thruster shorter and decrease radiative heat losses through a smaller exterior surface area. The local distributor for Watlow, Kurval B.V., was thus contacted to order two new heaters. Two options were given for the desired size (1 inch length, 0.125 inch diameter) and power / voltage combination (30 W, 24 V): one with and one without an integrated thermocouple. The non-thermocouple version was chosen, as it was half as expensive (∼€50) and the wire sleeving for the thermocouple version was only rated up to 250 °C.

4.3.2. Metal foam pressure drop modelling

All equations for metal foam in this section and the next are those described by Calmidi [10] as this author had a complete set of the needed equations for modelling of both heat exchange and pressure drop for a cross section of any shape. Some of the equations however could only be found in the review article by Mahjoob and Vafai [40] as the original thesis by Calmidi was not available for viewing.

For general 1D steady state pressure drop over a porous medium, the following equation can be used (general 3D transient form: [10], 1D steady state equivalent: [40, 59]):

$$\frac{\Delta p}{\Delta x} = \frac{\mu}{K} v + \frac{\rho F}{\sqrt{K}} v^2 \tag{4.27}$$

Here x [m] is the distance along the direction of flow, ρ [kg m^{-3}] is the fluid density and v [m s^{-1}] is the mean fluid velocity. The first term on the right hand side accounts for viscous friction, while the second is a semi-empirical non-linear correction term for other forms of drag at higher Re. The two constants in this equation, K [m^2] and F [-], the permeability and the inertial coefficient of the foam respectively,

can be calculated using the following empirical relations:

$$\frac{K}{d_\mathrm{p}^2} = 0.00073(1-\epsilon)^{-0.224}\left(\frac{d_\mathrm{f}}{d_\mathrm{p}}\right)^{-1.11} \tag{4.28}$$

$$F = 0.000212(1-\epsilon)^{-0.132}\left(\frac{d_\mathrm{f}}{d_\mathrm{p}}\right)^{-1.63} \tag{4.29}$$

In these equations d_p, d_f and d_c [m] are the mean pore diameter, mean fibre diameter, and diameter of a cubic representative unit of foam respectively. The porosity ϵ [-] of the material is also used, which equals the volume fraction of the foam that is empty space. Recemat, the manufacturer of the current metal foam samples, specifies ϵ, d_p, the specific surface area a_sf [m^{-1}], and the number of pores per linear inch of material PPI, though with unknown accuracy. a_sf is the ratio of exposed surface area inside the foam to its volume. From these specified properties, ϵ and PPI will be used as inputs for the rest of the models, following the same method as Stohr [59], using $d_\mathrm{c} = 0.0254/\mathrm{PPI}$. The ratio d_f/d_p needed to calculate K and F can be found from the below three equations.

$$d_\mathrm{p} = \frac{3-\chi}{2} d_\mathrm{c} \tag{4.30}$$

$$\frac{d_\mathrm{f}}{d_\mathrm{c}} = 1.18\sqrt{\frac{1-\epsilon}{3\pi}}\frac{1}{1-\exp\left(-\frac{1-\epsilon}{0.04}\right)} \tag{4.31}$$

$$\frac{\epsilon}{\chi} = \frac{\pi}{4}\left[1-\left(1.18\sqrt{\frac{1-\epsilon}{3\pi}}\frac{1}{1-\exp\left(-\frac{1-\epsilon}{0.04}\right))}\right)^2\right] \tag{4.32}$$

Reworking to get the ratio $d_\mathrm{f}/d_\mathrm{p}$ with just ϵ as an input gives:

$$\chi = \frac{4\epsilon}{\pi\left[1-\left(\frac{d_\mathrm{f}}{d_\mathrm{c}}\right)^2\right]} = \frac{4\epsilon}{\pi\left[1-\left(1.18\sqrt{\frac{1-\epsilon}{3\pi}}\frac{1}{1-\exp\left(-\frac{1-\epsilon}{0.04}\right))}\right)^2\right]} \tag{4.33}$$

$$\frac{d_\mathrm{f}}{d_\mathrm{p}} = \frac{2}{3-\chi}\cdot\frac{d_\mathrm{f}}{d_\mathrm{c}} = 1.18\frac{2}{3-\chi}\sqrt{\frac{1-\epsilon}{3\pi}}\frac{1}{1-\exp\left(-\frac{1-\epsilon}{0.04}\right)} \tag{4.34}$$

Here χ [-] is the tortuosity of the material, i.e. how “twisty” paths through its fibres are. As Recemat has specified more values than needed for these calculations, the specified d_p and a_sf are compared to modelled values for validation, see also equation (4.35). The results from this can be seen in Table 4.2, which shows good enough agreement between the two for this project, with a maximum deviation of 25 % for the foam types available. The values found for K and F also have similar values / orders of magnitude as data from Calmidi and Mahajan [10], who used comparable porosity foams.

$$a_\mathrm{sf} = \frac{3\pi d_\mathrm{f}}{\left(0.59 d_\mathrm{p}\right)^2}\left[1-\exp\left(-\frac{1-\epsilon}{0.04}\right)\right] \tag{4.35}$$

4.3.3. Metal foam heat transfer modelling

For heat transfer modelling, again a relation from Calmidi is used, which relates a specific Reynolds and Prandtl number Pr [-] to a Nusselt number Nu [-] in a metal foam heat exchanger:

$$\mathrm{Nu}_\mathrm{sf} = 0.52\mathrm{Re}_\mathrm{f}^{0.5}\mathrm{Pr}^{0.37} \tag{4.36}$$

Here, Nu_sf is composed of the fluid thermal conductivity k [$\mathrm{W\,m^{-1}\,K^{-1}}$], the total surface area heat transfer coefficient h_sf [$\mathrm{W\,m^{-2}\,K^{-1}}$] and the fibre diameter d_f of the foam. The Reynolds number Re_f

Name	ϵ	PPI	d_p			a_sf			F	K
	[-]	[inch^{-1}]	[mm]	[mm]	[%]	[m^{-1}]	[m^{-1}]	[%]	[10^{-2}]	[10^{-8} m^2]
	spec.	spec.	spec.	calc.	diff.	spec.	calc.	diff.	calc.	calc.
Ni-0610	0.95	6–10	2.30	2.81	+22	500	933	+87	8.144	10.4
Ni-1116	0.95	11–16	1.40	1.61	+15	1000	1633	+63	8.144	3.38
Ni-1723	0.952	17–23	0.90	1.12	+25	1600	2292	+43	8.164	1.67
Ni-2733	0.952	27–33	0.60	0.75	+25	2800	3438	+23	8.164	0.740
Ni-4753	0.952	47–53	0.40	0.45	+12	5400	5730	+6	8.164	0.266
Ni-5763	0.96	57–63	0.35	0.37	+6	6900	6354	-8	8.168	0.187

Table 4.2: Overview of Recemat nickel foam relevant properties from the available spec sheet[1] (spec.) and calculated with available relations (calc.) from PPI and ϵ. Samples of the two types indicated in bold are available at the SpE department.

is modified to include the fibre diameter and porosity, and the Prandtl number is unchanged from its standard definitions, as seen in the equations below:

$$\mathrm{Nu}_\mathrm{sf} = \frac{h_\mathrm{sf} d_\mathrm{f}}{k} \tag{4.37}$$

$$\mathrm{Re}_\mathrm{f} = \frac{\rho v d_\mathrm{f}}{\epsilon \mu} \tag{4.38}$$

$$\mathrm{Pr} = \frac{c_p \mu}{k} \tag{4.39}$$

Here c_p [J kg^{-1} K^{-1}] is the specific heat at constant pressure of the fluid. The velocity v [m s^{-1}] of the flow as used here was not explained in the work by Calmidi and Mahajan, but is assumed to be the average forward velocity of the fluid in the open sections of foam, resulting in:

$$v = \frac{\dot{m}}{\rho A_\mathrm{cs}} \frac{1}{\epsilon} \tag{4.40}$$

Where A_cs [m^2] is the total cross sectional area occupied by the foam, perpendicular to the direction of flow. The increase in specific enthalpy Δh [J kg^{-1}] of the propellant in a section of foam is then simply as follows:

$$\Delta h = \frac{h_\mathrm{sf} a_\mathrm{sf} (T_\mathrm{w} - T_\mathrm{f})}{\rho v} \Delta x \tag{4.41}$$

Here T_w [K] is the temperature of the wall / metal foam (assumed equal), and T_f [K] is the temperature of the fluid inside the foam.

4.3.4. Heat exchanger total modelled performance

With differential equations established for pressure drop and heat transfer, these can now be combined into a 1D simulation. To this end, similar to simulations employed by others for micro-thruster heat exchangers [15, 21, 44, 59, 67], the heating chamber is divided into small sections with length Δx. The pressure and temperature at the start are specified, together with a mass flow, and a constant wall / foam temperature is assumed. The pressure and temperature at each following node between the sections is then computed in sequence using the models laid out. Temperature differences over a section Δx can be found by first looking up the specific enthalpy for p and T_f at the starting node, changing the enthalpy according to the model, and then looking up which temperature corresponds to this new combination of enthalpy and pressure at the next node. Both of these look-up operations are performed with CoolProp [6].

With this model, the heater performance with a thruster body at 100, 200, 300 and 400 °C was simulated for the two types of foam available. The resulting propellant temperature, pressure drop, fluid velocity, and heater effectiveness over the length of the heater chamber are shown in Figure 4.5. The final heater design is used here, with the approximate lowest pressure and highest mass flow expected for the design. The heater effectiveness ε [-] shown here is essentially how close the propellant gets to

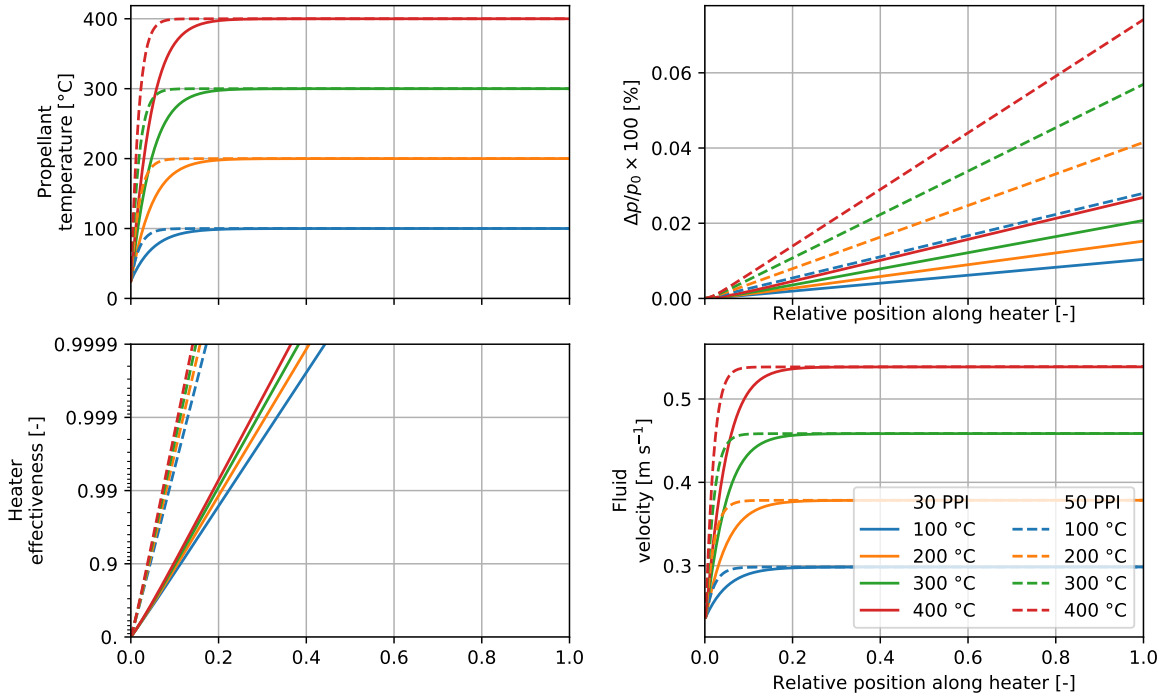

Figure 4.5: Modelled heat exchanger performance with 1.3 bar_a and 25 °C initial pressure and temperature, 20 mg s^{-1} total N_2 mass flow, and a 14.468 mm long heat exchanger with a 5 by 12 mm cross section.

the wall temperature, relative to the initial temperature difference between the cold propellant and the hot wall at the heater inlet [4]:

$$\varepsilon = \frac{T_\mathrm{w} - T_\mathrm{f}(x)}{T_\mathrm{w} - T_\mathrm{f,in}} \tag{4.42}$$

The heat exchanger size specified was primarily a result of the thickness of the available foam (5 mm) and the length of the cartridge heater, which produced a relatively large minimum thruster length compared to the nozzle size. This has resulted in a rather over-sized heater according to the model, with a very low pressure drop of less than 0.01 % and with the propellant already being close to thermal equilibrium with the wall at around 20 % of the total heater length. This does result in a very safe design, in the sense that the system should still heat the propellant to the desired temperature even if the modelled heat transfer and pressure drop are off by a reasonably large amount.

This also ties into the propellant temperature sensing concept, which relies on thermal equilibrium between the thruster wall and the propellant for an accurate reading, and thus benefits from an over-sized heater. With the final component packaging setup chosen, a smaller thruster body was also difficult to achieve, thus it was decided to simply make use of the available space and keep the large heat exchanger. Of the two types of metal foam available, the smaller pore size variant will be used, as this gave better heat transfer results at the cost of a negligibly higher pressure drop. Due to an absence of sensors for measuring propellant temperature rise and pressure drop over the heat exchanger, validation of this model unfortunately has to be left for future work.

4.4. Thruster body

The thruster body design is made to combine a number of different components, namely the nozzle profile, the foam heat exchanger, the inlet and pressure sensor tubing, the cartridge heaters, and bolts for nozzle assembly. The main issues encountered were: which type of copper to use, the proper sizing and shaping of the nozzle sealing surface, how to handle thermal expansion with the bolted connection used, and the packaging of the components. The first three of these are discussed here in order. Packaging is not discussed further as this was mainly a result of many (small) iterations in CAD.

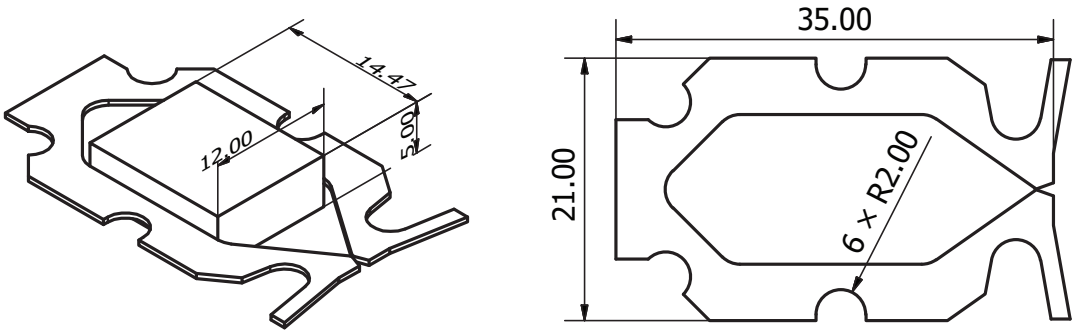

Figure 4.6: Isometric (left) and top view (right) of the final nozzle profile design with dimensions indicated in mm. The isometric view also shows the size and location of the rectangular prismatic piece of metal foam used as heat exchanger.

4.4.1. Copper type

For ease of ordering, the most widely available variant of unalloyed copper, Cu-ETP, was chosen. This has a high thermal conductivity (about 300 W m^{-1} K^{-1} to 350 W m^{-1} K^{-1} [2]) and relatively low yield strength for better possible sealing (about 200 MPa at room temperature, about 100 MPa at 400 °C). Its main downside is that subjecting it to brazing can introduce hydrogen embrittlement[3]. With the current design this is not expected to cause issues yet due to the blocks being designed much more robust at the brazed connections than strictly necessary.

As an alternative for future designs, an oxygen-free type of unalloyed copper can be used (e.g. SF-CU, Cu-HCP, Cu-DHP, Cu-OFE), which do not suffer from hydrogen embrittlement and have more or less the same physical characteristics otherwise. Unfortunately, these are slightly more of a specialty product, not as easily available in the right raw shape (rectangular bar stock), and several times more expensive than Cu-ETP.

4.4.2. Sealing surface

To seal the nozzle profile on both sides, the soft copper must be pressed onto either side with enough force to close off the internal volume. To allow for a large pressure at the contact surface while keeping the required clamping force low, the contact area was made small. Only a 0.5 mm thin edge of material around the edge of the internal nozzle profile contour was made to be in contact, with the rest of the surface being lowered by 0.3 mm. For ease of manufacturing a straight edge was chosen, so as to only need a single pass from a regular end-mill. It was realised later that this does introduce possible stress concentrations at the base of the ridge. To alleviate these stress concentrations, for a later iteration it is recommended to use a small ball or chamfer end mill to create a fillet or chamfer in place of this 90° corner.

The resulting surface area where material contact would take place was extracted from the CAD model and used to form an estimate of the required number and size of bolts to provide a sufficient amount of force. To derive the total force required for sealing, an estimate had to be made of the pressure needed first. This turned out to be more of an issue than originally anticipated, as little to no engineering standards or guidelines could be found for this (very) niche scenario. Thus, to start off, an educated guess was used instead, opting to first design for 15 % of the estimated material yield strength (30 MPa). This was chosen as a relatively low starting point, so that the device could first be tested without plastic deformation occurring, with the possibility of increasing the clamping force further if no adequate seal was formed yet. The bolts used were thus also chosen to operate at a similar or lower fraction of their yield strength, so that they could be used even if the copper would need to be plastically deformed to create a sufficient seal.

With the sealing surface area A_s [m^2] and desired stress σ_s [Pa] determined, the combination of the number of bolts n_bo [-] and force per bolt F_bo [N] is calculated by balancing these forces:

$$n_\mathrm{bo} F_\mathrm{bo} = \sigma_\mathrm{s} A_\mathrm{s} \tag{4.43}$$

[2] European copper association website: http://www.conductivity-app.org/alloy-sheet/33
[3] https://www.copper.org/applications/marine/cuni/pdf/Broschuere_Loeten_ENG.pdf

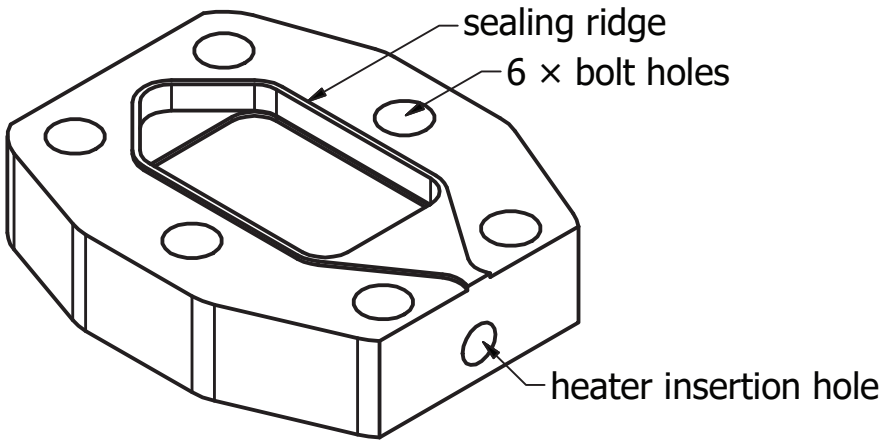

Figure 4.7: Schematic drawing of the final bottom copper sealing and heat spreading block.

The stress in the bolts σ_{bo} [Pa] can then be found by dividing F_{bo} by the effective cross sectional area $A_{\mathrm{b,cs}}$ [m^2] of the type of bolt used:

$$\sigma_{\mathrm{bo}} = \frac{F_{\mathrm{bo}}}{A_{\mathrm{b,cs}}} \tag{4.44}$$

Bolts only come in discrete sizes, thus only a limited number of combinations of n_{bo} and $A_{\mathrm{b,cs}}$ were possible. Also taking into account that size should preferably be kept to a minimum, six M3 shoulder bolts with a 4 mm shank diameter were eventually chosen. M3 bolts have an effective cross section of 5.03 mm^2, which results in $F_{\mathrm{bo}} = 183$ N and $\sigma_{\mathrm{bo}} = 36.4$ MPa. This is well below the desired 15 % of the yield strength of even the weakest of steel bolts, which normally start at around 480 MPa. Placement of the bolts around the seal was loosely based on a very basic FEM analysis, so as to distribute the sealing pressure roughly equally along the nozzle profile internal contour. The resulting design of the bottom block can be seen in Figure 4.7, with the final design of the body without bolts being shown in Figure 4.9.

4.4.3. Thermal expansion

Because of the increased temperature of the thruster body during operation compared to when it is assembled, some thermal expansion of components will take place. This is primarily an issue for the sealing bolts as these are made from a different material (steel) than the heating blocks (copper). There is thus a possibility of uneven thermal expansion of these components along the thruster's height.

The thermal expansion coefficient α [K^{-1}] of unalloyed copper normally ranges from $17 \cdot 10^{-6}$ to $18 \cdot 10^{-6}$ K^{-1}, while for steel values between $11 \cdot 10^{-6}$ and $20 \cdot 10^{-6}$ K^{-1} may be expected [20]. These ranges overlap, so it could be possible that both materials have the same expansion coefficient, though this is considered to be unlikely. If the copper expands more than the bolts, some initial calculations showed that material stresses in both could then increase above their yield limits. If it is the other way around, the pressure on the seal may become so low that it can come loose and start to leak. Transient behaviour, where (parts of) either component could be at a different temperature than the other, only exacerbates these problems.

To mitigate these issues, the stiffness of the bolted joints is drastically reduced by adding springs, so that expansion of either component only results in a minor change of the clamping force. Regular helical springs are usually quite large and do not have high enough stiffness to achieve the desired bolt forces in a small package. A different option is the use of disc springs, also known as Belleville springs/washers. These are conical disc shaped washers that have a relatively high stiffness for their size. They can be stacked in the same orientation for increased stiffness and load (parallel) or in alternating orientations for decreased stiffness and larger maximum deflection (series). This way the load they can bear and their spring stiffness can be easily adjusted. They are also relatively inexpensive and simple to acquire.

For modelling the required spring stiffness and maximum spring force, a simplified worst case sce-

nario was devised. It was assumed that the bolts and copper were infinitely stiff compared to the springs, with both their initial lengths L_0 [m] being equal to the distance between the top and bottom surface of the thruster body. A temperature increase of $\Delta T = 380\,\mathrm{K}$ was used (difference with a room at 20 °C). When using a spring with stiffness κ [$\mathrm{N\,m^{-1}}$] for each bolt, the additional bolt force and seal pressure can then be calculated from the changes in length of the components (subscript cu indicating the copper body):

$$\Delta L_{\mathrm{bo}} = \alpha_{\mathrm{bo}} L_0 \Delta T_{\mathrm{bo}} \tag{4.45}$$

$$\Delta L_{\mathrm{cu}} = \alpha_{\mathrm{cu}} L_0 \Delta T_{\mathrm{cu}} \tag{4.46}$$

$$\Delta F_{\mathrm{bo}} = \kappa \left(\Delta L_{\mathrm{bo}} - \Delta L_{\mathrm{cu}} \right) \tag{4.47}$$

$$\Delta \sigma_{\mathrm{s}} = \frac{\Delta F_{\mathrm{bo}} n_{\mathrm{bo}}}{A_{\mathrm{s}}} \tag{4.48}$$

For the case of the copper expanding more than the bolts, the worst mismatch of thermal expansion was assumed with $\alpha_{\mathrm{bo}} = 11 \cdot 10^{-6}\,\mathrm{K^{-1}}$ and $\alpha_{\mathrm{cu}} = 18 \cdot 10^{-6}\,\mathrm{K^{-1}}$. It was further assumed that ΔT_{bo} would only be 75 % of ΔT_{cu}, to take into account thermal transients. For the opposite scenario, the reverse worst case expansion was assumed, with $\alpha_{\mathrm{bo}} = 20 \cdot 10^{-6}\,\mathrm{K^{-1}}$ and $\alpha_{\mathrm{cu}} = 17 \cdot 10^{-6}\,\mathrm{K^{-1}}$. Here $\Delta T_{\mathrm{bo}} = \Delta T_{\mathrm{cu}}$ is used, as $\Delta T_{\mathrm{bo}} > \Delta T_{\mathrm{cu}}$ is only expected to occur during cool-down. This last scenario only results in lower sealing and bolt stresses, which are not critical during cool-down.

For values of the spring stiffness, the online catalogue of Amatec[4] was searched for springs with the right internal dimensions, preferably at a reasonably low cost. After some iteration, type S4214 springs were selected, which have a rated maximum deflection and force of 0.19 mm and 502 N, resulting in a stiffness of $2642\,\mathrm{N\,mm^{-1}}$. To allow for a relatively wide range of sealing pressures, two of these were stacked in parallel per bolt, bringing the maximum bolt force to 1004 N, equivalent to 164 MPa sealing pressure. For a lower total stiffness, three sets of these parallel stacks were placed in series for each bolt, bringing the effective stiffness to $2/3$ of the value of a single spring. A total of 36 disc springs were thus needed at a cost of €0.08 each, see Figure 4.8 for a drawing of a single shoulder bolt with the springs installed.

For the first scenario, these selected springs resulted in an additional sealing pressure and bolt force of 18 MPa and 111 N respectively. These values could have been decreased further with more springs in series, though this would have also taken up more space, made the bolts longer and opened up more area for radiation heat losses. For the second scenario, a decrease in sealing pressure of 5.6 MPa was found. Both of these outcomes were seen as acceptable, keeping in mind the maximum sealing pressure that can be applied with these springs is 164 MPa and that these are worst case scenarios.

4.5. Thermal insulation and tubing

In this section, the thermal insulation of the thruster body and the sizing of the tubing connecting it to the interface is treated together. This is because the sizing of the tubing is essentially a trade-off between strength/stiffness of the connection and the heat loss through them. Radiative heat losses from the thruster body are added to this to arrive at a total heat loss value, which is sized against the available heating power from the two 30 W cartridge heaters.

First, basic models for strength and stiffness of the tubing are derived, followed by combined conduction/radiation losses for the tubing. Next, the design of the pressure sensing tube and its heat loss model is updated slightly to counteract hot gasses reaching the sensor at start-up or due to natural convection. Following this, the radiative losses from the thruster body are modelled and the use of thermal radiation shielding is investigated. Lastly, a small overview is given of all the thermal losses that are to be expected with the chosen design for a range of temperatures.

4.5.1. Tubing strength

Two causes of stress in the propellant connection tubes is considered: internal pressure loading, and gravity loadings. The stress caused by internal pressure applied to the tubing is approximated using the equations for thin walled tubing. The walls of the different tubing sizes under consideration (see the end of this subsection) have thicknesses t [m] that vary from 7.5 % to 30 % of their mean radius R

[4] https://www.amatec.nl/

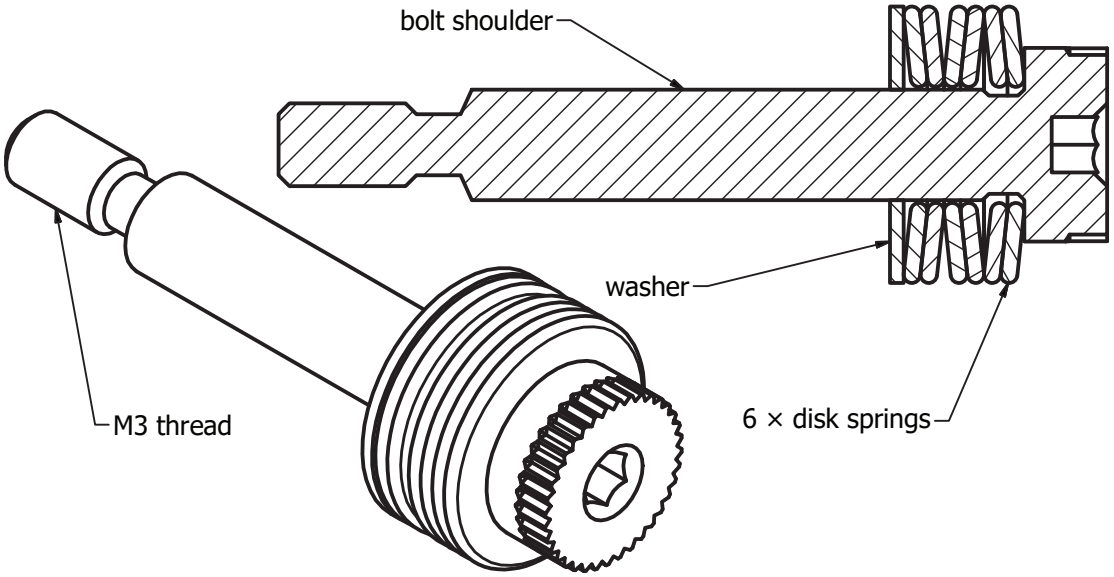

Figure 4.8: Schematic isometric (left) and cross sectional view (right) of one of the shoulder bolts with disk springs.

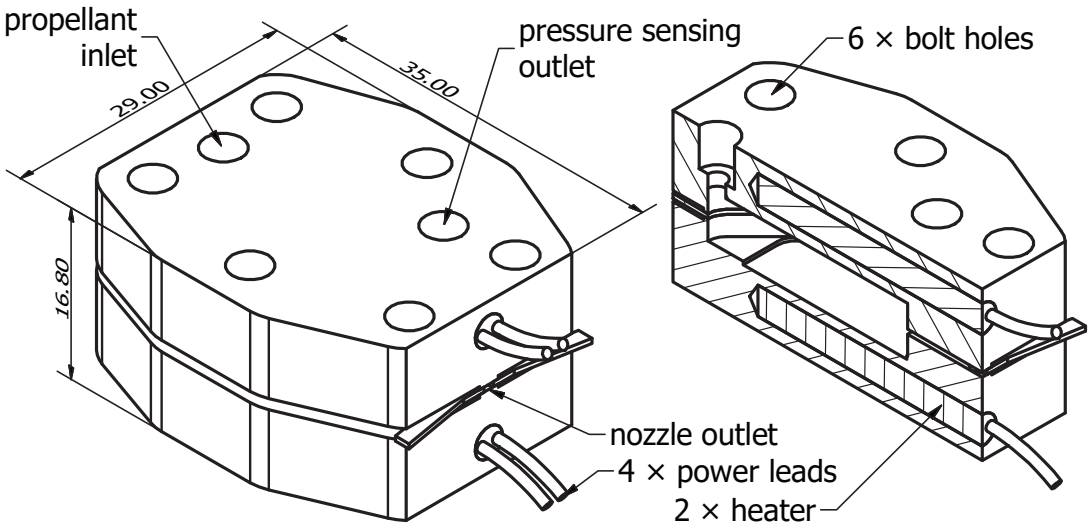

Figure 4.9: Isometric drawings of the thruster body (left, without bolts and foam), with a section view through the middle of the body (right). Several connections, components and dimensions indicated, all in mm.

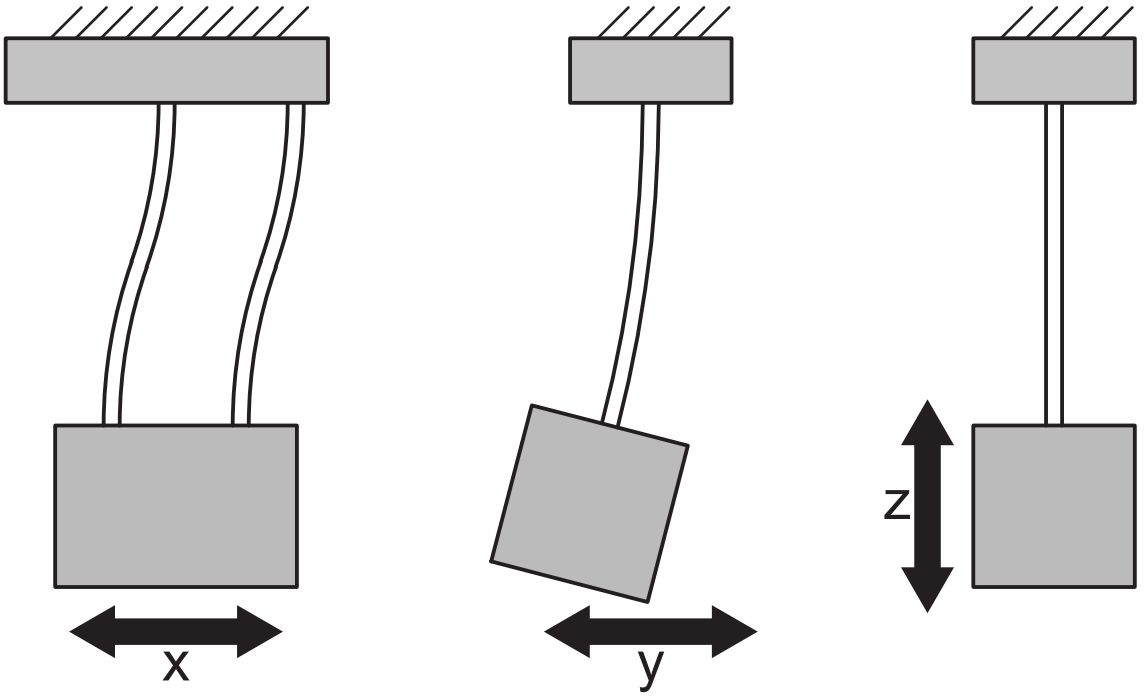

Figure 4.10: Schematic drawing of the three gravity loadings / resonant modes of the thruster body that were considered. The leftmost drawing is the thruster viewed from its side with the nozzle exit pointing to the right, the other drawings have the nozzle exit facing out of the page.

[m]. Usually the thin wall approximation is only used up to a thickness to radius ratio of 10 %, where the actual stress will be about 4 % higher than calculated [22, p. 409]. To take this into account, a generous factor of safety will be used.

The highest stress σ [Pa] for a cylindrical tube with internal pressure p [Pa] (operated in a vacuum) is in the circumferential direction c. This can be calculated from the inner r_1 and outer radius r_2 [m] as follows:

$$\sigma_\mathrm{c} = p\frac{R}{t} \approx p\frac{1/2\,(r_2 + r_1)}{r_2 - r_1} \tag{4.49}$$

Besides the stress due to internal pressure, there is also axial tensile stress due to gravity once the thruster is installed and the possibility of bending stress during assembly if the thruster is held sideways by its interface. The expected thrust is roughly 100 times lower than the weight of the thruster body and is thus not taken into consideration here. Three separate gravity load cases are looked into, with gravity pointing in the direction of thrust (x), up along the tubes (z), and sideways perpendicular to both (y), see Figure 4.10. These also correspond to resonant modes considered in the next subsection.

The load in each case is the weight of the thruster body W_tb [N], equal to the product of its mass $m_\mathrm{tb} \approx 0.15\,\mathrm{kg}$ and standard gravitational acceleration $g_0 = 9.806\,65\,\mathrm{m\,s^{-2}}$. The resulting individual maximum stresses when using n tubes of length L [m] are then as follows:

$$\sigma_\mathrm{x} = \frac{W_\mathrm{tb} L}{2n}\frac{r_2}{I} \tag{4.50}$$

$$\sigma_\mathrm{y} = \frac{W_\mathrm{tb} L}{n}\frac{r_2}{I} \tag{4.51}$$

$$\sigma_\mathrm{z} = \frac{W_\mathrm{tb}}{A} \tag{4.52}$$

The tube's second moment of area I [m^4] and cross sectional area A as used here can be calculated

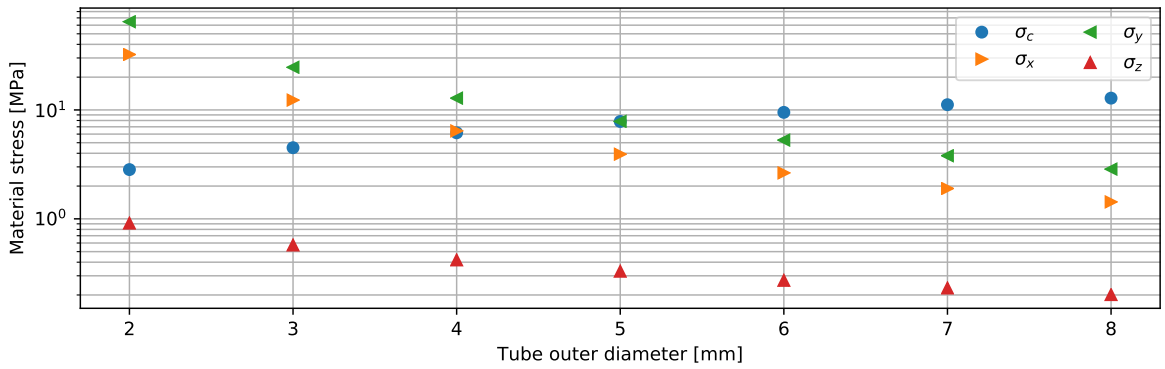

Figure 4.11: Material stresses in connecting tubing due to internal pressure (σ_c), and various gravity loadings of the thruster (σ_x, σ_y, σ_z) for the different sizes available, with tube length and thruster body mass at the final design values.

using the following equations:

$$I = \frac{\pi}{4}\left(r_2^4 - r_1^4\right) \tag{4.53}$$

$$A = \pi\left(r_2^2 - r_1^2\right) \tag{4.54}$$

Easily available small diameter stainless steel tubing was found in the form of supplies for model building hobbyists at two online stores[5,6]. More versions in the form of capillary tubing were found on more general larger web stores as well (Amazon UK and DE) though with shipping from China and a much longer expected lead time as a result. One specialty metal shop in the Netherlands also sells this type of material with fast delivery, though seemingly at an incredibly high markup compared to the other options (over 50 times the cost per length of the same type of tubing). The available sizes ranged from 2 to 8 mm in diameter, in 1 mm increments, all with 0.3 mm wall thickness. Resulting material stresses for the load cases discussed above can be seen in Figure 4.11 for the available tubing sizes. Here the final design tubing length of $L = 52.75$ mm is used, together with a maximum possible operating pressure of $p = 10$ bar (slightly above the maximum pressure of the feed system valves) and $n = 2$ for the propellant inlet and pressure sensing.

As can be seen in this figure, bending stresses become more critical for smaller diameter tubes while pressure stresses decrease due to the constant wall thickness. Only in case of the smallest size tubing do the expected stresses start to come close to the expected yield strength of the material (170 to 1000 MPa [20]), and only for the bending loads. Based on these numbers, 4 mm is seen as a very safe option for all load cases, with smaller diameters possible if assembly and transport is handled with care to avoid unexpected bending loads. Larger tubing would be excessive in terms of strength, and only serves to increase thermal losses.

4.5.2. Tubing stiffness

Stiffness of the tubing impacts the design in two main ways: deflection of components due to gravity and/or thrust force, and resonance effects. Compared to the size and mass of the system ($\sim$ 150 g), the thrust force ($\sim$ 1 g) is very low, so its effects are neglected here. Deflection due to gravity is constant during testing, and only results in pure tension in the tubing (no bending moment) due to the orientation of the device on the test bench. This is thus also neglected, leaving only resonance.

In this case, the primary interaction that can cause resonance during testing is that with the thrust bench, which is a (nearly) undampened pendulum. In previous experiments on the thrust bench TB-5m that will also be used here, its natural frequency was around 1.2 Hz [67]. A lowest natural frequency for the thruster support of $\geq$ 10 Hz is then assumed to be good enough to avoid resonance, even if the natural frequency of the pendulum was somewhat different or the calculations were not entirely accurate.

[5] https://www.modelbouwshopnederland.nl/search/?search=rvs+buis
[6] http://www.proton-modelbouw.nl/category.php?id_category=130

Only the three simplest resonant modes are investigated, front-to-back (x), side-to-side (y) and up-down (z), see Figure 4.10. Torsion was not included as in this two tube configuration this is a more complex superposition of bending and torsion of the individual tubes. Instead it was assumed that a high enough factor of safety on the other modes would also result in a high enough base frequency for the torsion mode.

The stiffness κ [N m^{-1}] of a simple supported beam can be derived from the tip deflection δ [m] that results when it is acted upon by a perpendicular force F [N] [22]:

$$\frac{F}{\delta} = \kappa = \frac{3EI}{L^3} \tag{4.55}$$

Here E [Pa] is the elastic modulus of the material. For the lowest stiffness front to rear, movement is parallel to the support, resulting in a stacked deflection of two half length simple beams. With n [-] tubes parallel, this results in the following front to back stiffness.

$$\kappa_{\mathrm{x}} = n \times \frac{3EI}{2\left(\frac{L}{2}\right)^3} = n\frac{12EI}{L^3} \tag{4.56}$$

For side-to-side swaying, the full length of the tube is available, but there are still n tubes parallel, thus:

$$\kappa_{\mathrm{y}} = n\frac{3EI}{L^3} \tag{4.57}$$

In similar fashion, the equation for z stiffness is as follows:

$$\kappa_z = n\frac{EA}{L} \tag{4.58}$$

with A and I the cross sectional area and second moment of area of each individual tube. Using the assumption that all the mass of the system is concentrated in a point at the end of the tubes, the natural frequency f [Hz] in each direction can be calculated with the following equation:

$$f = \frac{1}{2\pi}\sqrt{\frac{\kappa}{m}} \tag{4.59}$$

with $m = 0.15$ kg the mass estimate of the thruster body from CAD. From the equations for stiffness, it can be seen that $\kappa_{\mathrm{x}} = 4\kappa_{\mathrm{y}}$ so that $f_{\mathrm{x}} = 2f_{\mathrm{y}}$, resulting in the y motion always having the lower and thus more critical natural frequency of the two. For a simple comparison with the z motion as well, the natural frequencies for three different tube outer diameters and a range of lengths is visualized in Figure 4.12. It can be seen that for all tube lengths considered, f_{y} is the lowest and thus critical frequency.

A 4 mm diameter tube was previously selected for strength, which from this figure can be seen to be a very safe option with regard to stiffness as well. The tube length is chosen based on heat losses through it in the next seubsection.

4.5.3. Conduction losses

The only pathway for conductive heat losses thus far is through the two stainless steel tubes for propellant inlet and pressure sensing. Below a numerical approximation is made of the losses from the tube when radiation emitted from its exterior surface to the environment is also taken into account. Radiative heat exchange between the tubes and other components, and within the tube along its length is still neglected for simplicity.

A basic one-dimensional numerical approximation is used, which results in a boundary value problem to be solved for the temperature along the length of the tube. Taking x [m] as the coordinate along the length of the tube, T and T_{a} [K] as the temperature of the tube and ambient temperature respectively, t [s] the time, ρ [kg m^{-3}] the density of the tube material, c_p [J kg^{-1} K^{-1}] its specific heat, $\mathscr{P}$ [m] the tubes outer perimeter, and $\mathrm{d}V$ [m^3] an infinitesimal volume section of tube material at each location x. The following partial differential equation then describes the temperature distribution along the tube in steady state:

$$\rho c_p \frac{\partial T}{\partial t}\mathrm{d}V = k\frac{\partial^2 T}{\partial x^2}\mathrm{d}V - \sigma\epsilon\mathscr{P}\left(T^4 - T_{\mathrm{a}}^4\right)\mathrm{d}x \tag{4.60}$$

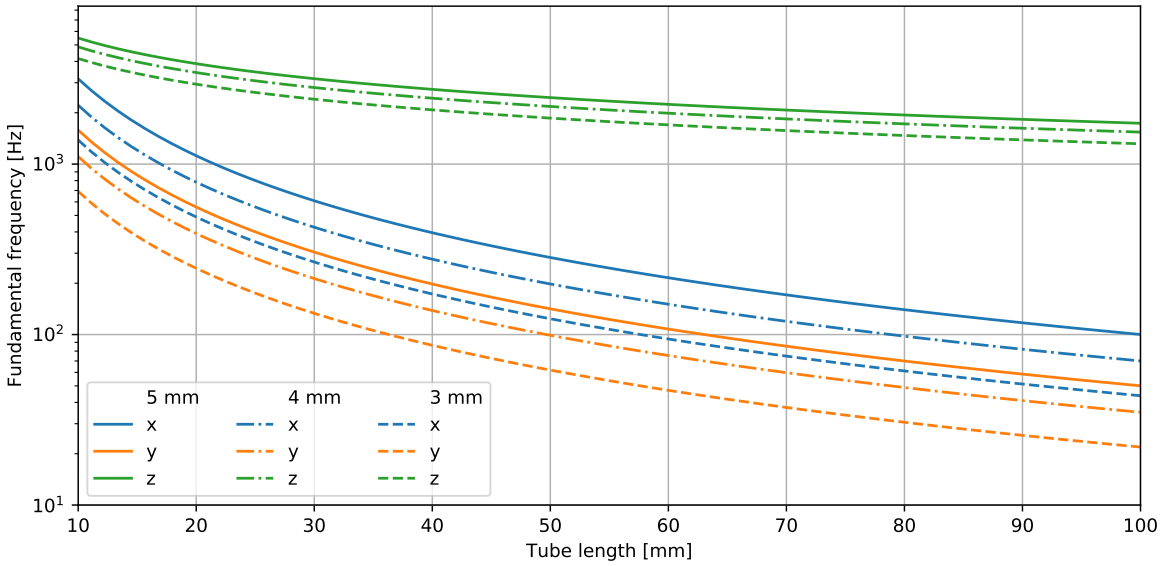

Figure 4.12: Fundamental natural frequencies of the thruster body for the three modes considered, with three different tube outer diameters and a range of lengths.

The first two terms here constitute the standard 1D transient conduction equation, with the last term on the right adding radiative heat loss from the tube exterior surface $\mathscr{P}\,\mathrm{d}x$ [48]. The tube is assumed to be a grey body with emittance ϵ [-], further using the Stefan-Boltzmann constant $\sigma = 5.670 \cdot 10^{-8}\,\mathrm{W\,m^{-1}\,K^{-4}}$. The left hand side of this equation is equal to the derivative of the internal energy of each volume section $\mathrm{d}V$ over time. For the steady state solution of interest here, this should be zero. Rewriting this to include the cross sectional area A [m^2] besides the tube outer perimeter length then results in the following:

$$0 = kA\frac{\partial^2 T}{\partial x^2}\mathrm{d}x - \sigma\epsilon\mathscr{P}\left(T^4 - T_\mathrm{a}^4\right)\mathrm{d}x \tag{4.61}$$

The equation is then discretized into n sections with $\Delta x = {}^{L}/_{n}$ and the second order derivative is replaced with its central finite difference approximation, with i indicating the node between sections at which the derivative is evaluated:

$$0 = kA\frac{T_{i+1} - 2T_i + T_{i-1}}{\Delta x^2}\Delta x - \sigma\epsilon\mathscr{P}\left(T_i^4 - T_\mathrm{a}^4\right)\Delta x \tag{4.62}$$

This equation is vectorized so that it can be solved by a standard vector function root finding algorithm (in this case `root()` from the scipy Python package):

$$\frac{kA}{\Delta x}\left\{\begin{bmatrix}T_2\\ \vdots \\ T_n\end{bmatrix} - 2\begin{bmatrix}T_1\\ \vdots \\ T_{n-1}\end{bmatrix} + \begin{bmatrix}T_0\\ \vdots \\ T_{n-2}\end{bmatrix}\right\} - \sigma\epsilon\mathscr{P}\Delta x\left\{\begin{bmatrix}T_1\\ \vdots \\ T_{n-1}\end{bmatrix}^4 - T_\mathrm{a}^4\right\} = 0 \tag{4.63}$$

Here, T_0 and T_n are the thruster and ambient temperature, and T_1 through T_{n-1} are the unknown temperatures at the nodes along the tube. The total heat loss is then simply the conduction from the 0th to the 1st node with added radiation heat loss at the 0th node:

$$\dot{Q}_{tot} = \frac{kA}{\Delta x}\left(T_0 - T_1\right) + \sigma\epsilon\mathscr{P}\Delta x\left(T_0^4 - T_a^4\right) \tag{4.64}$$

Results using this method can be seen in Figure 4.13, where temperature profiles along the length of the selected tube size are given for different emittance values. The tube thermal conductivity is estimated at $20\,\mathrm{W\,m^{-1}\,K^{-1}}$ (maximum value for stainless steel from [20]), and the interface is assumed to stay at ambient temperature. It can be seen here that for high emittance, the amount of heat lost can be several times the amount for pure conduction. As long as the surface quality is reasonably smooth,

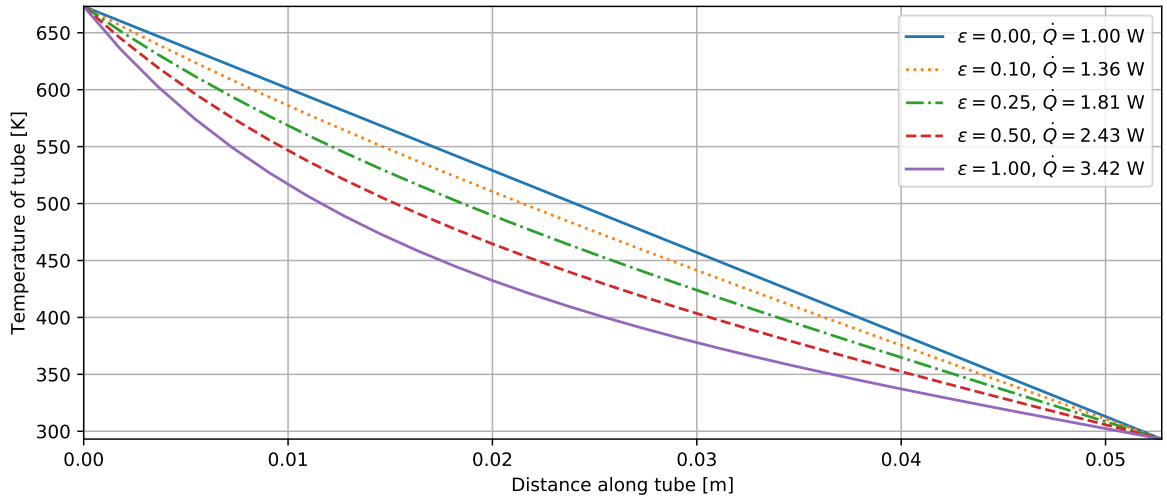

Figure 4.13: Temperature profile along connecting tubing from thruster body (left) to interface (right) with corresponding heat loss values. Conditions shown vary from pure conduction ($\epsilon = 0$) to the outside of the tube acting as an ideal black body ($\epsilon = 1$)

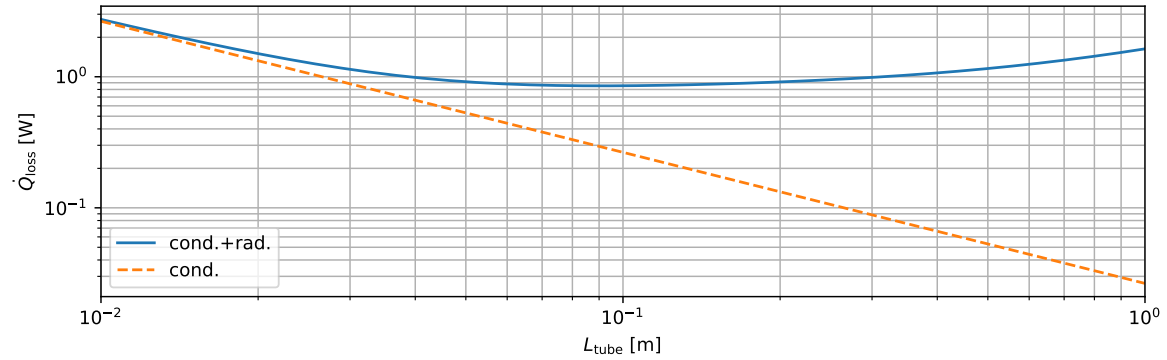

Figure 4.14: Variation with tube length of heat loss through a tube from the chosen design. Both a theoretical case without radiation losses ($\epsilon = 0$) and one with the assumed emissivity ($\epsilon = 0.25$) are shown.

a value of $\epsilon \leq 0.25$ can then be assumed [48], so that only around 1.8 W of heat loss through both tubes together is to be expected.

One last item of note is that the inclusion of radiation losses changes the way that the losses through the tubes scale with tube length. This is due to conduction being inversely proportional to $1/L$, but radiation actually increasing with area. As an example, the losses through a single tube for a range of lengths can be seen in Figure 4.14 for both pure conduction and conduction with radiation. For very short tubing, the values converge. For ever longer tubes however, the pure conduction losses are monotonically decreasing (scaling with $1/L$) whereas the combined losses show a minimum.

The location of the minimum depends on the various parameters in equation (4.63), and thus shows when making the tubing longer becomes detrimental to steady-state heat losses. Even before the minimum is reached though, the gains made in heat losses already flatten out, so that making the tubing longer at such a design point would only result in modest gains w.r.t. heat loss. The chosen design lies within this last region and is thus close to the theoretical minimum heat loss that can be achieved with this tubing cross section and material, according to the model.

4.5.4. Pressure sensing tube foam inserts

One aspect of the pressure sensor tube that was not yet taken into account during conceptual design is that at start of a thrust phase, the tube will be at vacuum conditions. Once nitrogen starts flowing through the heat exchanger, it will also quickly fill up the tube to the sensor, with the gas already having

been heated to a higher temperature than the sensor is rated for. If the design is left as it is, the sensor is likely to break due to this sudden influx of hot gas.

To address this issue, the tube towards the pressure sensor will be filled with small pieces of the metal foam that is also used for the heat exchanger. During start-up this will allow the heat from the incoming propellant to be transferred to the foam and the tube, so that any gas reaching the sensor will have cooled down sufficiently. How well this will work is left for testing as this issue was realised when the thruster body had already been machined, making major design changes impractical at best. Modelling this particular aspect of this design would also involve transient heat and fluid flow, which is considered to be a step above the complexity of other models in this work and consequently out of scope.

Had the issue been discovered earlier, a simpler conceptual solution could have been used, for example to switch to a much thinner ($\leq$ 1 mm diameter), longer, and coiled tube for the pressure sensing connection. This type of solution was also used by Leenders [37] for pressure sensing in a solar-thermal thruster up to 650 K, and is currently being used by fellow MSc student A. Takken for the same application.

An aspect that is also of interest and that can be modelled more easily is the impact of the added material on the heat loss through this one tube. To this end, first the effective thermal conductivity k_e [W m^{-1} K^{-1}] of the foam needs to be known, which can be calculated using the analytical relations below from Calmidi and Mahajan [10]:

$$k_\mathrm{e} = \frac{\sqrt{3}}{2}\left(\frac{r\frac{b}{L}}{k_\mathrm{f} + \frac{1}{3}\left(1+\frac{b}{L}\right)(k_\mathrm{s}-k_\mathrm{f})} + \frac{(1-r)\frac{b}{L}}{k_\mathrm{f} + \frac{2}{3}\frac{b}{L}(k_\mathrm{s}-k_\mathrm{f})} + \frac{\frac{\sqrt{3}}{2}-\frac{b}{L}}{k_\mathrm{f} + \frac{4r}{3\sqrt{3}}\frac{b}{L}(k_\mathrm{s}-k_\mathrm{f})}\right)^{-1} \tag{4.65}$$

Here, k_s and k_f [W m^{-1} K^{-1}] are the thermal conductivity of the non-porous solid and the fluid occupying the pores, respectively. $r = 0.09$ is a constant and b/L can be calculated with the next equation, using the porosity ϵ as used in earlier equations for foam heat exchange:

$$\frac{b}{L} = \frac{-r + \sqrt{r^2 + 4(1-\epsilon)\frac{1}{2\sqrt{3}}\left[2 - r\left(1+\frac{4}{\sqrt{3}}\right)\right]}}{\frac{2}{3}\left[2 - r\left(1+\frac{4}{\sqrt{3}}\right)\right]} \tag{4.66}$$

The foam used is made out of nickel with an estimated thermal conductivity of $k_\mathrm{s} = 90$ W m^{-1} K^{-1} [20]. The conductivity of N_2 varies somewhat with temperature between 0.0255 and 0.0489 W m^{-1} K^{-1} from 20 to 400 °C [6], but is also much lower than that of the solid. It thus only has a small impact on k_e, changing only the fourth significant digit of the results. An intermediate value at a temperature of 200 °C is subsequently used for evaluating k_f of N_2.

The foams used have a porosity of $\epsilon = 0.95$, which results in an effective thermal conductivity of $k_\mathrm{e} = 11.1$ W m^{-1} K^{-1} for the volume occupied by foam. Next, the same method as in subsection 4.5.3 is used for modelling conduction and radiation losses from the tubing. Due to the added metal foam, the term kA in equations (4.63) and (4.64) is then replaced with $k_\mathrm{w}A_\mathrm{w} + k_\mathrm{e}A_\mathrm{foam}$. Here $k_\mathrm{w} = 20$ W m^{-1} K^{-1} and $A_\mathrm{w} = \pi\left(r_2^2 - r_1^2\right)$ are the thermal conductivity and the cross sectional area of the stainless steel tube wall respectively. $A_\mathrm{foam} = \pi r_1^2$ is the cross sectional area of the metal foam or tube interior. The resulting heat loss can be seen for a range of temperatures for both the new case with foam and the standard case without it in Figure 4.15.

From this, the losses through the tube with the foam inserts are then expected to be twice those from the tube without them. These values are however still relatively small compared to the expected heat losses from the thruster body emitting radiation, as will be seen next.

4.5.5. Radiation losses

The thruster body is assumed to be at a uniform temperature, which results in its outer surface emitting thermal radiation. For limiting this radiative heat flow, first a basic radiation heat shield is considered for fully surrounding the thruster body, except around the nozzle exit. The area of the gap A_gap around the nozzle that is left unshielded is simply modelled as a grey surface emitting radiation to black body surroundings:

$$\dot{Q}_\mathrm{gap} = A_\mathrm{gap}\sigma\left(\epsilon T^4 - \alpha T_{ambient}^4\right) \tag{4.67}$$

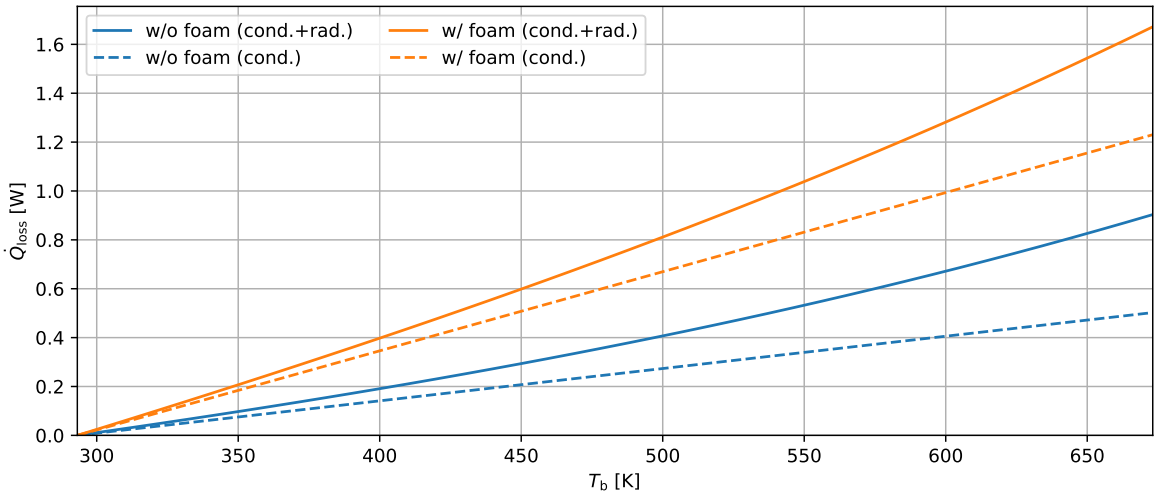

Figure 4.15: Heat losses through the final design connecting tube for both the propellant entrance tube (without foam) and the pressure sensor tube (with foam). For each case, both a theoretical sub-case without radiation losses ($\epsilon = 0$) and one with the assumed emissivity ($\epsilon = 0.25$) are shown.

For simplicity, the heat transfer from the thruster body to the heat shield is approximated as that between two grey surfaces, where the larger one fully encloses the smaller one, each having a uniform temperature [48, p. 473]:

$$\dot{Q}_{12} = \frac{A_1 \sigma \left(T_1^4 - T_2^4\right)}{\frac{1}{\epsilon_1} + \frac{A_1}{A_2}\left(\frac{1}{\epsilon_2} - 1\right)} \tag{4.68}$$

Here $\dot{Q}_{12}$ [W] is the net heat flow from the smaller inner surface (1) to the larger outer one (2), and A_x [m^2], T_x [K] and ϵ_x [-] are the surface area, temperature and emissivity of each surface x. The heat flow from the outside of the shield to the environment is then approximated in the same way as the nozzle outlet gap, though using the area and emittance of the outermost shield surface.

Emittance values depend somewhat on temperature, but can vary by an order of magnitude depending on surface quality and how much oxidation is present [48]. Polished copper can have an emittance of 0.05 for instance, while a thick copper oxide surface layer can increase this to 0.50.

To determine the influence of multiple layers of shielding, the above two equations are generalized into a form with n radiation shields between the thruster body and the environment. For the steady state condition, the radiative heat flows into and out of the shield need to be equal. Because only radiative heat flow is looked at here, an electrical circuit analogy can be used without having to resort to linearisation or numerical solutions [48]. The potential at each shield/node is then the radiosity $J_\mathrm{k} = \sigma T_\mathrm{k}^4$ [W K^{-4}], and the thermal resistance equivalent from surface i to j given as R_{ij} [m^{-2}] is then as follows:

$$R_{ij} = \frac{1}{A_\mathrm{i} F_{ij}} \tag{4.69}$$

Here, F_{ij} is a transfer factor, which takes into account the geometry of the surfaces exchanging radiation and differences in their emittance. For the concentric surfaces, thus for radiation exchange between thruster and shield and between individual shields, this factor is given by:

$$F_{ij} = \frac{1}{\frac{1}{\epsilon_i} + \frac{A_i}{A_j}\left(\frac{1}{\epsilon_j} - 1\right)} \tag{4.70}$$

And for the outermost shield to the environment it is simply equal to the emittance of the outermost shield surface ϵ_rs. The total heat flow through radiation is then:

$$\dot{Q}_{rad} = \frac{\sigma \left(T_t^4 - T_a^4\right)}{\sum R} \tag{4.71}$$

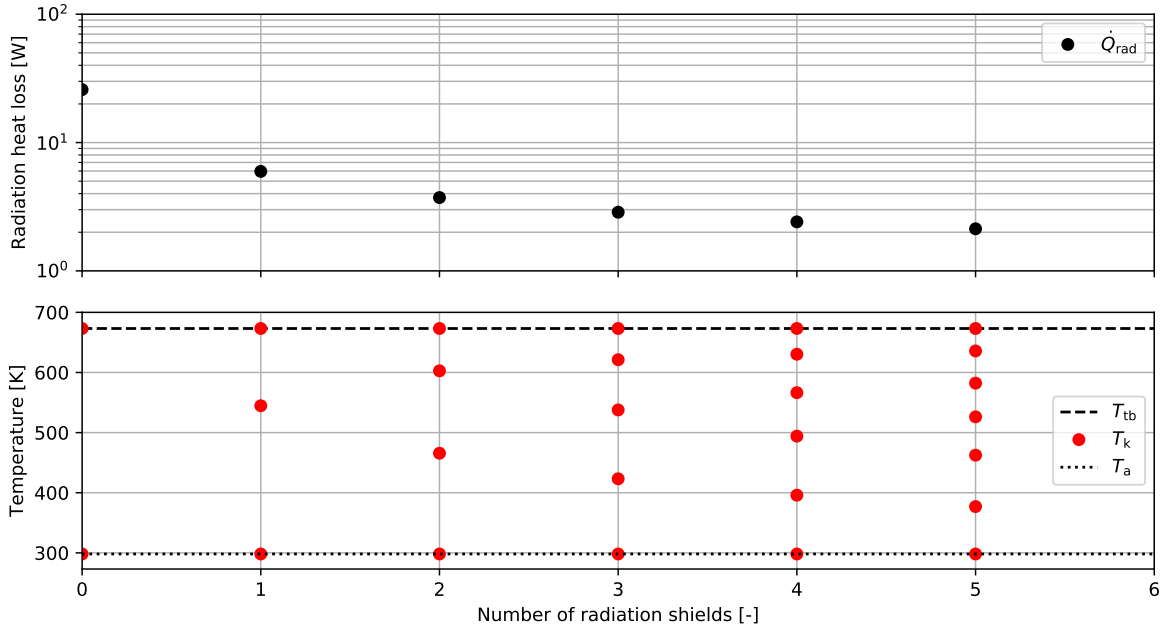

Figure 4.16: Radiation losses for varying numbers of radiation shields. The total heat lost only through radiation is shown on top, with the temperature of each shield layer shown in the graph below.

For a first estimate of how many shields may be needed and how large the heat flow will be, an approximation of a fully enclosed rectangular beam shaped thruster body and shields are used, with a fixed gap size between layers and a fixed radiation shield thickness. A basic investigation was then performed into the effectiveness of one to a few layered radiation heat shields, to be able to make a better informed choice on the number to be used. The original implementation for this was in a jupyter notebook and included interactivity for the emissivity of different surfaces, and the gap sizes between and thickness of shield layers. Figure 4.16 gives a snapshot at estimated reasonable parameter values with thruster body emittance at $\epsilon_{\mathrm{tb}} = 0.35$ (somewhat oxidized), radiation shields emittance at $\epsilon_{\mathrm{rs}} = 0.15$ (unpolished metal) and a thickness of 0.5 mm (thin sheet metal) and a gap size of 2.0 mm.

Considering that two 30 W heaters will be used for the thruster body, this gives an upper limit to how high the heat losses may be at the desired operating temperature. Looking at the preliminary results in Figure 4.16, a single radiation shield would be sufficient to bring down radiation losses to a level where even a single heater could safely be used. No shielding should also be possible, though convergence to the desired temperature will be slower, making testing a lengthy process. Multiple layers of shielding increase the complexity of the design, and offer increasingly smaller absolute gains per added layer. A single layer shield should thus suffice for this project, with the possible future addition of e.g. Multi Layer Insulation (MLI) or glass fibre blankets around it if increased thermal efficiency is desired. Lining the inside and outside of the radiation shield with reflective aluminium foil or similar could also be used to decrease radiation losses through lowering emittance, as well as simply making the device smaller.

The implementation of this radiation shield is a basic folded sheet metal part, made of two halve surrounding the thruster body, see Figure 4.17. For the material, two options were considered: steel and aluminium. The steel is only easily available down to a thickness of 0.8 mm, is roughly three times as dense as aluminium, but also has a lower thermal conductivity and higher stiffness. The aluminium on the other hand is available down to 0.5 mm thickness, effectively reducing the mass of the shield by roughly a factor 5, if the same design and layout are used. However, it also has a lower melting point, limiting its application to lower thruster body temperatures. The 400 °C goal of this project should still be attainable with it, though. Due to the lower mass it was decided to use aluminium for the main enclosure, with steel being used for brackets to connect the aluminium to the cold interface because of its higher strength/stiffness and lower thermal conductivity. The steel parts were made in a truss design to further limit thermal conduction and also reduce mass slightly.

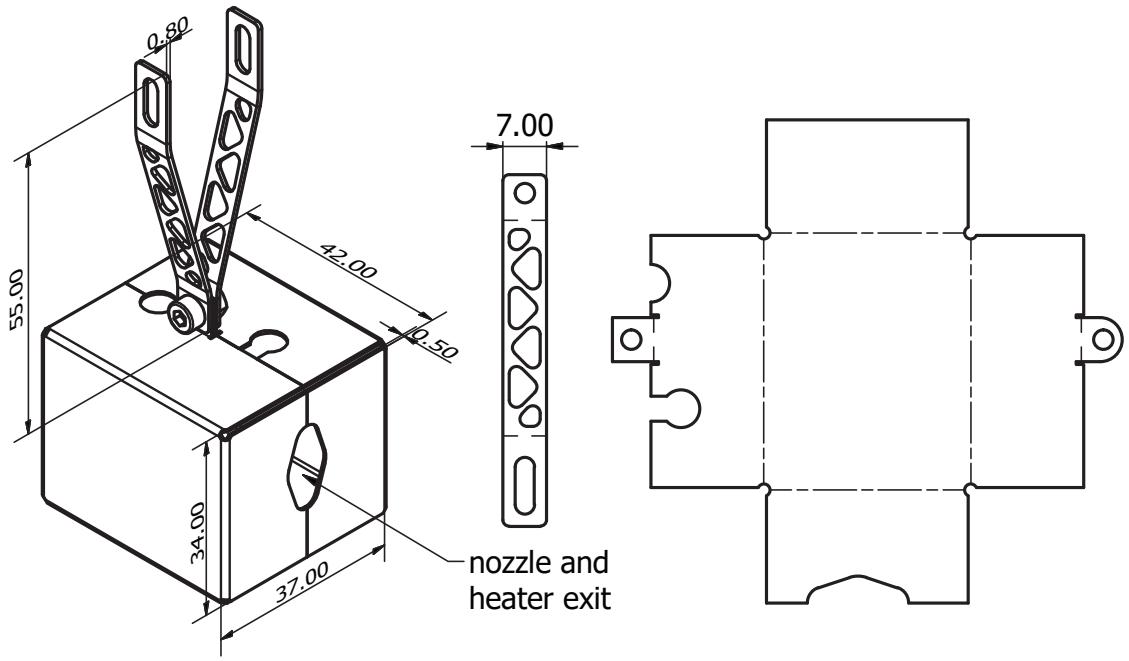

Figure 4.17: Thruster thermal radiation shield design, isometric view (left) and flat pattern of folded parts from one half (right).

4.5.6. Total expected heat losses

With the different sources of heat loss now accounted for, the total amount of heat loss can be calculated for the final design. The analytical approach used also allows for showing the contribution of each source, which can be used to determine avenues of future development that could yield the greatest improvement. As an overview, Figure 4.18 shows the expected heat loss in the range of temperatures that was designed for, together with a division by source. Heat losses are still just around 10 W, which should be more than adequate considering the two heaters used can deliver 60 W in total. With the estimated mass flow from the nozzle, a propellant heating power of ca. 5 W is expected [6], resulting in a steady state heating efficiency of around 33 % (not including losses due to needing to heat up the thruster body in the first place). The heating efficiency η_{heat} [-] is simply the power used to heat the propellant P_{p} [W] relative to the electrical power provided to the thruster P_{el} [W]. This can be calculated from the propellant mass flow, the change in specific enthalpy of the propellant Δh [J kg^{-1}], the heater current I [A], and heater voltage V [V], or with the heat loss to the environment $\dot{Q}_{\text{loss}}$. This efficiency value is also shown in Figure 4.18 for a thrust chamber pressure of $p_{\text{c}} = 1.345$ bar.

$$\eta_{\text{heat}} = \frac{P_{\text{p}}}{P_{\text{el}}} = \frac{\dot{m}\Delta h}{IV} = \frac{\dot{m}\Delta h}{\dot{m}\Delta h + \dot{Q}_{\text{loss}}} \tag{4.72}$$

The heating efficiency found is low compared to older, larger resistojets such as by Donovan et al. [17] (70 to 80 %), but is quite similar to the results of Bayt [4]. Regardless, the power efficiency of the design was not a design goal in and of itself, only that the device can be tested at the desired temperature. In that regard, the current design is seen as quite sufficient.

4.6. Sensors and interfaces

For being able to easily connect the thruster to the thrust bench and propellant feed system, an interface has to be made. Two local sensors are also needed for the thruster body temperature and the chamber pressure. The design and component selection of these is discussed here.

4.6.1. Thruster body temperature sensor

The choice for a temperature sensor primarily came down to rated temperature, cost and ease of use. The cheapest suitable temperature sensor available from a standard TU Delft supplier was the Type-K

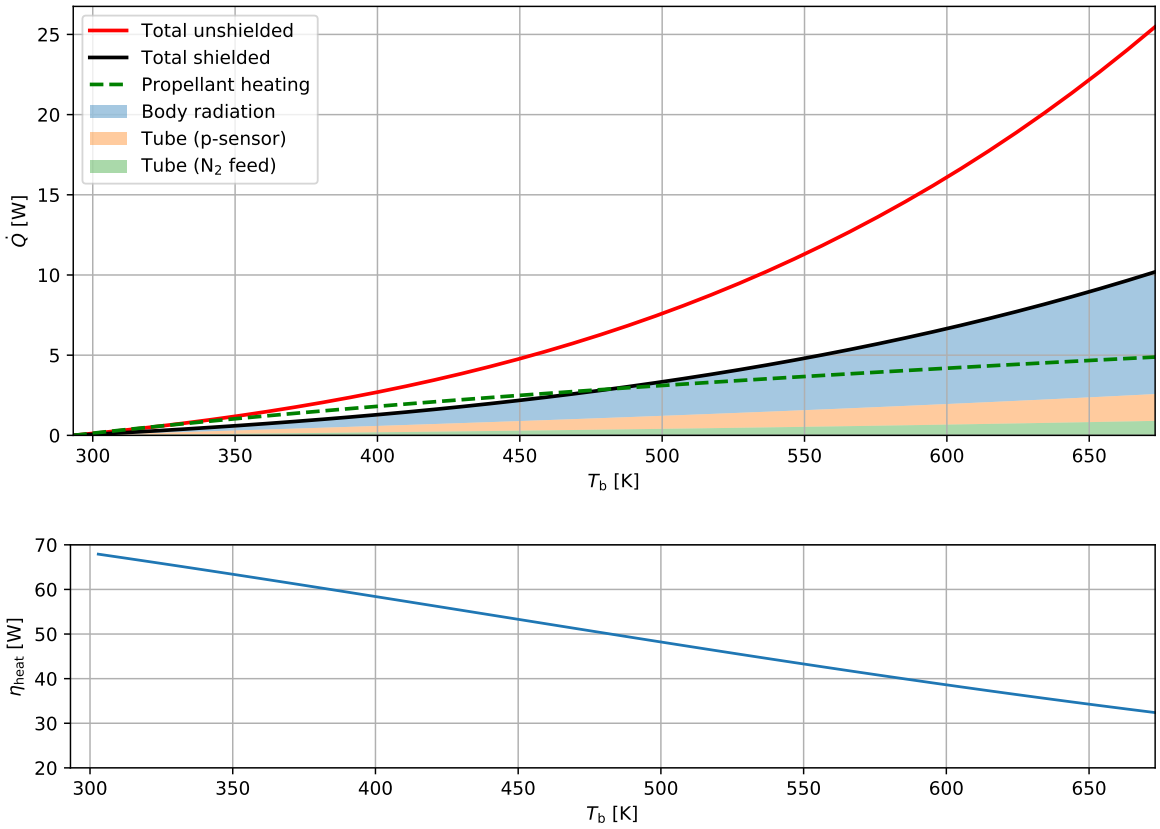

Figure 4.18: Analytically calculated heat losses for the final thruster design, with and without a radiation shield installed. Power used to heat up the propellant to T_b is also indicated, together with the resulting heating efficiency.

KA02 thermocouple from TME[7]. This is rated for operation up to 450 °C with an accuracy of ±1.5 °C. Its measuring tip is also small enough that it can fit snugly in the small gap between the two copper halves of the thruster body, requiring no additional machining for sensor ports, see Figure 4.21 on page 57. It has also been used in previous projects at the department, and can be easily read out using an available NI 9211 thermocouple DAQ, which already had the required adapter for being able to plug in the sensor connector. It will be installed by pushing it snugly into the gap between the two copper thruster halves, requiring no further machining.

4.6.2. Chamber pressure sensor

For the pressure sensor, a similar choice as for the temperature sensor was made, namely a sensor that had already been used previously, so that little to no adjustments would have to be made to existing data acquisition software. The chosen sensor was an MS5837 30 bar from TE[8] which measures absolute pressure up to 30 bar with an accuracy of 0.050 bar at room temperature. It also includes a temperature sensor, a built-in analog to digital converter (ADC) for both sensors, and a purely digital I^2C interface for communicating values. The location inside the thruster that the sensor connects to is indicated in Figure 4.19, and the position of the sensor itself can be seen in Figure 4.21.

It is quite small—only 3.3 by 3.3 mm—and normally a surface mounted device, though it has been used with thin wiring soldered to it at the department for previous projects (e.g. [41, 46]). It can be installed in a leak-tight manner by using a very small o-ring, but the specific size needed was difficult to source, thus it was decided to simply use glue to connect it to the interface. Communication with the sensor will be facilitated by an NI USB-8451 SPI/I^2C DAQ, as used previously at the SpE department.

[7] https://nl.farnell.com/tme/ka02/sensor-thermocouple-k-1m-50-to/dp/4920983
[8] https://nl.farnell.com/sensor-solutions-te-connectivity/ms583730ba01-50/gel-filled-pressure-sensor-30bar/dp/2771904

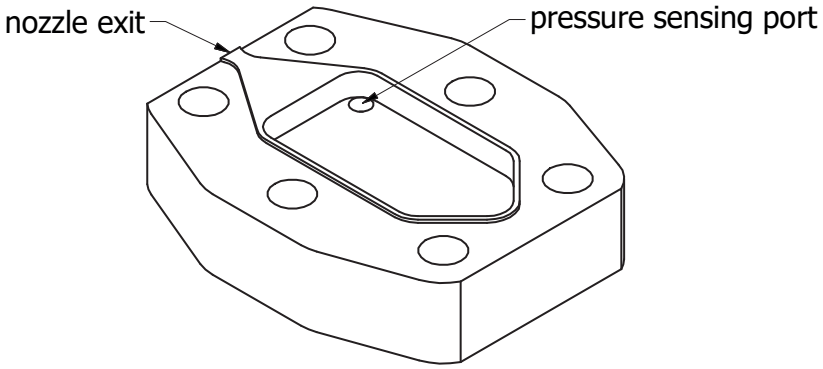

Figure 4.19: Location of the pressure sensing port in the thruster body top copper block.

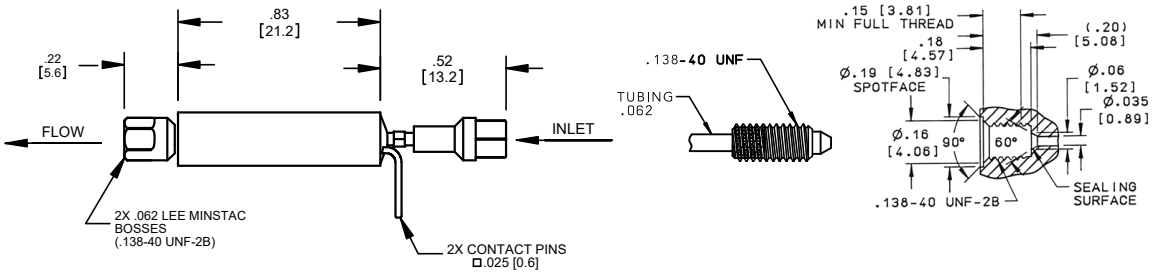

Figure 4.20: Technical drawings of the MINSTAC VHS type solenoid valve (left), standard MINSTAC 062 tube with fitting (middle) and a cross section of the corresponding internal threading and hole shape (right) [64, B3, L4, L8]. All dimensions are in inches [mm].

4.6.3. Propellant tubing interface

To again make the assembly and use of the thruster simpler, hardware that was already present was utilized for the connection to the propellant feed system. The system used in recent projects has been the proprietary *MINSTAC 062* standard from *The Lee Company* [64], which includes tubing, valves, fittings and more for microfluidics. For this project only a single valve to turn the thrust on or off was needed, as well as a piece of tubing to connect the valve to the propellant inlet of the thruster.

The feed system for N_2 already terminates in a fitting that is compatible with the valve, with both of the other components also being present already, specifically a number of VHS M/M 24-3.2 valves. Electrically, the valve requires a special driver to function properly, fortunately this was already installed at the vacuum chamber as well.

Unfortunately due to MINSTAC being a proprietary standard, the threading and shape used for the tube fittings is not a standard size, requiring a special set of taps and drills to make compatible leak-tight connections in components not made by The Lee Company. These tools can be ordered in the MINSTAC 062 Tool kit [64, B3], though were not yet present at the department. These are also only intended for soft materials such as plastic and aluminium and require a few more machining steps.

As a simple alternative, a tube with a MINSTAC 062 fitting on just one end will be used to connect to the valve, with the other end being glued in place to the thruster without a fitting. The tubing is made of PTFE/Teflon which normal glue will not stick to, so a special combination of *PE/PP Primer* and *MR INDUSTRIE KRACHTLIJM*[9] were used, which was know to work from a previous project [46]. Technical drawings of the components used and the shape of a compatible threaded port can be seen in Figure 4.20.

One change is made with respect to placement of the valve compared to previous work. The valve is placed on the pendulum itself, close to the thruster body, so that the tube running from the moving part of the pendulum to the fixed world is always pressurized. Previously, the valve was attached to the top of the vacuum chamber, so that the feed system tube to the pendulum was only pressurized during

[9] https://www.123lijm.com/industrielijm-dun-28-gram-plus-ml-pe-pp-primer/

thrust. The new arrangement should help to reduce the influence of pressure induced stiffness of the tubing on the overall stiffness of the pendulum and make the resulting measurements more accurate [4, p. 118].

4.6.4. Thrust bench connection

The last interface that is needed is a way to physically connect the thruster system to the thrust bench. An aluminium bolted clamp encompassing the vertical round pole of the thrust bench pendulum is used here for ease of assembly and manufacturing. This then consists of two separate pieces, see Figure 4.21 (parts 9 and 10 on page 60). The clamp is located at the rear to allow the 8 mm diameter pole of the thrust bench to which it connects to pass behind the thruster body and radiation heat shield. Aluminium is used because it easy to machine, cheap, and has a high specific stiffness and strength; there are also no material compatibility restrictions as all connections to the component are either glued or bolted.

One half of the clamp with two M3 threaded holes and a cut-out for the pole is incorporated into the propellant interface. This is attached to the steel tubes and already houses the pressure sensor and propellant feed tube. Threaded holes for attaching the radiation shield are also added onto its sides, with the bolts passing through rounded slots to allow for some height and position adjustment of the shield. These were made into through-holes for easier thread tapping by taking out a piece of material in between.

The second piece is then simply the other half of the circular clamp geometry with slightly oversized holes for the M3 clamping bolts.

4.7. Complete design

The finished, fully assembled design can be seen in Figure 4.21. An exploded view of the assembly is also provided on page 60, to show how the many individual components fit together. Components are also indicated with numbers in this exploded view, with a list of all of them available in Table 4.3. An overview of the design and its main specifications are given below.

Firstly, the nozzle design in section 4.1 follows that by Bayt [4], though with double the throat width at 130 µm and half the operating pressure at 1.345 bar. Using the analytical model shown in section 4.2 and when varying the chamber temperature from 300 to 700 K, thrust is predicted to range from 10.6 down to 8.4 mN, I_{sp} from 56.7 up to 72.5 s, and mass flow from 19.0 down to 11.9 mg s^{-1}. Accurate sensors for thrust and mass flow of this magnitude are all readily available in the SSE clean room, so that the design may be verified as intended.

As discussed in section 4.3, two Watlow FIREROD cartridge insertion heaters will be used for propellant heating. These have a maximum power output of 30 W each, for a total of 60 W. Heat will be transferred to the propellant through an open cell nickel foam heat exchanger. With a semi-analytical model, this was sized to be roughly 5 times longer than required for the propellant to approach the chamber wall temperature to within 0.01 %, with negligible pressure loss (< 0.1 %). This large margin should ensure that heater effectiveness will be close to 100 %, regardless of model inaccuracies, so that the propellant temperature at the nozzle entrance may be approximated by the thruster body temperature.

In section 4.4 basic calculations were also performed for sizing of the copper nozzle sealing surface, and a design was made to limit thermal stresses in the device by adding disk springs to the bolted connections. The chosen design with bolts and disk springs should allow for raising the pressure in the nozzle seal to 164 MPa while maintaining compliance for thermal expansion. Worst case scenario thermal expansion would then increase the sealing pressure by up to 18 MPa or reduce it by up to 5.6 MPa, which was considered to be sufficiently low.

Insulation was designed and sized based on (semi) analytical heat loss models in section 4.5. The expected total heat loss at 400 °C is 10.2 W, which would result in a propellant heating efficiency of 32 %. According to the model the primary contributor to this heat loss is radiation from the thruster body, which was 7.6 W with a single layer radiation shield, or a much higher 22.9 W if no shield had been used. The total power usage due to losses and propellant heating then comes to 15 W at 400 °C, resulting in a factor 4 margin with respect to available power from the cartridge heaters.

In parallel with the insulation design in section 4.5, the propellant tubing from the hot thruster to the cold interface was sized to be several times stronger and stiffer than needed for the load-cases that

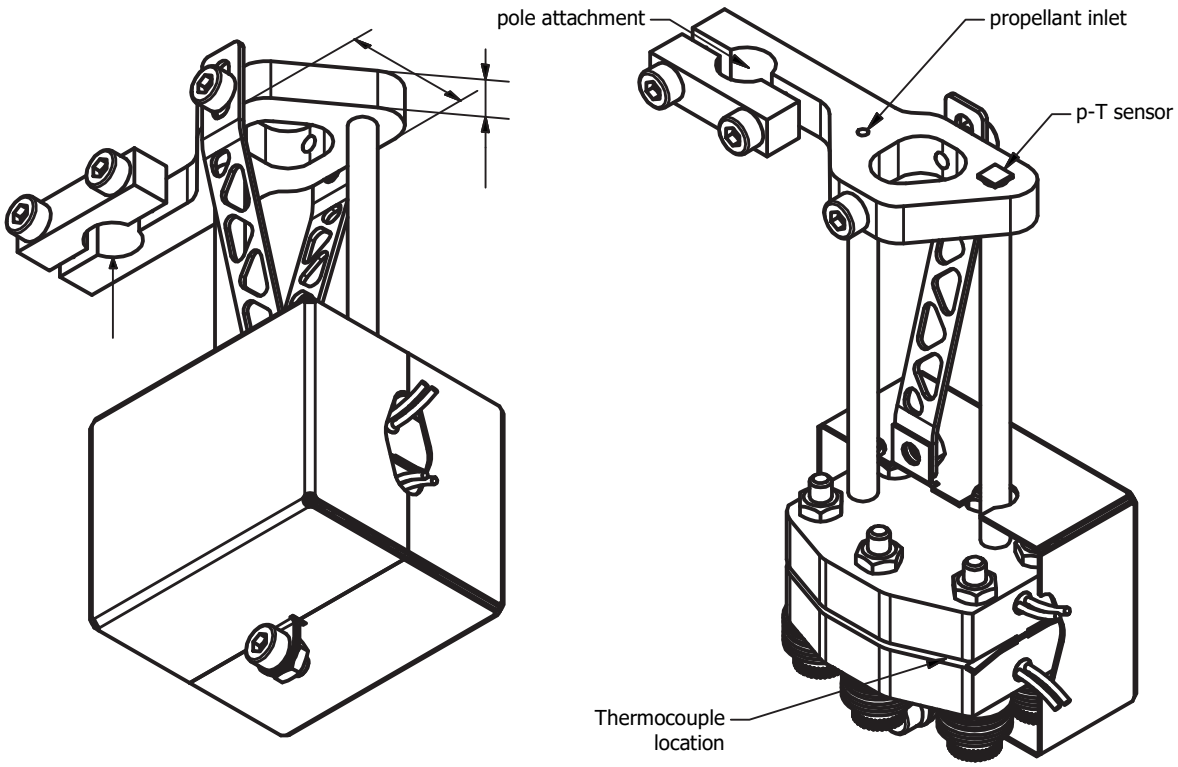

Figure 4.21: Schematic drawing of fully assembled thruster design, viewed from the bottom (left) and top with half of the radiation shield removed (right)

were looked into. This was done to make the design robust for handling and to avoid any resonance with the thrust bench pendulum, which has a natural frequency of ~ 1.2 Hz. A lowest natural frequency of ~ 100 Hz was calculated for the final design and a maximum stress for any single load case of ~ 15 MPa, well below the yield strength of stainless steel.

Specific sensors for propellant pressure and temperature were laid out next in section 4.6. Both should be easy to use with available equipment, as the sensor types have seen use in previous projects at the department. An interface was also designed to connect to an existing thrust measurement bench and propellant feed system with mass flow sensor, so that all measurements given in the guidelines can be obtained.

Though not explicitly mentioned for each component, a very rough cost estimate was kept up to date throughout the design process. Several components were also specifically chosen for their low cost (e.g. the heaters, disk springs, copper type). With a price estimate from DEMO for the nozzle of roughly €100, heaters costing around €120, and further raw material and small components, the total at this point in the project was projected to be between €300 and €400. This includes €0 for machining, as it was already confirmed that two friends could perform this free of charge. The project would also not have been possible within the given budget of €500 otherwise; an initial DEMO quote came to €800 for the four parts needed, see section 5.3. Actual cost of components is discussed further in the following chapter on fabrication. Considering all the above, the design process output is considered to be a success when comparing it to the design guidelines set out at the start of the previous chapter in section 3.1.

4.8. Conclusion

The detailed design process in this chapter is considered to be successfully concluded, as a design with large, safe margins has been realized which follows the design guidelines set out at the start of chapter 3. To keep the projected cost within the allotted budget of €500, two friends with access to a CNC-mill had to be contacted to perform component machining at no cost, as the quote from DEMO for

Part	Description	quantity	Material
1	Nozzle profile	1	stainless steel
2	Bottom thruster body sealing block	1	copper
3	Top thruster body block	1	copper
4	Compression shoulder bolts	6	steel
5	30 W cartridge heater	2	–
6	Left half of radiation shield	1	aluminium
7	Right half of radiation shield	1	aluminium
8	Foam heat exchanger	1	nickel
9	Propellant & connection interface	1	aluminium
10	Clamping connection bracket	1	aluminium
11	Propellant inlet/p_c-sensor tubing	2	stainless steel
12	Stack of 6 disk springs	6	steel
13	Washer	6	steel
14	MS5837-30BA pressure sensor	1	–
15	M3 nuts, multiple uses	8	stainless steel
16	M3×12 bolts for clamp	2	steel
17	M3×5 bolts for shield attachment	4	steel

Table 4.3: List of components as seen on the exploded view of the thruster design on page 60.

the same parts came to ~€800. This does mean that a similar project in the future may be impossible to complete without additional funding or contacts with machining access who are willing to work for (very) low rates.

With regard to thrust modelling of the reference thruster, the chosen analytical model predicts values better than IRT. Modelled values were always within 10 % of experimental outcomes for the reference design, for many cases even within 5 %. This was much more accurate than IRT, which was off by roughly 30 % at the highest chamber temperature of around $7 \cdot 10^2$ K and 20 to 25 % for cold gas conditions. This same model was consequently also used for thrust and I_{sp} prediction for the prototype micro-nozzle. Of note is that the model is slightly conservative, consistently under-predicting thrust and I_{sp}. Determining how well the model may work for planar micro-thrusters in general was not investigated and will require further research.

4.9. Recommendations

Based on the design process performed here and some later insights, several recommendations for future work are formulated. Firstly, many parts of the design still have a lot of room for optimization.

The thruster body geometry for instance could be made smaller if a different component packaging and/or smaller heater chamber is used. It should also be possible to remove more material from the copper blocks, which were kept quite simple here to keep machining time to a minimum. This can be done based on computer topology optimization for instance. A smaller thruster body should result in lower radiative heat losses, while the lower mass and reduced thermal capacity will result in faster warm-up with less energy needed.

Later searches for small COTS heaters by Zandbergen revealed an alternative to Watlow, namely the Kawai Corporation[10], who make two types of heater that may be of interest. Just like Watlow, they make cartridge heaters with a diameter of ⅛ inch, but with a 40 % smaller minimum length of 15 mm instead of 25.4 mm, and a temperature rating up to 1000 °C. They also have film heaters with a minimum area of 10 mm × 20 mm and a maximum temperature of 500 °C. These heater types could be used to further decrease the size of the thruster body, and allow for higher temperature operation.

The propellant tubing may also be made with a smaller diameter (1 or 2 mm) as the current design is quite over-sized in terms of stiffness and strength. These tubes may then also be set up in a triangular set of three or with additional pieces in a 3D truss like formation to have a stiff connection with little to no heat loss through both radiation and conduction.

The main point of heat loss that should be addressed in future versions is that through radiation

[10] https://www.kawaidenki.co.jp/english/

from the thruster body, though. This can be decreased by making the thruster body smaller, having more reflective surfaces or for instance wrapping the radiation shield in glass / ceramic blankets.

With the use of primarily analytical models, it should also be relatively simple to put all of their parameters together and numerically optimize certain aspects of the design as a whole.

Future research may also look into validation of the metal foam heat exchanger model for the type of foam used at this small scale. If it can be validated, the model could then be used for more accurate optimization of the heat exchanger size. More advanced models may need be created afterwards if accuracy of the current model is insufficient, taking heat transfer through the solid foam and the copper body into account for instance, or looking at boiling behaviour for use as a VLM.

From later insight gained, it would likely also be beneficial to not have the raised copper sealing surface as a straight edge down, but at a 45° angle for example, to avoid stress concentrations at places other than the seal itself. More in-depth Finite Element Method analyses would also be warranted to allow for more confidence in the design.

Lastly, for pressure sensing it may be beneficial to use a much thinner ($\leq$ 1 mm) coiled tube as seen in commercial high temperature pressure sensors and other projects at the department. With this the foam inserts would no longer be needed and much lower conduction and radiation losses from this tube in particular could be achieved.

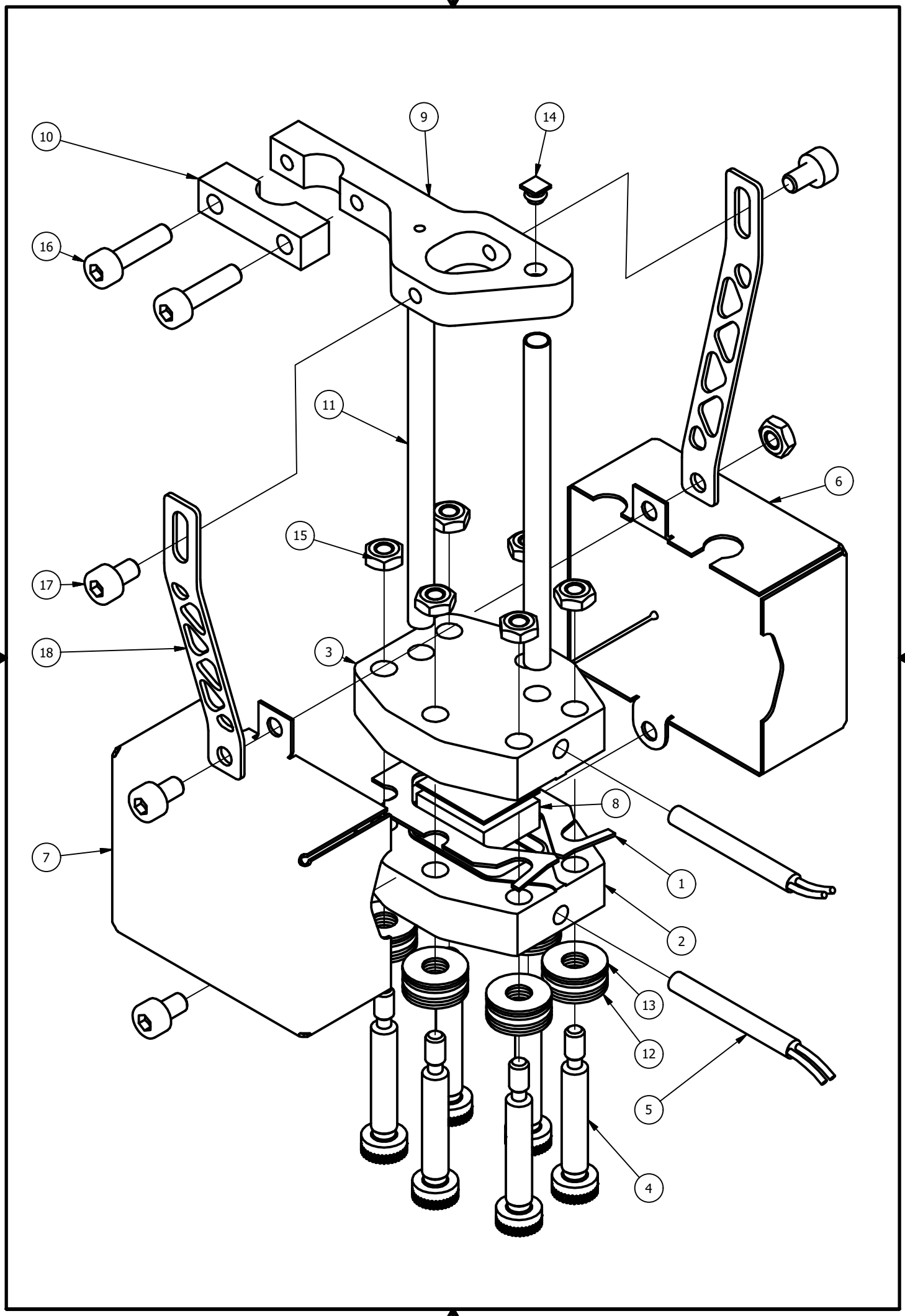
10
9
14
16
11
6
15
17
18
3
8
7
1
2
13
12
5
4

5

Cold gas thruster fabrication

With the detailed design finished, the steps to go from this to a finished physical system are described here. First an overview of all the work that needs to be performed, together with some project management tools used, is given in section 5.1. The various components are then discussed in sections 5.2 through 5.8. For each of these the fabrication steps, cost and time are discussed, as well as any issues that may have occurred. Subsequently, the assembly process of the thruster is laid out in section 5.9. Following this, basic characterization and verification of the thruster is performed regarding nozzle geometry in section 5.10, and leak-tightness of the design and its metal seal in section 5.11. These steps are taken to determine if thruster fabrication was successful enough to commence thrust testing, or if the system has to be fixed in some way. Cost and production time of the fabrication process is then compared to the existing silicon etching method in section 5.12. Lastly, a conclusion is given in section 5.13 and recommendations for future work are laid out in section 5.14.

5.1. Work overview and management tools

For the created design, quite a few components were needed from multiple different suppliers, with many of the components having several fabrication steps. To make this entire process more manageable, three tools were used. Firstly, a Work Breakdown Structure (WBS) was created to split everything into manageable tasks. Secondly, a Gantt chart was created and maintained to keep track of delivery and manufacturing times, and how this aligned for components that needed to be put together. Lastly, for keeping track of tasks on a day-to-day basis, a personal Kanban board was used. These three tools are briefly discussed here in order. Expenses and expected costs were also checked against the €500 budget at regular intervals, which is not further elaborated on here.

5.1.1. Work breakdown structure

As mentioned, a WBS was used to create a tree of all individual tasks that need to be performed for the entire fabrication process. The created WBS for both the cold and hot gas thruster versions together can be seen in Figure 5.1. This is also used as a reference to keep track of which tasks have been completed. In this chapter only the cold gas parts are elaborated on, with the exception of the metal foam manufacturing, which was essential to figure out early on and could be done in parallel with other tasks.

5.1.2. Gantt chart

A Gantt chart was used to plan ahead and keep track of time during the manufacturing process. This is essentially a several week long, detailed subsection of the original thesis project plan with rows for some general time consuming steps and how they depend on one another (not necessarily the same as those in the WBS). With the software used for this, GanttProject[1], the progress of each step could also be recorded. A snapshot of the chart in the middle of manufacturing can be seen in Figure 5.2.

[1] https://www.ganttproject.biz

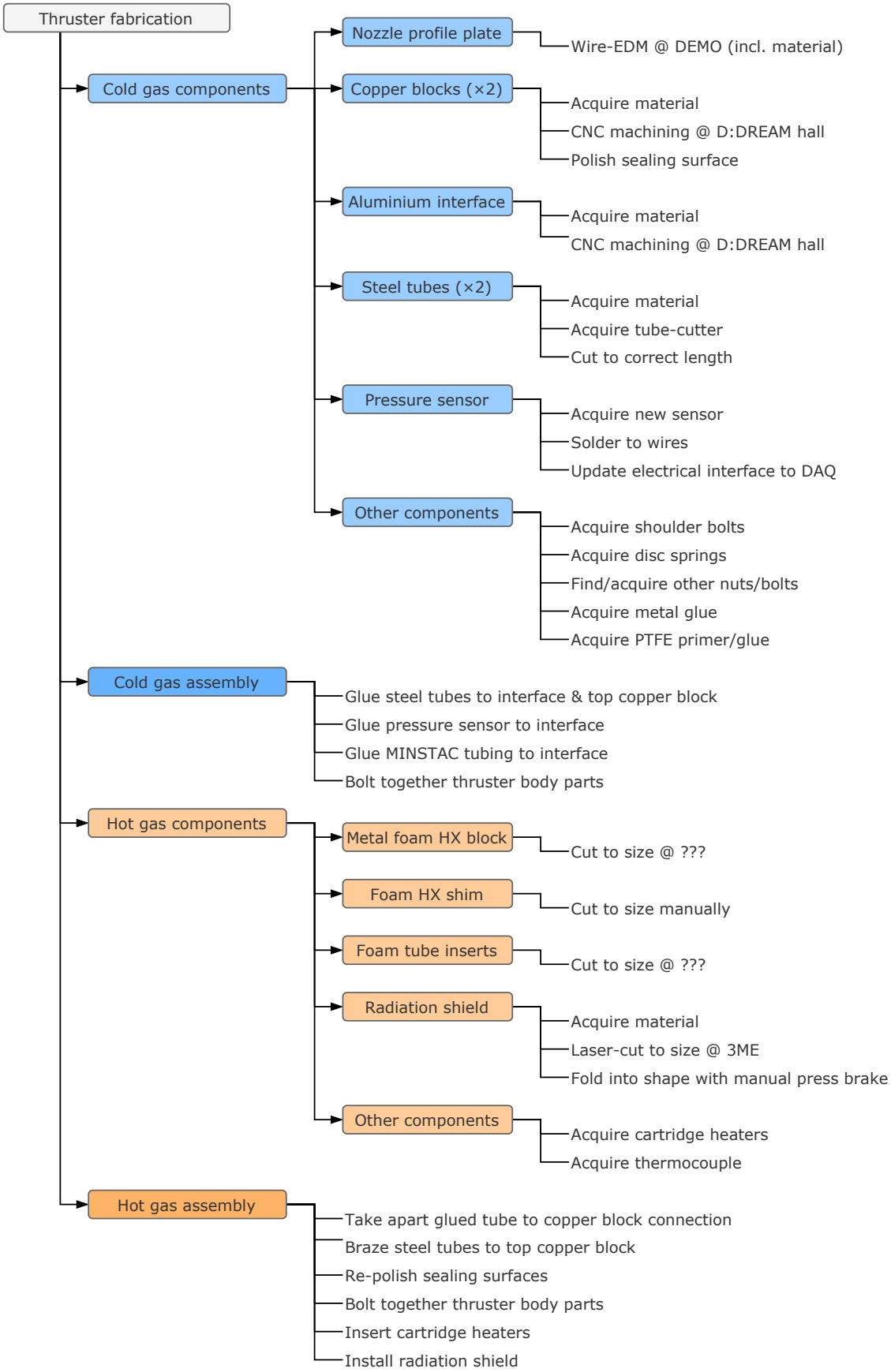

Figure 5.1: Work breakdown structure for manufacturing of the cold and hot gas system.

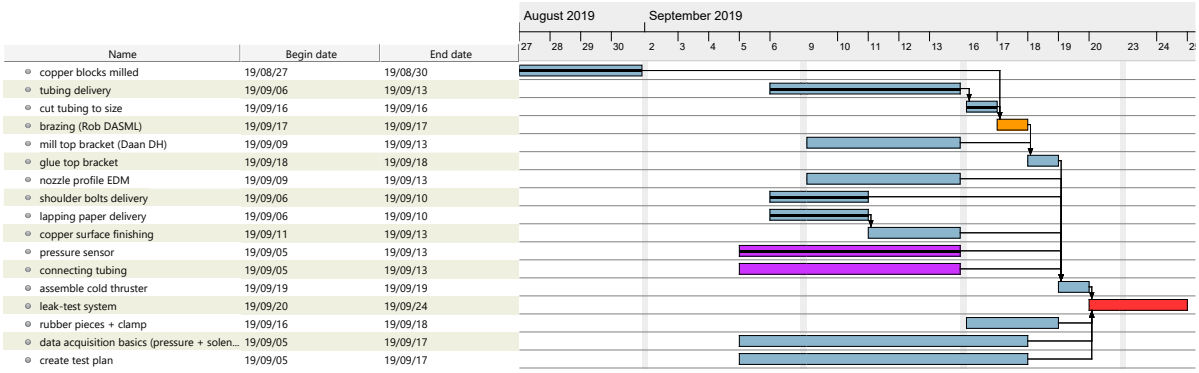

Figure 5.2: Snapshot of Gantt chart for the manufacturing process.

Header	Description
To Do	New tasks are added here. Contains tasks that have not been started yet and also will not have to be started on for the next few days/week.
This Week	For tasks that have to be started on in the next few days/week.
In Progress	For tasks that are currently being worked on.
Impeded	For tasks that are being impeded due to external factors, e.g. component delivery, fabrication by a different party, etc.
Documenting	For completed tasks which have not been documented yet.
Done	For tasks that have been completed *and* documented.

Table 5.1: Kanban board column headers and descriptions.

5.1.3. Kanban board

Kanban is used as an agile project management tool for assigning tasks to people and keeping track of the stage each task is in. In this case the team of people consists of just the author, thus this is only used to keep track of tasks. The particular implementation employed here is nearly identical to the one used by the Forze student team during the time the author was part of it. In this case it consists of a board with six columns, titled in order: To Do, This Week, In Progress, Impeded, Documenting, and Done. Descriptions for each of these can be found in Table 5.1. New tasks are created in the leftmost column, and moved to a new column when the stage which it is in changes.

The board was first implemented on a physical blackboard at the author's home during the design process, with each task written on a post-it note. Later, when more time was spent at the faculty, it was moved to a digital version on `https://www.trello.com` for better access. This also came with some additional benefits, for example the ability to add a list of check-boxes per task with top-level visual indication of progress.

5.2. Nozzle profile

As discussed before, the nozzle profile is machined using wire-EDM at DEMO, in the main workshop at the electrical engineering faculty. The contact person for the whole process was Leon Roessen[2]. Through discussion with them, stainless spring steel was chosen as the material for the nozzle. This has a very accurate and consistent thickness, and has a low surface roughness, requiring no polishing step beforehand. It was also in stock with thickness values ranging from 0.010 to 1.00 mm, including 0.50 mm as needed here, requiring no ordering of new material and no waiting for material delivery. This variety of material thickness may also be used for creating future micro-thrusters with different nozzle channel heights.

The low roughness/high flatness of the material also meant that several layers could be stacked for parallel production. In consultation with the wire-EDM operator at DEMO, it was decided to attempt this with two pieces of 0.50 mm spring steel and two pieces of 1.00 mm spring steel all stacked together.

[2] `L.T.Roessen@tudelft.nl`

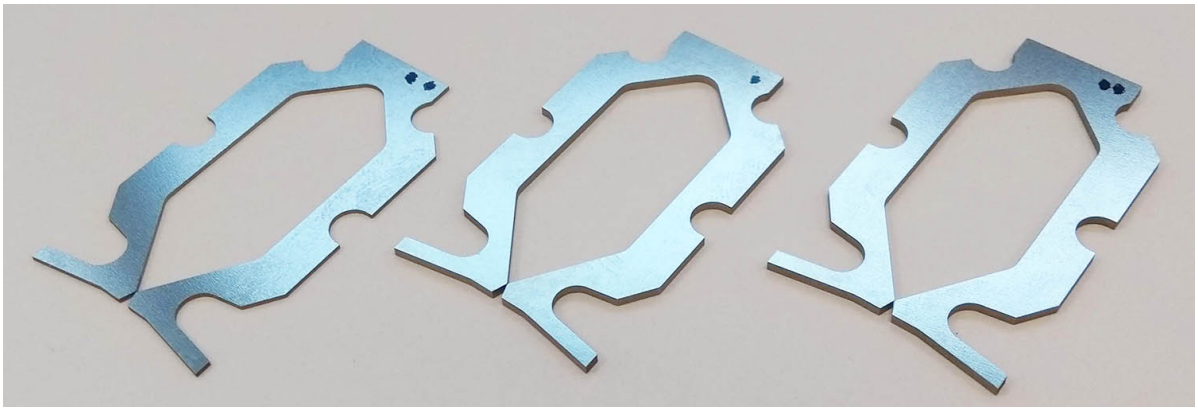

Figure 5.3: Three of the four wire-EDM cut nozzle profiles. From left to right: one 0.5 mm thick nozzle (N0.5-02) and two 1.0 mm thick nozzles (N1.0-01 and N1.0-02). The other nozzle (N0.5-01) was used during this project.

This was done based on the operator's assessment that it should then only cost slightly more than just a single item, not four times as much. The main expense would be for the man-hours spent operating the machine, with material cost being negligible in comparison due to the small size.

The machining time taken is mainly a function of the desired surface roughness of the cut and the contour length [29]. To reduce the time needed, it was communicated that only the profile sonic and supersonic flow sections would need a low surface roughness, with a quicker and rougher cut being possible for other parts.

One thing that was further mentioned by the machine operator was that due to the the open contour of the profile, minor internal stress build-up from the cutting process may result in slight warping of the profile after cutting. This was seen as an acceptable risk as the component should be flexible enough to allow for slightly elastically deforming it back into the correct shape during assembly. Three of the four nozzles that were made can be seen in Figure 5.3.

In the end, from placing the final order at DEMO to the components being ready took roughly two and a half weeks. This was mostly due to the machine operator being occupied with other projects, as the machining operation itself only takes a few hours at most. All four nozzles were successfully made, though the operator did opt to individually machine each throat and supersonic expansion section to maintain accuracy.

Due to the individual machining of the components, the cost for these components turned out unexpectedly high at €640, or €160 each. This is consistent with the earlier quote by DEMO of roughly €100 for a single component, but not what was desired when ordering the four pieces to be machined in parallel. This also caused further issues as a single component would have worked inside the given budget of €500, but four of them already exceed this, without taking into account any other parts that need to be bought. If any other parts are attempted to be cut in parallel with wire-EDM in the future, it would thus be advised to clearly state how many should be made in the event that parallel machining is unsuccessful.

One of each nozzle thickness variant was briefly inspected on a Keyence VR-5000 wide field optical 3D microscope at the Delft Aerospace Structures and Materials Laboratory (DASML). The resulting height and roughness measurement for one of the 1.00 mm thickness profiles (N1.0-01) can be seen in Figure 5.4, together with an optical image of the nozzle contour. The surface roughness on the sealing surface is acceptable with measured values for the shown section of $R_a = 1.231\,\mu m$[3] and $R_z = 13.921\,\mu m$[4]. It can also be seen that one side of the profile is around 40 µm higher than the other. When looked at from the front this could be seen to be due to the aforementioned warping from machining stresses, not due to material being a different thickness on each side. This is seen as an acceptable amount of warping that can still be rectified during assembly, with no major deformation besides this being visible. The general shape of the nozzle contour was also seen to be correct.

More in-depth quantitative measurements of the geometry of the nozzle profile that is used in the actual system (N0.5-01) are shown later in section 5.10. There, further verification of the manufactured

[3] The mean absolute deviation of the surface height from its average.
[4] The maximum peak to peak distance of the surface height.

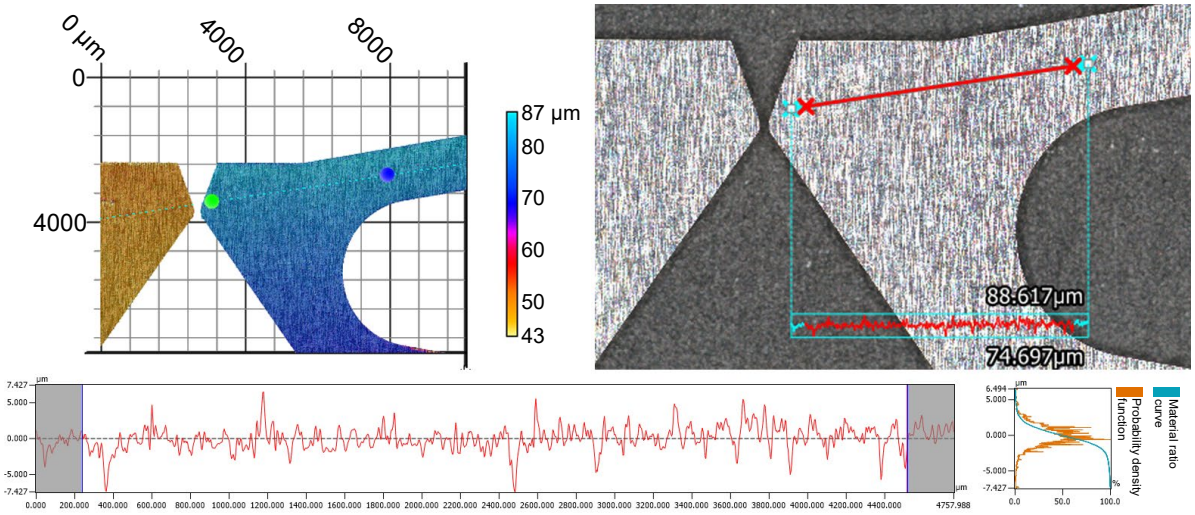

Figure 5.4: Nozzle N1.0-01 top surface height map (top left), optical image with path of roughness measurement indicated (top right), and surface roughness and material distribution graph (bottom), all from Keyence VR-5000.

nozzle dimensions is carried out, together with measurements of the fully assembled nozzle. As the nozzle profile is slightly compliant, its throat width can vary until it is fully clamped down, and can thus only accurately be determined after assembly.

5.3. Copper blocks and aluminium interface

In total, four different components required CNC machining, the two copper blocks for sealing in the nozzle profile, the top aluminium interface, and the accompanying small clamping bracket (parts 2, 3, 9 and 10 on page 60, respectively). Because these used largely the same fabrication methods they are discussed together.

5.3.1. CNC machining

Initially DEMO was contacted for the machining of these components as well but gave a quote of around €800. This was far beyond the budget of this project, even if no other parts were needed. As an alternative, two of the author's colleagues from the Forze student team were contacted, who had CNC milling experience and access to a Maple CNC mill in the D:DREAM hall. These were willing to perform the machining free of charge as a favour, if the material was provided. The people who performed the machining were Frank Overes for the two copper blocks, and Daan Treurniet for the aluminium pieces and resurfacing of the two copper blocks after a polishing mishap.

It should be noted for future thesis projects that this is a relatively exceptional circumstance, and that without such contacts a project requiring machined parts will likely require additional funding. Machining can take some time and hourly rates of machinists add up quickly, even for small projects. This is especially true for single units where overhead from tool-path programming and setup may be large.

The chosen material—Cu-ETP bar stock—can be ordered from for example metaalwinkel [5] in Rotterdam for €10 when picking it up yourself, or slightly more including shipping. Other companies that can provide this material are usually more geared towards larger orders and in many cases only do business with companies, making ordering more difficult. For this project, the material was actually ordered from DHZ store[6], which has roughly the same material cost per volume as metaalwinkel. The minimum material size was larger though, resulting in a somewhat higher cost at €42, and €10 shipping. Enough material is left over from this for roughly 5 similar thruster bodies though. The cheaper option was not used because it was only found after the material had already been ordered, which was under some time constraint due to the availability of the person who would machine the pieces.

Unalloyed copper is quite a soft and gummy material, which can be potentially problematic for machining operations, as chips may not break off or start to melt onto the mill or drill being used. As

[5] https://www.metaalwinkel.nl/
[6] https://dhzstore.nl/

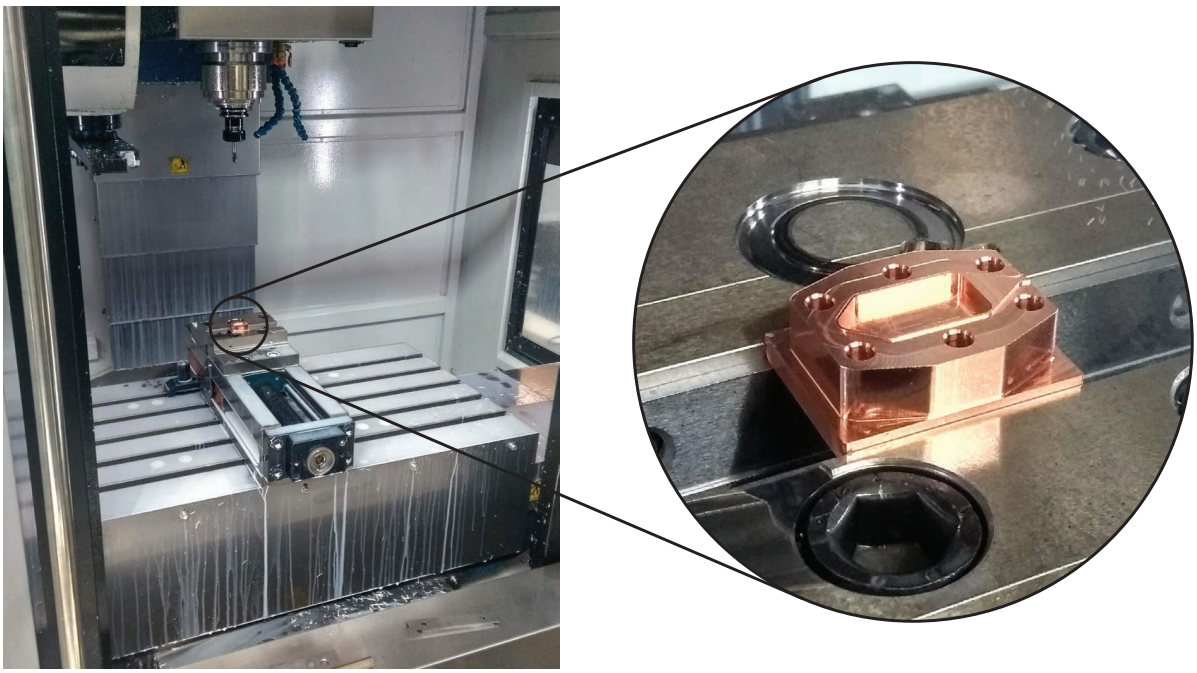

Figure 5.5: One of the thruster body copper blocks midway through CNC milling.

a backup material, some brass was also ordered together with the copper for €8, which is easier to machine, though also has a higher yield strength and lower thermal conductivity. This was not needed however, as the machinability turned out to be quite decent when using the right tools and settings. An image of one of the copper blocks midway through milling can be seen in Figure 5.5.

Based on advice from DEMO, very sharp High Speed Steel tooling was used with plenty of coolant, combined with speed and feed settings normally used for aluminium. The total time spent by the two machinists was roughly 8 hours, including CNC programming with Fusion 360, cutting the bar stock to the correct length and cleaning up. This also included the instances of re-surfacing one side of each copper block.

All four M3 holes in the aluminium interface were threaded with a hand operated tap, and exterior sharp edges were deburred with a small file. The bolt holes on the copper blocks were also reamed by hand to the required 4 mm diameter slip fit for shoulder bolts after CNC machining had concluded. This later turned out to have been a mistake resulting in the bolt holes being slightly off from perpendicular to the sealing surface, making assembly with the shoulder bolts essentially impossible as the sealing surfaces were no longer parallel. This problem was circumvented by using different bolts, see section 5.9 on assembly.

5.3.2. Copper finishing

For most of the blocks surfaces and for all of the aluminium parts, the surface quality produced by CNC machining is good enough. For the sealing surfaces though, which also include the top and bottom part of the nozzle contour, a better surface finish was desired. Several options were investigated with the aim to create a surface with $R_a < 1\,\mu m$, so that surface roughness would not adversely affect the nozzle performance [36]. A very low surface roughness may also help to create a better metal-metal seal, as the material has to deform less to fill up gaps. The created sealing surfaces should also be flat relative to each other for making sure all parts of the seal touch.

For relatively rough surface finishing, sandpaper can be used, with the higher grit variants (up to roughly 10000) going down to just a few micron grain size. After this, wet polishing compounds can be used to create an even smoother finish down to about 1 µm. It was however difficult to find a single company/shop that sold both at a reasonable price.

A first alternative was found in the form of 3M lapping film. This is essentially a specialty sandpaper, with grain sizes down to 0.3 µm, a pressure adhesive backing, and can be used both wet and dry. It can be stuck onto flat surfaces like a machining surface plate (very flat) or a plane of glass (slightly less flat),

to keep the finishing surface flat as well. A sample pack of the full range of grain sizes was obtained from workshop heaven[7] in the UK, one of the few consumer shops that sell it in small quantities.

A first attempt was made to polish the sealing and channel surface of one of the blocks with the lapping film. It was attached to a 5 mm thick glass plate from Ikea, stacked on top of a second same glass plate, to provide a reasonably flat, though affordable background. The lapping paper was used down to 3 µm, as finer grades had some issues with small bubbles and/or particulates between the sheet and the glass causing scratches. This provided an adequate surface finish, mirror-like, but still with noticeable fine scratches. Due to incorrect application of force on the workpiece during the process, the rear section with less surface area was unfortunately ground down more than the front section, resulting in an an unacceptable slope of the sealing surface on one copper block. The top of this copper piece thus had to be re-milled to get the sealing surface back to its original height and flatness. As mentioned, this was done by Daan Treurniet.

As a second attempt to go beyond the still scratchy surface finish achieved with lapping film, a small tube of "Unipol" liquid polishing compound and a fine polishing cloth was acquired from Thomann[8]. The ordered polishing compound turned out to mainly remove stains from oxidation, and not to remove any minute scratches from the surface. This is also useful, as copper stains quite quickly, so it could be used to clean up other surfaces, but this was not what it was intended for.

As a final alternative, it was discovered that DASML also has polishing facilities, which are normally used for polishing material samples for microscopy. This can be done with diamond polishing compound grain sizes down to 1 µm, after which the surface quality can be inspected on a nearby Keyence VR-5000 microscope. These can be used after following a general aircraft hall safety training and a short instruction by the person responsible (currently Durga Mainali[9] for polishing and microscopes). Some overzealous use of too low grit / large grain size sandpaper on here did unfortunately necessitate re-milling of the sealing surface of the other one of the blocks as well though. In both re-milling instances, the sealing surface geometry was essentially lowered by 0.35 mm, just below the original sealing ridge height of 0.30 mm.

For the next polishing attempt after the re-milled surface was ready, only the three available steps of diamond grain polishing compound with ethanol as lubricant were used; with grain sizes of 6 µm, 3 µm and 1 µm. Working from the largest grain size to the smallest, and using their respective polishing disks, a satisfactory result was achieved. Surface roughness measurements for the bottom block, pre and post polishing can be seen in Figure 5.6 and Figure 5.7, with a more zoomed out visual quality indication in Figure 5.8. The polishing step has not dramatically improved the average roughness, (going from $R_a = 1.115$ µm to = 0.895 µm), but has made height variations much smoother and taken out the obvious scratches that were left over from the milling process. The small steps that can be seen in the roughness profile from the paths that the mill took can also be seen to be largely smoothed out.

5.4. Stainless steel tubing

The type of tubing used in the design is easily available in sections of 1 m length from one of at least two webshops in the Netherlands: Modelbouw Shop Nederland[10] and Proton Modelbouw[11]. For both, the cost of the item was roughly €10, with similar shipping costs. The first option was used as the item cost was below the minimum order amount for the other.

The material was unfortunately not in stock and took two weeks to arrive at the shop. From that point, shipping only took a single day though. For future projects, it is recommended to be mindful of specialty product availability and perhaps call/send an e-mail in advance, as the indicated stock on websites does not always match with what is actually available.

During this two week lead time, several other ordering options were investigated, including Amazon, another model building hobby shop and Salomon's metalen. The first unfortunately only had shipping from China, with vague and long delivery times (though quite inexpensive). The second showed the product as in stock on their website, but upon asking quoted a 3 week delivery time as it was actually not available. The last quoted much higher prices than any of the other options, with €25 shipping, and around €75 material cost for two pieces of 60 mm in length (versus €10 for 1000 mm of material for the

[7] https://www.workshopheaven.com
[8] https://www.thomann.de/nl/index.html
[9] D.P.Mainali@tudelft.nl
[10] https://www.modelbouwshopnederland.nl
[11] https://www.proton-modelbouw.nl

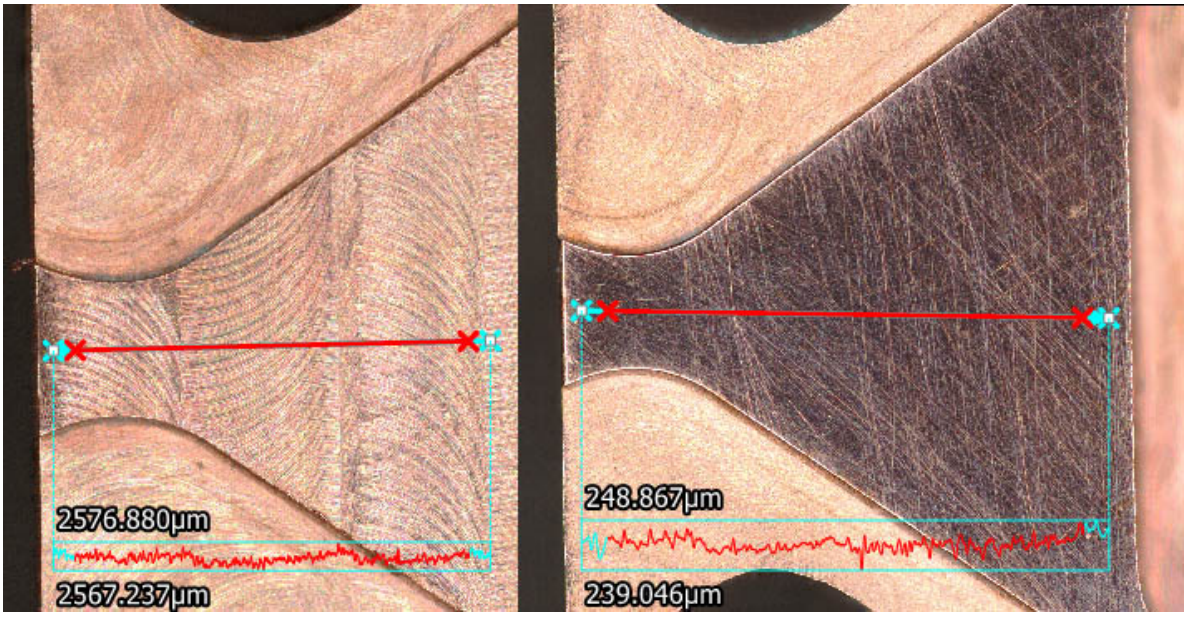

Figure 5.6: Optical images of the bottom copper block sealing surface nozzle section, before (left) and after (right) polishing.

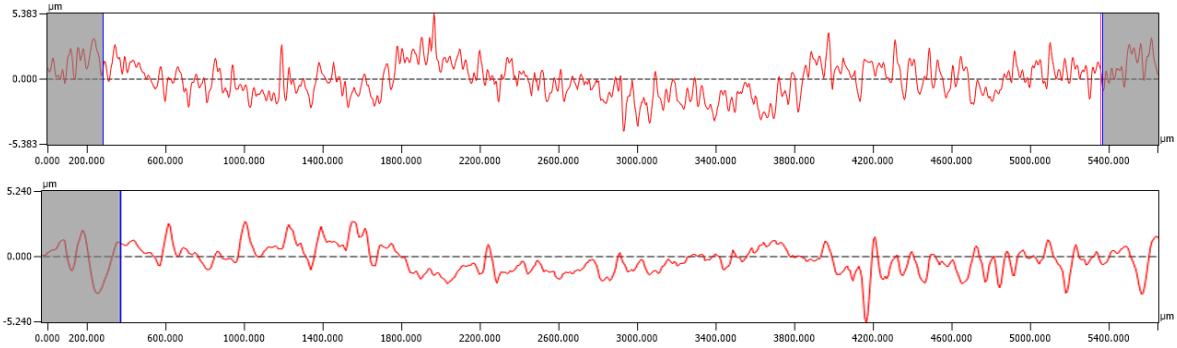

Figure 5.7: Surface roughness graphs for the paths indicated in Figure 5.6, for before (top) and after (bottom) copper polishing.

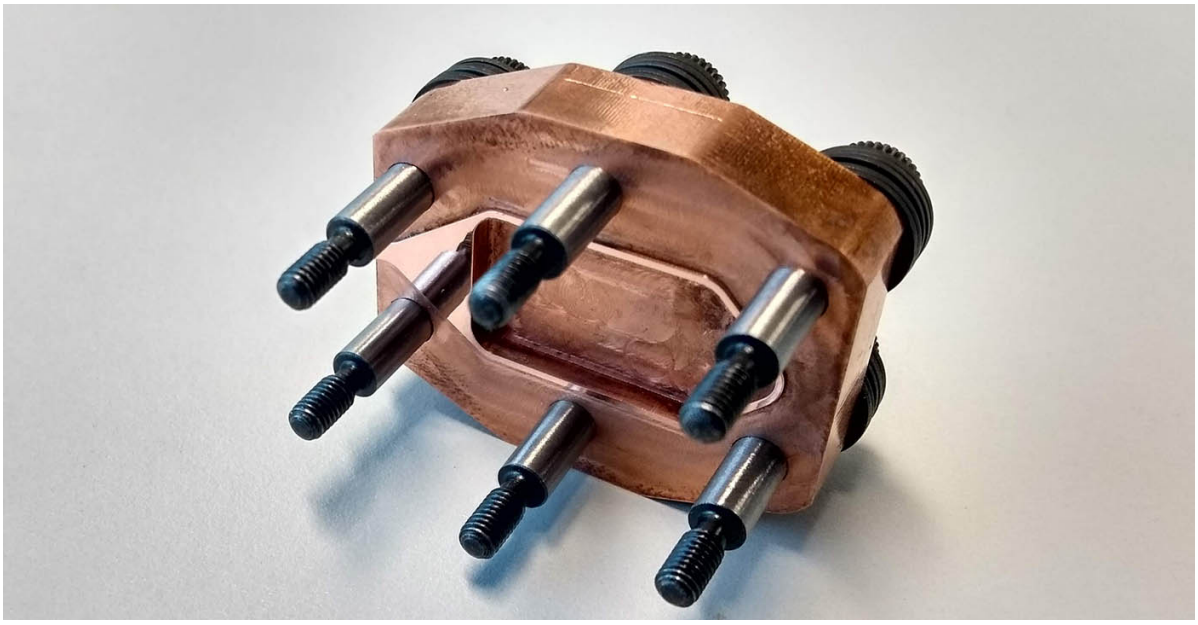

Figure 5.8: Polished bottom copper block with shoulder bolts inserted, showing the mirror finish of the sealing surface.

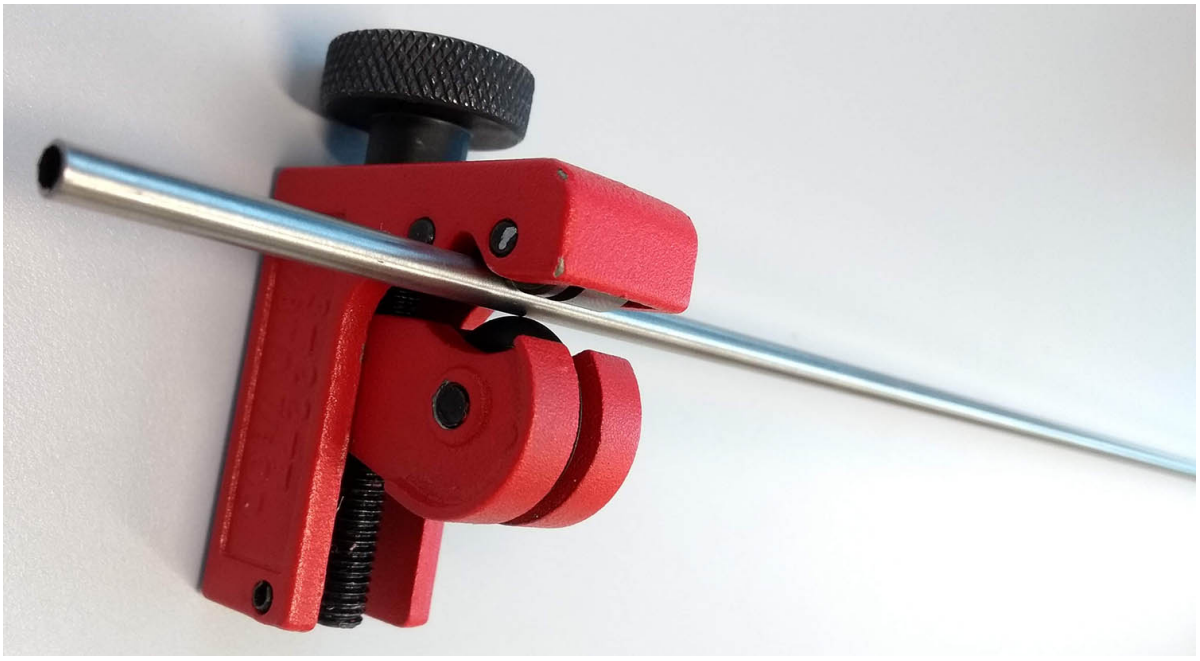

Figure 5.9: Stainless steel tube with tube cutter.

first option). Consequently, none of these were used, and other parts of production were tackled while waiting in the meantime.

After the material arrived, a small tube cutter was bought for €11.95 from a local hardware store to be able to cut the material to the desired length with a straight end, see Figure 5.9. This tool is now part of the SSE workshop inventory. Such a device could not be found with contacts or within the department before, and the use of the available metal hacksaw was seen as too risky without the use of a sawing guide for keeping the cut straight. After cutting the two pieces to the same length, a countersink drill bit from the SSE workshop was used to deburr the inner perimeter of the ends.

5.5. Metal foam heat exchanger

The material for the metal foam heat exchanger was already available from earlier thesis projects at the department [33, 59]. Unfortunately there were some issues with cutting the material into the right shape during these projects. The material has low strength due to its high porosity, which means that many standard cutting methods result in unwanted plastic deformation. To find ways to cut the material to size without adversely affecting its properties, the manufacturer (Recemat) was contacted, who gave the following options that they used themselves:

- *Cutting with a diamond coated saw blade*: fast & cheap, but smears out the pores on the cutting edge somewhat.
- *Cutting with a water jet*: fast, but abrasive particles may be left behind in the pores.
- *Cutting with a laser*: fast, but requires some specialized settings to avoid burning the pores at the cutting edge.

Of these, the laser cutting would be preferred as this does not smear out the pore material and will not leave residue in the pores. Recemat offered to cut the desired component as part of a batch job they were doing for a different customer on their laser cutter, for a minimum order cost of €50. This price could also include several more pieces of similar size, as they are quite small. The tolerance they can deliver with this is about 0.3 mm, which is quite large compared to the rest of the system, but not unusable if the component is made slightly smaller and potential gaps are filled up with metal foil. Several versions could also be made covering the required size and tolerance range, so that the best fitting among them can be used.

At TU Delft, there is also a laser-cutter available at the Mechanical, Maritime and Materials engineering faculty (3ME) which can be used free of charge for student (thesis) projects. This was a new

Setting (Dutch)	(English)	Value
Tijd laser	Time laser	0.5
Vermogen	Power	15 %
Snelheid	Speed	10.0
Puls freq.	Pulse frequency	400
Puls breedte	Pulse width	0.25

Table 5.2: Settings for cutting Ni-4753 Recemat nickel foam at the 3ME faculty laser cutting facilities

material for them to cut, but after a test cut in a slightly warped piece of the available material, appropriate settings were found (see Table 5.2 for future reference) These resulted in no noticeable burned spots and open cells on the cut edge. These settings were then used to cut a final piece out of intact material, which only took a few minutes, including set-up. The resulting component can be seen in Figure 5.10.

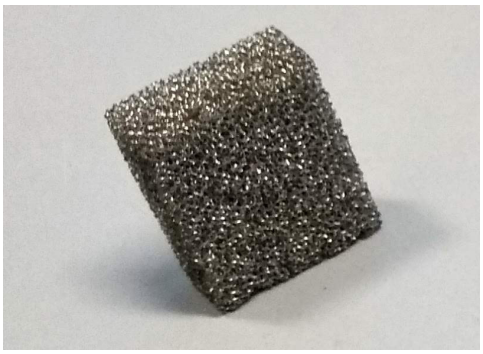

Figure 5.10: The laser-cut piece of nickel foam.

The dimensions were found to be smaller than the design by only 0.1 to 0.15 mm, which could also be compensated for in the future, as these are mainly a result of the beam width and fairly consistent throughout. For now, the rest of the material will be saved for later, and the small gaps will be left alone. These are several times smaller than the average pore size of the material (0.5 mm), and should thus not results in a noticeable amount of flow bypassing the heat exchanger foam. The gaps would also be at the side of the foam, where propellant would be exposed to the hot copper side walls so that any flow that does pass through there would still be heated.

For future projects, one of the laser cutter operators at 3ME also suggested the use of water jet cutting *without* abrasive at DEMO. Through a conversation with the contact person there (Leon Roessen), it was determined that this could also be an option, for the cost of around €40, which is mainly set-up costs, as water jet cutting is quite fast. Another option given by DEMO would be the use of wire-EDM cutting, which they have used in the past to cut porous pieces of metal such as sintered packed beds. This would be slightly more expensive (a similar cost as the nozzle) but would allow for somewhat tighter tolerances, with most of the cost again being for the work set-up.

5.6. Foam tube inserts

As discussed in the design chapter, the stainless steel tube leading up to the propellant pressure sensor is to be filled with pieces of the same metal foam as used in the heat exchanger. A very similar fabrication method as for the rectangular metal foam block from the previous section is employed.

The circular pieces needed to fill the tube were unfortunately too small to be cut individually on the 3ME laser cutter. This is operated with a shielding gas that would have blown these pieces away at high speed after cutting, making it nigh impossible to find and retrieve them. To solve this, the needed pieces (12 + 2 spare) were made into a connected pattern with small material bridges in between so that it would remain as one piece during cutting. The diameter of the pieces was made slightly larger than the specified inner diameter of the tube to account for the laser beam width (3.6 mm instead of 3.4 mm).

After cutting, the pieces were removed individually by manual bending and breaking; the connections were quite fragile for rotation around the normal of the foam top plane. Some burrs from the connections then remained, which were partially flattened out by manually rolling each piece over a flat surface with a minor amount of force until each piece could be inserted snugly into the tube. The cutting pattern used and the resulting metal foam pieces can be seen in Figure 5.11.

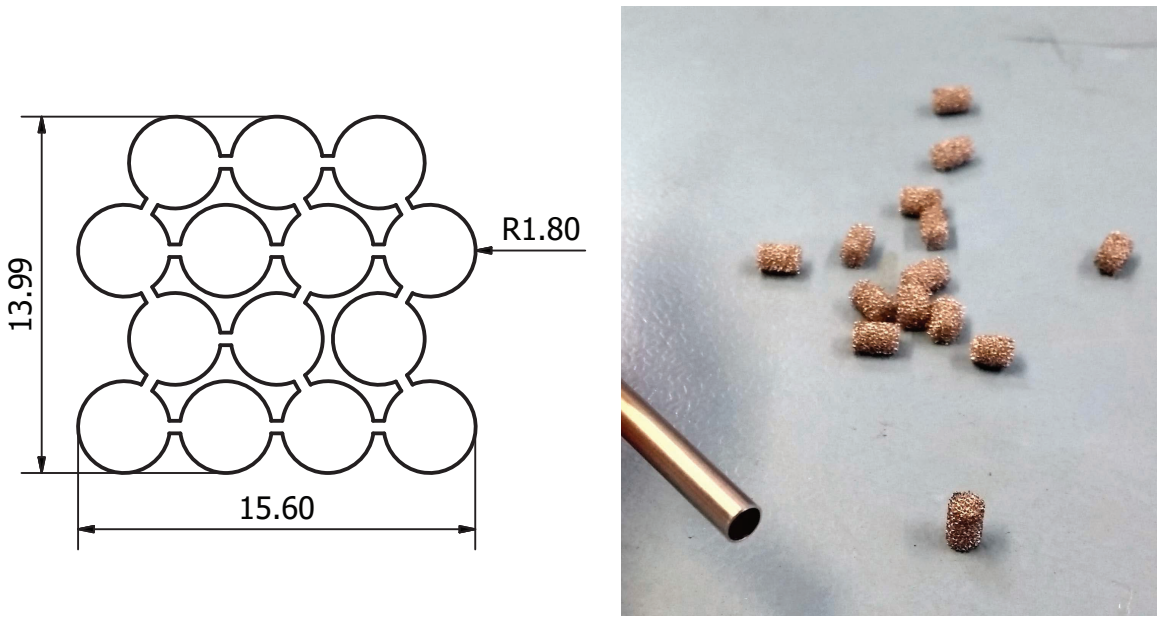

Figure 5.11: The cutting pattern used for the foam inserts (left) and the resulting components next to the steel tube they are to be inserted into (right).

5.7. Pressure sensor

For measuring the thrust chamber pressure, a TE Connectivity MS5837-30BA pressure/temperature sensor is used, for which the necessary electrical interface and LabVIEW software for using it were already available from previous thesis projects. These were ordered through Vidhya Pallichadath[12] the coordinator for micro-propulsion projects at the department. Three of them were acquired from Farnell[13] for €19 a piece, one for current use and two as backup or for future projects. After ordering, they arrived within one or two days.

The sensors are surface mounted devices and have quite small electrical contacts, making soldering wires to them a difficult process. Fortunately, Şevket Uludağ[14], the department clean room and workshop manager who had also soldered these sensors in the past, was able to perform the precision soldering task without issue with two sensors (one as backup). The wires were roughly 80 cm in length so no extension cable would be needed, and the same colour coding was used as with previous projects for consistency and compatibility with the existing electrical interface, see Table 5.3.

The pressure sensor has an an-board 24-bit analog to digital converter and can be communicated with over an I²C bus, which can be read out with the available NI USB-8451 DAQ, which is specifically made for interfacing with I²C and SPI devices. This electrical bus requires two pull up resistors from the data and clock lines in order to function, with this sensor in particular also requiring a 100 nF capacitor for power supply smoothing, see the schematic in Figure 5.12. For previous projects, this was achieved through a somewhat cluttered breadboard, which connected the four leads coming from the pressure sensor to the the USB-8451 for data and a USB-6008 DAQ for a 2.5 V power line. This was quite cumbersome to work with. Thus, in an effort to streamline testing, a smaller adapter was made while waiting for other components. This time the interface circuit was fully soldered without a breadboard, and used the same colour coding as the sensor wire. The old and new electrical interface can also be seen in Figure 5.12.

Only one sensor can be connected to this new interface, but it is now colour coded, much smaller, less fragile, and thus easier to pick up and handle. The new cable was tested and found to be working with three different instances of the MS5837-30BA pressure sensor (two from this project, one from an earlier one). One attempt was made to make the system work with just the USB-8451 by using one of its digital out pins set to 3.3V as the power supply. This unfortunately resulted in the signal periodically

[12] V.Pallichadath@tudelft.nl
[13] nl.farnell.com (product code: 2771904)
[14] M.S.Uludag@tudelft.nl

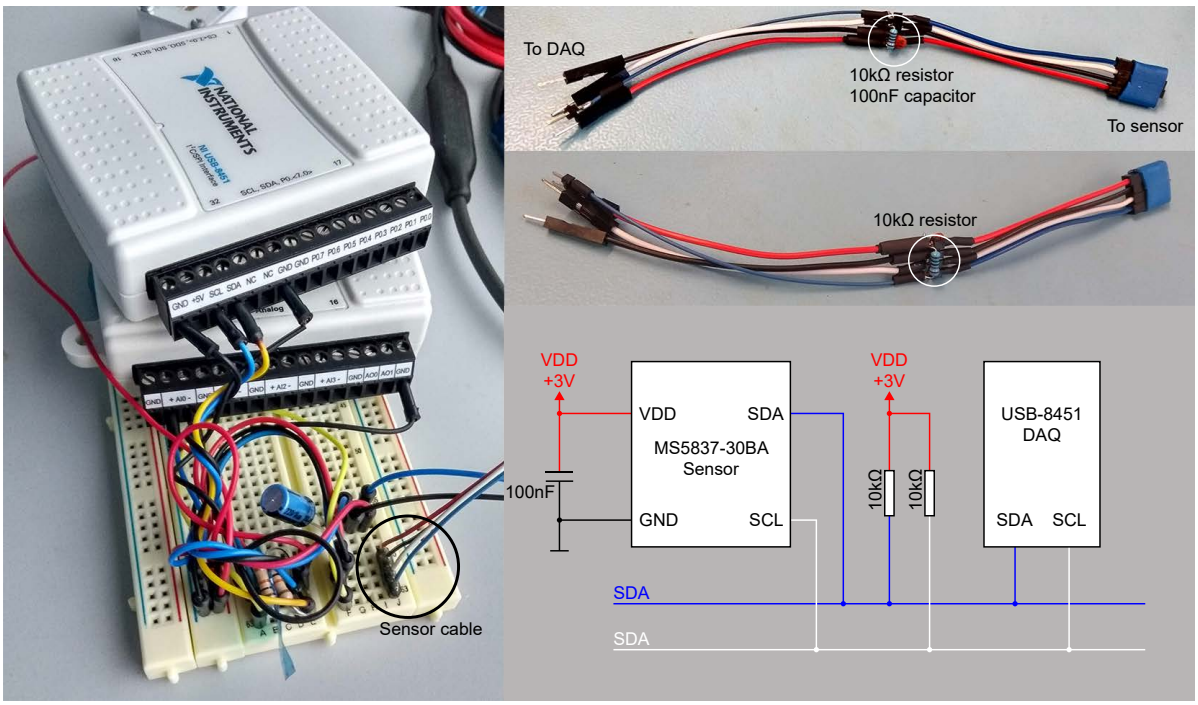

Figure 5.12: The old I²C bus connection (left) between the sensor and the USB-8451 DAQ, the new connection (top right), and a colour coded schematic of the electrical components and wires involved (bottom right)

Wire colour	Line	Description
Red	VCC	positive voltage supply
Black	GND	ground
White	SCL	I²C clock
Blue	SDA	I²C data

Table 5.3: Wiring of I²C pressure-temperature sensor

dropping out / returning large negative values, so the setup was switched back to using the 6008 DAQ as a power supply, which did not have this issue. During a subsequent test, one of the soldered leads also came loose again, which fortunately could quickly be re-soldered. A drop of the glue intended for bonding the Teflon feed system tube was used to prevent this issue from occurring in the future.

5.8. Other components

Some components were already available or only had to be ordered and required no further fabrication steps, these are discussed in this section.

5.8.1. Shoulder bolts

For clamping the nozzle sections together, shoulder bolts (ISO 7379 M3-04x20) are used. These have a standard hex slot head and threaded section, but come with a straight, smooth section in between with tight tolerances for a slip-fit. These are precision machine components and thus somewhat more expensive than regular mass production bolts. The webshop that was found to offer these for the lowest cost without a high minimum order amount was Norelem[15] (component number 07534-04X20). For a total of €25.29, 9 of these bolts (minimum order amount) were acquired with €7.50 shipping (all excluding VAT). The components were in stock and arrived within a few days of ordering.

[15] https://www.norelem.com/nl/en/Home.html

Figure 5.13: Several of the shoulder bolts and disk springs.

5.8.2. Disk springs

For mitigating thermal stresses on the bolted thruster body, Belleville type disk spring washers were needed. The correct size (S4214 DIN2093) was available for €0.08 each at Amatec[16]. With the number of springs needed (36), the minimum order amount for this shop of €17.50 was not reached, so first the rest of their stock of these springs was added for a total of 56, after which a few extra springs were added to increase the total over the minimum order value. Amatec also charges an additional flat fee of €8.95 for shipping and handling. All springs were in stock and arrived the next day. Several of the springs and shoulder bolts can be seen in Figure 5.13.

5.8.3. Metal glue

For connecting the stainless steel tubes to the top interface a type of metal glue was needed. To this end, the same glue was employed as previous MSc student Melaika [46] had used for this application: Bison Kombi Metaal. This was acquired from a local Hornbach hardware store for €8.19. It was later discovered that unknown to department staff there was still glue left from this previous project, located on a table in the clean room, which could have also been used.

5.8.4. Teflon glue

For connecting to the N_2 feed system, a piece of Teflon MINSTAC tubing has to be attached to the top aluminium interface. To this end, a special combination of primer and glue was used as mentioned in section 4.6. This was acquired from 123lijm.nl[17] for €23.50 with an additional €2.95 in shipping. The primer is first applied to the PTFE, which alters the chemical properties of its surface so that the glue can bond to it. Both substances were recommended to be kept refrigerated for the longest shelf-life.

5.8.5. MINSTAC tubing

The piece of MINSTAC tubing for connecting to the N_2 feed system was a short piece of left-over tube from the project by Melaika [46], which had already been cut in half. This was used based on advice from Vidhya Pallichadath, to avoid having to order new components.

5.8.6. Remaining small components

Lastly, nuts bolts and washers for other parts of the design were already available in the department clean room workshop and thus did not have to be ordered.

5.9. Assembly

For assembling the system, several components had to first be glued together, after which the two thruster body pieces had to be bolted together with the nozzle profile in between. First the stainless steel

[16] https://www.amatec.nl/
[17] https://www.123lijm.com/industrielijm-dun-28-gram-plus-ml-pe-pp-primer

Figure 5.14: 3D printed brackets (red) as used to align the metal tubes to the top interface (left) and thruster body (right) during glueing. The metal foam pieces that were inserted into the pressure sensing tube are also shown (middle).

tubes were glued to the top bracket with the metal glue, for which the pieces to be joined were first lightly sanded to provide a better bonding surface. To make sure that the tubes were aligned correctly with the interface, a two-piece mould was designed and 3D-printed on the department Makerbot Replicator, to hold the tubes in place while the glue was drying. The same was also done for gluing the tubes to the top copper block, see Figure 5.14 for images of both of the moulds in use.

The metal o-ring groove of the pressure sensor was subsequently glued into its corresponding hole on the top interface with the same metal glue. After this, the piece of MINSTAC tubing was glued into its respective hole using the Teflon primer and glue. After having waited 24 hours each time for all the glue to have dried sufficiently, the glueing assembly steps were finished.

The following assembly of the thruster body is then a purely mechanical affair, with the six shoulder bolts, washers and nuts, to compress the two copper blocks with the nozzle profile section in between. The 36 disk springs were also used to see how they would react under the force required to create an adequate seal. Here, the nozzle profile N0.5-01 was used, the first 0.50 mm thick version.

As alluded to before, it was unfortunately realised that the hand reaming of the tight tolerance bolt holes had resulted in them no longer being perpendicular to the sealing surface. With the slip fit of the shoulder bolt shank and the holes, still trying to use the shoulder bolts would have resulted in stressing the copper blocks in ways they were not designed for, as well as having the bolts grind against the side of the holes. It was further noticed that the holes cut into the nozzle profile were in some cases slightly too small for the shoulder bolt or slightly misaligned with the (hand-reamed) holes in the blocks. The shoulder bolts could thus not be used.

As a quick and simple solution, standard stainless steel torx-head M4 bolts were used to replace them, which were available in the correct size from the department workshop stock. These have a bit more “wiggle-room” than shoulder bolts and could thus fit in the slightly skewed/undersized holes without issue. This does come at the cost of not being able to align the three body parts mechanically with them any more.

To not fully rely on imprecise manual layer alignment, two of the shoulder bolts were still used. These were inserted in the back-most two holes of the bottom block (furthest from the nozzle exit), where the holes in the nozzle profile were actually large enough to fit these. The nozzle profile and top block were laid on top, with the bolt shanks only being inserted a few mm into the top block to avoid stresses from non-parallel holes, but still allow for layer alignment. Following this, the standard M4 bolts were inserted (with springs and washers) into the remaining four holes and lightly tightened until the layers could no longer move. The two shoulder bolts were then replaced by standard M4 bolts before all six were tightened further to an initial value of 0.50 N m with a torque wrench. This value was estimated based on the bolt force needed to achieve the design value of roughly 30 MPa of clamping pressure over the sealing surface This was then translated to a bolt torque value using an online tool

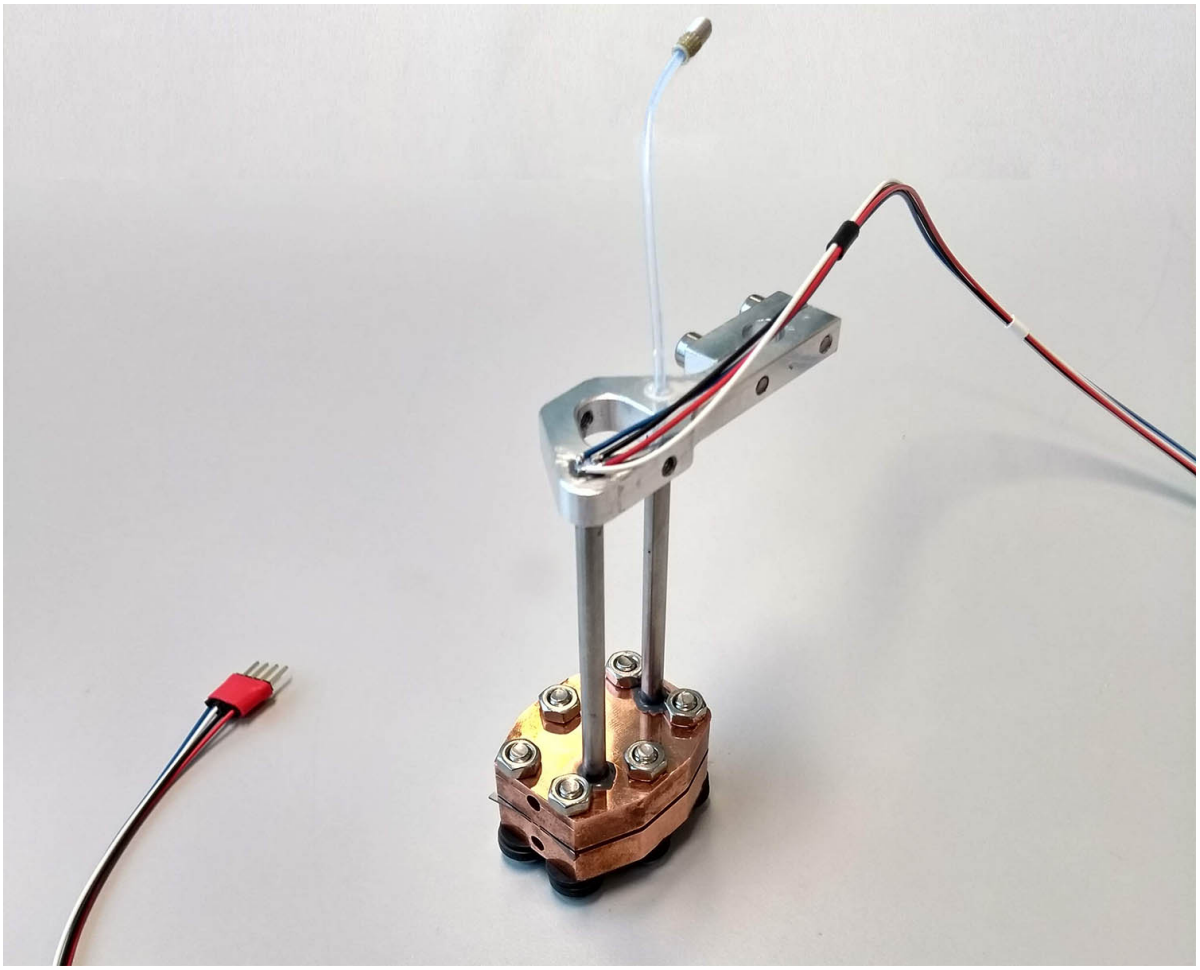

Figure 5.15: Finished cold gas micro-thruster.

used in a mechanical engineering bachelor course attended by the author[18]. Further tightening of the bolts was done in parallel with leak tests, see section 5.11

This concludes the manufacturing of the cold gas system, with the completed device being shown in Figure 5.15.

5.10. Nozzle geometry characterization

Optical microscopy was used to characterise the dimensions of the created nozzle (N0.5-01) and compare them to their design values. These dimensions were also needed for thrust testing to calculate the ideal thrust outputs, measured efficiencies and model predictions. These are the same values as shown in Table 4.1 on page 30, namely h_t, w_t, A_t, $r_{t,c}$, ϵ, w_e, θ, and ψ.

For testing the functionality of this *particular* thruster, the exact dimensions of the nozzle are not very important, as long as they are *known* so they can be corrected for. The general contour shape is more important as this should still be similar to that of Bayt, so that the two can be compared. Preliminary inspection of the nozzles earlier in section 5.2 already showed that general nozzle shape was as designed. This section is thus primarily aimed not at accepting or rejecting these specific parts, but at measuring the created nozzle geometry for thrust testing and determining the accuracy of wire-EDM as a fabrication method.

Unlike the silicon MEMS thruster, which used a plane of glass on one side of the thruster, both sides of the nozzle are now covered in opaque material. This means that some measurements can only be made when the nozzle profile is disassembled, in particular $r_{t,c}$ and θ. As an extra difficulty, the sides of the nozzle profile can move slightly towards or away from each other due to the horseshoe shape

[18] https://www.werktuigbouw.nl/sub9.htm sub-category “aanhaalmoment”

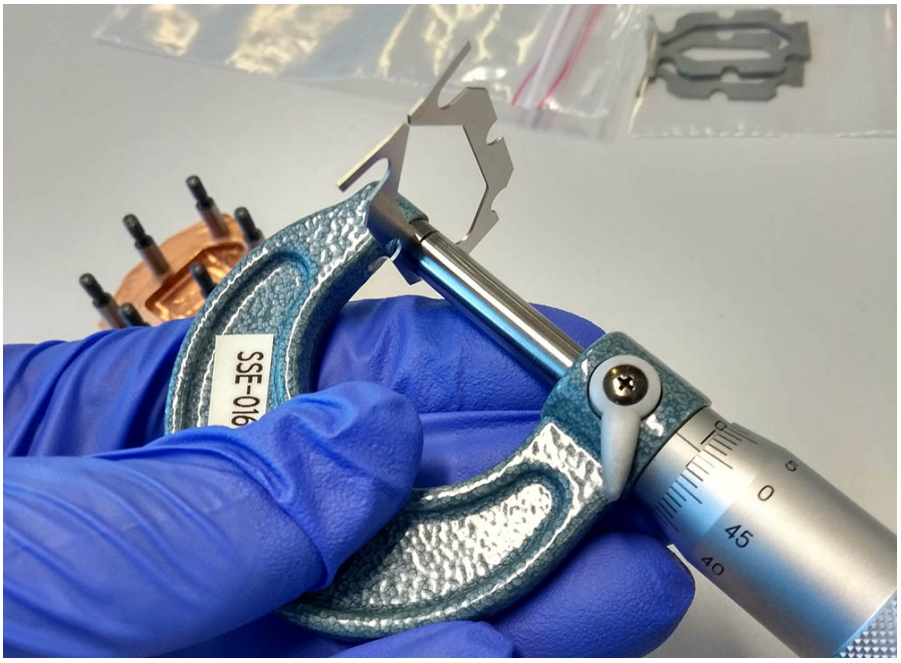

Figure 5.16: Nozzle profile thickness (channel height) measurement using a micrometer.

of the nozzle profile. This could be used later for adjusting w_t manually, but for now means that w_t can only directly be measured when the nozzle is installed and fixed in place.

This brings up the last difficulty, in that the nozzle throat could not be seen clearly through a microscope once assembled, due to not enough light reaching into the very small nozzle hole. The device was also too large to be imaged with the scanning electron microscope at DASML, which would have been able to image the assembled throat. This last issue was only discovered after assembly, so that some of the measurements made here were actually performed *after* cold gas thrust testing, when the thruster had been partially disassembled again.

To still have a measurement of the throat dimensions, the throat height of the disassembled nozzle was first measured with a standard micrometer from the SSE clean room, see Figure 5.16. With this a value and estimated uncertainty of (496 ± 4) µm was found.

Measurement of the throat width was somewhat more involved. For this, the assumption was made that if the sides of the nozzle profile moved inward or outward, they would do so without rotation, i.e. the angle between the side walls would not change. With this assumption, the throat width of the assembled thruster $w_{t,as}$ could then be calculated from the measured throat and exit widths of the disassembled thruster $w_{t,da}$ and $w_{e,da}$, together with the measured nozzle exit width of the assembled thruster $w_{e,as}$:

$$w_{t,as} = w_{t,da} + \left(w_{e,as} - w_{e,da}\right) \tag{5.1}$$

Two microscopes at DASML were used for these and following measurements, a Keyence VHX-2000 high magnification optical microscope and a Keyence VR-5000 wide-field optical 3D microscope, see Figure 5.17. The first was used because it was the only high magnification microscope where the thruster would fit between the translation stage and the lens. The second was used for its 3D and surface roughness measurement capabilities. For measurements with the VR-5000, a plastic bracket was 3D printed to keep the thruster upright and facing the lens, as the geometry of the system normally does not allow for this. All length measurements with these microscopes were performed in their accompanying software with available measuring tools.

Measurements of the disassembled throat and exit width for all four nozzles were first performed with the higher magnification VHX-2000. Unfortunately it was realized afterwards that the two sides of the nozzle were at slightly different heights due to slight warping from manufacturing. This made it impossible to focus on both sides simultaneously and also meant that the distance measurements were unreliable due to the side walls being slightly askew.

The measurements of the convergent / divergent angle and throat radius of curvature were not

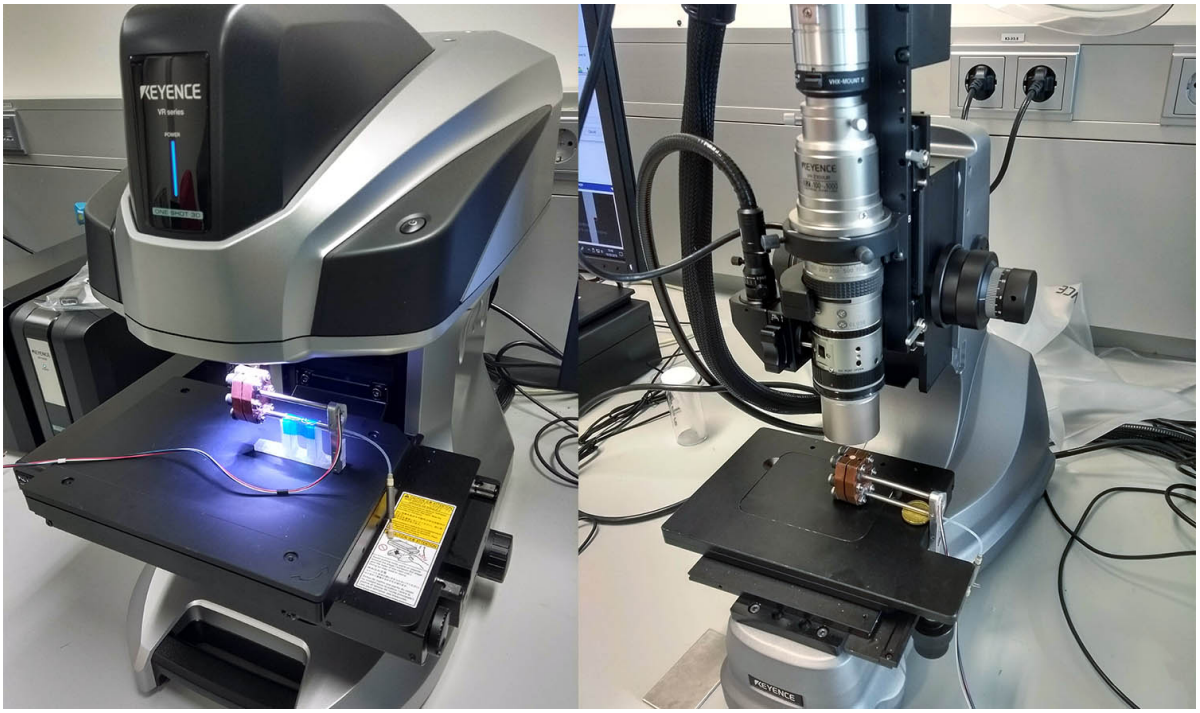

Figure 5.17: The Keyence VR-5000 (left) and VHX-2000 (right) microscopes used for geometry characterization.

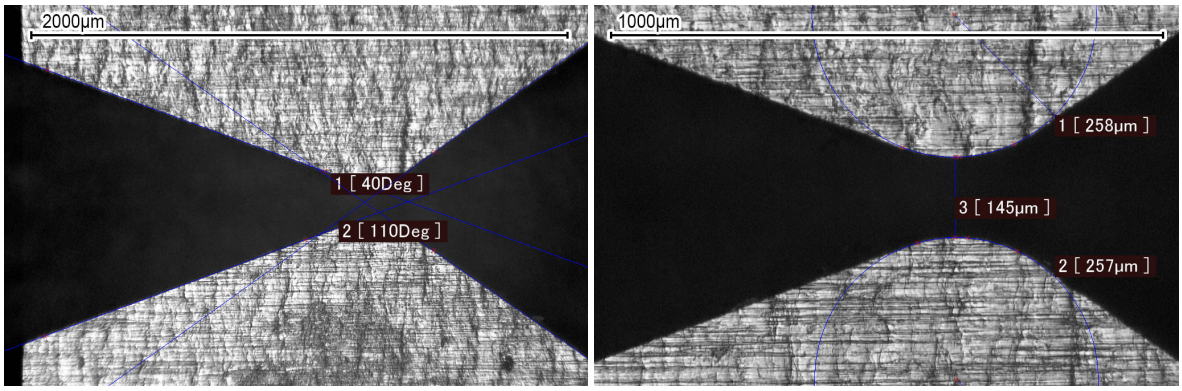

Figure 5.18: Nozzle N0.5-01 convergent and divergent angle, and throat curvature radius measurements with the VHX-2000.

affected by this and could thus be used from these measurements, see Figure 5.18. The values found for these were $2\psi = (70.0 \pm 0.5)°$, $2\theta = (110.0 \pm 0.5)°$, and $r_{\mathrm{t,c}} = (258 \pm 20)$ µm. The uncertainty in this last value is quite high due to the sensitivity of manually fitting a circle over the short arc-shaped edge of the nozzle throat.

To remedy the nozzle skewing issue, the nozzle profile was subsequently clamped down onto a flat surface with another 3D printed bracket and angled upwards towards the lens, see Figure 5.19. The angle setup was added to more easily determine the edge of the nozzle throat and exit. This was difficult when viewed from the top due to the rounding of the throat obscuring where the minimum distance was.

These measurements were performed just before hot-testing was to commence and were thus under some time pressure. Unfortunately, at this point the lens on the VHX-2000 had been swapped to a higher magnification version which did not allow for viewing the exit width in one image. The lower magnification VR-5000 was thus used instead in the interest of time. The resulting images with measurements can be seen in Figure 5.20. The values found here were $w_{\mathrm{t,da}} = (145.6 \pm 5.6)$ µm and $w_{\mathrm{e,da}} = (1072.5 \pm 5.6)$ µm. The single sided uncertainties for these are estimated as equalling the length equivalent to 3 pixels in the image.

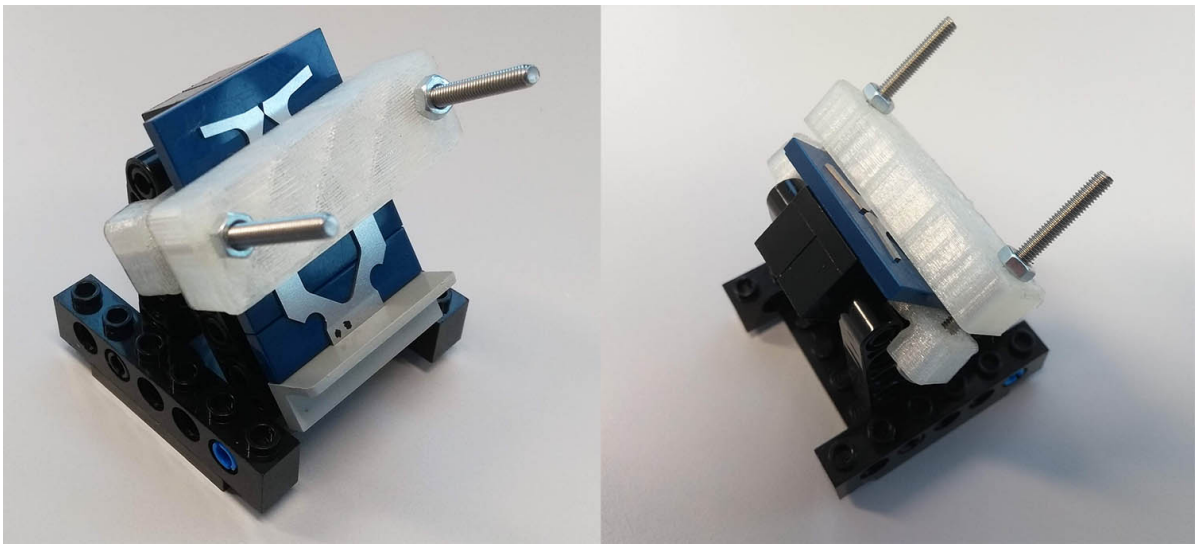

Figure 5.19: Setup bracket for looking at nozzle throat at an angle of 36.9° from the microscope axis. The bracket has a 3-4-5 Pythagorean triangle side-profile and incorporates a 3D-printed clamp for flattening the two nozzle sides.

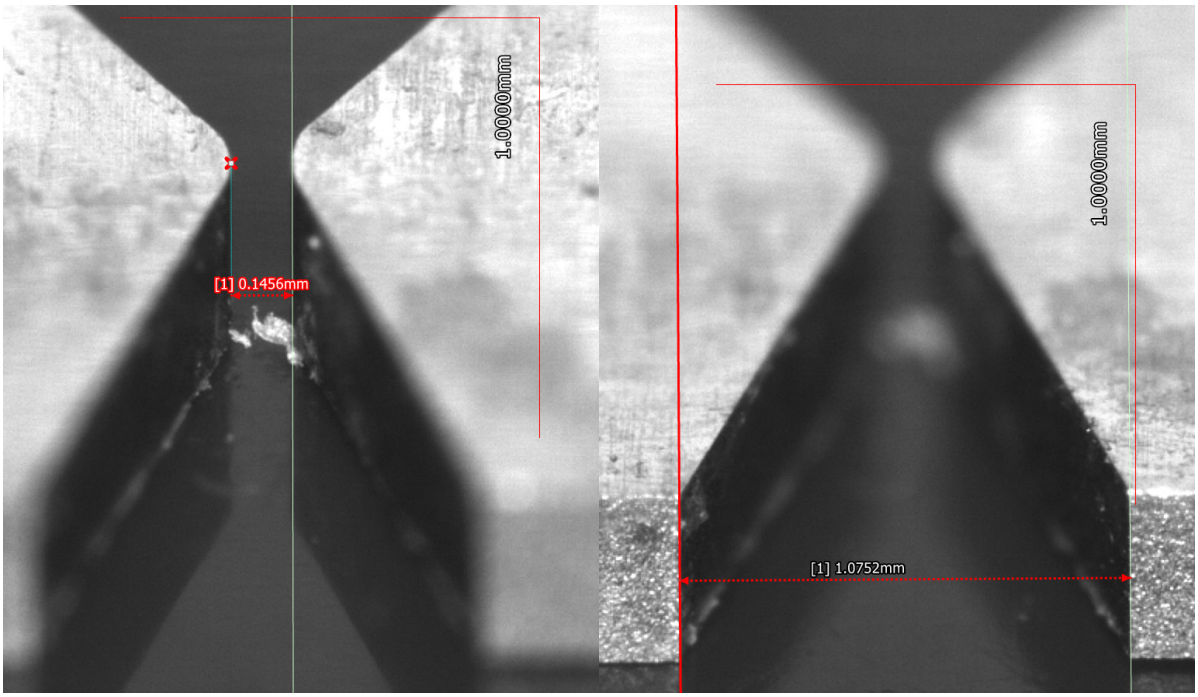

Figure 5.20: Nozzle throat and exit width measurements of N0.5-01, used for hot and cold testing. Made using the VR-5000 microscope. The small slivers of material visible at the throat are plastic scrapings from moving the nozzle around on the angle bracket (Figure 5.19) and did not end up in the assembled thruster.

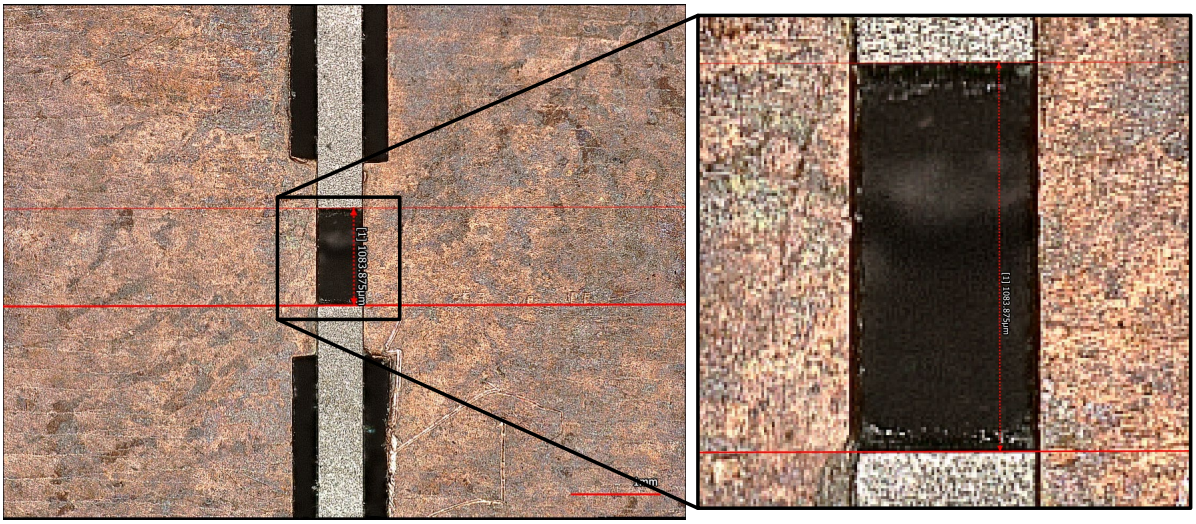

Figure 5.21: Assembled nozzle exit width measurement with the VR-5000.

Lastly for the assembled exit width, unfortunately only a single lower magnification image from the VR-5000 is available for use, see Figure 5.21. Some higher magnification images were made on the VHX-2000, but some later measurements showed inconsistent pixel scales on different days from this microscope, so data from this was not seen as reliable enough. This was not seen as an issue for the earlier throat curvature measurement as the uncertainty there was already quite high. Also its value is only used in the discharge coefficient calculations, with low sensitivity. The lower magnification resulted in somewhat higher uncertainty, with the value found being $w_{\mathrm{e_{as}}} = (1083.9 \pm 14.8)\,\mu\mathrm{m}$. The equivalent length of only two pixels was used here for the single sided confidence bound, due to each pixel covering a wider area.

With this exit width measurement, a 3D image was also produced from which the alignment of the three thruster body layers at the nozzle can be deduced. This can be seen in Figure 5.22, which shows quite excellent alignment, especially for the manual assembly procedure used. Both copper blocks and the front of the nozzle are essentially parallel and at the same height.

All the required dimensions have now been measured. The last value that must then be computed is the nozzle expansion area ratio ϵ, which is simply equal to $w_{\mathrm{e,as}}/w_{\mathrm{t,as}}$. Uncertainties for calculated values are worked out with the method described later in subsection 6.2.2. A comparison of all the measured values with their design equivalent is then shown in Table 5.4. Throat area and throat and exit aspect ratios are also included for completeness.

The difference between dimensions of the design and the actual system is only in the order of 1 % in most cases, with the main outliers being all the values that greatly depend on w_{t}, which is (19 ± 13) % larger than designed. The disassembled measurements for this value were slightly closer to the design at 145.6 µm, but still too large by (12.0 ± 4.3) %. This increase in throat width can likely be attributed to two passes from wire-EDM being needed for its fabrication, increasing the minimum slit width compared to the single pass estimate given beforehand. A slightly larger minimum throat size for wire-EDM fabrication of $\sim 150\,\mu\mathrm{m}$ should then be used for future designs to take this into account.

Design and measured values for geometry of the most recent silicon VLM thrusters at the department [41], were shown earlier in Table 4.1 on page 30. Comparing the accuracies of the two fabrication methods, wire-EDM performs considerably better, as the throat width is only (19 ± 13) % larger, instead of 61 % smaller than designed for the silicon etching method. After taking into account the larger minimum throat width for wire-EDM for future designs, this fabrication accuracy may be improved further. Angles and larger shapes are on par for both methods in terms of fabrication accuracy. Silicon etching can theoretically reach better accuracies, as showcased by Bayt [4] for example. This does however require additional investment in testing of etching recipes which, like the fabrication itself, is not a cheap process.

Wire-EDM does have an additional advantage in that a nozzle fabrication error can be rectified with just 2 to 3 hours of machining, costing only around €160. A fabrication error with silicon etching on the other hand can results in *all* of the thrusters on a wafer having the same defect or being completely

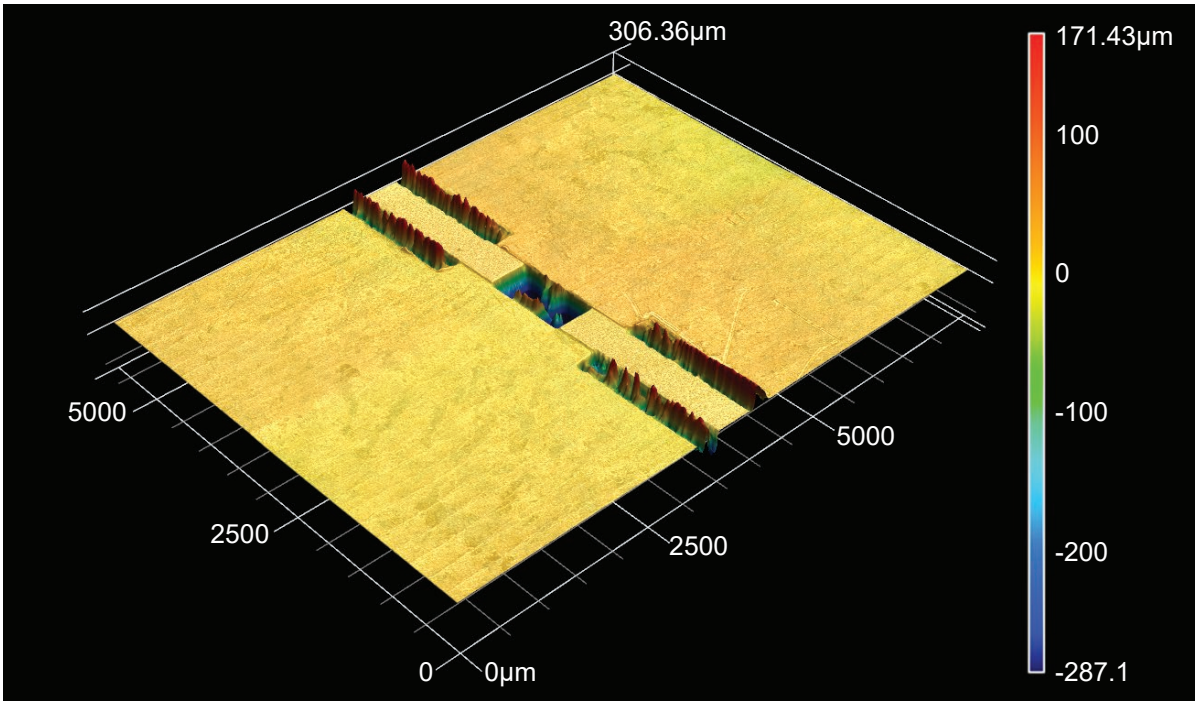

Figure 5.22: 3D surface measurement of the nozzle exit area with the VR-5000.

Parameter	Unit	Symbol	Design value	Measurement	Difference [%]
Throat height	µm	h_t	500	496 ± 4	-0.80 ± 0.80
Throat width	µm	w_t	130	154 ± 17	$+19 \pm 13$
Throat aspect ratio	–	h_t/w_t	3.85	3.21 ± 0.35	-16.4 ± 9.1
Throat area	10^4 µm^2	A_t	6.50	7.65 ± 0.84	$+18 \pm 13$
Throat radius of curvature	µm	$r_{t,c}$	260	258 ± 20	-0.8 ± 7.7
Expansion area ratio	–	ϵ	8.25	7.03 ± 0.68	-14.8 ± 8.2
Nozzle exit width	µm	w_e	1072.5	1084 ± 15	$+1.1 \pm 1.4$
Nozzle exit aspect ratio	–	h_t/w_e	0.466	0.4576 ± 0.0073	-1.8 ± 1.6
Divergent half angle	°	θ	20	20.0 ± 0.4	$+0.0 \pm 2.0$
Convergent half angle	°	ψ	35	35.0 ± 0.4	$+0.0 \pm 1.1$

Table 5.4: Design and measured values for parameters defining the shape and size of the nozzle (cold gas thruster).

unusable, as seen recently with Ganani [19]. If replacements are to be made, an additional week of clean room work and roughly €$6 \cdot 10^3$ are then required.

5.11. Leak testing

To verify the functionality of the different seals in the system and check whether thrust tests can be executed next, leak testing is performed. For acceptance criteria, leakage mass flow below 0.1 % of expected nozzle flow is considered excellent as this is an order of magnitude below the accuracy of the thrust and mass flow sensors. It is also low enough to not have a noticeable effect on thrust performance if the design were to be used on an actual spacecraft. Leakage flow of around 1 % is considered acceptable for this project, as this is similar in magnitude to the mass flow and thrust sensor accuracy. This will however require taking leakage into account when interpreting thrust test results, and require some further work to reduce leakage in a future project. Higher relative leakage is considered unacceptable and will require additional design and fabrication to alleviate the issue.

Based on a reasonably comprehensive list on leak-testing of devices, assembled by previous TU Delft MSc student Melaika [46], one way to locate and another way to characterize the extent of possible leaks was used. Two steps of testing were performed: exploratory (just after initial assembly of the

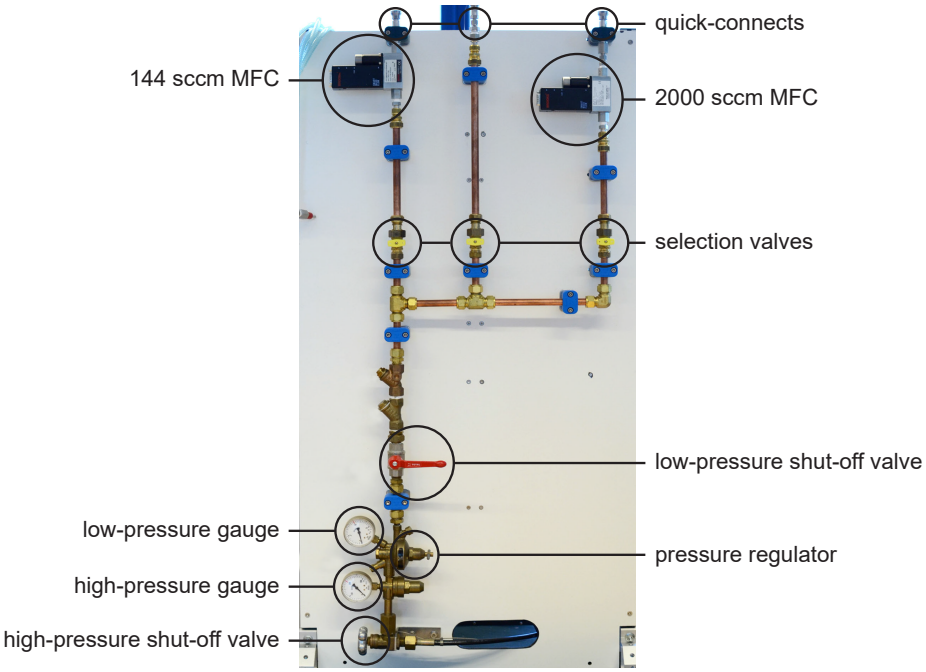

Figure 5.23: Nitrogen gas feed system with components indicated.

device) and enhanced (with a better way to seal the nozzle).

For locating a leak, an available can of leak-finder fluid was used (Electrolube DDF, a soapy liquid). This can be sprayed on potential leak locations and results in the formation of bubbles wherever gas is forced through it, only requiring visual inspection for locating the origin of a leak. For quantitatively determining how much gas is being lost through all leaks combined, the dynamic behaviour of pressure inside a closed fixed size pressurized volume is used, in this case the thruster chamber. This method is described for this specific instance in the subsection below.

5.11.1. Pressure dynamics leak testing

For this test the thruster is connected to the N_2 feed system, as seen in Figure 5.23, and the nozzle is plugged. The thruster chamber is subsequently pressurized by first opening the control solenoid valve and closing it again once the pressure has stabilized. After closing of the valve, the pressure inside the thruster chamber is recorded using LabVIEW. For a more detailed test procedure, see Appendix C.1.1 through C.1.4.

The rate of change of the chamber pressure $\dot{p}_c$ [Pa s^{-1}] can then be related to the total mass flow escaping through all leaks $\dot{m}_{leak}$ [kg s^{-1}] by equation (5.2). This is derived from the ideal gas law, and further assumes constant gas temperature T_c, internal volume V_c [m^3] and composition.

$$\dot{m}_{leak} = \dot{p}_c \frac{V_c M}{R T_c} \tag{5.2}$$

The last two assumptions should be valid as the thruster is made of relatively stiff, fixed components and operated at a low pressure so that changes in its internal volume should be negligible. Also, no gas producing or absorbing chemical reactions are known to take place in the chamber filled with (unreactive) nitrogen gas, keeping the composition constant. The validity of the constant temperature assumption depends if the leak is small enough for isothermal expansion to take place and if the surroundings stay at a constant temperature, which is measured during testing.

For the actual calculation, the time derivative of the pressure, $\dot{p}_c$ is calculated numerically using a first order finite difference approximation. The results from this were quite noisy, requiring the use of a digital low pass filter, in this case a 100 sample moving average type—applied forward and backward for no signal phase delay—using the `signal.filtfilt()` function from the Python `scipy` package.

An estimate of V_c was made based on the CAD model, which resulted in internal volume values for different components as seen in Table 5.5. The volume inside the top aluminium interface bracket

Part	Volume [cm^3]	notes
Bottom copper block	0.596	
Nozzle profile layer	0.140	
Top copper block	0.614	includes holes up to tubes
N_2 inlet tube	0.545	
Pressure sensor tube	0.518	filled with 95 % porous foam
MINSTAC tube to solenoid valve	0.048	~ 6 cm long, max. 0.04 inch inner diameter
Total	2.461	

Table 5.5: Internal pressurized volume of thruster components based on CAD model.

was not taken into account as most of this is already occupied by the pressure sensor, MINSTAC 062 fitting and tube to the valve and the internal volumes of the stainless steel tubes. The inner diameter of the MINSTAC tube was unknown, so the worst case value was assumed for the highest mass flow rate, corresponding to the largest internal volume. The value used was then based on tubing available from the supplier, with the largest inner diameter for this tube type being 0.04 inch. The length of the tube was estimated at 6 cm, which included parts going partially into the valve and into the aluminium interface.

5.11.2. Exploratory testing

For the exploratory tests the nozzle exit was (attempted to be) plugged with a piece of tape and further closed with a gloved finger. The results from this were inconclusive, some leakage was measured (primarily with the pressure method), but it could not be determined if this was due to an actual leak or just an insufficiently plugged nozzle. The starting clamping force as determined in section 4.4 was quite insufficient, as N_2 flow could be heard coming from different sides of the thruster body and light could seen through the nozzle coming in from the back of the thruster.

With this in mind and the somewhat dubious results from the leak testing, a small torque wrench (FACOM A.402 0.5-2.5 Nm) was used to gradually increase the torque on all the bolts equally for a better clamping seal. Steps of 0.1 N m were taken first, though this was later increased to 0.2 N m as the small increments were not resulting in noticeably better leak test results. Eventually a value of 1.4 N m was settled on which resulted in a reasonably low, but not yet adequate leakage flow, with no more holes visible through the nozzle and the disc springs nearly bottomed out.

5.11.3. Final testing

To obtain more conclusive results, and thus to determine if the current torque was actually enough, the method for plugging the nozzle was changed. A small piece of non-porous medium hardness rubber was pushed into nozzle with a clamp to provide both a more compliant sealing surface and a higher, consistent force keeping the plug in place. A piece of rubber was also added to the back of the thruster to prevent the clamp from damaging it, with both pieces being held onto the thruster by a piece of tape on the outside for easier assembly. A picture of the setup can be seen in Figure 5.24

An initial test was performed using this set-up which showed promising results, with a pressure measurement based leakage flow of around 1 µg s^{-1}, or 0.005 % of the cold mass flow. This was performed in ambient air at a slightly higher pressure (2.35 bar) than what will be used for thrust testing (1.34 bar). The pressure ratio is above the critical pressure ratio for nitrogen though, and should thus be sonic and independent of the ambient pressure.

For additional insight into leakage, the pressure test was repeated for a long time period (more than 15 h) overnight. The results from this can be seen in Figure 5.25. It can be seen in these results that the (absolute) temperature of the device stayed relatively constant, and with the low flow rate, the gas inside should be at roughly equal temperature. Based on this, the original assumption of constant T_c for calculating the mass flow using equation (5.2) should be valid.

Besides the expected asymptotic trend of the internal pressure towards atmospheric pressure, a strange kink can be seen, with the pressure first converging towards 2000 mbar. A current hypothesis regarding the cause of this is that some gas may have been leaking *into* the thruster through the valve up to that point, with the pressure difference over the valve only pushing it fully closed afterwards. The

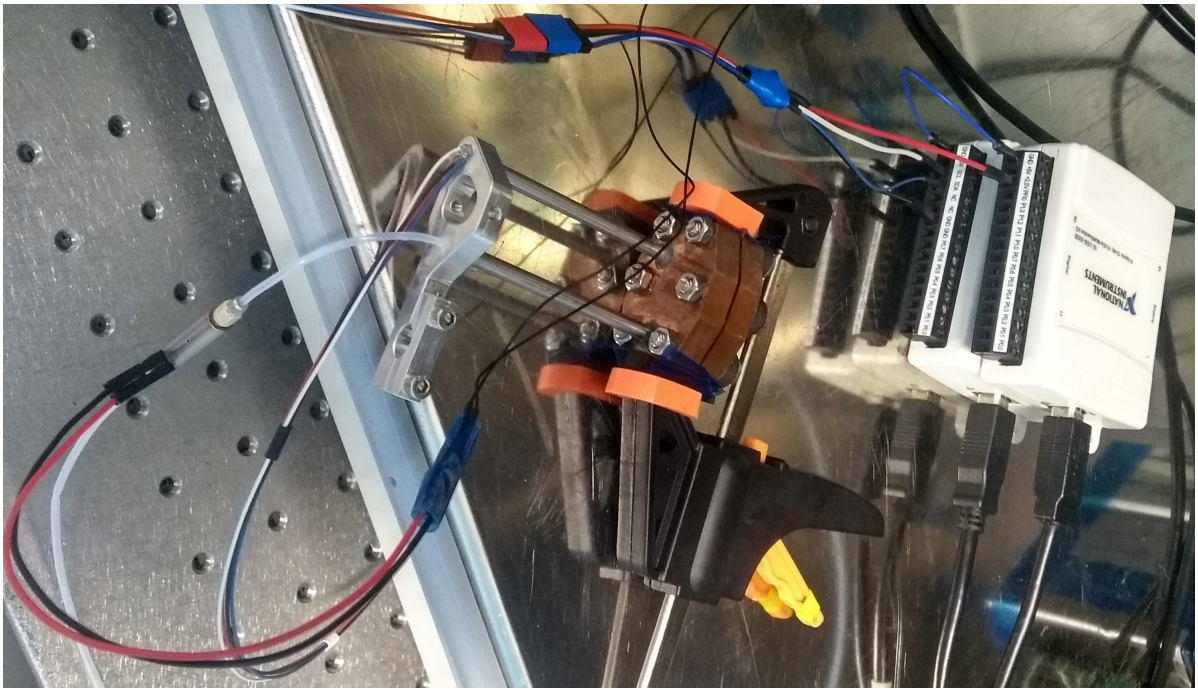

Figure 5.24: Setup for thruster leak testing, with the nozzle plugged by a clamp. The solenoid valve can be seen on the left, with the two DAQs for reading out the pressure sensor on the right.

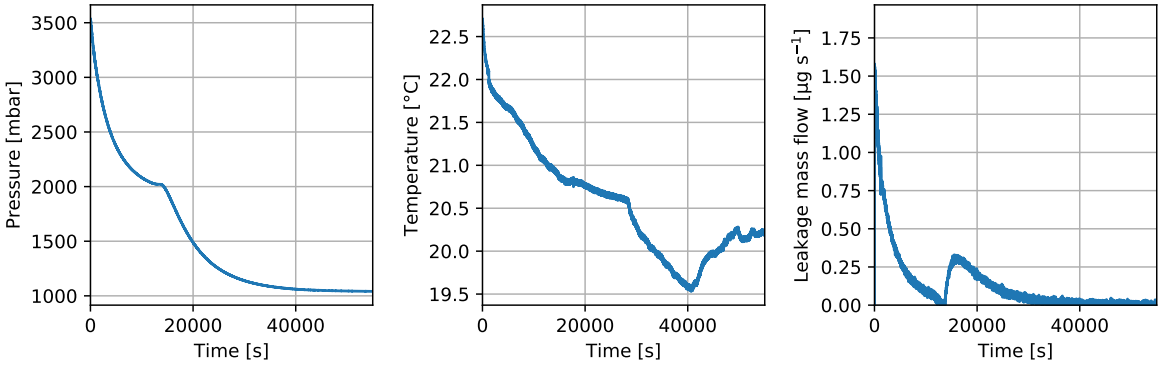

Figure 5.25: Overnight leak test results with the measured pressure, measured temperature and calculated leak mass flow from left to right.

internal design of the valve does allow for downstream pressure to push it open in such a manner [64, B9]. Possible further investigation of this effect is left for future work. In any case, the leakage flow below 2000 mbar was similar in magnitude to the earlier tests and remains well below the threshold of 0.1 %. The leak-tightness of the device is thus concluded to be excellent.

5.12. Cost and production time

With the goal of this project in mind, it is warranted to compare the cost and production time of the newly created design with the previous silicon MEMS version. The total expenses, excl. VAT, can be seen in Table 5.6, which unfortunately exceed the given budget of €500 by €324. This is due to the nozzle profile manufacturing miscommunication, where the nozzles were manufactured individually after a parallel attempt had failed. The three additional nozzles account for a total of €480 of extra cost that would not have been necessary.

In the same table an estimate of the cost of a brand new thruster is also given, which only takes into account the material that is actually used, and disregards one-time purchasing of tools. For example,

Component name	Total expenses [€]	Single new thruster (est.) [€]
Nozzle profile	640	160
Copper & aluminium material	60	15
CNC milling	0	360
Shoulder bolts	33	33
Pressure sensor	19	19
Teflon glue	22	1
Metal glue	8	1
Disk springs	13	13
Steel tube & cutter	29	4
Total	824	606

Table 5.6: Expenditures for cold gas thruster manufacturing, excluding VAT, including shipping costs. Expected cost is also given for the case if a new thruster was to be made, taking acquired material and tools into consideration.

the stainless steel tube was enough for 5 systems, only a very minute amount of glue was needed and the tube cutting device only has to be bought once. CNC milling was free in this instance, but likely won't be in future projects if DEMO has to be used. The programming and machining time in this case was around 6 hours, not taking into account the re-surfacing instances. This can be used for future cost estimates, which at an approximate hourly rate of €60 for DEMO come to €360. The cost for a new cold gas thruster then comes to roughly €600.

The cost estimate for the silicon MEMS thrusters was around $€7 \cdot 10^3$ per batch and $€2 \cdot 10^2$ per thruster chip, not including any interface components. A single cold gas thruster with this new design has a comparable unit cost, if machining for the silicon VLM interface is also taken into account. The new design does have the advantage that it can be made as a single unit though, so that its batch cost and unit cost are the same, making a new thruster design far less expensive than for the silicon MEMS thruster. If only a new nozzle shape is desired for testing, it may also be possible to just re-surface the current copper components to a new contour and have a new profile made, reducing machining time and cost down to an estimated €200 to €300.

The production time here took between 1 and 1.5 months, which was primarily spent waiting for several components to arrive and for example finding the appropriate method for polishing the sealing surfaces. With the knowledge and components acquired, many of the processes could be sped up greatly, with a production time of 1 to 2 weeks estimated to be possible if a very similar thruster were to be produced now. Only a day or two may be needed if just a new nozzle profile shape is desired and the rest of the thruster is left intact.

5.13. Conclusion

Despite some minor mishaps, cold gas thruster fabrication went well and was on schedule, with the whole process only taking 1 to 1.5 months. With knowledge gained this should now even be possible in 1 to 2 weeks. A similar unit cost could be achieved as for the silicon VLM with its interface, coming in at an estimated €600 for creating another thruster of the same design. Only creating a new nozzle profile and re-surfacing the copper sealing blocks to match is estimated to cost even less at €200 to €300. The new fabrication method also comes with the advantage that it has a batch size of one, so that fabrication errors can be cheap and quick to fix, besides requiring much less up-front investment compared to $€7 \cdot 10^3$ for a new batch of 30 to 40 silicon thrusters. Disregarding the accidentally incurred cost for multiple nozzle production, the project would have kept to the €500 budget, though only through the use of unpaid CNC machining from friends. As alluded to in the previous chapter, without these special circumstances, a budget of €500 would not have been sufficient for a project involving similar amounts of machining.

Regarding the thruster itself, the nozzle shape was as designed, though with an $(18 \pm 13)\,\%$ larger throat area and lower expansion ratio. This was seen as an acceptable deviation and can be attributed to the increase in throat width compared to the design; two cutting passes were needed to create the nozzle throat geometry with wire-EDM instead of one, increasing the minimum width. Compared

to previous silicon thrusters at the department, where recent measurements showed a 61 % smaller throat, the throat area was actually much closer to the design value for the new thruster. Accuracy of other sections of the design were on par for silicon etching and wire-EDM at around 1 %. Subsequent leak testing of the thruster showed excellent results with less than 0.01 % of the expected mass flow through the nozzle being lost to leakage. The thruster fabrication process is thus concluded to have been successful, and cold gas thrust testing may commence.

5.14. Recommendations

For future projects, several recommendations can be made based on experiences during manufacturing of this thruster. Firstly, the issue regarding bolt holes not being perpendicular to the sealing surface could have been prevented. The holes should have been reamed during CNC machining, not afterwards by hand, which would have made sure the reamed surface was still aligned properly. Something that was realized later is that using six shoulder bolts also over-constrains the whole assembly. Only two of them are actually needed for fully fixing / determining the positions of the copper blocks and nozzle profile. The remaining bolts and bolt holes then do not need such tight tolerances, simplifying fabrication.

With laser cutting at the 3ME faculty determined to be a suitable method to cut metal foam, different heat exchanger geometries may be used for future projects. For example, the direction in which the cut components are installed can be rotated 90° so that the top plane of the metal foam sheet is facing forward towards the nozzle instead of up. This would allow for making heater cross sections with different shapes and a thickness other than 5 mm, though the chamber length would then be fixed at a multiple of 5 mm. Cross section shapes such as ovals, circles or chamfered rectangles would then be possible, allowing for chamfering of the heater interior walls, reducing possible stress concentrations in the copper.

It is also advised for a new design to “balance” the amount of surface area of the sealing surface, to make it easier to avoid polishing it into a slope. The thin edge would then be limited to the sides of the heating chamber. A quick concept drawing of a sealing block with metal foam incorporating some of the mentioned recommendations can be seen in Figure 5.26.

Another option might be to use a thinner variant of the porous metal foam, as this is available from Recemat down to 0.5 mm, the same thickness as the current nozzle profile. This would allow for making the sealing surface completely flat without cut-outs in the middle, simplifying machining and polishing even further. Other metals and alloys such as copper or nickel-chromium are also available for e.g. higher thermal conductivity or better corrosion resistance, though not for 0.5 mm thickness.

Next, for working with DEMO on experimental production methods or in general, always clearly state up front what should happen in case something does not work as planned. In this case around €480 could have been saved if it had been specified that only one nozzle profile should have been made if parallel production did not work.

In addition, it is recommended to incorporate the larger minimum throat width that can be achieved with wire-EDM in the design phase, and combine this with an active method to control the throat width during installation. Both of these can reduce fabrication uncertainty of the throat width, and the second can also be used to narrow the throat width beyond what is possible with machining alone. Finding a method to accurately measure the throat size during and after assembly would also be a part of this. At the moment the throat width after assembly can vary from that of the profile before assembly due to its compliance, without any control over how much this variation is. This is not desired for actual production as this introduces an element of randomness into the fabricated nozzle size. Oppositely, the profile can also be made much more rigid to reduce the possible throat width variation, though this does mean that this width would then be limited to $\geq$145 µm for wire-EDM cutting.

It would also be recommended not to use leak-finder fluid near the nozzle, as this leaves a nasty residue, possible impacting performance. For the current design, it is also not useful for finding leaks around the metal seal. This seal is hidden inside the small gap between the two copper blocks, obscuring the location where bubbles/gas may be originating from.

Lastly, it is important to state the value of practical experience when working on a thesis project where similar design and fabrication efforts are required. The author of this report had somewhat more of this than a standard aerospace engineering student due to having completed a BSc in mechanical engineering with ample practical project work, as well as having been a full-time member of a student

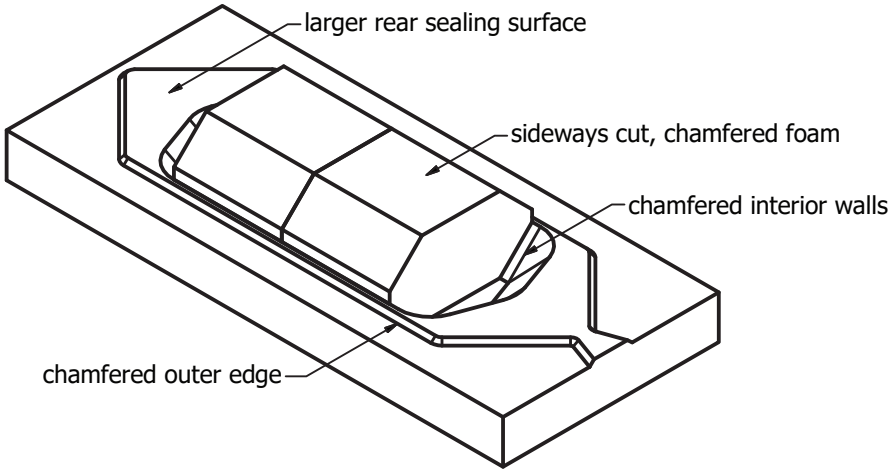

Figure 5.26: A schematic drawing of a sealing block with metal foam heat exchanger pieces incorporating some of the recommendations.

engineering team for a year. Without such experience, a similar project would have been difficult to complete successfully in a timely manner.

6

Cold gas thrust testing

In this chapter, everything pertaining to thrust testing of the created thruster with cold (ambient temperature) gas will be discussed This is done to verify the functionality of the thruster for cold gas thrust production and to provide some initial data for comparison with model predictions. The thrust testing hardware, software, and general setup are discussed in section 6.1. The measurements from thrust testing and how these are further manipulated into results is then laid out in section 6.2. The results are then compared with those from the reference design and model predictions in section 6.3. Lastly a conclusion to the chapter is given in section 6.4, followed by recommendations in section 6.5.

As the reference thruster is essentially a single point of comparison and the geometry of the new thruster is not exactly the same, acceptance criteria for verification are kept relatively lax. From an engineering perspective, the specific impulse is the main point of interest, as this is the primary factor in determining how much propellant will be needed for a certain amount of Δv. If the new fabrication method from this report is to compete with silicon alternatives, it should thus have similar or better I_{sp} efficiency. For verification then, the new design shall have $\geq$90 % of the I_{sp} efficiency of the reference design, at the same throat Reynolds numbers. Mass flow and thrust are seen as less important as they can be adjusted by using a design with a different throat area or chamber pressure.

6.1. Thrust testing setup

In this section, the existing hardware and accompanying software used to measure thrust in vacuum is discussed. Upgrades to the software are also detailed, including a switch from calibrated distance measurements to electromagnetic force compensation as the working principle of the thrust bench. The magnetic actuator used in this process is also calibrated once more. Finally, thrust tests are performed in vacuum for three pressures around the desired operating point, with each operating point being repeated thrice. This number of tests was seen as an acceptable compromise between the time available and performing many more tests to show repeatability and behaviour over a wider range of inputs. The goal here is also functional verification of the prototype, not gathering large amounts of data for general model validation.

6.1.1. Thrust bench hardware

The thrust measurement bench that is used is TB-5m, which mainly consists of a hanging pendulum suspended on frictionless hinges to which the thruster is attached. The mass of the pendulum and a small rotary spring push it towards an equilibrium position, while the force from the attached thruster causes displacement away from this equilibrium point. The amount of pendulum displacement during thrust relative to its equilibrium position can be related to the thrust force. For this the relation between displacement and force applied to the pendulum needs to be known, for which an electromagnetic calibration actuator is used. This essentially simulates a thrust force with an accurately known magnitude to obtain a function relating force to and from displacement. For a more in-depth look into the working principle and the thrust bench design and components see the work by Bijster [8].

The thruster of interest is normally attached to the bottom of the pendulum for a maximum thrust measurement of 5 mN (hence the designation TB-5m). This range can be increased in exchange for

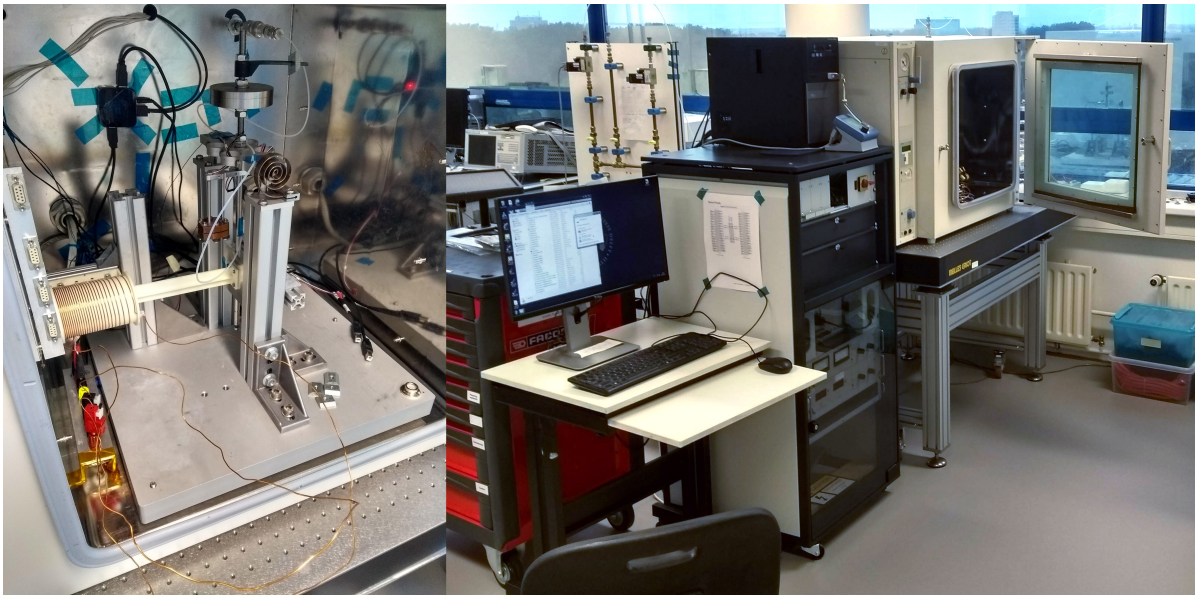

Figure 6.1: Overview of the thrust bench used for testing (left) and the equipment used to operate it in a vacuum (right).

some accuracy by moving the thruster closer to the pendulum pivot, which is required in this case as the current thruster is expected to produce 10 to 15 mN. This particular device was chosen for this project during the earlier literature study [68] as it was the only one that would fit inside the vacuum chamber without modification and had a simple and accurate calibration mechanism that also works in a vacuum. The device and the surrounding equipment can be seen in Figure 6.1, including the vacuum chamber, data acquisition and control computer, power supplies and the N_2 feed system. A list of the components used for measurement and control can be viewed in Table 6.1, together with a short description of their function.

6.1.2. Thrust bench software

The actuators and sensors are controlled and read out through the clean room PC running LabVIEW. The existing program facilitating this was apparently made during the work of De Athayde Costa e Silva [14], has not been updated since and did not include any major documentation. As a result it included many features that were no longer needed and was overall difficult to comprehend and adjust for the needs of this specific project. Due to this it was decided to simplify the program features and rework its internal structure to make it easier to understand for the current author and future users, and to allow for easy adjustment and adding of sensors and actuators later. An overview of the created LabVIEW programs and their structure is shown in Appendix D.

The approach that was taken for this was to keep the base logic for communicating with sensors and actuators intact, and implementing these one by one, making sure to verify their functionality each time a new device was implemented. The structure of the main data acquisition state was changed to one loop per group of sensors/actuators with the same sampling frequency and one loop for saving *all* of the data to a single file. Instead of saving to disk in a Comma Separated Value (CSV) text file as before, the proprietary National Instruments TDMS binary format[1] was used. This allows for combining data with different sampling rates into the same file, while also storing data in its original binary representation, which greatly lowers the disk space required compared to a text file containing the same data and precision.

To make working with the data easier, the time since start of the program was now also included for each of the sampling frequencies, and data channels saved to the TDMS file were also given names including their units and quantity in a standardised format. This was done in an effort to make the data usable without needing to know the specifics of the program that created it. The naming of save files was further streamlined by having the user specify a test name, which was then automatically used together with the current date and time in ISO-8601 format to create unique file/folder name combinations each

[1] http://www.ni.com/product-documentation/3727/en/

Component	Function
Sensors	
Brooks 5850S mass flow controller	Measure N_2 gas mass flow from feed system. Valve override is turned on, no active mass flow control.
TE Connectivity MS5837-30BA p-T sensor	Measures absolute pressure in the thrust chamber and temperature of the interface (integrated with thruster).
με CS2 displacement sensor	Measures displacement/position of pendulum.
Vacuubrand VSP 3000 pressure sensor	Measures absolute pressure in the vacuum chamber.
Actuators	
Electromagnetic calibration actuator	Creates a know force for thrust bench calibration.
Delta Elektronica SM-7020-D power supply	Controls and measure current through calibration actuator.
The Lee Company solenoid valve	Turns mass flow to thruster on or off.
Solenoid spike and hold driver	Controls the current to the solenoid valve.
Arduino board	Controls spike and hold driver and interfaces with clean room PC over a serial connection.
Delta Elektronica E-030-10 power supply	Provides one of two required input voltage levels for spike and hold driver.
Delta Elektronica D-030-10 power supply	Provides the other required input voltage level for spike and hold driver.
Vacuubrand RZ-6 Rotary vane pump	De-pressurizes vacuum chamber.
Data Acquisition Devices	
Clean room PC	Reads out sensors and actuators through other DAQs, runs data acquisition software, saves data.
NI-8451 I^2C-SPI DAQ	Reads out MS5837-30B over I^2C and interfaces with clean room PC over USB.
NI-6008 USB DAQ	Provides 2.5 V power line for MS5837-30B.
NI-PCI-6229 DAQ	Interfaces with 7020-D PSU and 5850S MFC using analog 0-5 V channels, is built into clean room PC as a PCIe card.
Vacuutherm DCP 3000 Vacuum gauge	Reads out pressure from VSP 3000 and interfaces with clean room PC over a serial connection.
με DT6220/DL6230 DAQ	Reads CS2 sensor signal and converts it to a normalized digital value, interfaces with clean room PC over ethernet.

Table 6.1: Overview of sensors, actuators and data acquisition devices used in the thrust measurement setup.

time the program was run. This was implemented so that older data files could never accidentally be overwritten.

The user interface for monitoring sensor values and controlling actuators was changed to fully fit on the pc display, without having to scroll, so as to have all information and controls available at all times. The charts for live plotting of data were changed to have time on their horizontal axis, instead of the number of samples, to keep signals in sync with each other. The whole program and its interface look were lastly updated to the latest available LabVIEW version and graphical style (2018, and NXG respectively). An overview of all the LabVIEW files used, their function and internal structure can be found in Appendix D.

One last point of interest is that the existing software assumed a 5 mm range distance sensor (model CS5) for converting the normalized value from the sensor DAQ to an actual measurement. In actuality, a 2 mm distance sensor (model CS-2) is installed (verified by comparison with calliper measurements), meaning that some of the previous work using this software version used incorrect distance measurements. This should not have a detrimental effect on previous results however, as only *changes* in distance have been used for measurements. Both force calibration and force measurement used the same (incorrect) range, cancelling out its effect.

6.1.3. Electromagnetic force compensation

A problem with the existing setup was that pendulum damping was very low, with as a consequence that sudden starting and stopping of thrust caused large oscillations that obscured thrust measurements for tens of seconds, sometimes minutes. Any outside influence or signal can also cause persisting oscillations, obscuring results. Some form of additional damping would thus be useful in this case as it would decrease oscillations, making the signal due to thrust more clear [4, 8].

Physically such a feature can be provided by a viscous liquid [12] or magnetic [8] damper of some sort, but for the current project this would be too complicated and too much extra time and effort. It was realized however, that the necessary hardware for making a damper were present in the form of the available magnetic calibration actuator and the distance sensor, which could both be controlled and read out by the same LabVIEW program. This allowed for implementing a simple feedback loop with a digitally implemented damper by taking the (filtered) time derivative of the distance sensor data and using that signal to drive the actuator force counter to the movement of the pendulum.

Implementing this and testing it showed promising results. This led to the further realization that it should be possible to use these same components to create a full controller for the position of the pendulum. Such a system was also previously mentioned to the author as an alternate thesis topic, and a desired thrust bench upgrade by supervisor Zandbergen.

This is useful because the force that the actuator exerts is known very accurately [8] and when the position of the pendulum is kept constant with a controller, any change in the known actuator force can be directly related to the thrust force. This means that the previous intermediate steps of relating force to displacement using the calibration actuator and subsequently measuring the displacement and relating it back to force become redundant. Any changes in stiffness of the pendulum between tests (e.g. due to wiring, tubing) are then also much less influential as no displacement results in no additional force/moment.

For simplicity a basic discrete time Proportional Integral Derivative (PID) controller was implemented in LabVIEW. The implementation was made based on the discretized equations from the work of Åstrom and Wittenmark [3], which can be seen below. All values are thus only computed when the distance sensor is sampled (at roughly 100 Hz), with (k) indicating the current sample.

$$e\,(k) = [r\,(k) - y\,(k)] \tag{6.1}$$

$$P\,(k) = K_{\mathrm{p}} e\,(k) \tag{6.2}$$

$$I\,(k+1) = I\,(k) + \frac{K_{\mathrm{p}} h}{T_{\mathrm{i}}} e\,(k) \tag{6.3}$$

$$D\,(k) = \frac{T_{\mathrm{d}}}{T_{\mathrm{d}} + Nh} D\,(k-1) - \frac{K_{\mathrm{p}} T_{\mathrm{d}} N}{T_{\mathrm{d}} + Nh} [y\,(k) - y\,(k-1)] \tag{6.4}$$

$$u\,(k) = P\,(k) + I\,(k) + D\,(k) \tag{6.5}$$

Here e is the error signal, the difference between the user reference input r and the measured value y, with all these values being distances [mm] in this instance. The proportional term P for the controller

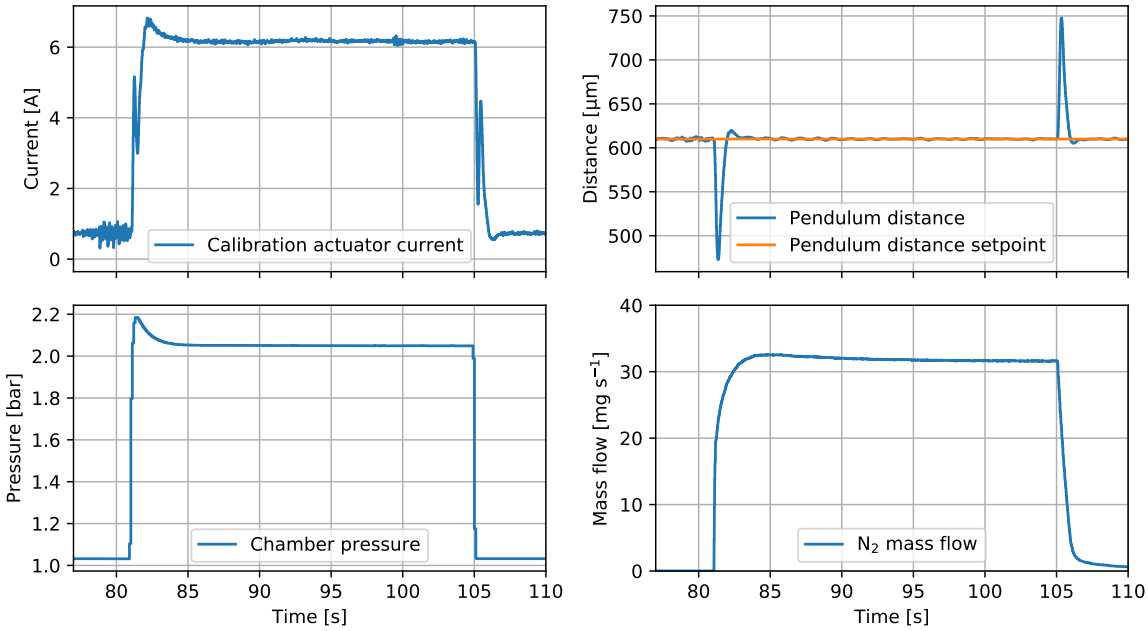

Figure 6.2: Results from testing the PID controller on the test bench with the thruster, in ambient conditions.

is then simply the error signal multiplied by a tunable proportional constant K_p [A mm^{-1}]. The current integral term I is calculated at the previous sample using a zero order hold, rectangular approximation, and is limited for anti-windup (not shown). This further incorporates the size of the time step between samples h [s] and a second tunable parameter, the integration time T_i [s]. The derivative term D is somewhat more involved as it also includes low-pass filtering for stability. It is also only calculated using the derivative of y, not e as would be the case for classical PID, which means it essentially acts just as a digital viscous-like damper. This helps with stability as step setpoint changes would otherwise result in unwanted large values for D. Additional tunable parameters used for D are the filtering constant N [-] and the derivative time T_d [s]. The output sent to the calibration actuator u [A] is then simply the sum of P, I and D.

The controller was first tested and tuned on the thrust bench to simply change its positions without the disturbance force from a thruster. The parameters were tuned manually until the dynamic behaviour was deemed satisfactory: fast response with little overshoot and oscillations. The values from this tuning that are used from this point on are $K_\mathrm{p} = 2\,\mathrm{A\,mm^{-1}}$, $T_\mathrm{i} = 0.02\,\mathrm{s}$, $T_\mathrm{d} = 4.5\,\mathrm{s}$ and $N = 200$. Next, a preliminary test under ambient pressure conditions was performed with the thruster installed to see how the system would react to the sudden disturbance from turning on the thruster. The results from which can be seen in Figure 6.2.

These results show that the controller can compensate for the thrust created, with only a short period at the start and end of the thrust when the equilibrium is disturbed due to the rapid changes in thrust force. At the start of the thrust period there are also some leftover dynamic signals with a small pressure overshoot, the actuator current converging towards a final value, and the somewhat slow response of the mass flow sensor. For steady state measurements, this period should be avoided, thus thrust test times of at least $\sim 10\,\mathrm{s}$ should be used.

There are also still some oscillations left in the pendulum distance signal with amplitude of around 1 to 2 µm. These could not be eliminated with the current combination of sensor, controller and actuator. The electromagnetic implementation of a damper simply has its limits due to phase delays in the control loop and the inherent instability of numerical derivatives. This meant that the damping parameter T_d could not be further increased, else steady state oscillation amplitude would actually increase and in some cases even make the system unstable. Because the distance is oscillating around the desired distance with a relatively low amplitude, and resulting signals in the actuator current can be filtered out, this is not seen as an issue.

A last observation from these results is that the actuator already has a non-zero current before and

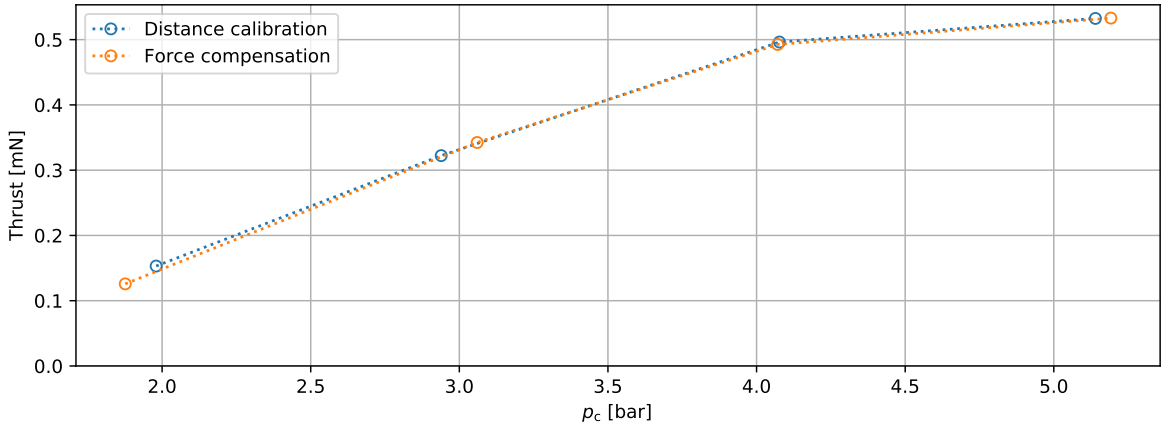

Figure 6.3: Comparison data for thrust measurement with force compensation and distance calibration, courtesy of A. Papadimitriou. This data uses a force correction factor $\lambda = 0.6499$ as the thruster was attached at the bottom of the pendulum, scaling the range of the thrust measurement down by a factor 2.8 compared to the current work.

after the thrust phase. This is the case because it was observed that damping became less effective at or very near the pendulum equilibrium point. The power supply can only provide current in one direction, thus cannot provide damping for up to half of the time if the distance setpoint is at the pendulum equilibrium. However, this zero thrust distance should also be kept low to limit the current going through the coil to prevent it from heating up too much and so as not to saturate the power supply output for larger thrust forces.

In total, this method of measuring thrust was deemed to be suitable. It also takes out some intermediate conversion steps in the measurement, improving accuracy by having fewer terms contribute to uncertainty. Furthermore it also allows for taking thrust measurements at any time, regardless of (small) changes in stiffness of the pendulum. It is thus no longer necessary to perform a force-distance calibration before and after each test, which took around 15 min per calibration in the past [41].

No comparison measurements were made by the author to check if this altered method gave the same results as the previous distance-based measurements, which was validated previously by [8]. However, the exact same hardware, actuators and sensors are used as with the previously method. The new method also just essentially skips two steps of the previous process where force was converted to distance and back. Based on these considerations and in the interest of time it was not deemed necessary to perform this comparison at this time. After testing had concluded for this project however, fellow student A. Pappadimitriou did use both methods for measuring the thrust of a silicon MEMS thruster at the department and found essentially the same results between the two, see Figure 6.3. Differences between (interpolated) values from the two methods were $<1\,\%$, except for the smallest forces ($\sim 5\,\%$) where absolute accuracy starts to become dominant. This is in line with the expected accuracy of both methods and provides further validation of the method, on top of the earlier reasoning.

6.1.4. Magnetic actuator calibration

With this electromagnetic force compensation setup for measuring thrust in place, an important aspect is accurately knowing the force produced by the magnetic actuator for a given current. This calibration was last performed by Jansen [27] in 2016. To determine whether the current-force relation had changed over the past few years, it was deemed necessary to re-calibrate it.

To do this, the test procedure and equipment from their work were used with some minor alterations. This method employed a high-precision Mettler Toledo AG245 scale for force measurement, above which the actuator coil was mounted vertically with the magnet arm resting on the scale. The relative position of the coil and arm were the same as on the thrust bench. A laboratory power supply was then used to send a range of current values through the coil, which were measured with a multi-meter. The force and current values were then manually documented and used to construct a current to force relation.

The alterations made to this process were as follows. Firstly, the power supply was switched to be

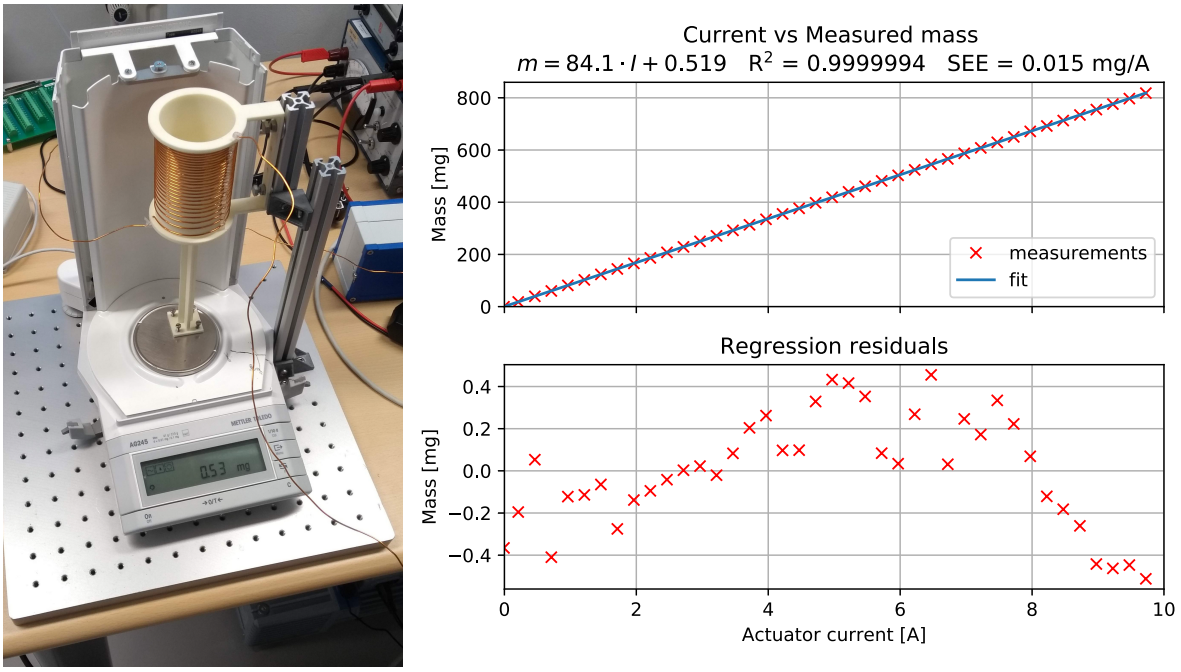

Figure 6.4: The magnetic actuator calibration setup on the left (excl. power supply and computer), with the resulting current to mass linear fit and residuals on the right.

Test name	a [mg A^{-1}]	b [mg]	SEE_a [mg A^{-1}]	σ_{res} [mg]
C-01	84.11	0.519	0.0147	0.27
C-02	84.43	0.882	0.0144	0.26
C-03	83.96	0.405	0.0114	0.21
C-04	84.22	1.071	0.0176	0.32

Table 6.2

the same device that is also used for powering the actuator during thrust measurements. This meant that the accuracy of the current measurement was no longer important, only its repeatability, as the combination of power supply and actuator would now be calibrated as a whole. It also meant that setting the current level and measuring its value could be done automatically with a simple LabVIEW script, only requiring the force/mass measurements to be written down manually. With this automation, the resolution of the current samples could also be increased without increasing the time needed per calibration. The program was thus set to increment the current through the actuator in steps of 0.25 A (down from 1 A) every 10 s from 0 A to 10 A and then repeat. This gave just enough time for the scale to settle and for the results to be written down. A single calibration then takes just under 7 min, excluding the time needed to set-up the scale and actuator, which takes somewhat longer. For a detailed test procedure see Appendix C.2.

The test setup used and the results from a single test (C-01) can be seen in Figure 6.4. It was repeated three more times (C-02 to C-04) by fellow MSc. student A. Pappadimitriou on a separate occasion, with very similar results (<0.6 % difference). The least squares fit used relating the measured mass m [mg] to the actuator current I [A] is of the form $m = aI + b$. As only differences in current will be used during measurements, the intercept b is not needed, only the slope a. Results for these values from the four tests can be viewed in Table 6.2. These also includes the standard error of the estimate of a, SEE_a, and the standard deviation of the residuals σ_{res} (i.e. the proportional and constant uncertainty of the fit).

The cause of the differences between the tests is unknown at this point, possibly slightly different wire placement or coil positioning, as this is done by eye. However, the variance is small enough that the accuracy of the results is seen as acceptable. The total slope for current to mass is then based on the average value of the different tests and the sample standard deviation: $\overline{a} = (84.2 \pm 0.2)$ mg A^{-1}

(1σ). SEE_a is ignored here as it is more than an order of magnitude smaller than the standard deviation from combining the results of the different tests.

The conversion from mass to force then still has to take place, which depends on the gravitational acceleration where the AG245 scale was calibrated, which is unknown. To be somewhat on the safe side a value of $(9.81 \pm 0.01)\,\mathrm{m\,s^{-2}}$ was used to cover most values found in the Netherlands and surrounding countries. The uncertainty due to the scale not having been calibrated recently is assumed to be part of this value. In total the relation from current differences ΔI [A] to force differences ΔF [mN], using 3σ confidence bounds, then becomes:

$$\Delta F = (0.826 \pm 0.006) \cdot \Delta I \pm 0.0078 \tag{6.6}$$

Comparing this to the last known values from calibration by [27], the results are very similar, with one test having the same result (a slope of $a = 0.826\,\mathrm{mN\,A^{-1}}$), a second being only 1σ off (0.827) and a third only 1.5σ (0.829). The current-force characteristic of the actuator has thus seemingly not changed by a significant amount in the past few years, as the 1.5σ confidence bound of the new relation still covers the previous ones. This shows that past projects that used the previous relation were correct to do so and that the actuator has been stable over time. Re-calibration is a relatively quick process with each test only taking 10 to 20 minutes and the surrounding tasks requiring a few hours at most. This could thus be performed for each new project with relative ease and at no cost, though the stability of the relation up to now would suggest this may not be entirely necessary.

6.1.5. Force conversion factor

Unlike the interface for the previous silicon-based thrusters, the interface for the current one allows it to slide along the pendulum vertical arm, instead of being limited to attaching it to the very end of the arm. This does mean that the moment arm for the thrust force about the pendulum axis of rotation L_{thr} [m] can vary between installations. This measurement, together with the moment arm for the electromagnetic actuator L_{act} [m], determines the conversion factor λ [-] to calculate the thrust force F_{exp} from the known actuator force F_{act}, based on moments from both balancing out ($\sum M = 0$):

$$F_{\mathrm{exp}} L_{\mathrm{thr}} = F_{\mathrm{act}} L_{\mathrm{act}} \tag{6.7}$$

$$F_{\mathrm{exp}} = F_{\mathrm{act}} \frac{L_{\mathrm{act}}}{L_{\mathrm{thr}}} = F_{\mathrm{act}} \lambda \tag{6.8}$$

The length of each of these moment arms, and for the thruster and actuator respectively, was measured using Mitutoyo digital callipers. Due to the geometry of the thrust bench and thruster it was not possible to determine each length with a single measurement, so several measurements were performed which were combined to arrive at a value for λ. This introduces a slightly larger uncertainty in the total value compared to a single measurement (though still quite low compared to other measurements).

A schematic overview of the measurements taken can be seen in Figure 6.5, with the values and confidence bounds for each of them being given in Table 6.3. Care was taken to have many of the measurements be between parallel surfaces around which the calliper ends could be placed, to avoid errors from measuring at an angle. The shortest, perpendicular distance between the surfaces was then found by first aligning the callipers by eye, followed by shifting them back and forth slightly until a minimum was found. Confidence bounds were estimated based on the resolution of the callipers and by how much the measurement changed when moving the calliper ends slightly around the minimum.

With these measurements, λ can be calculated as follows:

$$\lambda = \frac{L_{\mathrm{act}}}{L_{\mathrm{thr}}} = \frac{L_0 + L_3 + {}^1\!/_2 L_4 - L_2}{L_0 - {}^1\!/_2 L_1 - L_2} \tag{6.9}$$

With this, $L_{\mathrm{act}} = (163.45 \pm 0.13)$ mm, $L_{\mathrm{thr}} = (90.12 \pm 0.12)$ mm, and $\lambda = 1.8137 \pm 0.0013$ are found as the results. The confidence bounds for these values were calculated using the method described later in subsection 6.2.2.

One thing to note here is that the measured actuator distance is quite different from the previously reported value of 179.66 mm [41]. This seems to be due to this previous work using the distance to the centre of the CS2 displacement sensor, instead of the actuator. These distances used to be the same, [8, 67], but the sensor target and actuator arm have seemingly moved up at some point since then. The value of λ used by [41] would then have to be 0.6670 instead of the reported value of 0.7331, resulting in 9 % lower thrust.

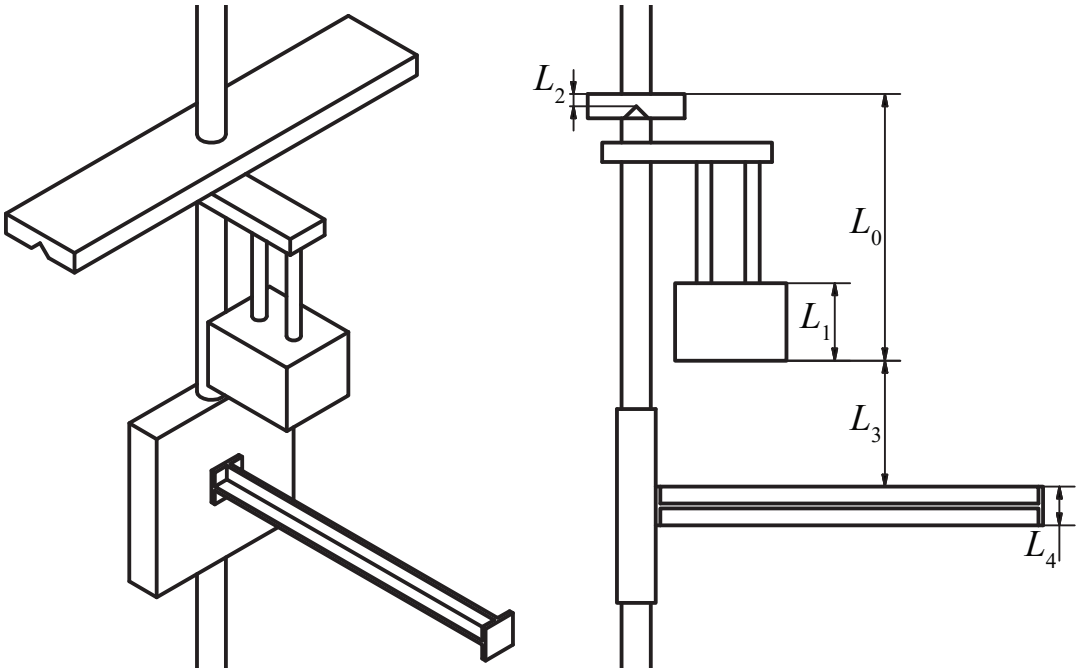

Figure 6.5: Isometric (left) and sideways (right) schematic views of the thrust test pendulum with installed thruster. Indicated are the length measurements that were used to find the moment arms of the thrust and actuator forces.

Name	Length [mm]	Description
L_0	103.80 $\pm$ 0.10	Top of pendulum horizontal beam to bottom of thruster body
L_1	16.87 $\pm$ 0.05	Top to bottom of thruster body
L_2	5.25 $\pm$ 0.05	Top of pendulum horizontal beam to frictionless pivot point
L_3	52.35 $\pm$ 0.05	Bottom of thruster body to top of actuator beam
L_4	25.09 $\pm$ 0.05	Top to bottom of actuator beam

Table 6.3: Measurements of lengths indicated in Figure 6.5.

6.1.6. Vacuum thrust testing

For measuring the thrust in vacuum, the entire thrust bench with thruster and DAQs is placed inside a Heraeus vacutherm vacuum oven. Vacuum pass-throughs are available for three power channels for e.g. calibration actuator and heaters, a USB cable for the DAQs, the CS2 distance sensor cable, and multiple connections for miscellaneous electronics such as the solenoid valve wiring. There is also a pass-through for the N_2 propellant lines which end in a quick-connect fitting on the inside of the vacuum chamber, for easy (dis)assembly.

The thruster is attached to the pendulum arm above the actuator magnet holder (for larger thrust force measurements) with the nozzle exit facing in the direction of the calibration actuator. This is different from experiments with earlier thrusters where the nozzle faced the opposite way as now the actuator force compensates for the thrust instead of simulating it. Alignment of the thruster exit direction perpendicular to the pendulum axis of rotation was done by eye, which introduces a small amount of uncertainty in the thrust measurement. A picture of the thrust bench with the thruster installed inside the vacuum chamber can be seen in Figure 6.6.

As with previous thrust tests using TB-5m, the electrical wires and nitrogen feed tube were installed over the side of the pendulum cross-beam, close to the rotation axis to minimise their influence on system stiffness. Also as before, these were secured using pieces of tape to prevent movement during testing.

One aspect where the setup deviates again is that the solenoid valve is now on the pendulum, instead of being attached to the vacuum chamber ceiling. This was done in an effort to have the pressure remain constant in the propellant tubes running between the moving and stationary part of the pendulum, to avoid pressure stiffening of the tubes from influencing results [4]. What was not

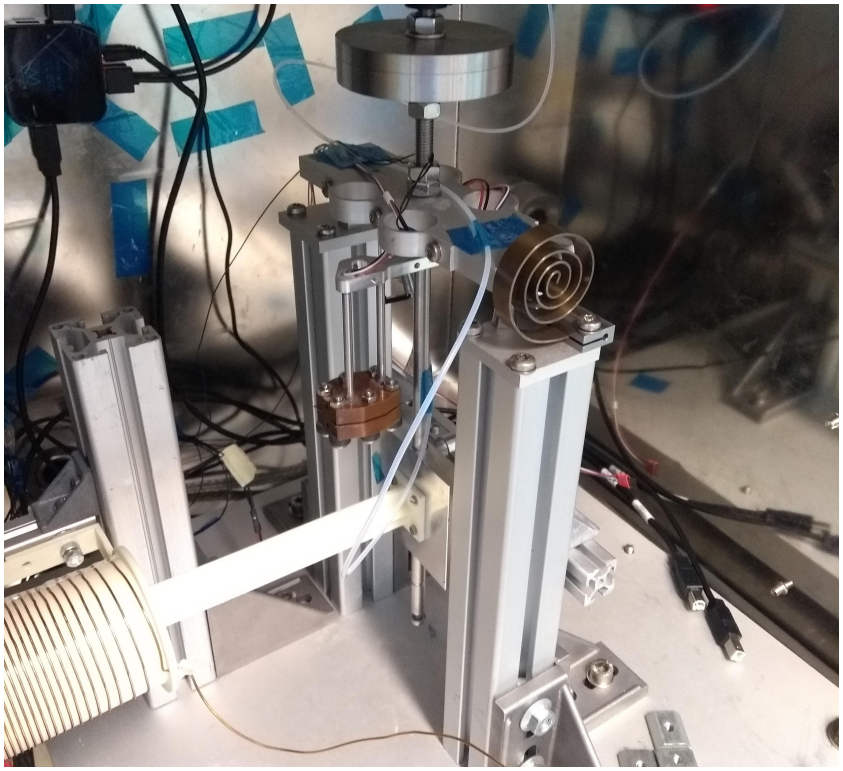

Figure 6.6: Thruster installed on the thrust bench inside the vacuum chamber for testing.

realized at the time however is that the feed system has a relatively high pressure drop (on the order of one to several bar) for even the small mass flows in use here. Thus the pressure in the lines does still change when the thruster is engaged, though now from a high pressure at no flow *without* pressure loss, to a lower operating pressure at the steady state flow *with* pressure loss. The possible impact of the effect was only realized after experiments had been concluded and was not characterized, its magnitude is thus unknown. See this chapter's recommendations in section 6.5 for a further discussion on this aspect.

Three sets of three tests were subsequently performed, each set with a different pressure through adjusting the feed system pressure regulator. The resulting three values of p_c are set around the design pressure of 1.34 bar by tuning the pressure for the first set to be somewhat lower at 1.11 bar and subsequently incrementing it slightly for the next two to 1.27 and 1.45 bar. This gives more information than just testing at the design pressure. It is also simpler to achieve than tuning to a very specific pressure as adjusting the pressure up gives immediate feedback on the low-pressure gauge, while adjusting it down does not. This is because the regulator can only increase the pressure of the (closed) system, for lowering the pressure the extra gas also has to be vented, either through the thruster or through one of the quick connects on top of the feed system. The indicated pressure is also higher than the chamber pressure due to the pressure drop over the tubes when mass flows through them during thrust.

For performing the thrust tests, the air was evacuated from the vacuum chamber using a Vacuubrand RV6 rotary vane pump. This is able to reduce the pressure inside to 20 Pa if left running for long enough. In this case a pressure around 40 Pa was achieved before starting each thrust test to save some time, as the convergence to the final pressure shows asymptotic, slow behaviour. During thrust the pressure also rises 100 to 200 Pa due to the mass flow from the thruster and the small size vacuum chamber, so that the initial pressure is not as influential. This pressure is also measured and taken into account for calculations, though due to the low expansion ratio of the nozzle it has little impact on the thrust.

For each thrust test the desired position of the pendulum for the PID controller was set slightly above its equilibrium position (around 10 µm). The controller was subsequently turned on and the pendulum distance was allowed to settle. The solenoid valve was then opened for $\sim$ 15 s, so that any transient effects from thrust start would no longer be present towards the end of the measurement period. After

thrust had ended the pendulum distance and controller were again allowed to settle so that an zero-thrust actuator current could be measured both before and after thrust, so that any drift during the test could be identified. A full test procedure for cold gas thrust testing can be found in Appendix C.3.

The measurement results around the thrust period are visualised in Figure 6.7. Signals with high frequency noise and/or low frequency oscillations from the pendulum were filtered to reduce the influence of these effects on outputs and to make the mean signal clearer for visual inspection. The filter used is a 100 sample moving average filter that was applied backwards and forwards using `signal.filtfilt()` from the `scipy` Python package. This ensures that there is no phase delay between filtered and original signal while also doubling the effective gain of the filter.

For calculating results, short time-window average values are used to arrive at a single set of inputs per test. The windows all last for 1.00 s, and are defined relative to the recorded time of the solenoid valve opening and closing. The timespan of 1.00 s was chosen as a compromise: longer windows allow for more noise and oscillation reduction while shorter windows result in less variation of non-constant inputs (e.g. the vacuum chamber pressure) and consequently smaller confidence bounds for these.

Three windows are defined: one before start of thrust for getting the zero-thrust actuator current, one during thrust, and another one afterwards for measuring the zero-thrust current again (to determine possible pendulum drift). The first window starts 1.2 s before solenoid valve activation, the middle window starts 1.0 s before and the final window 5 s after valve deactivation. These time offsets were used to avoid the time periods when the filtered signals have transients around thrust start/end and for the final window to allow the controller to settle again. These windows, as well as the filtered signals, can also be seen in Figure 6.7.

6.2. Test results

With the measurements taken in the previous section, thrust performance results and efficiencies can now be calculated. For this, it is first shown which outputs are calculated and which inputs are used for each output. Next, the method to calculate confidence bounds for outputs is detailed, after which the confidence bounds for all independent measurement inputs is given.

6.2.1. Output calculation

The first output that is calculated is the experimentally measured thrust F_{exp} which is based on the change in actuator current from before thrust I_{start} to during thrust I_{mid} to after thrust I_{end}. The two separate baseline current measurements are used to see if any drift in pendulum position has taken place during the thrust period. The average difference, $\Delta I = I_{\text{mid}} - (I_{\text{start}} + I_{\text{end}})/2$, is used to calculate the thrust, and the spread of I_{start} and I_{end} is incorporated into confidence bounds. The actuator force difference between thrust and no thrust is then calculated using the slope a (equation (6.6)), which is subsequently multiplied by λ to arrive at the thrust force F_{exp}.

The second output is the specific impulse I_{sp}, which is calculated using F_{exp} and the experimentally measured mass flow $\dot{m}_{\text{exp}}$ [kg s^{-1}] as well as the standard gravitational acceleration $g_0 = 9.806\,65\,\text{m s}^{-2}$ (see equation (4.6)). $\dot{m}_{\text{exp}}$ is measured by a mass flow sensor which has a 0 to 5 V output, corresponding to a standardised volume flow of 0 to 2000 sccm (standard cubic centimetres per minute). This can be converted to a mass flow using the specified standard conditions, in this case a pressure of 1013.25 mbar and a temperature of 0 °C as found in the component manual. For N_2 this results in a standard density of 1.250 077 kg m^{-3} [6], so that 1 sccm equals $2.083\,462 \cdot 10^{-8}$ kg s^{-1}.

Modelled versions of F, I_{sp} and $\dot{m}$ are also calculated based on the equations from section 4.2. Both the ideal values from IRT and the modelled values with losses are calculated using the measured thrust chamber pressure p_{c} and temperature T_{c}, the vacuum chamber pressure p_{a}, and measured nozzle geometry. T_{c} is assumed to be the same as the interface temperature for these cold gas tests, based on an assumed thermal equilibrium between the interface, the propellant and the surroundings.

For comparison purposes, the throat Reynolds numbers for the modelled and measured outputs are computed. For both versions of Re the measured throat dimensions are used together with T_{c} for evaluating the propellant viscosity at throat conditions (via equation (4.11) for T_{t}). The modelled version uses $\dot{m}_{\text{model}}$ though, whereas the one for measured values uses $\dot{m}_{\text{exp}}$. This way, all modelled values depend on the controllable inputs p_{c} and T_{c}, and not on F_{exp} or $\dot{m}_{\text{exp}}$. The model then shows thrust predictions when neither F_{exp} nor $\dot{m}_{\text{exp}}$ can be measured, as would be the case on board of a small spacecraft.

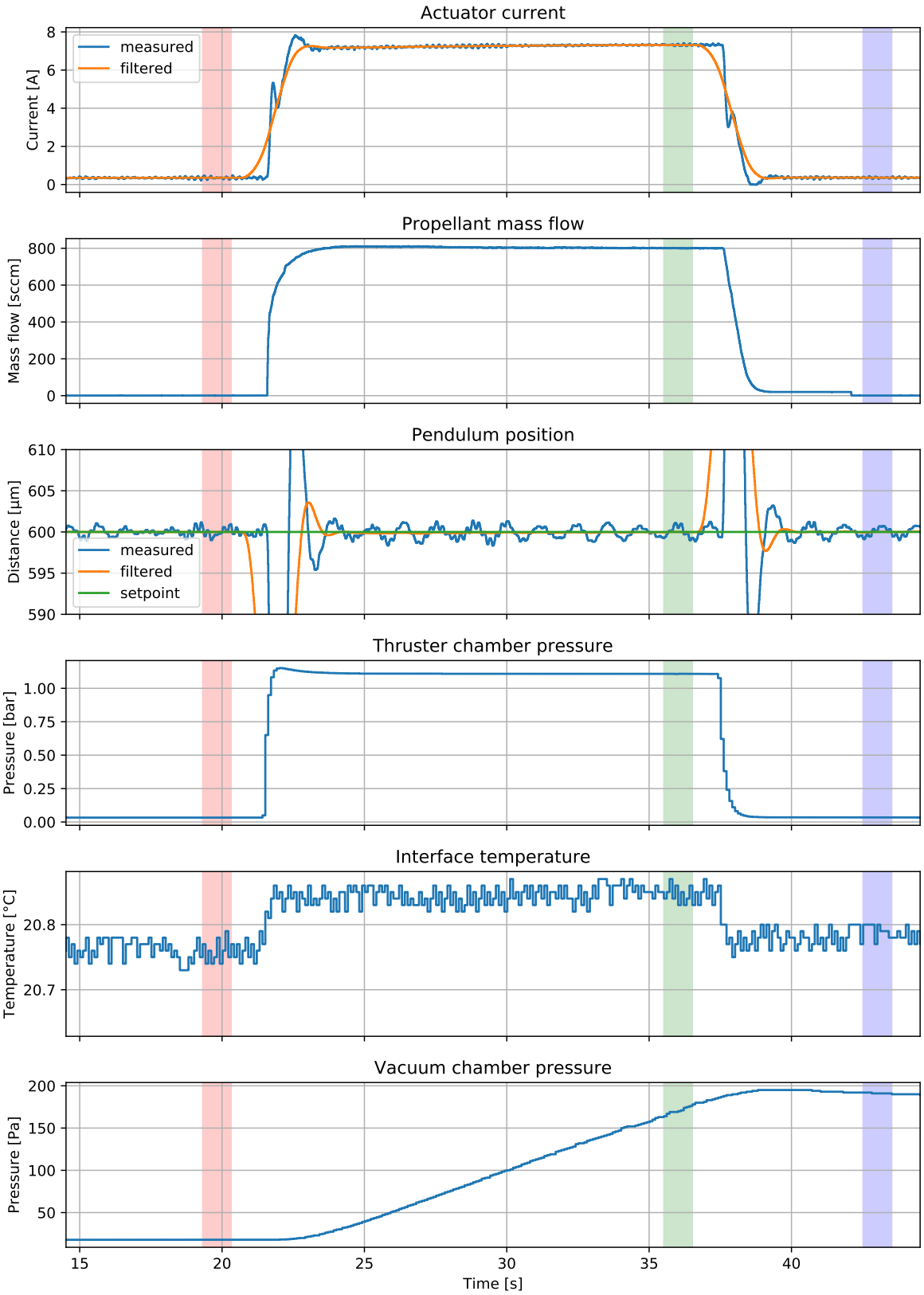

Figure 6.7: Measurement results from cold gas test TTC-1.1 for all time-varying signals used. Filtered signals are also shown if they were used for calculations. Windows for time-averaging of signals are indicated with red, green and blue regions for before, during and after thrust measurements, respectively.

In total the following input-output relations are thus used, with f_x indicating a generic function and $\mathcal{G}$ indicating measured nozzle geometry:

$$\begin{aligned} F_{\text{exp}} &= f_1\left(I_{\text{start}},\, I_{\text{mid}},\, I_{\text{end}},\, \lambda,\, a,\, \mathcal{G}\right) \\ I_{\text{sp,exp}} &= f_2\left(I_{\text{start}},\, I_{\text{mid}},\, I_{\text{end}},\, \lambda,\, a,\, \mathcal{G},\, \dot{m}_{\text{exp}}\right) \\ \text{Re}_{\text{t,exp}} &= f_3\left(\dot{m}_{\text{exp}},\, T_{\text{c}},\, \mathcal{G}\right) \\ F_{\text{model}} &= f_4\left(p_{\text{c}},\, T_{\text{c}},\, p_{\text{a}},\, \mathcal{G}\right) \\ I_{\text{sp,model}} &= f_5\left(p_{\text{c}},\, T_{\text{c}},\, p_{\text{a}},\, \mathcal{G}\right) \\ \text{Re}_{\text{t,model}} &= f_6\left(p_{\text{c}},\, T_{\text{c}},\, \mathcal{G}\right) \end{aligned}$$

Lastly with these values, the specific impulse efficiency ξ_{F} and the discharge coefficient C_{D} for both the modelled performance and measured performance can be calculated:

$$\xi_{\text{F,model}} = \frac{I_{\text{sp,model}}}{I_{\text{sp,ideal}}}, \qquad \xi_{\text{F,exp}} = \frac{I_{\text{sp,exp}}}{I_{\text{sp,ideal}}}$$

$$C_{\text{D,model}} = \frac{\dot{m}_{\text{model}}}{\dot{m}_{\text{ideal}}}, \qquad C_{\text{D,exp}} = \frac{\dot{m}_{\text{model}}}{\dot{m}_{\text{ideal}}}$$

6.2.2. Output confidence bounds

All sensors used in these experiments have some finite level of accuracy, which essentially gives a range of values that a measured quantity may be in reality, given that a sensor reports a certain value. Sensor accuracy is here taken to be equivalent to confidence bounds of the reported value, which is normally given with a confidence level (how likely it is the actual value is within the given range). Most sensor manufacturers do not provide strict confidence levels, only figures such as the "typical" and "maximum" accuracy. Here, the worst case accuracy is then used which is assumed to be for a $\pm 3\sigma$ confidence level (3 standard deviations σ above and below the reported value), or a confidence level of roughly 99.7 % in the case of normally distributed data.

The accuracy of sensors is assumed to be due to random *systematic* errors, originating from e.g. calibration of the individual device, and is thus tied to the specific hardware being used. This type of error thus cannot be negated by taking multiple measurements with the same sensors. Noise on top of sensor signals is taken care of with aggressive filtering and averaging and therefore does not need to be included in this analysis. Here it is discussed how confidence bounds are propagated from independent inputs to calculated outputs with the next subsection going into the confidence bounds of the inputs themselves.

For propagation of confidence bounds a simple linearised approach is used [62], with the assumptions that all measurement errors of calculation inputs are random, independent from one another, and relatively small compared to any non-linearities in the calculations. Given a generic function $f\left(\mathbf{x}\right)$ with the elements of vector $\mathbf{x} = [x_1,\, x_2,\, \cdots,\, x_{\text{n}}]$ as inputs with corresponding independent standard deviations σ_{x_1} through $\sigma_{x_{\text{n}}}$, the resulting standard deviation of f, σ_f, can then be calculated with the following equation:

$$\sigma_f = \sqrt{\left(\sigma_{x_1} \left.\frac{\partial f(\mathbf{x})}{\partial x_1}\right|_{\overline{\mathbf{x}}}\right)^2 + \left(\sigma_{x_2} \left.\frac{\partial f(\mathbf{x})}{\partial x_2}\right|_{\overline{\mathbf{x}}}\right)^2 + \cdots + \left(\sigma_{x_n} \left.\frac{\partial f(\mathbf{x})}{\partial x_n}\right|_{\overline{\mathbf{x}}}\right)^2} \tag{6.10}$$

σ_f is thus taken to be equal to the root sum square of the input variances $\sigma_{x_{\text{i}}}$ multiplied by the partial derivatives of $f\left(\mathbf{x}\right)$ to their respective input x_{i}, evaluated at the central measurement point $\overline{\mathbf{x}}$. In this case, 3σ confidence bounds are used for inputs and outputs, for which the same equation above can still be used by just multiplying all different instances of σ by 3.

This equation is exact if f is linear for all inputs x_{i}, and is reasonably accurate for small $\sigma_{x_{\text{i}}}$ and somewhat non-linear f. It also always results in symmetric confidence bounds. Confidence bounds for most inputs here are on the order of ± 1 % with the geometry having the highest uncertainty at around ± 10 %, with all performed calculations being reasonably linear around the input values found. Based on this, the method described here is seen as a reasonable way to calculate confidence bounds for the calculated outputs described in the previous subsection.

For simple functions, the partial derivatives can be worked out by hand quite easily, which is also done for a few basic instances here. For most outputs from the previous subsection however, the analytical expressions would be very long, difficult to derive. In many cases these would even be impossible to find due to the use of numerical root finding methods and database lookups within the calculations for finding p_e, γ and μ. To get around this issue, a forward finite difference approximation for the derivatives is used instead:

$$\left.\frac{\partial f(\mathbf{x})}{\partial x_i}\right|_{\overline{\mathbf{x}}} \approx \frac{f([\overline{x}_1, \cdots, \overline{x}_i(1+\delta), \cdots, \overline{x}_n]) - f(\overline{\mathbf{x}})}{\overline{x}_i \delta} \tag{6.11}$$

Here a relative step size of $\delta = 10^{-5}$ is used, small enough to be accurate, but not so small that the finite resolution of the internal numerical methods causes issues. The method implementation was verified with an intermediate calculation value, namely D_h, which depends on several of the geometry inputs in a simple way. This allows for analytical derivatives to be worked out. The numerical and analytical results were compared and found to be within 0.002 % of each other for all inputs that affect D_h. The same verified code was also used for other input-output relations as well.

6.2.3. Measurement confidence bounds

Here the confidence bounds of the independent measurement inputs are laid out. With all of these signals the quantisation error due to conversion to a digital signal is negligible compared to other error sources, and thus not taken into account.

For all time-varying signals recorded during thrust testing average values from specific time windows are used as described before. This does give rise to a form of uncertainty/accuracy in that the signal may vary during this time period, spreading out the measured point slightly. For a clear example, see the vacuum chamber pressure in Figure 6.7. The effect is taken into account by computing the standard deviation of the data samples within the time window and adding triple this value to the sensor's original accuracy (root sum square, following equation (6.10)). Noisy or slightly oscillating data (only the actuator current in this case) is first filtered with the 100 sample forward and backward moving average filter mentioned earlier, before computing the standard deviation, to disregard effects from noise and constant pendulum oscillations.

First up for measurements is the current from the Delta Elektronica SM-7020-D power supply [16] to the magnetic actuator. This was calibrated for force output together with the magnetic actuator, so that its accuracy is incorporated fully into the current-force relation (equation (6.6)) Its zero offset is also of no concern as only *differences* in current are used, and repeatability errors are assumed to be negligibly small, as no mention of them was made in the device manual. What *is* incorporated is the spread of the input data from using three average current values to arrive at a single input current difference, $\sigma_{I_{start}}$, $\sigma_{I_{mid}}$ and $\sigma_{I_{end}}$. The difference between the no-thrust current before I_{start} and after thrust I_{end} is also added to the confidence bound, using the difference between either value and their mean as 3σ bound. This brings the total uncertainty for the measured current to the following:

$$\Delta I = I_{mid} - (I_{start} + I_{end})/2$$

$$3\sigma_{\Delta I} = \sqrt{(3\sigma_{I_{mid}})^2 + \left(\frac{3}{2}\sigma_{I_{start}}\right)^2 + \left(\frac{3}{2}\sigma_{I_{end}}\right)^2 + \left(\frac{I_{start} - I_{end}}{2}\right)^2}$$

Values for these parameters vary per test, but the resulting output $3\sigma_{\Delta I}$ was always between 0.005 and 0.014 A or between 0.075 and 0.15 % of ΔI.

For calculating the force from ΔI, two equations/values with confidence bounds have already been derived: equation (6.6) for ΔI to F_{act} and λ for F_{act} to F_{exp}. One more aspect has to be taken into account for this, which is the alignment of the thrust direction relative to the pendulum rotation axis. This alignment is performed manually and estimated to have a maximum misalignment angle of $\phi = 2°$. The conversion factor between measured thrust force and actual thrust force is then $1/\cos(\phi)$. This relation is slightly problematic for the linearised error approach however, as the derivative of this factor is 0 at $\phi = 0$. The actual thrust can also only ever be lower than measured thrust as the relation has a maximum at $\phi = 0$. The change in measured thrust from this misalignment angle is furthermore only

0.06 %, an order of magnitude less than that from e.g. the ΔI to F_{act} relation. With this all in mind it was decided to leave out the uncertainty due to thruster misalignment.

The Brooks MS5850S mass flow sensor is somewhat simpler regarding accuracy. If it has recently been calibrated (as is the case here [19]), and has been allowed to warm up for the recommended period of 45 min, its accuracy is specified to be 0.7 % of the measurement value with a minimum of 0.2 % of its full scale at low flows (i.e. 4 sccm, or 0.08 mg s^{-1})[2]. Additional uncertainty due to the reading out the sensor over an analog 0 to 5 V line with a National Instruments PCI-6229 DAQ is assumed to be negligible compared to the specified accuracy.

The pressure in the thrust chamber is measured with a TE Connectivity MS583730BA pressure sensor [63], which has an internal analog to digital converter. It communicates its values digitally over an I^{2}C bus, thus its accuracy is fully determined internally. This has a specified maximum accuracy which depends on the measured pressure and temperature. For this project, only the 0 to 6 bar pressure range is of interest, for which the accuracy is $\pm$50 mbar if the temperature of the sensor is between 0 and 40 °C, or $\pm$100 mbar in the extended temperature range of $-$20 to 85 °C. For cold testing only the lower temperature range is of importance, while for hot testing the higher temperature accuracy may start to play a role. There are no additional uncertainties from pressure drop estimation from the place of measurement, as the sensor port is positioned directly upstream of the nozzle convergent section.

The same sensor used for measuring the thrust chamber pressure also includes a temperature sensor used for measuring the ambient temperature, which is assumed to be equal to the propellant temperature for cold gas testing. For pressures between 0 and 10 bar, the accuracy once again depends on the sensor temperature. At roughly room temperature, 25 °C, the accuracy is $\pm$1.5 °C, in the range 0 to 60 °C it is $\pm$2 °C, and between $-$20 and 85 °C it is $\pm$4 °C. Only the room temperature accuracy is used for cold gas testing.

The vacuum chamber pressure is measured with a Vacuubrand VSP 3000 Pirani pressure sensor [66]. This has an accuracy of $\pm$15 % of the measured value if this value is below 1000 Pa, for higher pressures no accuracy statement is made. The DAQ used to forward this measurement to the clean room PC, a Vacuubrand DCP 3000, does not add any noticeable error to this measurement.

A Pirani type pressure sensor relies on the thermal conductivity of the gas being measured, which differs for different substances at the same pressure. According to the manual [66], for the operating regime of this device the thermal conductivity at a certain pressure is primarily dependent on the mean molar mass of the gas. The device has been calibrated for air ($\sim$ 29 g mol^{-1}) at the factory and measurements with similar molar mass substances can thus be made with the standard accuracy specified. Examples given in the manual are O_2 (32 g mol^{-1}) and CO (28 g mol^{-1}), which means the measurements with primarily N_2 (28 g mol^{-1}) in the vacuum chamber from the thruster exhaust can use the standard accuracy. For possible future experiments with water as propellant (18 g mol^{-1}) some adjustments or re-calibration would be warranted though.

The pendulum displacement measurement from the Micro-Epsilon CS2 sensor is not directly used for measurements here, though it is used in the actuator current control loop. As a single distance is maintained throughout each test, only the (short term) repeatability and the accuracy with which the controller can maintain the position are then important. The repeatability for the specific demodulator (DL6230) and control unit combination (DT6220) are not specified on publicly available spec sheets. Similar devices have values downwards from 0.0003 % of full scale (2000 µm), i.e. 0.006 µm, which would be a negligible amount. This repeatability is thus assumed to be negligibly small.

For the accuracy with which the controller reaches its setpoint, the filtered distance signal is compared to the distance setpoint. The largest average deviation during the thrust window is roughly 0.1 µm, and for the pre- and post thrust window it is only 0.02 µm at maximum, with most tests having deviations several times smaller. To get an estimate of what this means for the accuracy of the measured thrust, the relation between thrust force and distance is estimated.

[2]The data sheet for this (old) model no longer seems to be available online, this accuracy figure was taken from the work of Bijster [8] who used the same hardware.

At the start of each test the pendulum is brought to its distance setpoint with an initial current. The difference in distance and current between the starting state and the controller on state is used to derive an estimated relation between pendulum distance and actuator current. A value of roughly 0.033 A µm^{-1} was found, which with equation (6.6) results in 0.0027 mN µm^{-1} (actuator force). This is quite close to the value of 0.011 mN µm^{-1} found by [41], when taking into account the factor 2.5 difference in used measurement range (2000 µm here versus 5000 µm for them). With this distance-force sensitivity, the positional accuracy found and the factor λ, the maximum deviation for the force measurement from this comes to around 0.005 mN. This is a negligible amount for the thrust magnitudes measured here, as well as compared to other force measurement errors and is thus not incorporated.

Measurement uncertainties with regard to geometry have already been discussed at the time of measurement in section 5.10 and are therefore not further elaborated on here.

6.3. Analysis of results

With all the equations, sensor accuracies and confidence bound calculations discussed thus far, the thrust performance results are calculated. These results are discussed here in steps. First some initial impressions are given regarding the data on its own. The cold gas thrust results are then compared to values from the reference thruster, and subsequently to model predictions.

Any additional results not shown here for e.g. model predictions and thrust coefficients are tabulated in Appendix B.2. Test results are numbered chronologically in groups of increasing pressure from TTC-1.1 to TTC-3.3 (Thrust Test Cold). Longer term reproducibility of the results, i.e. tests not performed in succession on the same day, is left for future work. This will only be possible for the later hot gas thruster though (chapter 8) as the thruster used here has already been disassembled for upgrading it to the heated version.

6.3.1. Initial impressions

When looking at the results on their own in Table 6.4 and 6.5, no immediately wrong aspects are apparent. All specific impulse efficiencies and discharge factors are below 100 %, and decrease with lower Re_t, as expected. In the same table it can also be seen that mass flow and thrust values increase with increasing thrust chamber pressure, and the steady rise in vacuum chamber pressure is in line with predictions based on chamber volume and the ideal gas law for the mass flows measured [68]. The magnitude of the measured thrust is also roughly between 10 and 15 mN as expected. In addition, subsequent tests at each input pressure have nearly identical results, showing good repeatability when the feed system pressure regulator is left unchanged.

Looking at the tabulated data, confidence bounds for values that rely heavily on the throat width are quite wide due to the relatively inaccurate measurement of this value. The measurement value with the largest uncertainty is C_D due to its dependence on $\dot{m}_\mathrm{ideal}$ which scales linearly with throat area, the least accurately known value. Reynolds values for measurements also have smaller confidence bounds due to them using the more accurate $\dot{m}_\mathrm{exp}$ and not $\dot{m}_\mathrm{ideal}$. Interestingly, Re_t based on throat width has smaller confidence bounds than that based on D_h due to w_t partially cancelling out of its equation ($w_\mathrm{t}/A_\mathrm{t} = 1/h_\mathrm{t}$). For some other values the uncertainty from w_t almost completely cancels out, for example $I_\mathrm{sp,ideal}$ and the I_sp efficiency are largely independent of throat size. For more accurately determining the discharge factor and throat Reynolds number in the future, a recommended first step would then be to measure the throat dimensions with higher accuracy.

6.3.2. Comparison with reference thruster

To reiterate, the data from Bayt used for comparison here can also be found in Appendix A. The values used for comparison will primarily be the efficiencies ξ_F and C_D at specific Reynolds numbers, which are all dimensionless quantities. This is done so that most direct scaling effects from nozzle size—for example seen in raw thrust and mass flow—don't have to be taken into account.

Two main things can be noted from the comparison in Figure 6.8. Firstly that C_D for the newly created thruster is consistently around (10 ± 10) % lower than that of the reference thruster, and secondly that ξ_F is consistently around (10 ± 5) % higher. The confidence bounds for C_D are relatively large and overlap with those from the reference design, making it difficult to say how much of the difference between these is just a result of measurement uncertainty. Even at the edges of the confidence bounds

Test name	p_c [kPa]	T_c [K]	p_a [Pa]	F_{exp} [mN]	$\dot{m}_{exp}$ [mg s^{-1}]	$I_{sp,exp}$ [s]
TTC-1.1	110.8 ± 5.0	294.0 ± 1.5	170 ± 28	10.430 ± 0.067	16.69 ± 0.12	63.74 ± 0.61
TTC-1.2	110.7 ± 5.0	294.1 ± 1.5	179 ± 28	10.439 ± 0.067	16.69 ± 0.12	63.77 ± 0.61
TTC-1.3	110.7 ± 5.0	294.1 ± 1.5	174 ± 27	10.431 ± 0.067	16.69 ± 0.12	63.74 ± 0.61
TTC-2.1	127.6 ± 5.0	294.2 ± 1.5	246 ± 38	12.165 ± 0.078	19.40 ± 0.14	63.94 ± 0.61
TTC-2.2	127.4 ± 5.0	294.2 ± 1.5	226 ± 35	12.155 ± 0.078	19.40 ± 0.14	63.90 ± 0.61
TTC-2.3	127.3 ± 5.0	294.3 ± 1.5	227 ± 34	12.142 ± 0.078	19.36 ± 0.14	63.95 ± 0.61
TTC-3.1	144.8 ± 5.0	294.3 ± 1.5	222 ± 37	13.959 ± 0.091	22.17 ± 0.16	64.20 ± 0.61
TTC-3.2	144.7 ± 5.0	294.4 ± 1.5	225 ± 38	13.956 ± 0.091	22.13 ± 0.16	64.30 ± 0.62
TTC-3.3	144.5 ± 5.0	294.4 ± 1.5	225 ± 35	13.927 ± 0.090	22.11 ± 0.15	64.22 ± 0.61

Table 6.4: Cold gas thrust test results.

Test name	$C_{D,exp}$ [%]	$\xi_{F,exp}$ [%]	Re_{t,exp,w_t} [10^2]	Re_{t,exp,D_h} [10^2]
TTC-1.1	85 ± 10	90.18 ± 1.00	33.69 ± 0.93	22.08 ± 0.25
TTC-1.2	85 ± 10	90.24 ± 1.00	33.69 ± 0.93	22.09 ± 0.25
TTC-1.3	85 ± 10	90.17 ± 1.00	33.68 ± 0.93	22.07 ± 0.25
TTC-2.1	85.7 ± 10.0	90.60 ± 1.00	39.1 ± 1.1	25.66 ± 0.29
TTC-2.2	85.8 ± 10.0	90.47 ± 1.00	39.1 ± 1.1	25.65 ± 0.29
TTC-2.3	85.7 ± 10.0	90.53 ± 1.00	39.1 ± 1.1	25.60 ± 0.29
TTC-3.1	86.3 ± 10.0	90.79 ± 1.00	44.7 ± 1.2	29.32 ± 0.34
TTC-3.2	86.2 ± 10.0	90.94 ± 1.00	44.6 ± 1.2	29.26 ± 0.34
TTC-3.3	86.3 ± 10.0	90.82 ± 1.00	44.6 ± 1.2	29.23 ± 0.33

Table 6.5: Cold gas discharge factor and specific impulse efficiency with corresponding throat Reynolds numbers.

of ξ_F on the other hand, the difference between the reference and new thruster is still 5 % at minimum.

This may be attributed to the small differences in design between the two thrusters such as the different aspect ratios, or may be due to experimental error that has not been accounted for. A main suspect here is the different pressure stiffening of the tubing coming from the pendulum, with higher pressure inside of it before and after, and lower pressure during firing. This effect was not investigated here further. The hot gas thrust tests did use a different tube geometry arrangement for comparison though, and several recommendations are given for future work at the end of this chapter to negate or investigate this possible effect.

In all, the criterion of ≥90 % I_{sp} efficiency of the reference design at the same throat Reynolds numbers has been met, and cold gas thrust functionality of the system has thus been verified.

6.3.3. Comparison with model predictions

Compared to the model predictions in Figure 6.9, regardless of using w_t or D_h for Re_t, the experimental values show higher ξ_F and lower C_D. The confidence margins for both model predictions are all quite small, due to them being relatively insensitive to their main input $Re_{t,model}$. Thrust and mass flow predictions on the other hand are much less accurate due to their direct reliance on A_t (Table B.4).

$C_{D,model}$ actually closes in on $C_{D,exp}$ when using w_t instead of D_h, though only a few percent. The confidence bounds for experimental values are quite wide though and overlap with the modelled values in both cases, but only just. How much of the difference between these values is due to either experimental or modelling errors is thus unknown and would require a more accurate measurement of the throat area and $C_{D,exp}$ for future study.

On the other hand, $\xi_{F,model}$ is actually closer to experimental values when using D_h—not w_t—which was also the case when comparing the model with the reference thruster. It is still quite a ways off though, underpredicting ξ_F by 13 to 15 % with D_h and 16 to 19 % with w_t. For this, the confidence

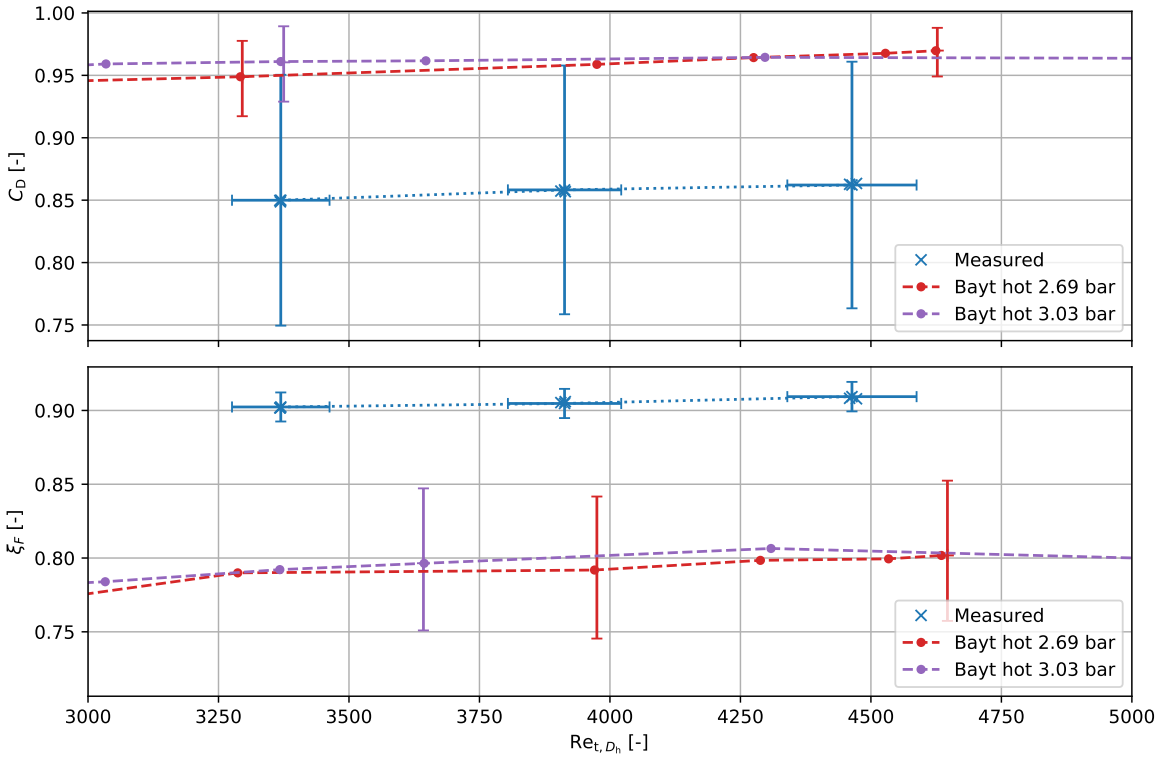

Figure 6.8: Comparison of discharge factor and specific impulse efficiency for the cold gas measurements from this project and the reference thruster by Bayt [4], with $\mathrm{Re_t}$ using D_h as characteristic length.

bounds of both values are quite small and do not overlap in the slightest. If all experimental errors have been accounted for, this difference can then only be attributed to model inaccuracy. It can also be seen that $\xi_{\mathrm{F,exp}}$ is actually closer to the IRT value than to either of the model predictions. The caveat here is that IRT overpredicts $\xi_{\mathrm{F,exp}}$ by 10 % while the model is much more conservative and underpredicts it by 14 %. Looking back at the earlier comparison of the model with the reference thruster (Figure 4.3 on page 36), the difference between the two was smaller at a 1 ± 6 to (10 ± 6) % underprediction. At the moment it is unclear what causes this difference in model prediction accuracy for these two similar thrusters, though the slight geometry differences and pressure stiffening may once again be looked into.

A further interesting point to note is that the predicted thrust with D_h is actually much closer to experimental values than the mass flow or specific impulse (see Appendix B.2). This can be attributed to the higher prediction of C_D essentially cancelling out the lower prediction of ξ_F. The good agreement between experimental and modelled thrust is therefore mainly considered to be a coincidence.

In total, contrary to what was found for the reference thruster, the chosen model with D_h thus does not provide a good (within 10 %) prediction of the specific impulse of the new design. Ideal rocket theory predictions are actually closer to experimental values, though still too optimistic by roughly 10 %. Results were inconclusive for the discharge coefficient, as the experimental value could be anywhere between 0 and 20 % lower than the model predictions. For C_D the model predictions were always closer to experimental values than IRT though.

6.4. Conclusion

Vacuum thrust tests were performed to verify the functionality of the new thruster design by comparison with experimental results from the reference design. Verification was concluded to be successful as the I_sp efficiency of the new design was roughly 13 % higher than that of the reference thruster at similar throat Reynolds numbers. Fabrication and testing of the heated gas version was thus commenced afterwards.

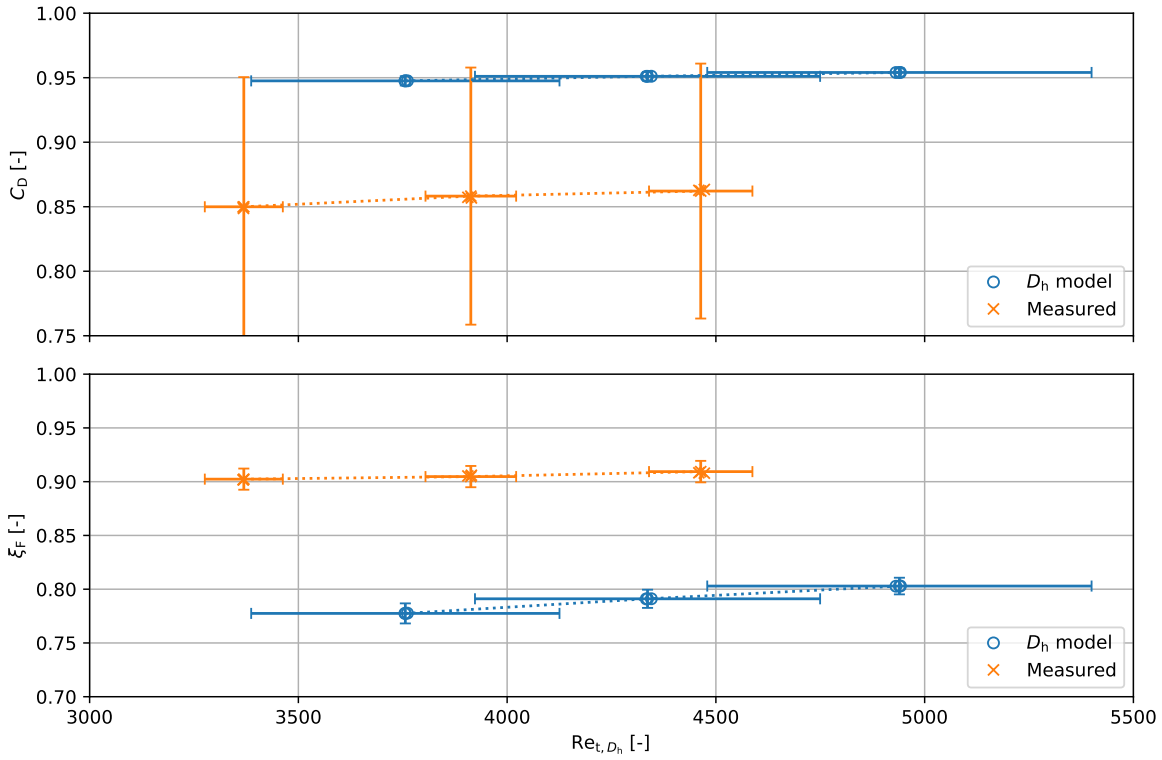

(a) $\mathrm{Re_t}$ with D_h as characteristic length.

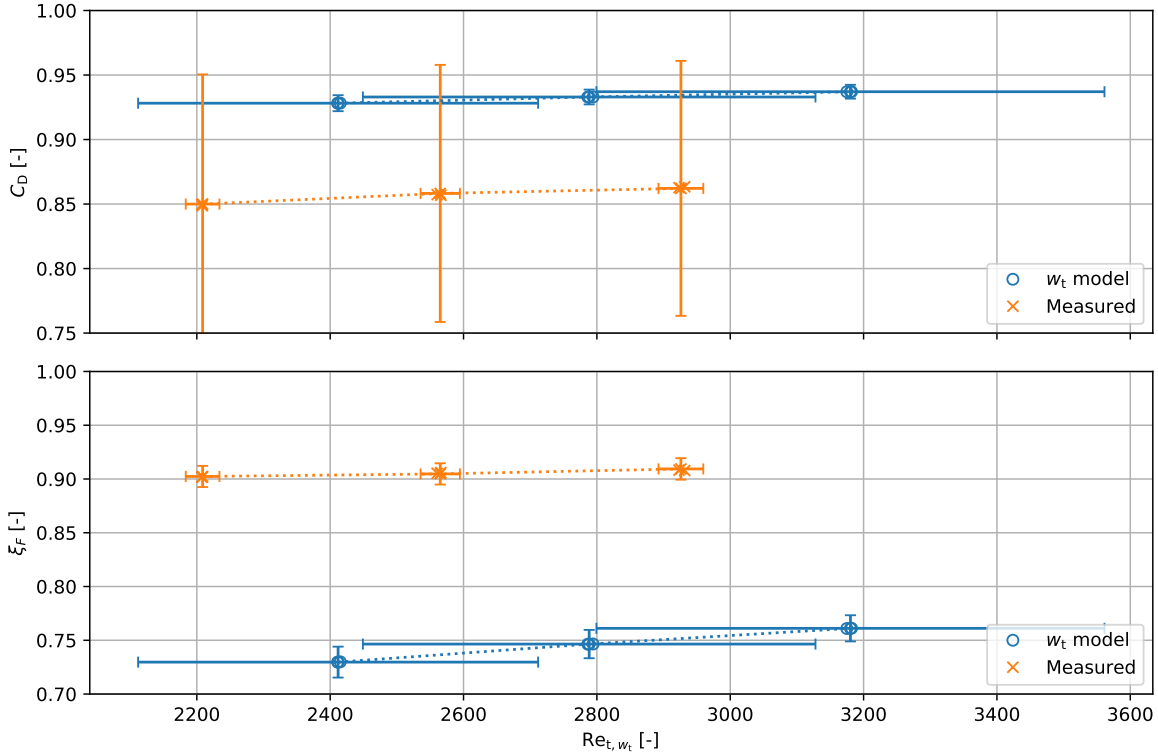

(b) $\mathrm{Re_t}$ with w_t as characteristic length.

Figure 6.9: Measured and modelled hot gas discharge factor and specific impulse efficiency.

The experimental results were also compared with predictions from the model shown in section 4.2. The discharge coefficient showed consistently lower experimental values than the model predicted, though the comparison was inconclusive due to large experimental uncertainty. The model with losses was always closer to the experimental values than IRT though. Specific impulse efficiency on the other hand was consistently too low by around 14 %, with IRT actually being somewhat more accurate. This only (optimistically) overpredicted experimental values by 10 %. Due to differences in C_{D} and ξ_{F} cancelling out, the predicted thrust was actually within a few percent of the experimental values. This is not seen as an indication of model accuracy though, but purely attributed to coincidence.

It is unknown at this point what may be behind the higher than expected experimental values of ξ_{F}. The cause may lie in the slight differences between the designs of the two thrusters, or the influence of pressure stiffening on the propellant tube connected to the thrust bench pendulum. Recommendations to negate possible effects from this last point are given in the next section, one of which is implemented for later hot gas thrust testing.

6.5. Recommendations

A number of recommendations for future work are given here, divided into two categories: hardware improvements, and future experiments.

6.5.1. Components and upgrades

As a first basic measure to possibly reduce the effects of pressure stiffening is to have the feed system tube connected to the pendulum in such a way that its contribution to overall system stiffness is minimal. This was also attempted for the later hot gas thrust tests in chapter 8, by routing the tube with a much more gradual curve in the plane perpendicular to the thrust direction. The addition of an electrically controlled pressure regulator for the propellant inside or very close to the vacuum chamber would also be recommended, which is discussed further in the next subsection.

For the magnetic calibration actuator it would be quite useful to have some form of alignment mechanism for the coil and magnet arm. Currently this entails aligning a rectangle to be in the centre of a circle by eye, which introduces some unknown uncertainty. A suggestion might be the use of crosshairs or distinct visual points on both components that can be lined up more easily in a visual manner, or with something like a laser-pointer.

The plastic base of the magnetic calibration actuator coil is also quite flexible, and is attached with regular bolts, making fine adjustment of its position and orientation a difficult and time-consuming process. It would be beneficial to re-make the plastic part of the actuator coil for increased stiffness and attach it onto an XYZ translational stage for simple fine adjustments of its position.

Lastly, it is recommended to add some kind of viscous-like damper to the pendulum. At the moment, the main limit for response time of the pendulum distance controller is the derivative / damping term, which cannot be increased without making the system unstable at this point. A physical damper does not suffer from the same issues encountered here such as signal delay and numerical differentiation instability. Adding a physical damper is then a simple way to increase the damping ratio of the system, allowing faster responses while also decreasing steady state oscillations. This could be implemented with an eddy-current damper [8] or a viscous vacuum-oil based device [12], for example.

6.5.2. Testing and procedures

Concerning the possible issue of feed tube pressure stiffening, it is recommended to perform tests to characterize the effect this has on thrust measurements, as the magnitude of this is currently unknown. This is hypothesized to depend on how the tubes are attached between the fixed frame and pendulum arm, as well as the pressure difference inside the tube between thrust and no thrust phases. A possibility to take this out of the equation entirely is to look into the use of an electrically controlled pressure regulator in the vacuum chamber. As this would be much closer to the sonic nozzle than the current regulator, it would allow for keeping the pressure nearly constant in the tubes during firing. As an added benefit, this can then also be used for easier, accurate on-the-fly feed pressure adjustments. This is currently very cumbersome due to the large unknown pressure drop from the current regulator to the nozzle and the very rough scale on the pressure gauge near it.

Another option to determine if pressure stiffening or any other unknown factor has had a major effect on results would be to test the thruster on a different thrust bench, e.g. at third party. This

may be expensive though, and would only give one point of comparison, leaving possible issue as an unknown factor for future testing of thrusters on TB-5m.

As a further point, the AG-245 scale could be calibrated once more for mass *and* force measurement, as this has not been done in several years. The scale can then be used more with more confidence regarding its reported values for calibrating the magnetic actuator. Recent actuator calibration measurements were still consistent with those from several years back though, suggesting the device has remained stable over the past few years.

There were also some issue with the mass flow sensor output remaining at 50 mV for a long time after a spike in the measured value, even when no flow was possible. The issue was resolved by re-zeroing the device, based on a suggestion by the manufacturer (Brooks). This artefact of the sensor can still be seen (with much reduced duration) in data from cold and hot testing in Figure 6.7 and 8.5, but can be ignored according to Brooks. If this is found to occur with longer durations in the future, the device can once again be re-zeroed.

Lastly, an in-depth comparison of the force compensation and calibrated distance measurement methods would also be warranted, to fully verify that both methods produce accurate results.

7

Hot gas thruster fabrication

With cold gas testing successfully concluded, the thruster could now be modified for hot gas testing. For this, first the steps that need to be performed are laid out in section 7.1. The partial disassembly of the cold gas thruster is then discussed in section 7.2 Next, the individual components that are newly manufactured or ordered are discussed individually in sections 7.3 through 7.5. Following this, the brazing of the thruster tubing and the remaining re-assembly is detailed in section 7.6 and 7.7 respectively. Similar to the chapter on cold gas thruster fabrication, characterization of the nozzle geometry is discussed in section 7.8 and leak testing of the assembled thruster in section 7.9. An updated comparison with the silicon VLM regarding production time and cost is then given in section 7.10. Lastly, the chapter is concluded in section 7.11 and recommendations are given in section 7.12.

7.1. Work overview

The work to be performed in this chapter was already detailed in the earlier chapter on cold thruster fabrication (Figure 5.1, page 62). Only a few steps of this larger overview remain, which are shown again in Figure 7.1 for clarity. The number of steps is much smaller, with steps also being shorter, so it was not seen as necessary to still use a Gantt chart here. The Kanban board from cold fabrication was maintained for keeping track of tasks though.

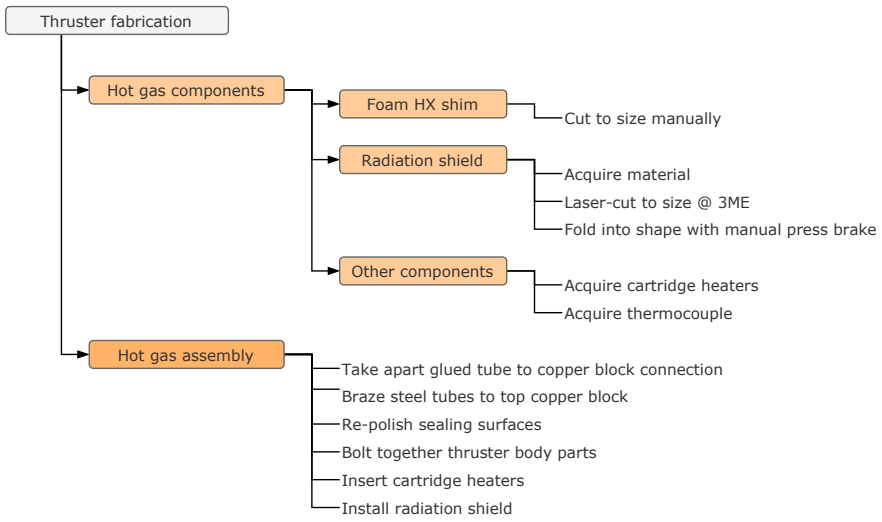

Figure 7.1: Work breakdown structure for modifying the cold gas system to the hot gas version.

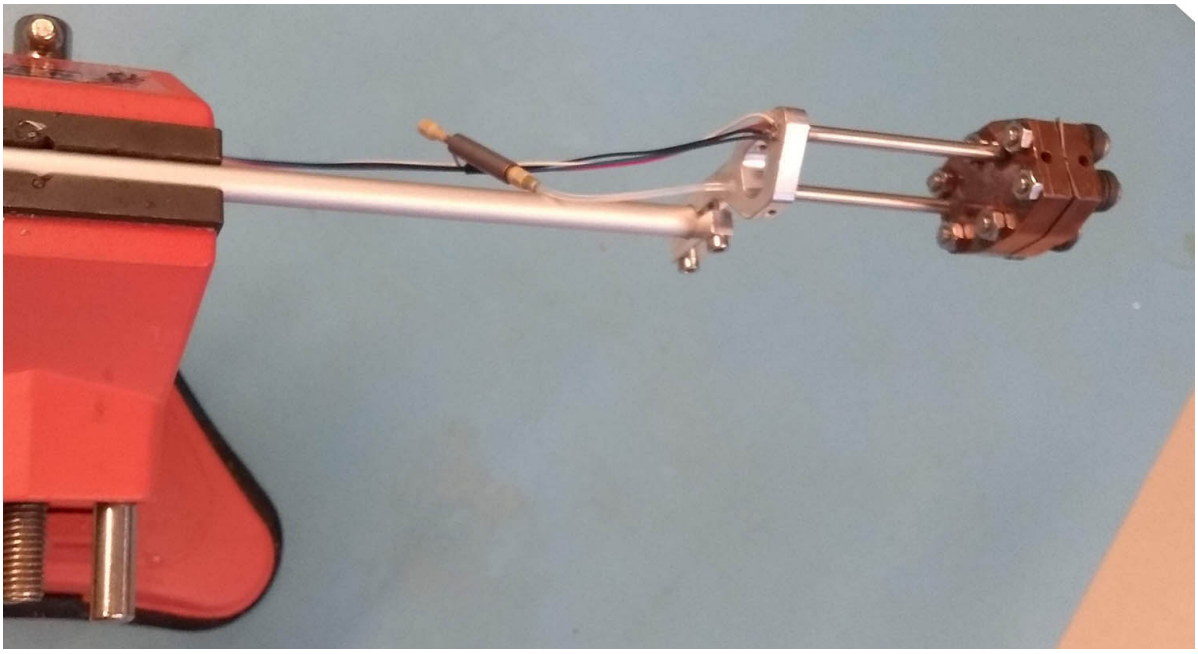

Figure 7.2: Setup for heating the thruster body to break the glued connection to the steel tubes.

7.2. Cold thruster disassembly

Some parts of the existing cold gas system have to be disassembled to allow for the necessary modifications to take place (as shown in the WBS, Figure 7.1). The bolted thruster body parts have to be taken apart to be able to insert the metal foam heat exchanger, and to make space for the tube brazing process. For the brazing of the steel tubes to the top copper block, the glue that is currently holding this joint together has to be removed.

Undoing the glued connections was expected to possibly require some force, thus this was tackled first, so as to not expose the inside of the thruster during this process. For this, the heat gun from the SSE workshop was used to heat the glue to above its temperature rating of 100 °C, at which point the body would be gently pulled from the tubes.

There were two difficulties in this process. Firstly, there are three more connections with the same type of glue on the aluminium interface, roughly 5 cm from the ones that need to be disassembled. A pressure sensor with a maximum allowed continuous temperature of 85 °C is also in that same area. Luckily, the tubes have already been designed with thermal insulation in mind, and thus should keep heat away from the interface. To negate most convective heat transfer between the body and interface now that the system is not in a vacuum, the tubes were aligned horizontally and the heat gun was aimed at the thruster body from below, pointing away slightly from the interface.

Secondly, because of the high thermal conductivity of copper, it would be necessary to essentially heat up the entire thruster body to over 100 °C. This means that the body would be too hot to safely touch and should not be resting on a (plastic) table top. To overcome both these issues, the interface was clamped to a piece of 8 mm diameter aluminium tubing from the workshop, which was put in a vice. The whole system was thus floating horizontally over the table edge during heating, see Figure 7.2. The hot thruster body was then pulled off the tubes with a pair of pliers clamping onto the bolt ends (oven mitts could also be used), after which the body was allowed to cool on a metal surface for a few dozen minutes.

Next, the thruster body bolts were removed with a wrench and torx screwdriver, and the different components were separated and laid out on a table for visual inspection, see Figure 7.3. It can be seen that there has been some build-up of residue from the leak-finding fluid on the exterior of the copper blocks, the exposed areas of the nozzle profile and the polished copper surfaces at the nozzle expansion area. This may have influenced the thrust performance during previous cold gas tests, though the exact effect it may have had is currently unknown.

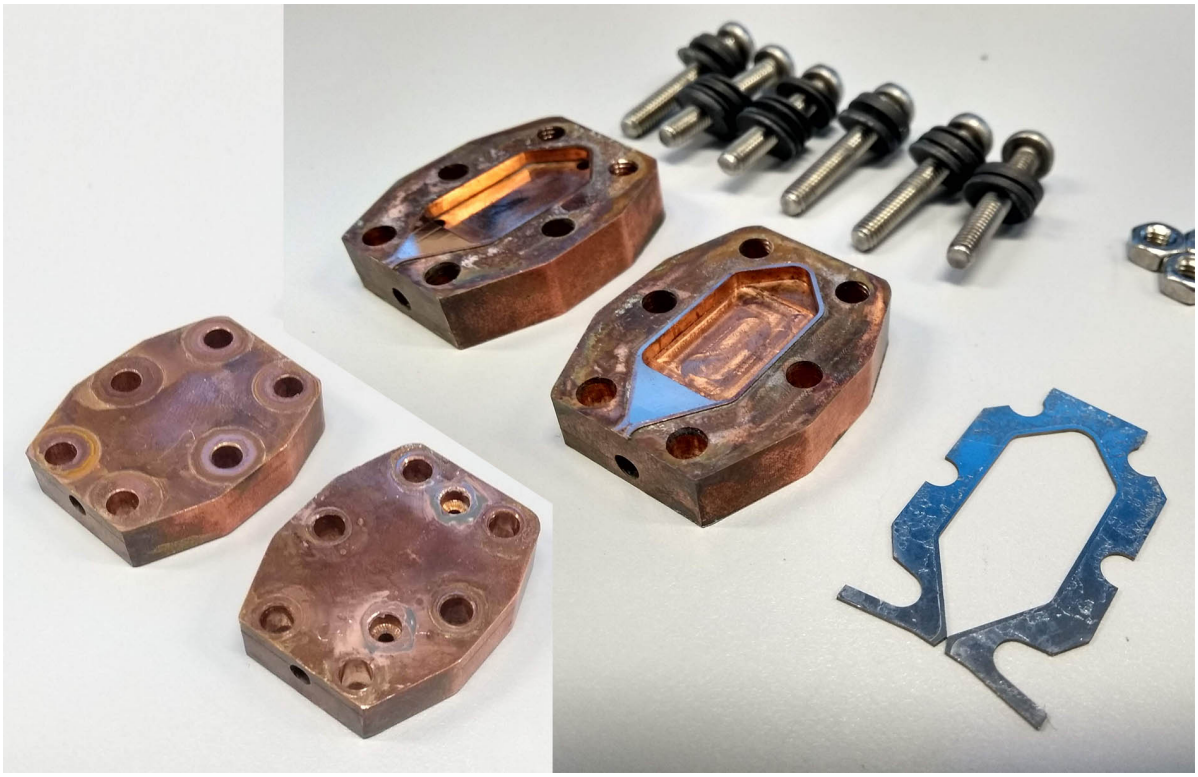

Figure 7.3: Disassembled thruster body outside (left) and inside (right) with the nozzle profile. Visible stains are due to the use of leak-finder fluid.

The residue on the copper blocks was cleaned off with the Unipol polishing compound, and remaining bits of glue were also removed. The residue on the nozzle profile plate was left there, for fear of affecting the nozzle geometry during polishing. The sealing surfaces on the copper were re-polished later, after the top section had been brazed, see section 7.6.

7.3. Thermal radiation shield

For insulation against radiative heat losses, a (thermal) radiation shield is placed around the thruster body. This consists of two pieces of aluminium sheet metal and two pieces of steel sheet metal, both first laser-cut and then bent into shape on a manual press brake.

The two types of sheet metal required, 0.5 mm thickness aluminium and 0.8 mm thick steel were gifted by a friend who still had some available. All four parts were laser-cut into the correct flat pattern at the 3ME faculty laser cutter, free of charge. After this, the parts were hand-bent into shape on a press brake in the D:DREAM hall. The four sheet metal pieces of the radiation shield can be seen in Figure 7.4, with the fully assembled shield being shown later as well in Figure 7.9. Due to the hand bending part of the process, some of the bends on the finished part have moved slightly (max. ~1 mm), resulting in some small gaps between parts of the shield in certain places. This may increase thermal radiation losses somewhat, as now more radiation can bypass the shield, though the gaps are considered small enough to not be an issue for now.

7.4. Temperature sensor

For cold testing, the propellant was assumed to be in thermal equilibrium with the environment, and thus the integrated temperature sensor on the chamber pressure sensor could be used, which is attached to the much cooler top interface. For hot testing, a separate thermocouple is used for measuring the actual thruster body temperature, which is rated up to 450 °C. Two of the TME KA02 K-type thermocouples, as previously selected, were ordered from Farnell[1], for €12 each (one for use, the other as a spare).

[1] nl.farnell.com (product code: 4920983)

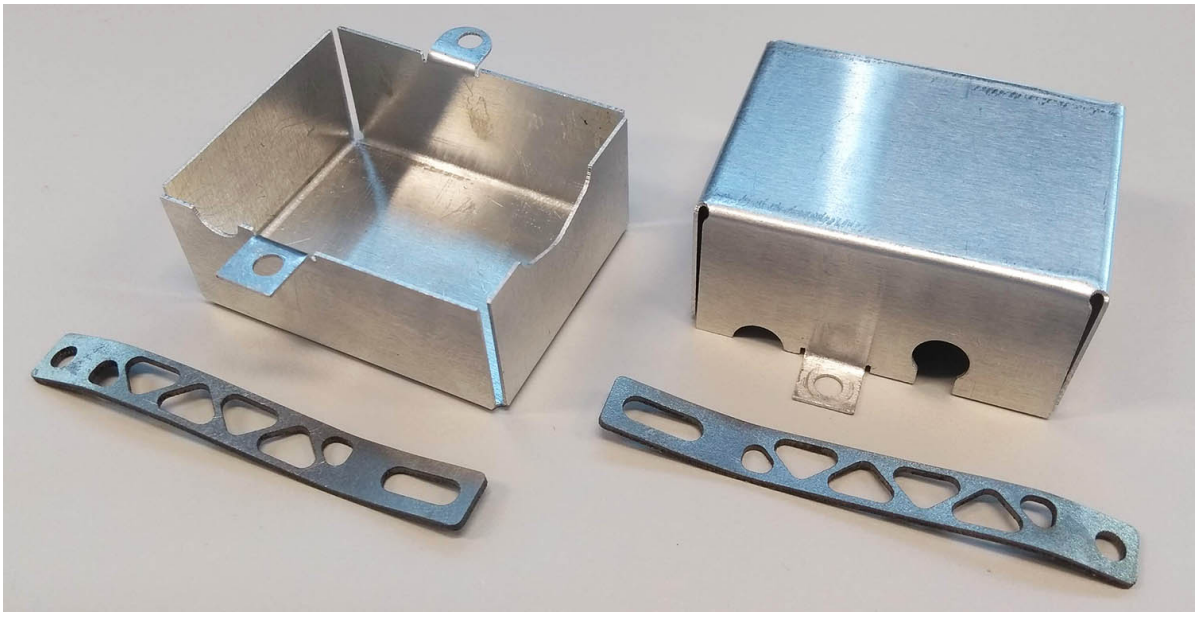

Figure 7.4: The finished custom radiation shield components.

As with the pressure sensors for cold testing, this was again done through Vidhya Pallichadath, with the components being available for other micro-propulsion projects later.

These sensors come with 1 m long cables and have been used in previous projects at the department. Interfacing and read-out equipment was consequently already available in the form of an NI 9211 thermocouple DAQ module (with compatible K-type female plug) in an NI USB-9162 USB dock for connecting to the clean room computer. Placement of the thermocouple is discussed later in section 7.7.

7.5. Cartridge heaters

For heating the thruster body, two Watlow FIREROD cartridge heaters were used, specifically $^1/_8$ inch diameter, 1 inch long versions with MGT wire (max. 450 °C) These were ordered from Kurval B.V., the distributor of Watlow parts in the Netherlands (component code: Frd. 2077-1380 Ø1/8”x1”). The heaters were €52.80 each (excl. VAT), with a handling and shipping fee of €15 for all orders under €200.

Kurval only allows orders from other businesses, so the order was placed through the university. Unfortunately somewhere in this process, the information that two of these items should be ordered was lost, resulting in only one heater being delivered after two weeks lead time. A second order was thus placed, which did unfortunately result in paying for the handling fee twice, and a delay of roughly two weeks before hot testing could commence. The long lead time of these components was known beforehand, so they were ordered as soon as the cold leak testing was found to be successful, limiting the delay on the project as a whole due to the late arrival of the second heater.

The heaters could basically be used out of the box, as they are essentially small power resistors with special packaging. Their wire ends were outfitted with male banana plugs in the SSE workshop though, see Figure 7.5, to make them compatible with the power pass-through unit in the vacuum chamber, which is outfitted with female banana plugs.

Two additional power supplies were also required to provide power to these heaters. With some experimentation, two more working units from Delta Elektronica were found in the clean room. These were an SM-7020 and an ES-030-10, which also shared the same analog interface as the SM-7020D that is used for the thrust bench magnetic actuator. With the knowledge that the NI PCI-6229 DAQ in the computer still had two analog output ports available, the two extra power supplies were connected to the PCI-6229 so that the heaters could be controlled individually from LabVIEW. The interface also provides feedback channels for monitoring the voltage and current, which were also connected to the PCI-6229 for data acquisition and live resistance estimation. The LabVIEW software part of the heater control is further elaborated in in the next chapter, section 8.1.

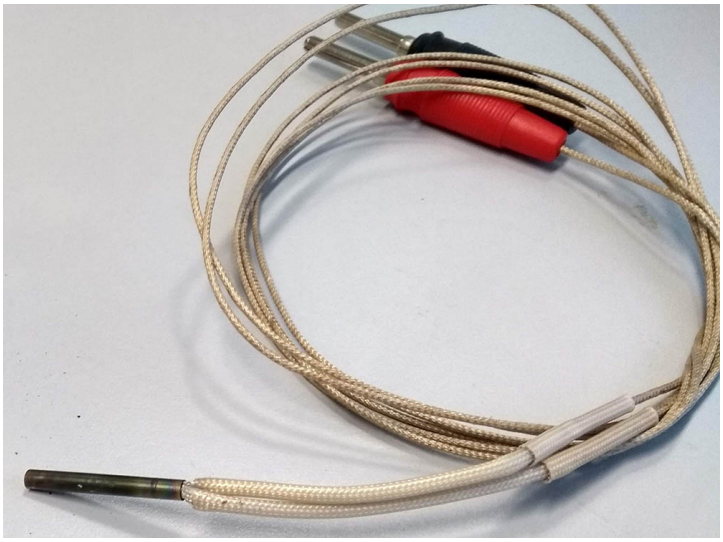

Figure 7.5: Top copper block cartridge heater (after first heating test) with installed banana plugs.

Contrary to the magnetic actuator PSU which uses current control, these were set to voltage control as this is more stable with temperature variations. Constant voltage control has some negative feedback from higher temperatures increasing the resistance, which decreases the dissipated power ($P_{\mathrm{el}} = V^2/R$), which slightly lowers the temperature again. The heater was also rated for a specific voltage (24 V) and power (30 W), not a current.

7.6. Steel tube brazing

The brazing of the steel tubes to the top copper block is discussed here separately, as it is more complex than the other assembly steps and required some finishing afterwards. The brazing was done at DEMO DASML (aerospace faculty) by Rob van der List[2] for €37. A standard gas torch was used, which introduced three issues.

Firstly, the steel tubes were still connected to the top interface, which was only allowed to be heated to around 85 °C as otherwise the pressure sensor could break and the glue might break down. The tubes could potentially be removed from the top interface and a new pressure sensor could be installed. This would leave the tubes as loose parts however, which would then have to be aligned to each other, the interface and the thruster body in some manner. The previous solution for alignment with glue, 3D-printed brackets, was not possible here due to the extreme temperatures involved.

To circumvent this alignment issue, Rob van der List suggested first wrapping the top interface in some wet cloth followed by layers of aluminium foil for insulation. This is the method that was used, as it kept the tubes aligned to each other and the interface during the brazing. Also, if something were to go wrong, components were at hand to fix the glue and sensor on the top interface.

Secondly, as mentioned, alignment of the thruster body to the steel tubes was still an open issue. As there was little play in the assembly to begin with, manual alignment was seen as acceptable in this case, which was left to Rob. What little play there was, was also around the line connecting the two bottom ends of the tubes. This is primarily in the direction of the exhaust and thus has little to no influence on thrust direction and thrust measurements.

Lastly, because copper is such a good thermal conductor, the *entire* top block had to be heated to the melting point of the brazing compound for the process to be successful. This resulted in a large amount of oxidation on the entire surface of the copper block, as it was heated to over 600 °C in an oxygen-rich atmosphere, see Figure 7.6. The sealing surface was cleaned up and re-finished with the same equipment at DASML used for polishing before. A longer period was spent with the largest grain size polishing compound to take off the relatively thick, tough oxide layer.

Polishing of the sealing surface was done for both top and bottom block until they visually had the same mirror-like finish as before the cold gas testing. This was assumed to have the same acceptable

[2] R.J.S.T.vanderList@tudelft.nl

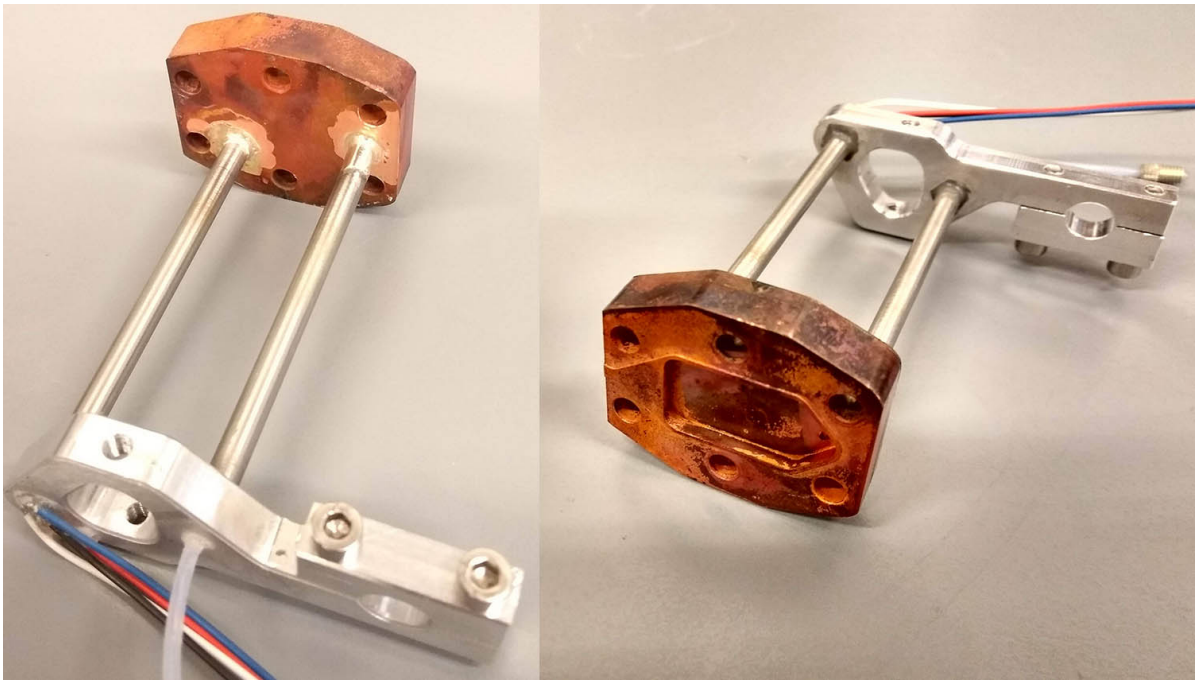

Figure 7.6: Top (left) and bottom (right) of the upper copper block after brazing. Non-oxidized lighter spots around the tubes are from the use of flux around the brazed joint.

surface roughness as that measured previously, and no further optical surface roughness measurements were performed. See Figure 7.7 for an impression of the surface finish on both blocks.

The Unipol polishing compound used to remove light staining before had no effect on the oxide layer elsewhere, and the DASML polishing machine could not reach most areas of the assembled block, as this was a flat spinning disk. The rest of the copper block was thus left in its oxidized state. The only detrimental effect of this is that this copper block now likely has a higher emittance, resulting in somewhat higher radiative heat losses. The design has enough spare heating power that this should not be an issue for this project though.

7.7. Further assembly

The rest of the thruster body re-assembly is similar to the process for the cold gas system. First the foam heat exchanger has to be inserted and the body aligned and bolted together, after which the additional thermocouple and radiation shield can be installed. The first part is the most crucial as this also affects how well the seal between the three metal parts performs.

For the insertion of the metal foam heat exchanger, a thin spacer had to be added to make sure the metal foam was compressed against both top and bottom blocks for effective heat transfer to the foam, see Figure 7.7. This was achieved by cutting small pieces of kitchen variety aluminium foil (13 µm thickness) with a pair of scissors and stacking these on top of each other between the foam and the bottom block. The spacing was checked intermittently by putting the foil stack and metal foam in place and carefully placing the two copper halves together *without* the nozzle profile, until the left-over space was just enough to slide the profile in between.

Alignment of the layers and bolting them together was then done in the same fashion as for the cold gas system (section 5.9). The layer alignment with two bolts and the installed thermocouple on the finished thruster (sans shield) can be seen in Figure 7.8. The tightening of the bolts was again performed simultaneously with a leak test, which is detailed later in section 7.9. Next, the thermocouple tip was squeezed in between the two copper blocks, so that it was lightly held in place by compression. Its wire was then guided along the front steel tube and attached to it with a small piece of tape on the cold side.

The last step was to install the radiation shield, which only requires four M3 bolts and two nuts. This is normally done only *after* the thruster is installed on the thrust test bench, to allow for measuring the

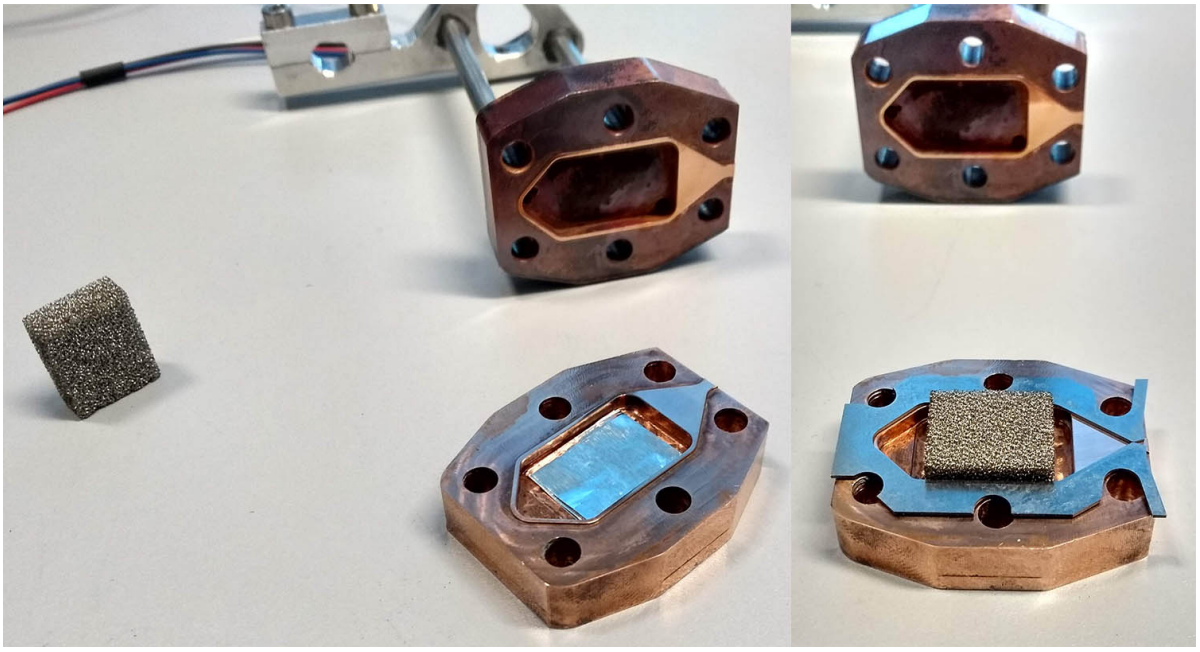

Figure 7.7: Re-polished copper blocks with aluminium foil spacer (left), nozzle profile, and metal foam (right) during assembly.

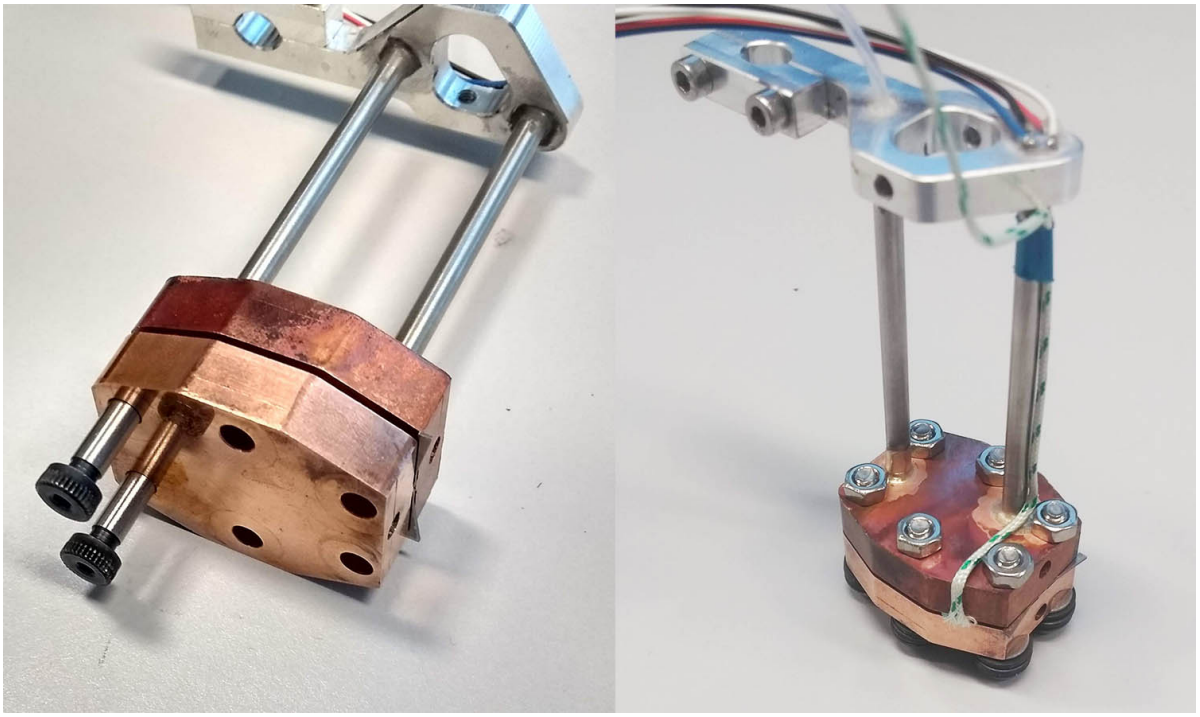

Figure 7.8: Thruster body layer alignment using shoulder bolts (left) and the fully re-assembled thruster with installed thermocouple (white-green sleeved cable) (right).

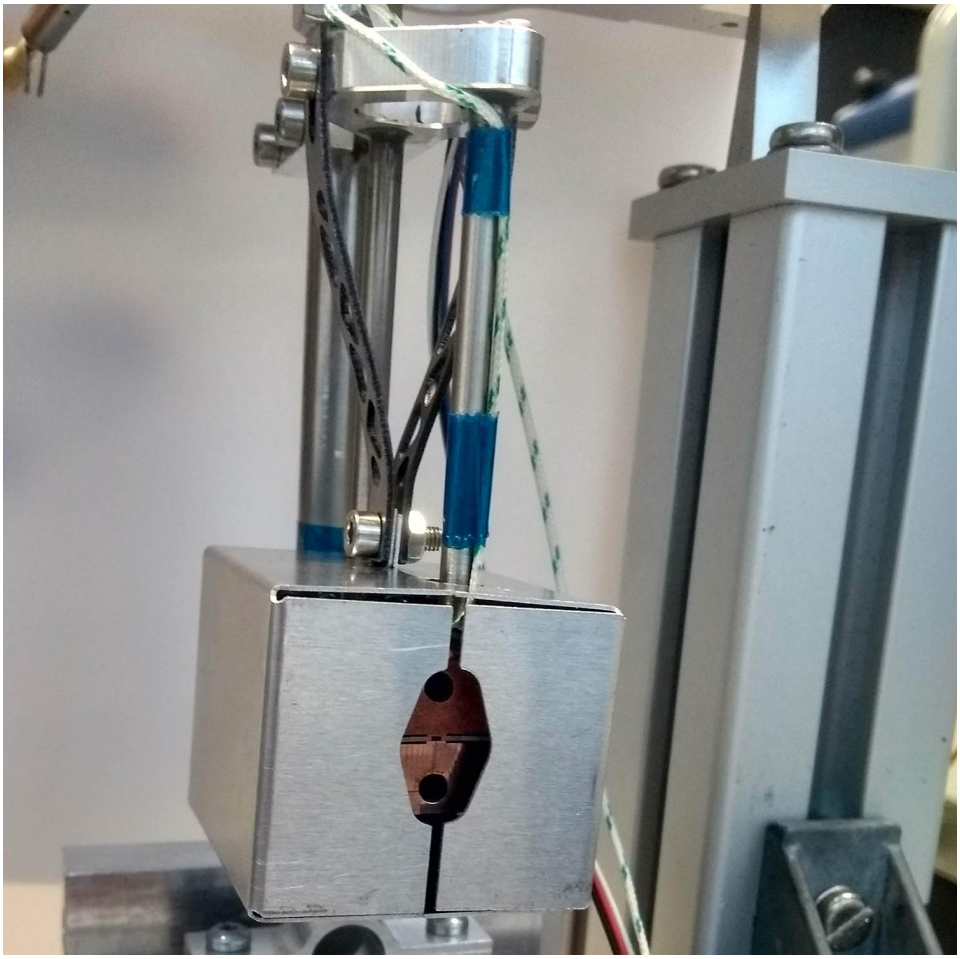

Figure 7.9: Thruster with thermal radiation shield installed. Lower piece of blue tape was only used to keep the thermocouple wire in place during shield assembly and is removed for hot testing.

thrust moment arm L_{thr}. Care must be taken to not dislodge the thermocouple cable when installing the left half of the shield. This was made easier by temporarily taping the cable to the steel tube near the top of the shield. The tape was later removed before testing commenced.

The position and height of the shield relative to the thruster body is manually adjusted so these do not touch one another. The adjustments are made by rotation of the bolted joints and translation of the topmost bolted connections through the slot in the shield connection bracket. The assembled thruster with heat shield, as installed on the thrust bench, can be seen in Figure 7.9.

The last components needed are the cartridge heaters, which are simply inserted into the holes at the front of the thruster body before the start of a test. These fit in their holes with relatively little friction, so they are primarily held in place by the stiffness of their relatively thick power leads.

7.8. Nozzle geometry characterization

The same nozzle profile (N0.5-01) was used in the hot gas system, thus most measurements to determine the nozzle geometry had already been performed during cold gas thruster fabrication (section 5.10). The nozzle profile has been taken out of the assembly and put back in though, thus the throat width may have changed from the cold gas version due to the nozzle profile compliance. The only new measurement that is then required is the assembled nozzle exit width $w_{\mathrm{e,as}}$. This time, the VR-5000 was set to its highest magnification for better accuracy, see Figure 7.10. This resulted in $w_{\mathrm{e,as}} = (1071.9 \pm 5.6)$ µm. The other values that were already known and those newly calculated with this measurement can be seen in Table 7.1.

The throat measurements are now closer to the design values, with reduced uncertainty compared to the ones found for the cold gas thruster (Table 5.4 on page 80). The conclusions regarding production

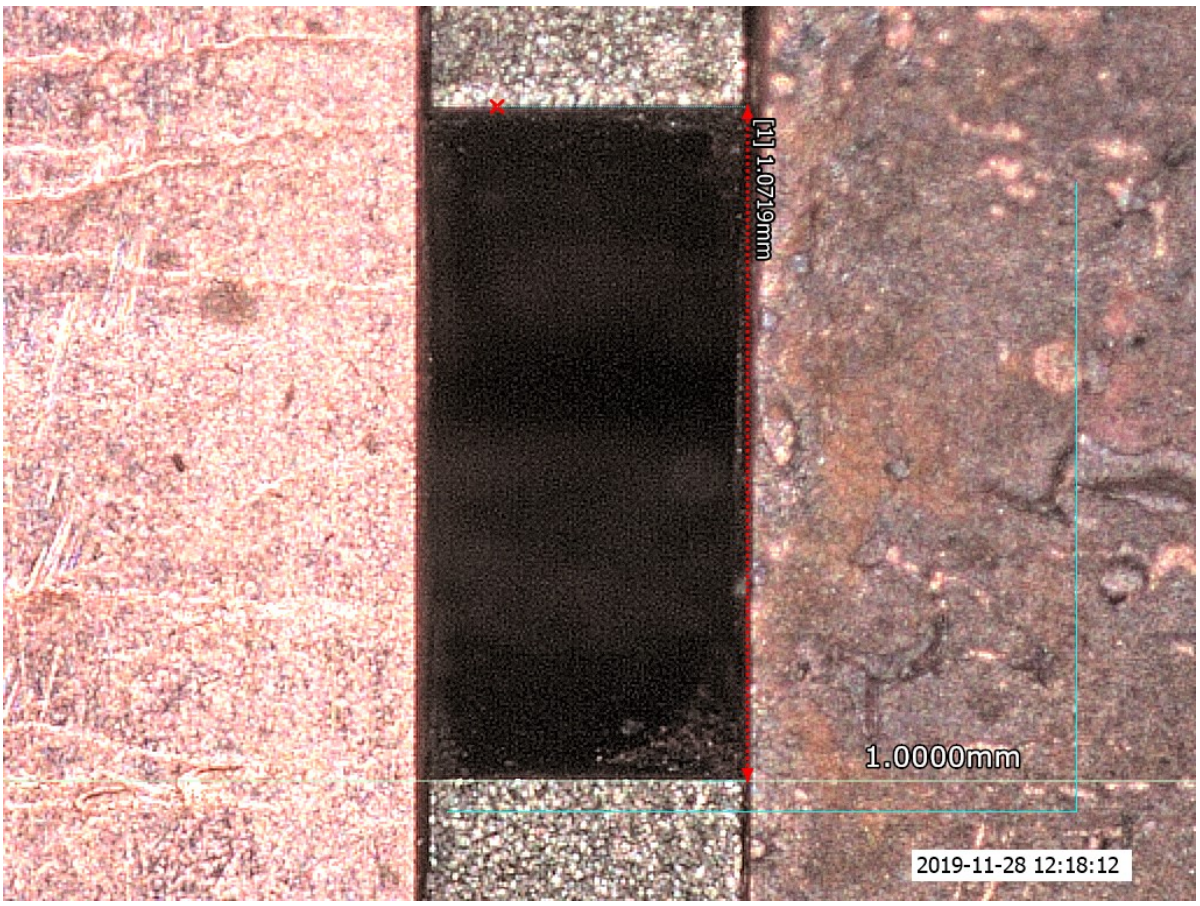

Figure 7.10: Image of the hot thruster nozzle exit area, with exit width measurement indicated.

Parameter	Unit	Symbol	Design value	Measurement	Difference [%]
Throat height	µm	h_t	500	496 ± 4	-0.8 ± 0.8
Throat width	µm	w_t	130	142.3 ± 9.6	$+9.5 \pm 7.4$
Throat aspect ratio	–	h_t/w_t	3.85	3.49 ± 0.24	-9.4 ± 6.2
Throat area	10^3 µm^2	A_t	65.0	70.6 ± 4.8	$+8.6 \pm 7.4$
Throat radius of curvature	µm	$r_{t,c}$	260	258 ± 20	-0.8 ± 7.7
Expansion area ratio	–	ϵ	8.25	7.53 ± 0.49	-8.7 ± 5.9
Nozzle exit width	µm	w_e	1072.5	1071.9 ± 5.6	-0.14 ± 0.52
Nozzle exit aspect ratio	–	h_t/w_e	0.466	0.4631 ± 0.0045	-0.7 ± 1.0
Divergent half angle	°	θ	20	20.0 ± 0.4	0.0 ± 2.0
Convergent half angle	°	ψ	35	35.0 ± 0.4	0.0 ± 1.1

Table 7.1: Design and measured values for parameters defining the shape and size of the nozzle (hot gas thruster).

accuracy from the cold gas thruster thus still stand (section 5.10), including how this compares to fabrication with silicon etching. The total manufacturing accuracy for the nozzle throat is now actually even better at just a (9 ± 7) % difference with the design for w_t, A_t, and aspect ratio. This may in part be due to the nozzle width actually being slightly smaller with this fresh installation, or it may have only shown up because of the higher accuracy measurement of $w_{e,as}$. The recommendations from section 5.14 for decreasing fabrication uncertainty of the nozzle throat size also still apply.

At the same time as the optical length measurement, a 3D surface measurement of the exit area was also made on the VR-5000 to inspect the alignment of the thruster body parts, see Figure 7.11. The top block can be seen to be at a slight angle compared to the bottom block and the profile sides, with the top surface of the nozzle sticking out a few dozen micrometers. This may indicate an issue

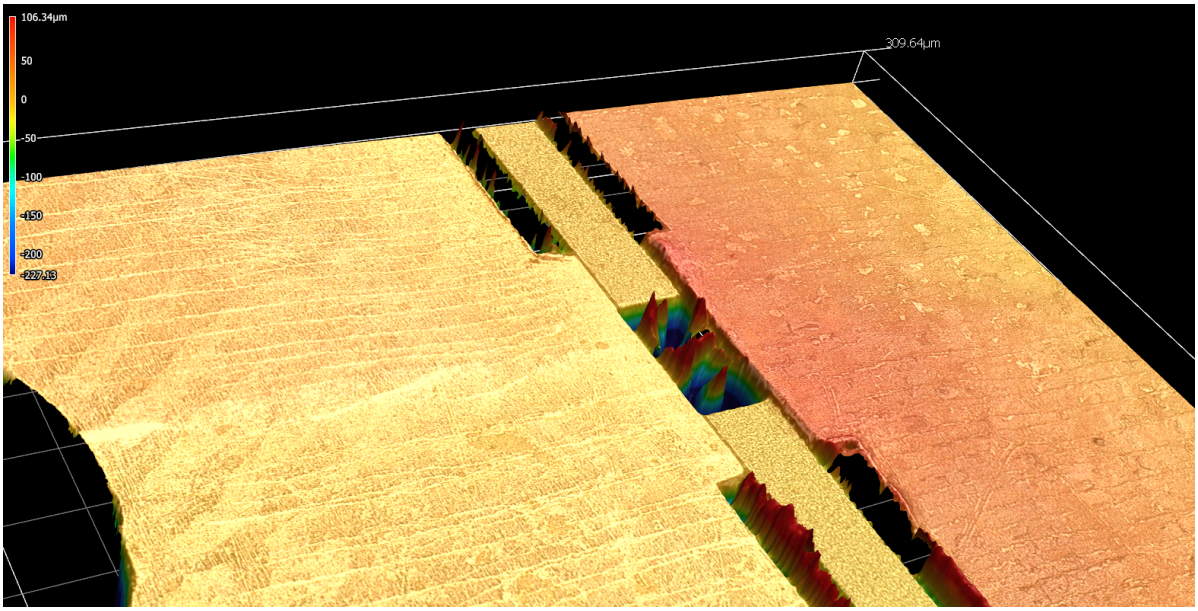

Figure 7.11: 3D surface measurement of hot thruster nozzle exit area.

with the sealing surface ridge, as the two blocks should be parallel.

7.9. Leak testing

The same approach as for the final cold gas leak tests was used here at first (section 5.11), though without using the leak-finder fluid. The same acceptance criteria are also used. Initial tests in ambient conditions unfortunately indicated much more severe leaking than with the cold gas system, namely in the order of 1 % of the total expected flow, not 0.01 %.

Unfortunately, even after tightening to the same final torque values as for the cold gas thruster, the leak persisted. Gas flow could be heard coming from the seal of the nozzle profile, based on which other possible less severe leak sources were not looked into until this main leak was fixed. The brazed connection was also visually seen to be fully leak-tight, with the brazing compound having spread and wetted around the entirety of both tubes. The glued parts had also not changed since cold testing.

A 1 % leakage flow would still be acceptable for the current project according to the criteria laid out for cold gas testing. This will then have to be taken into account when analysing the thrust test results though, and should be looked into for future designs on how to prevent such a leak. For acceptance without caveats, a leakage flow of <0.1 % was needed.

To get a more accurate measurement of this leak, so that it could better be accounted for with thrust test analysis, the conditions of the thrust tests were replicated more closely during the leak test. The setup was placed in the vacuum chamber to measure the mass flow under the same internal and external pressure conditions as what would be tested at. The high temperature could unfortunately not be simulated, as the rubber used for plugging the nozzle will break down below 400 °C. Estimated leakage mass flows based on measurements from two instances of this test can be seen in Figure 7.12. The cold gas mass flow for the leak is then around 0.20 mg s^{-1} at a chamber pressure of 1.4 bar.

The chamber pressure was set at the desired test pressure of 19.5 psi_a, but due to the needed filtering, no mass flow rates could be calculated for the highest pressures, as the transition was smoothed out. For this highest pressure region, a small extrapolation is used instead. This was based on a linear least squares fit with all available data from 2 tests for pressures over 1 bar, which should give a reasonable estimate of leakage flows between 1.2 and 1.5 bar chamber pressure.

Based on the cold gas measurement data (Table 6.4) and corrected for the new throat width, a leakage mass flow relative to the total nozzle flow of 0.91 % at 1.11 bar to 1.04 % at 1.45 bar is expected. Scaling with temperature is unknown and will depend on if the gas flowing through the leak reaches the thruster body temperature or if it is still cold when exiting. The worst case would then be a cold leak with fully heated gas flowing through nozzle. For sonic flow this would make the leak a factor

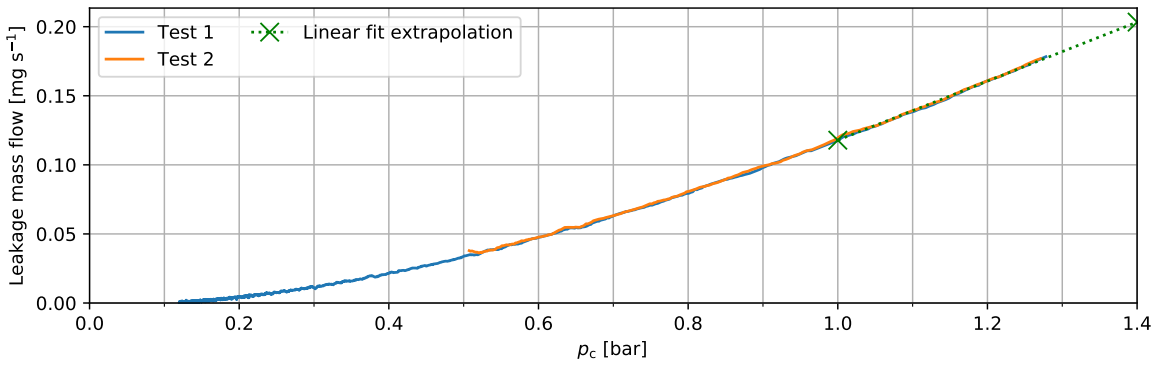

Figure 7.12: Estimated leak flow versus chamber pressure with a small extrapolation from a linear least squares fit of data with $p_c > 1$ bar.

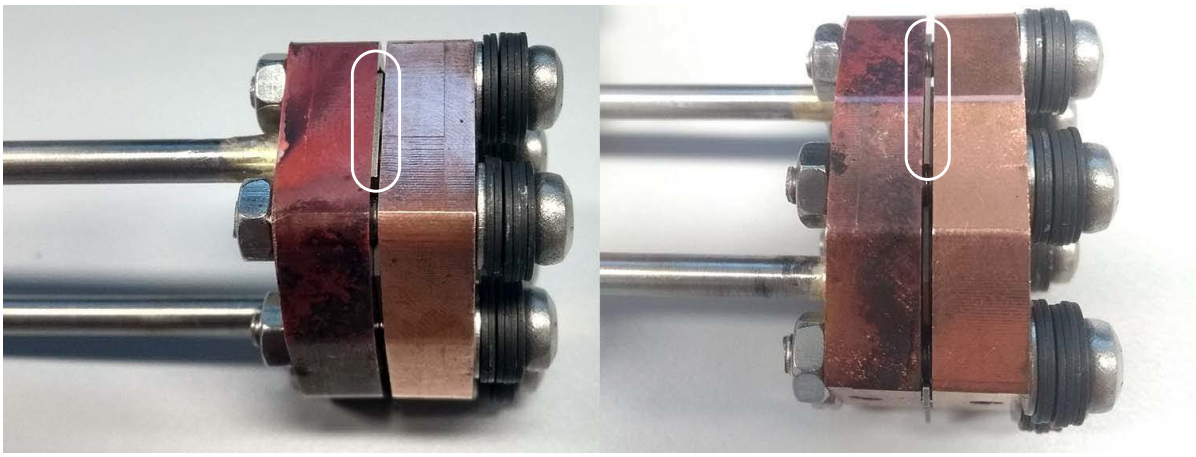

Figure 7.13: Side-view images of the hot thruster with areas indicated that show the gap between nozzle profile and top block tapering off towards the rear with both even touching at the very end.

$\sqrt{T_{\text{hot}}/T_{\text{cold}}} \approx \sqrt{700/300} \approx 1.5$ worse, approximately. Per the criteria set out, this potential leakage rate is considered acceptable (~ 1 %), but not excellent (<0.1 %). Some part of the re-installation and brazing process has thus resulted in degradation of the leak performance.

An option for fixing this issue during the project could have been to re-mill the sealing surfaces again, but the people who performed the CNC milling before were unavailable. It would also have been difficult with the tubes and interface still attached. Lastly it was unclear at this point if this strategy would have worked without giving both copper blocks identical heat treatments as well, to synchronize their material properties.

One current hypothesis regarding what may have caused this leak is that the brazing process resulted in only the top block undergoing a heat treatment, resulting in the two sealing surfaces having different hardness values. Tightening the bolts may then have caused one of the thin sealing ridges to stay intact and the softer one to collapse. Visual indications for this hypothesis can be seen in Figure 7.13, where the nozzle profile is clearly shown pressed against the top block, when a 0.3 mm gap should have been present. Another indication is the slope of the top block seen in Figure 7.11. This indicates either a slope in one or both surfaces before assembly or that one or both of the sealing surfaces became sloped during tightening. This hypothesis could be checked if / when the thruster is disassembled, though this will not be done here, as the system was still needed intact for a subsequent thesis project.

Component name	Total expenses [€]	Single new thruster (est.) [€]
Cold gas thruster	824	606
Cartridge heaters	136	0
Brazing	37	37
Temperature sensor	12	0
Radiation shield	0	5
Upgrade total	185	42
Total	1009	648

Table 7.2: Expenditures for hot gas thruster upgrades, excluding VAT, including shipping costs.

7.10. Cost and production time

As new components have been ordered and manufactured, an update to the cost and production time figures of the cold gas system from section 5.12 is given here.

An overview of all expenses incurred for this part of the fabrication is given in Table 7.2. Through the use of COTS heaters, brazed joints and a very basic radiation shield, costs have remained quite manageable. For the thruster in total the cost would have come to just 6 % over the given budget of €500, had the multiple nozzle fabrication mishap not occurred. As a note on the given cost for a new thruster in the table, the COTS heaters and temperature sensor can easily be reused for other projects as they are not permanently attached to the thruster.

It is basically impossible to say what costs and production time would be associated with manufacturing a similar hot gas version of the current silicon thruster as this has never been successfully used at the temperatures aimed for here. It can be seen though that the additional cost for heaters and brazing is relatively small compared to expenses for cold gas thruster machining and components. The previous conclusion for the cold gas system that the design has roughly the same unit cost and far batter batch cost compared to the silicon thruster is thus deemed to still apply.

Regarding production time, in general the fabrication here was a quick process, with the exception of the lead time for the cartridge heaters (which took 2 to 3 weeks to arrive). Ordered thermocouples can arrive the next day, brazing of the components can be done in an afternoon, and the cutting and bending of the radiation shield takes a day or two at most. If the heaters are ordered at the start of production though, their lead time can run in parallel with other component manufacturing (the heaters can be inserted just before testing) so that the entire production of a new thruster could be performed in 2 to 3 weeks. Overall, the upgrades were also relatively simple to execute. It must be noted though that most important fabrication steps needed for the hot gas upgrades to work had already been performed for cold gas thruster production.

7.11. Conclusion

Production was again completed in a timely fashion, with the longest lead time being 2 to 3 weeks for the cartridge heaters and other steps and components only taking a day or two each. In total, the project would have only been 6 % over its €500 budget, if not for the three extra produced nozzle profiles, which essentially doubled the expenses. It should be reiterated that this cost was still only possible through unpaid machining by friends, as another ∼€360 (possibly more) would have been needed otherwise. With the now available equipment and reusable parts, a cost of around €650 for a new device with the same design should be possible. Additionally, such a new device could then be created from scratch in around 2 to 3 weeks with the knowledge gained here. Compared to the minimum batch cost of a silicon thruster, this is still roughly an order of magnitude lower, while offering high temperature functionality that the silicon thruster currently cannot provide.

Inspection of the nozzle geometry after reassembly showed that the throat width was closer to the design value than for the cold gas thruster, being just (9 ± 7) % larger instead of (18 ± 13) %. The measurement accuracy was also improved through the use of higher magnification microscope images. Leak testing was less successful than with the cold gas system as the leakage flow had increased after

reassembly from <0.01 % of the total mass flow through the nozzle to ∼ 1.0 %. This is still considered acceptable but will be taken into account explicitly when analysing thrust test results, considering its effect on e.g. I_{sp} and the measured discharge factor. The increased leakage flow was hypothesized to be caused by a partial collapse of the copper sealing surface edge, as a result of heat treatment from the brazing process. Ways to avoid such an issue are discussed in the recommendations. With the exception of this increased leakage, the hot gas thruster upgrades are considered to be successful, thus hot gas thrust tests can be performed next.

7.12. Recommendations

The main recommendation that can be given is that the form of brazing used here is not the best option for attaching tubing to this thruster body. Gas torch brazing is quite a crude process, and the inevitable formation of an oxide crust all over one half of the thruster body is definitely not desired. It also results in an unknown heat treatment, changing the material and thus sealing properties of just one of the blocks. A welding / brazing type of connection is still preferred as this can be leak tested at low temperatures and still be assumed to function at high temperatures. It also requires a much smaller connection than compression / threaded fittings, an important aspect when optimizing size and mass of a future micro-thruster.

As an alternative to the more crude gas torch brazing, a first option to try instead may be laser welding / brazing, which is listed as one of the capabilities of DEMO on their website[3]. When asked about this, the author was told that DEMO did not in fact provide such services and was referred to Rien Waaijer of the TU Delft Reactor Institute (RID) for any specialty welding operations. This lead should be followed up on, or even more unique welding methods could be looked into, e.g. electron beam welding and diffusion welding (though these may not be available on campus).

To counter the material altering effects of brazing, it may be possible to anneal / harden / heat treat both copper blocks in the same manner afterwards, but before installing the nozzle profile. This could be done in the vacuum oven to prevent oxidation, and possibly using the available cartridge heaters, if they can be made hot enough. This does require some more in-depth knowledge of the material science and heat treatment “recipes” of the specific type of copper used though.

What also might be considered is to re-mill the sealing surface after each installation to take off any previously deformed piece of material. This was not possible this time due to both people that had previously performed the CNC machining being unavailable.

Next, it is recommended that the nozzle and sealing surfaces be re-inspected after each disassembly from now on. This was an oversight here, which meant that no detailed images and surface measurements of the sealing face were made. This could have resulted in valuable information regarding the roughness and height of the leak-finder fluid leftovers and how much the seal had permanently compressed the copper edge.

Lastly, if the current device is ever used for tests with water, the aluminium foil shim should be taken out to prevent galvanic corrosion inside the heating chamber.

[3] https://www.tudelft.nl/demo/faciliteiten/

8

Hot gas thrust testing

This chapter serves to detail all the tests performed to measure the thrust performance of the hot gas thruster. The goal of these tests is to verify the functionality of the created system in terms of thrust performance, heat losses and attainable temperature. Heating of the thruster body is tested on its own in section 8.1, to provide an estimate for heat losses and to see if the desired temperature of 400 °C can be attained. Heat loss results are also compared with model predictions from the detailed design phase to determine possible points for model improvement. The heated thrust tests are then described in section 8.2 and their results are analysed in section 8.3. Lastly, a conclusion to the chapter is given in section 8.4, followed by recommendations in section 8.5.

8.1. Heater testing

The goals for the initial heating tests (without thrust) were to test the control of the cartridge heaters in the thruster, to see what temperature can be achieved and to estimate heat losses. The results were also compared with the modelled heat loss from section 4.5, to see how accurate this earlier prediction was and what aspects of the model might need to be improved first in the future. As this is just a single instance and the model incorporates many different design aspects and estimates, actual model validation will require more work beyond what is done here. For ease of assembly the thruster was installed on the TB-5m, after which the whole assembly was placed in the vacuum chamber. As no propellant had to flow into the vacuum chamber for this, a relatively constant ambient pressure between 40 and 17 Pa was maintained.

As mentioned in the previous chapter, the two cartridge heaters were voltage controlled from within LabVIEW (see also Appendix D). A live heater resistance estimation subVI was made beforehand based on filtered current and voltage measurements from the power supplies. This was intended to allow for using power P_{el} as a user input to the heater control instead of voltage V to have the relation from user input to power output be linear instead of quadratic. This could then also be extended to estimate heater internal temperature from the measured resistance.

Unfortunately there was an issue with this, which after some investigation turned out to be a default setting deep within LabVIEW. By default, LabVIEW apparently shares memory between two instances of a used subVI[1], which also affected the filters for current and voltage used here. Because the resistance values for both heaters were not identical, the two resistance estimates oscillated slowly between their two actual values, making their outputs essentially useless for this test.

The heater power was also reported in the LabVIEW interface based on the product of the measured current and voltage. As fast heater control was not needed, the power level could simply be tuned to the desired value by changing the voltage. It was determined to be easier to just use this manual tuning method than get the resistance estimation to work properly, thus this function was not used further.

As for the results from the test, the temperature was gradually increased to (454 ± 6) °C, after which it was allowed to cool down in the vacuum, see Figure 8.1. The device was not heated further as this is the maximum temperature of the sheathing of the heater power cables, even though the available

[1]Default behaviour is "*Shared Reentrant*", while "*Preallocated Reentrant*" is needed, see https://knowledge.ni.com/KnowledgeArticleDetails?id=kA00Z0000019L4zSAE&l

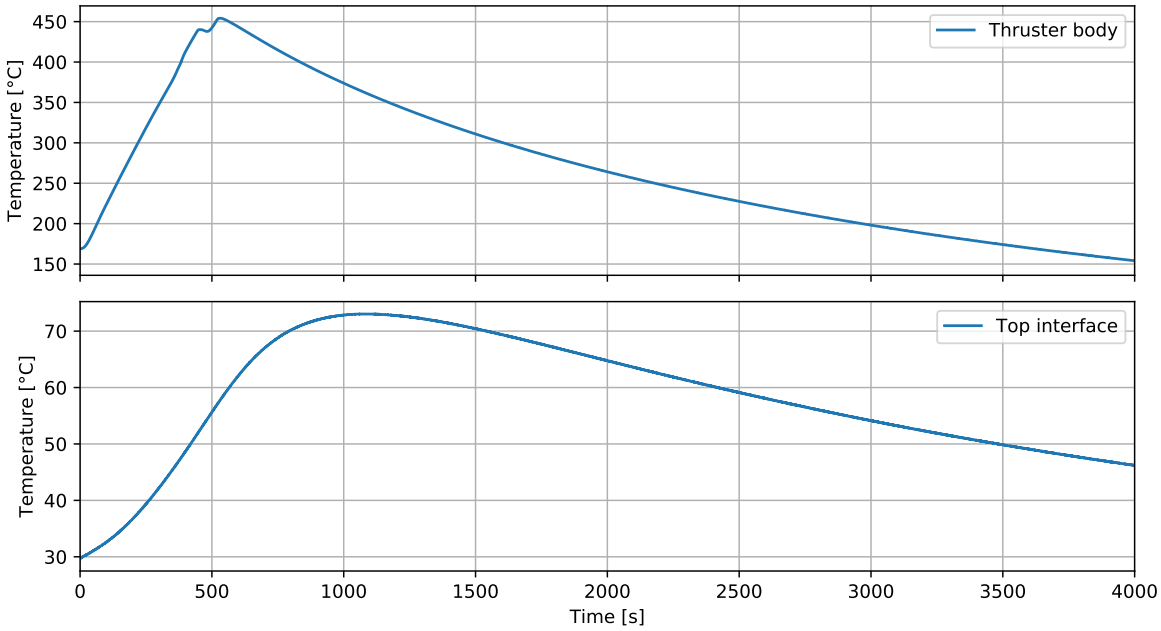

Figure 8.1: Temperature of the thruster body and interface over time during the heater test.

power would have allowed for it. This also already exceeded the desired design temperature of 400 °C, and is around 300 °C above the temperature that has been reached by the current silicon VLM [14]. The heaters performed as expected, with the bottom one set to a slightly lower power as lower heat loss was expected from this due to fewer physical connections and a less oxidized surface.

The interface temperature (p-T sensor) could also be seen to increase to a little over (72 ± 4) °C, lagging behind the thruster body somewhat. Keeping the thruster body at its peak temperature of (454 ± 6) °C would thus likely have resulted in even higher interface temperature, coming dangerously close to the sensor limit of 85 °C.

The heat losses as a function of thruster body temperature are estimated based on the time derivative of this same temperature. For this, the overall thermal capacity of the thruster body also needs to be known. This could be estimated based on the mass of all the components from CAD data and approximate thermal capacities, though this would have been quite labour intensive, with possibly large uncertainty. As a different approach, both temperature transient data from during heating and cooling was used. At each temperature considered, the following system of equations should then hold:

$$\begin{cases} \dot{Q}_{\text{loss}} &= -\overline{c}_p m_{\text{tb}} \cdot \frac{\mathrm{d}T_{\text{tb}}}{\mathrm{d}t} \\ \dot{Q}_{\text{loss}} &= -\overline{c}_p m_{\text{tb}} \cdot \frac{\mathrm{d}T_{\text{tb}}}{\mathrm{d}t} + P_{\text{heat}} \end{cases} \tag{8.1}$$

This has only two unknowns, the heat losses $\dot{Q}_{\text{loss}}$ [W] and the overall thermal capacity of the thruster body $\overline{c}_p m_{\text{tb}}$ [J K^{-1}], and can thus be solved. There is still some uncertainty in this calculation due to the sensor accuracy and temperature distribution over the thruster body, but it should be accurate enough for now. Also only some of the heating phase, when heating power was kept constant, could be used. Other times the inertia of the temperature measurement resulted in wildly oscillating results.

To solve these equations, first an estimate of $\overline{c}_p m_{\text{tb}}$ was made, based on the mass of just the copper blocks (0.149 kg from CAD) and a copper specific heat capacity $\overline{c}_p$ of 0.38 J kg^{-1} K^{-1} [20]. Solving was then done visually by plotting $\dot{Q}_{\text{loss}}$ versus T_{tb} for both heating and cooling, and adjusting $\overline{c}_p m_{\text{tb}}$ until both lines overlapped. This was achieved with a 29 % increase of $\overline{c}_p m_{\text{tb}}$ over the initial estimate, which is plausible considering components such as bolts, springs and heaters had not been taken into account yet. The resulting graphs can be seen in Figure 8.2, which also shows the modelled heat losses for comparison.

The modelled values can be seen to be quite close to the measurements, especially considering the number of simplifications made for the model. The relative difference between model and experiment

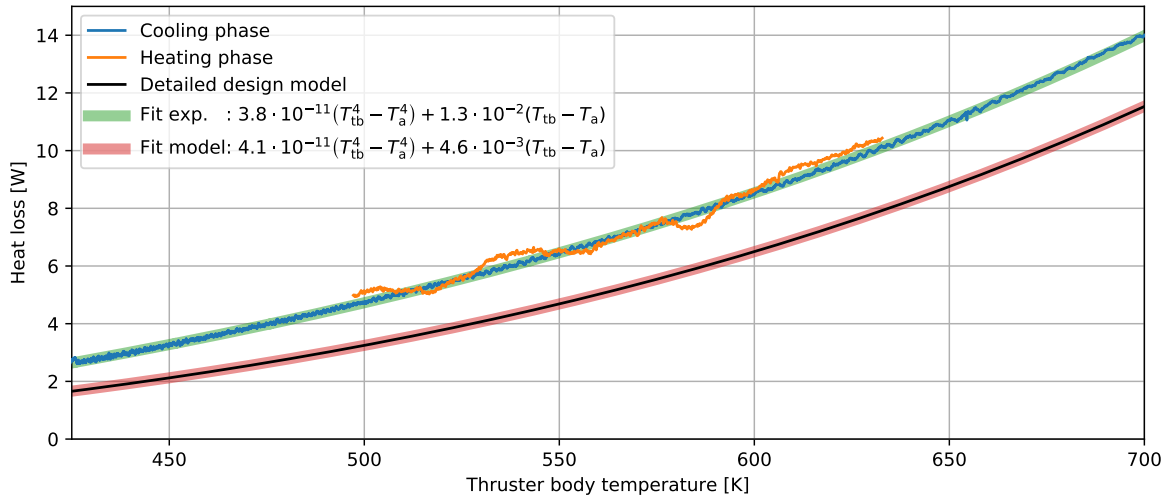

Figure 8.2: Estimated heat loss of thruster versus thruster body temperature from measurements, together with the heat loss as modelled during detailed design (section 4.5) and least squares fits for both the experimental and model data.

is larger at lower temperatures though, with experimental heat loss being $\sim 50\,\%$ higher at 425 K but only $\sim 20\,\%$ higher at 700 K. To further investigate this varying difference, both model and experimental data was fitted to a simple equation of the form $c_{\mathrm{rad}}\left(T_{\mathrm{tb}}^4 - T_{\mathrm{a}}^4\right) + c_{\mathrm{cond}}\left(T_{\mathrm{tb}} - T_{\mathrm{a}}\right)$, where the first term is to account for radiative heat loss and the second for conductive heat loss. c_{rad} [W K^{-4}] and c_{cond} [W K^{-1}] are the unknown fitting constants, and an ambient temperature of $T_{\mathrm{a}} = 20\,°\mathrm{C}$ was used. Results for this are also shown in Figure 8.2, which shows excellent agreement between the fits and their original data.

The difference in the scaling constants c_{rad} and c_{cond} would then suggest that the radiative heat loss prediction was only around 10 % too high, while conductive heat loss predictions were actually too low by a factor of 2 to 3. At 700 K, these values still suggest that radiation is the primary source of heat loss, though at 64 % of the total instead of 84 % for the model prediction. Whether this relatively accurate radiative heat loss contribution is actually due to the model being correct, or a result of several incorrect parameter estimations cancelling out, cannot be determined from this data alone. Some points may be noted regarding conduction though, as the difference there is much larger.

The main suspected causes for this, in order of severity, are: the (thick) power leads of the heaters, the wire of the thermocouple, and the connection of the radiation shield. All of these are metal components connected to the thruster body (or shield) that were not taken into account during modelling. The first two of these are also electrical conductors (which are normally good thermal conductors as well), so that these may have similar heat losses as the propellant tubing, even though they have a smaller cross sectional area. Due to the more accurate radiative heat loss prediction increasing more rapidly with temperature than conduction, the influence of the latter decreases for higher temperatures, which is also what could be seen in the graph. For more accurate heat loss predictions in the future, it is thus recommended to also investigate the heat loss due to conduction via electrical leads connected to the thruster body.

The components themselves performed admirably under these high temperatures. The copper blocks showed no difference in appearance, while the heaters were (partially) oxidized on their exterior, see Figure 8.3. This oxidation is hypothesized to originate from oxides already present in the copper insertion holes (from brazing and handling), as no other components were affected to this degree. There was also some flaking of the wire sheathing near the heaters, indicating the temperature of the heaters themselves may have exceeded the limits of the sheathing.

8.2. Thrust testing setup and results

Essentially the same setup was used here as for cold thrust testing. The LabVIEW control software was changed to include heater control and thermocouple temperature measurements, but was otherwise identical to the version used previously (see Appendix D). With the addition of the heaters and the

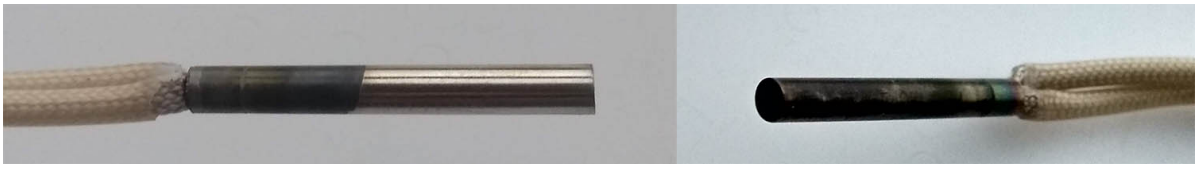

Figure 8.3: Heater from bottom block (left) and top block (right), with oxidised surface after first heater test.

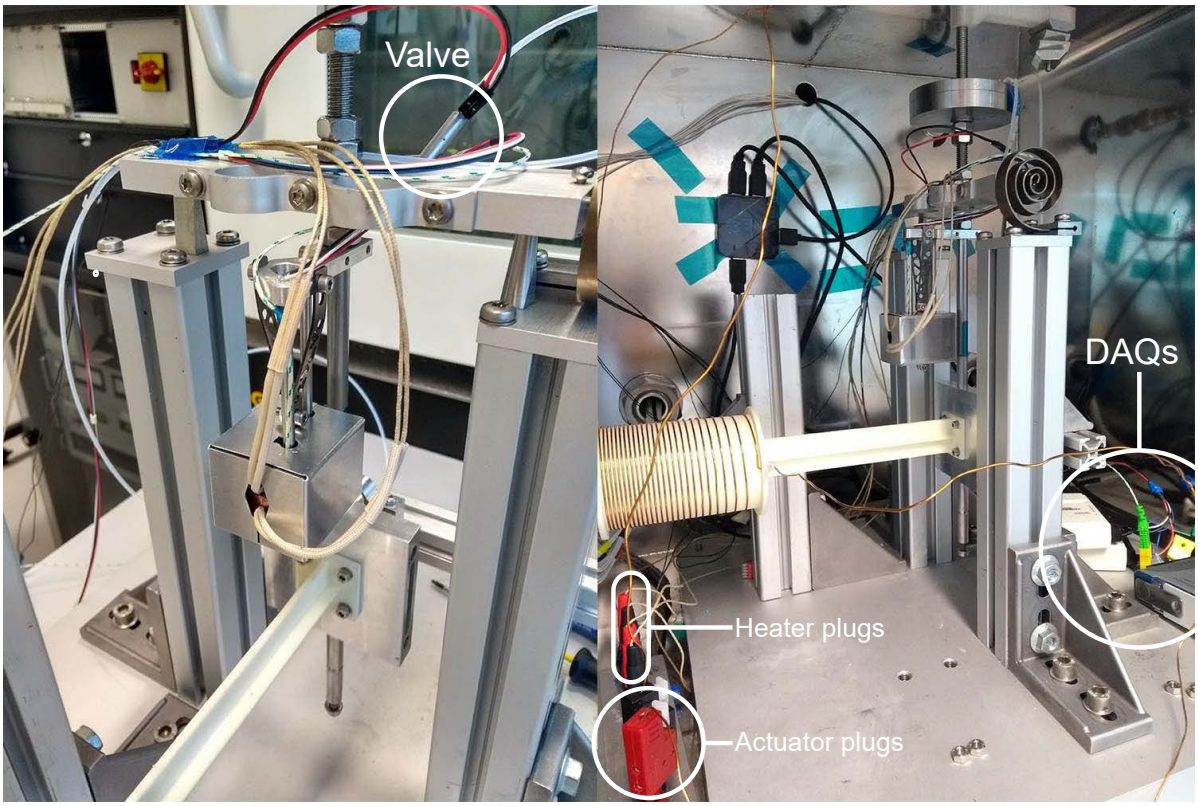

Figure 8.4: Test setup for hot gas thrust testing, with several components indicated for clarity, both outside (left) and inside (right) the vacuum chamber.

Name	Length [mm]	Description
L_0	102.70 ± 0.10	Top of pendulum horizontal beam to bottom of thruster body
L_1	16.80 ± 0.05	Top to bottom of thruster body
L_2	5.25 ± 0.05	Top of pendulum horizontal beam to frictionless pivot point
L_3	53.45 ± 0.05	Bottom of thruster body to top of actuator beam
L_4	25.09 ± 0.05	Top to bottom of actuator beam

Table 8.1: Measurements of lengths for calculation of force correction factor, see Figure 6.5.

thermocouple, five more wires now had to be guided down from the pendulum. This was done in a gentle curve downwards, from the side of the pendulum in the plane perpendicular to the thrust direction. The valve was also placed differently so that the propellant tubing could also follow the path of the wires, hopefully reducing the influence of the pressure induced stiffening effect mentioned before. This setup can be seen in Figure 8.4.

After installation of the thruster, but before the radiation shield was added, a new measurement of the force correction factor λ was made. The measured distances can be seen in Table 8.1, which resulted in a new value of $\lambda = 1.835 \pm 0.001$.

8.2.1. New measurement confidence bounds

The pressure sensor is operated at elevated temperatures, resulting in reduced accuracy. For temperatures up to 40 °C, the accuracy is ±50 mbar, while above that up to 85 °C it is specified as ±100 mbar. The temperature used for determining which of these is applicable is the one measured by the pressure sensor itself.

For the propellant temperature a completely different sensor was used, namely a thermocouple. The accuracy associated with this is ±1.5 °C from the sensor itself, ±2.5 °C for the measurement by the NI 9211 DAQ used. An estimated ±5 °C was added for uncertainty due to temperature variations over the volume of the thruster body. These were assumed to be random and independent, resulting in a total temperature sensing uncertainty of $3\sigma_{T_c} = \sqrt{1.5^2 + 2.5^2 + 5^2} \approx 5.8\,\mathrm{K}$.

8.2.2. Test procedure and issues encountered

After this the procedure for thrust measurement was nearly identical to the cold gas tests, with a few exceptions. Firstly, the feed system pressure was tuned so that it would result in the design chamber pressure of (1345 ± 50) mbar during thrust. Tests were also only performed for varying temperatures, with the pressure regulator remaining fixed during the whole process. Temperatures to be tested at were ambient, 100 °C, 200 °C, and 400 °C, with three tests performed at each temperature. These were also all performed in the same sitting in sequence.

The heaters were turned off during actual thruster firing to not influence the electro-magnetic actuator with stray magnetic fields from their wires, which were quite close. The energy for gas heating is then provided from the thermal capacity of the copper blocks alone. The tests should be short enough ($\sim$ 15 s), and the thermal capacity high enough to allow for this. For longer tests, and for future tests in general, it is recommended to move the power feed-through block in the vacuum chamber to the opposite side, to not have this issue in the first place.

During a first attempt at the test at around $T_c \approx 100\,°\mathrm{C}$, the heater in the bottom block suddenly showed no more current flowing through it, indicating that it was no longer conductive and thus may be broken. The first test was aborted and the heater was investigated outside of the vacuum chamber. Through experimentation and sheer luck, the issue was seemingly fixed by putting a spike voltage into it for a short duration ($> 30\,\mathrm{V}$). This turned out to be only temporary though, as this behaviour occurred a few times again during the second test, with the fix no longer working after a few cycles. The test was continued with a single heater and some extra measures to give a more equal temperature distribution. For each temperature, the thruster was heated to around 10 °C higher before being allowed to cool down again slightly. This was repeated several times to give the bottom block more time to heat up to the desired value. Due to the excess of heating power available, the temperature of 400 °C could still be reached, albeit more slowly. All the 12 thrust tests at varying temperatures were performed, with raw measurements from a successful test at 400 °C being shown in Figure 8.5.

An interesting trend was noticed during this: the equilibrium position of the pendulum gradually shifted a few hundred µm towards the sensor when increasing the temperature from ambient to 400 °C. Between tests at the same temperature, the equilibrium position was relatively constant though.

A second, possibly related trend that was spotted was that at temperatures other than ambient, the actuator current after firing I_{end} would be consistently lower than before firing I_{start}. This difference also increased with higher temperatures, and is indicated in the top graph of Figure 8.5.

Based on this found behaviour, the measured thrust results were split into two per test. One result using $I_{\mathrm{mid}} - I_{\mathrm{start}}$, and one using $I_{\mathrm{mid}} - I_{\mathrm{end}}$, indicated with start and end respectively. These values diverged in a very consistent manner with increasing temperature, see Figure 8.6. The difference between I_{start} and I_{end} can be seen to be essentially linear with the temperature difference with ambient. This lead to the thought that this difference was systematically related to thruster temperature and not just a random shift/drift in pendulum equilibrium position during thrust.

For some of the tests the effect was small enough to not be noticed at first, which unfortunately invalidated some of the thrust results. For these tests the actuator was not able to return the pendulum to the desired zero position after firing had concluded, as it would have needed a negative actuator current to do so. This also resulted in oscillatory behaviour of the pendulum as the controller could no longer provide effective damping. The tests where this occurred are TTH-2.1, 2.2., 2.3, 3.1 and 3.2, i.e. all 100 °C data and the first two of the 200 °C data. Results from these tests are still included in figures, but are indicated in red. Mass flow measurements from these tests were not affected by this.

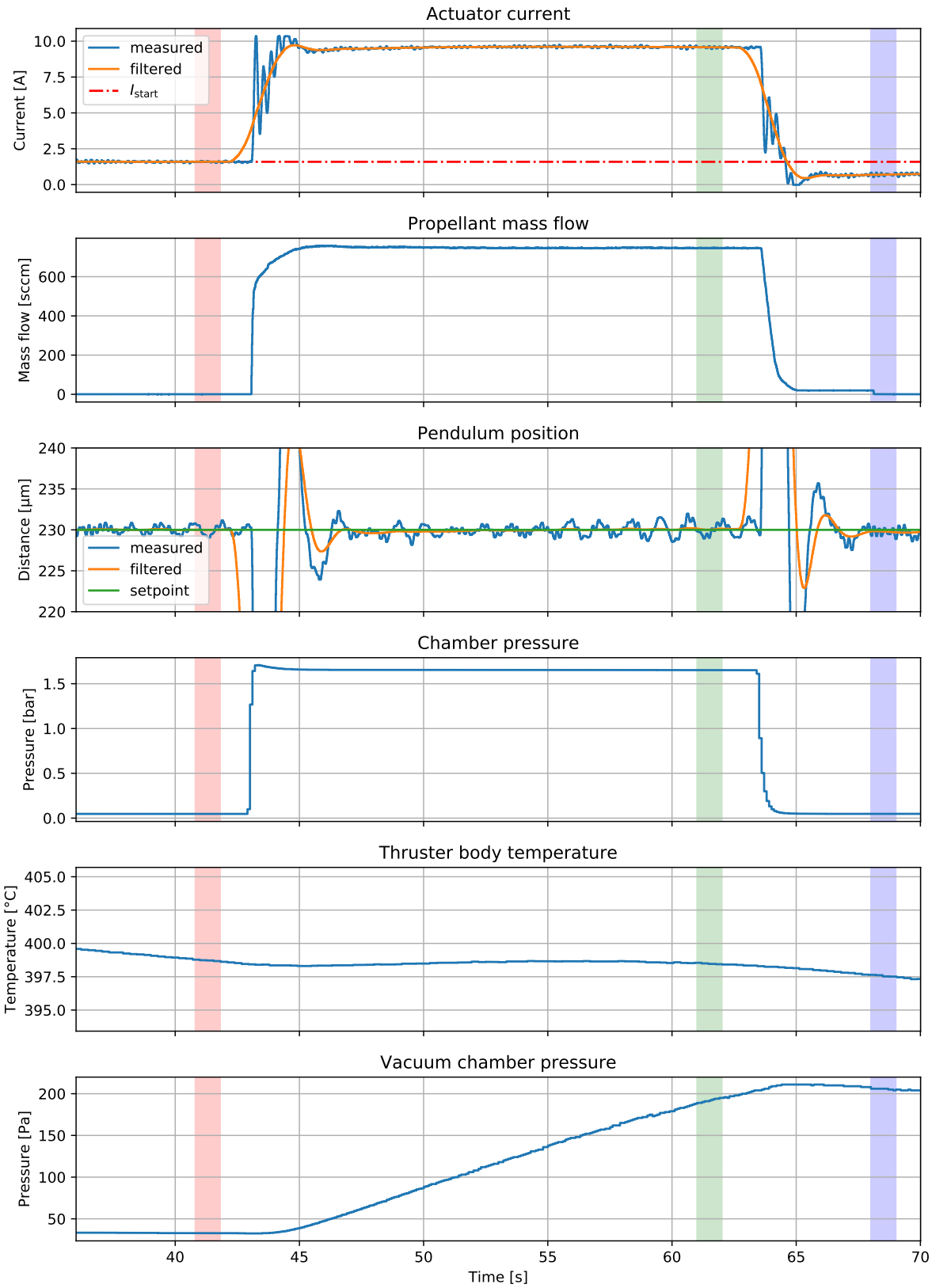

Figure 8.5: Measurement results from the hot gas test TTH-4.2 for all time-varying signals used. Filtered signals are also shown if they were used for calculations. Windows for time-averaging of signals are indicated with red, green and blue regions for before, during and after thrust measurements, respectively. The constant controller current I_{start} before thrust is also shown as a horizontal line for comparison with the current after thrust.

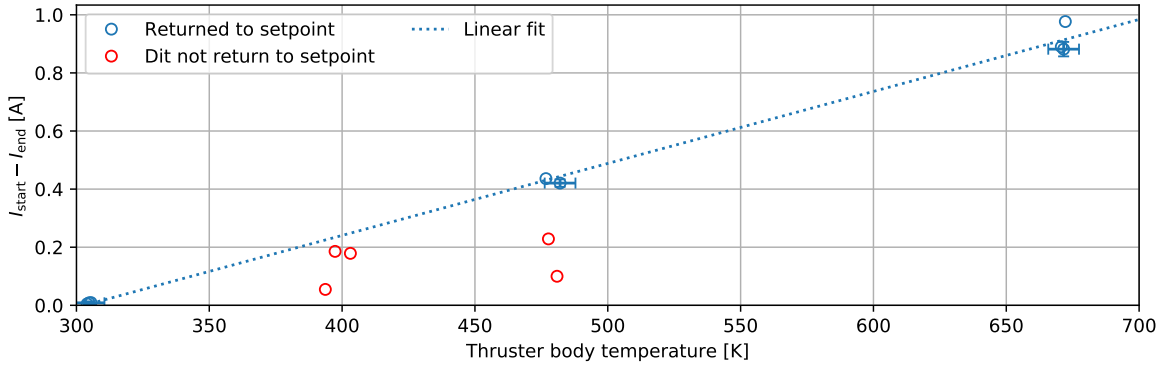

Figure 8.6: The difference in actuator current needed before thrust (I_{start}) and after thrust (I_{end}), versus thruster body temperature. Tests when the actuator current dropped to 0 before reaching the pre-thrust distance setpoint are indicated in red. A linear least squares fit through the other points is also shown.

The issue was rectified between TTH-3.2 and 3.3 by starting thrust testing at a position further away from the pendulum equilibrium position. This meant that the start current was higher and the end current would no longer dip below zero.

The current hypothesis is that the shift is caused by thermal expansion and contraction of the stainless steel propellant tubes between the interface and body. These will expand when heated, though possibly not in equal amounts due to the metal foam presence in the front pressure sensing tube. Uneven expansion of both can cause the thruster body to shift and become slightly askew relative to its room temperature position. This shifts its centre of gravity, which is quite influential in the COG of the overall pendulum due to it being quite a large, heavy copper block. This in turn moves the equilibrium position of the pendulum.

The result of this supposed effect was something that could be observed from the pendulum equilibrium position moving towards the distance sensor with increasing temperature. This then may relate to the behaviour during thrust testing due to the propellant regeneratively cooling the entrance tube, which then contracts due to becoming colder. This in turn would skew the body further towards the pendulum arm, reducing moment on the pendulum arm from the thruster body weight and shifting the pendulum equilibrium towards the actuator, as seen in the tests.

After thrust and mass flow had stopped, the equilibrium position could be seen to move back to its original location from before. This would then be because the tube was no longer being cooled, allowing its temperature to increase and the tube to expand to its hot length once more.

When taking this hypothesis into account, the actual thrust force measurement would be the end value, which then measures the difference in force for the same tube expansion/contraction. This is assumed to be the case here for analysis in the following section, though results for both start and end will still be shown. Further calculations or experiments regarding this hypothesis are left for future work. If this is indeed the case, future (hot) thrust tests may then benefit from a thrust bench that is independent of thruster COG location. A thruster design with a COG that is independent of propellant tubing expansion may also be an option, for instance by having separate structural supports and thin propellant tubing with bent sections for low stiffness.

8.3. Analysis of results

The results obtained in the previous sections are discussed here in steps. First some initial impressions are given regarding the data on its own, followed by comparison with the previous cold gas thrust results. The new hot gas results are then compared to values from the reference thruster, and lastly to model predictions.

Any additional results not shown here for e.g. model predictions and thrust coefficients are tabulated in Appendix B.3. Test results are numbered chronologically in groups of increasing temperature from TTH-1.1 to TTH-4.3 (Thrust Test Hot). Longer term reproducibility of the results is left for future work.

Test name	p_c [kPa]	T_c [K]	p_a [Pa]	F_{exp} [mN]	$\dot{m}_{exp}$ [mg s^{-1}]	$I_{sp,exp}$ [s]
TTH-1.1	135.6 ± 5.0	305.5 ± 5.8	184 ± 29	11.839 ± 0.076	19.14 ± 0.13	63.07 ± 0.60
TTH-1.2	135.5 ± 5.0	304.8 ± 5.8	203 ± 31	11.847 ± 0.076	19.16 ± 0.13	63.05 ± 0.60
TTH-1.3	135.2 ± 5.0	304.0 ± 5.8	214 ± 33	11.831 ± 0.077	19.12 ± 0.13	63.11 ± 0.60
TTH-2.1	143.1 ± 5.0	393.7 ± 5.8	243 ± 37	12.149 ± 0.078	17.70 ± 0.12	69.98 ± 0.66
TTH-2.2	144.0 ± 5.0	403.1 ± 5.8	219 ± 34	12.326 ± 0.079	17.57 ± 0.12	71.55 ± 0.68
TTH-2.3	143.4 ± 5.0	397.3 ± 5.8	300 ± 45	12.35 ± 0.13	17.64 ± 0.12	71.36 ± 0.91
TTH-3.1	150 ± 10	477.7 ± 5.8	213 ± 33	12.550 ± 0.082	16.81 ± 0.12	76.13 ± 0.73
TTH-3.2	151 ± 10	480.9 ± 5.8	224 ± 34	12.315 ± 0.079	16.76 ± 0.12	74.93 ± 0.71
TTH-3.3	151 ± 10	482.0 ± 5.8	216 ± 33	12.775 ± 0.083	16.76 ± 0.12	77.75 ± 0.75
TTH-3.4	151 ± 10	476.7 ± 5.8	240 ± 36	12.886 ± 0.085	17.04 ± 0.12	77.10 ± 0.74
TTH-4.1	166 ± 10	670.7 ± 5.8	209 ± 32	13.492 ± 0.097	15.61 ± 0.11	88.14 ± 0.89
TTH-4.2	165 ± 10	671.6 ± 5.8	195 ± 30	13.417 ± 0.094	15.55 ± 0.11	87.96 ± 0.87
TTH-4.3	165 ± 10	672.2 ± 5.8	220 ± 34	13.434 ± 0.088	15.51 ± 0.11	88.31 ± 0.85

Table 8.2: Hot gas thrust test results, based on *end* thrust values. Tests where the pendulum could not reach its distance setpoint after the thrust phase are emphasized in red.

8.3.1. Initial impressions

The experimental results in Table 8.2 and 8.3 show no immediate abnormalities, with all efficiencies below unity and decreasing with lower Reynolds numbers / higher temperatures. There is a very slight increase of C_D for the highest temperature / lowest Reynolds number, though this could simply be due to a measurement error of e.g. the pressure sensor. This sensor becomes less accurate as it heats up, which can also be seen in Table 8.2 from the larger confidence bounds at higher temperatures.

One other thing that is apparent is that the chamber pressure steadily increases with temperature. This is due to the mass flow decreasing with temperature, which lowers the pressure drop over the feed system, increasing the thrust chamber pressure in turn. This resulted in mass flow decreasing less with temperature than expected and thrust actually *increasing* with temperature. If the chamber pressure had remained constant, thrust should have remained constant or decreased slightly with temperature. These higher pressures were not intended, but should have no consequences for analysis and comparison.

following up on this response to temperature changes, the mass flow changes with pressure and temperatures as expected, which is evidenced by the nearly constant discharge factor (within 0.5 %). This suggests that mass flow thus indeed scales with $p_c/\sqrt{T_c}$, which in turn indicates that the propellant temperature after the heat exchanger does attain the same temperature as the thruster body. This shows that the heat exchanger and related temperature sensor are working as intended.

The spread of the data is also slightly higher for some groups of tests than for cold gas thrust testing. This may be attributed to the fact there are now two inputs, p_c and T_c. The first is the output from a mechanical pressure regulator and is very stable between tests if its handle is left untouched. T_c on the other hand is manually controlled, and only has a indirect integrating relation to the actual user controlled heater power (with slow response). As a result, T_c was difficult to control for these short term tests and thus shows some variability between repeats from the same temperature group.

8.3.2. Comparison with cold gas results

For comparison with the earlier cold gas data, first the produced thrust and mass flow are compared when plotted versus p_c, see Figure 8.7. Only the unheated data from the hot gas tests is shown, to provide a fair comparison without temperature variations. When using the same nozzle, the data should intersect, but here an $\sim$ 8.6 % lower thrust and $\sim$ 7.3 % lower mass flow can be seen for the same p_c. The same pressure sensor was used for both tests, thus experimental errors for all p_c measurements are the same and cannot explain the difference. This suggests that the throat size is now smaller, which was also found with the nozzle geometry characterization in section 7.8. The slightly lower difference in mass flow could then be explained by the leakage that was found before in section 7.9. This results

Test name	$C_{\mathrm{D,exp}}$ [%]	$\xi_{\mathrm{F,exp,start}}$ [%]	$\xi_{\mathrm{F,exp,end}}$ [%]	$\mathrm{Re}_{\mathrm{t,exp},D_\mathrm{h}}$ [10^2]	$\mathrm{Re}_{\mathrm{t,exp},w_\mathrm{t}}$ [10^2]	η_{heat} [%]
TTH-1.1	87.9 ± 6.9	87.1 ± 1.2	87.2 ± 1.2	38.18 ± 0.89	24.56 ± 0.46	–
TTH-1.2	88.0 ± 6.9	87.2 ± 1.2	87.3 ± 1.2	38.28 ± 0.90	24.63 ± 0.46	–
TTH-1.3	87.9 ± 6.9	87.5 ± 1.2	87.5 ± 1.2	38.27 ± 0.90	24.62 ± 0.46	–
TTH-2.1	87.5 ± 6.8	84.7 ± 1.1	85.2 ± 1.1	28.94 ± 0.61	18.62 ± 0.29	48
TTH-2.2	87.4 ± 6.7	84.1 ± 1.0	86.0 ± 1.1	28.21 ± 0.59	18.15 ± 0.28	48
TTH-2.3	87.5 ± 6.8	84.7 ± 1.1	86.7 ± 1.3	28.64 ± 0.60	18.43 ± 0.28	48
TTH-3.1	87.2 ± 8.3	81.6 ± 1.0	83.9 ± 1.0	23.76 ± 0.47	15.29 ± 0.21	44
TTH-3.2	87.0 ± 8.3	81.3 ± 1.0	82.3 ± 1.0	23.57 ± 0.47	15.16 ± 0.21	43
TTH-3.3	87.1 ± 8.3	81.01 ± 0.95	85.3 ± 1.0	23.52 ± 0.47	15.13 ± 0.21	43
TTH-3.4	87.8 ± 8.4	80.74 ± 0.96	85.1 ± 1.0	24.12 ± 0.48	15.52 ± 0.22	44
TTH-4.1	87.5 ± 8.0	73.06 ± 0.81	81.18 ± 0.94	17.23 ± 0.32	11.09 ± 0.14	33
TTH-4.2	87.6 ± 8.0	72.87 ± 0.81	80.92 ± 0.92	17.16 ± 0.32	11.04 ± 0.14	33
TTH-4.3	87.6 ± 8.0	72.32 ± 0.80	81.26 ± 0.91	17.10 ± 0.32	11.00 ± 0.14	33

Table 8.3: Hot gas discharge factor and specific impulse efficiency with corresponding throat Reynolds numbers and a rough estimate of heating power efficiency.

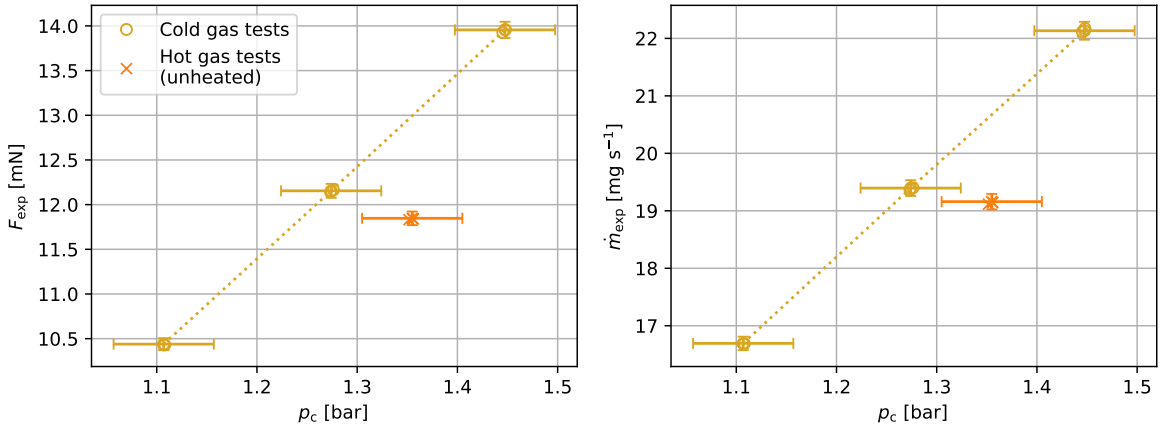

Figure 8.7: Comparison of thrust and mass flow values for the cold gas thrust tests and the unheated group of the hot gas thrust tests (TTH-1.1 to 1.3).

in roughly an extra 1 % of measured mass flow that does not produce thrust.

A further comparison can be seen in Figure 8.8. Confidence bounds for cold and hot results overlap fully, which could mean C_D is actually the same as before. The actual values found for the hot gas tests are a few percent higher than for the cold gas tests though. Part of this may be due to the leak of $\sim 1\,\%$ of the total flow, which may not actually go through the nozzle, but does show up as additional flow in $\dot{m}_{\mathrm{exp}}$. Measured mass flow is then higher than the flow through the nozzle, which inflates $C_{\mathrm{D,exp}}$. Another part of the difference may be the new (higher accuracy) throat width measurements.

In the same figure it can be seen that the specific impulse efficiency has actually decreased somewhat. The difference is in the order of 2 to 3 % and may thus partially be caused by the leakage that was found, which was around 1 % of the total flow. Leakage flow is still measured by the sensor, but may produce little to no thrust, lowering $I_{\mathrm{sp,exp}}$ and $\xi_{\mathrm{F,exp}}$. Other causes may be slight changes in geometry due to reassembly, or the different routing of the propellant feed tube to the pendulum, which may have decreased the influence of pressure stiffening.

8.3.3. Comparison with reference thruster

When comparing the experimental results to the data from the reference thruster (Appendix A) in Figure 8.8, the values found for C_D now overlap quite nicely, especially for lower Reynolds numbers / higher

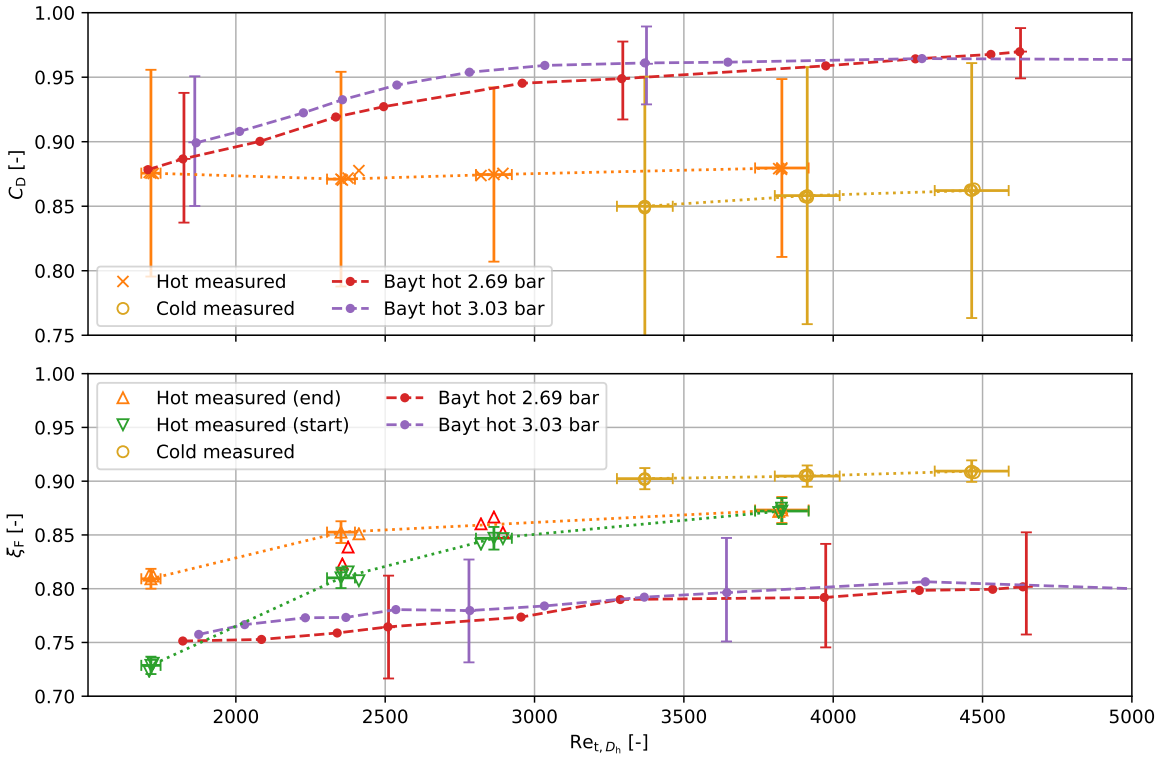

Figure 8.8: Comparison of discharge factor and specific impulse efficiency for the hot and cold gas measurements from this project and the reference thruster by Bayt [4], with Re_t using D_h as characteristic length. Tests where the pendulum could not reach its distance setpoint after the thrust phase are indicated in red.

temperatures. ξ_F is still around (10 ± 6) % higher though. As with the cold gas performance comparison, only data with Re_t based on D_h is shown. Using w_t essentially only scales all the Reynolds data by the same amount due to the similarity of the designs, and thus provides no new information. As ξ_F has decreased by 2 to 3 % from the cold gas tests, it is now closer to the values found by Bayt than before. Values from both thrusters also converge for lower Reynolds numbers.

As a further comparison, an I_{sp} versus thrust graph is provided in Figure 8.9. The directions that the values on this graph move towards when increasing pressure and / or temperature are also indicated. This is to illustrate that data from the reference thruster has independent changes in p_c and T_c, while both are increased simultaneously for the thruster tested here. As stated earlier, the increase in thrust with temperature that can now be seen in this figure is thus purely a result of the increase in p_c from a lower feed system pressure drop. Had pressure remained constant, the found values for $C_{D,exp}$ and $\xi_{F,exp}$ suggest the thrust versus I_{sp} graph would have looked similar to the ones of the reference thruster. The new thruster can thus be seen to operate in the same region of thrust, I_{sp} and temperature as the reference design. It also still meets the criterion of ≥90 % of the specific impulse efficiency at the same throat Reynolds numbers, and its thrust production functionality is thus considered to be verified.

8.3.4. Comparison with model predictions

Comparing the results with the theoretical model, essentially the same differences and trends can be seen as with the cold gas thrust tests (section 6.3). The model values for C_D and ξ_F can be seen plotted against Re_t based on D_h in Figure 8.10a and Re_t based on w_t in Figure 8.10b. Again, the confidence bounds for C_D overlap, while for ξ_F they do not. Values for the latter are a few percentage points closer to the model predictions now though. Thrust predictions with D_h can be seen to be within 10 % of experimental values (Appendix B.3), though again only because of mass flow overprediction and I_{sp} underprediction, which just happen to cancel out.

The trend for ξ_F with Re_t is also similar in shape, albeit with the model predictions shifted down by 12 to 14 % for D_h and by 15 to 23 % for w_t. The model thus still consistently underpredicts specific

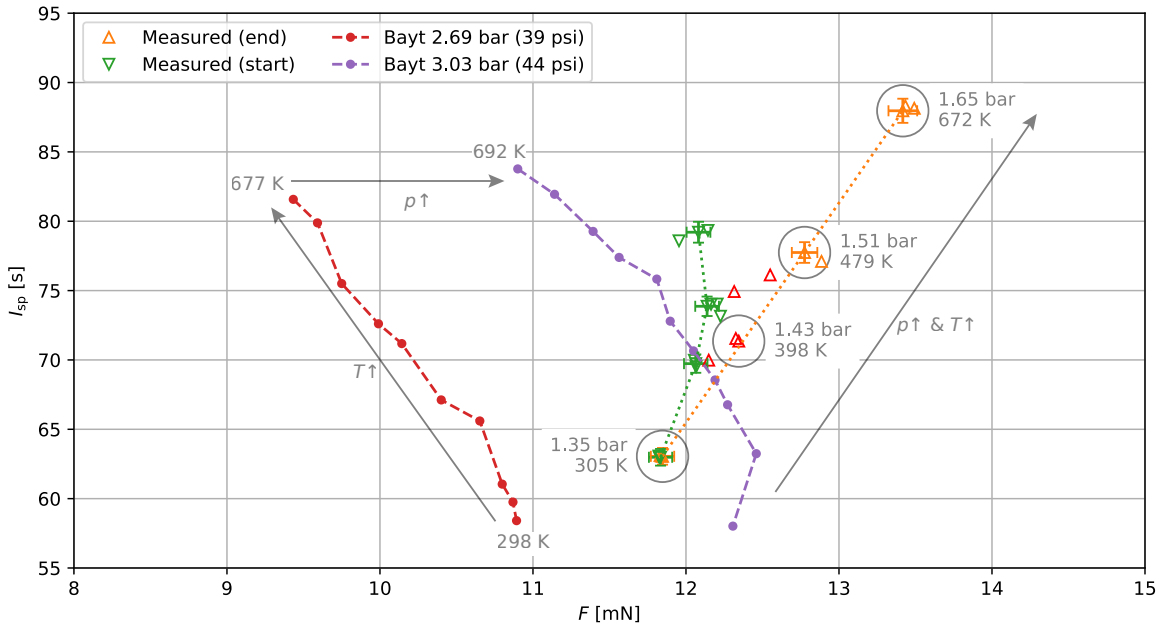

Figure 8.9: Specific impulse versus thrust for the hot gas system in comparison with hot thruster data from Bayt [4]. Tests where the pendulum could not reach its distance setpoint after the thrust phase are indicated in red.

impulse efficiency by more than the specified threshold of 10 %. The variant using D_h does provide more accurate predictions for experimental values than IRT now though, especially for the lower Reynolds numbers.

Drawing a conclusion regarding the accuracy of the C_D model is not as straightforward, due to the comparatively large confidence bounds of the measurements. For the lowest Reynolds numbers and using w_t, the probability that the model prediction and experimental value are within 10 % of each other is close to 100 %. For higher Re_t or when using D_h (which was a better fit for the reference thruster data), the maximum deviation of 10 % cannot be guaranteed though. Looking at both the data obtained here and that from the reference thruster, the model using w_t provides the best estimate, with nearly all predicted values within 10 % of the measurements (including confidence bounds). It should be noted though that using a constant value of $C_\mathrm{D,model} = 0.9$ would have essentially the same result.

More accurate measurements are thus needed to determine the actual validity of either model, as the differences in $C_\mathrm{D,model}$ over the range of Reynolds numbers tested at here is only a few percent. For cold gas tests the main influence on accuracy was the throat area measurement, which is still the case here. For the highest temperatures with hot gas testing however, the pressure sensor also becomes influential with ±6 % confidence bounds. This is thus also a point of improvement for future tests.

Lastly, a brief look was taken into possible simple adjustments to make the ξ_F model more accurate for both the new and reference thruster. Through some minor experimentation it was found that decreasing the fitted constant of 17.6 in the empirical thrust coefficient loss factor by Spisz et al. [58] (equation (4.23) on page 35) could decrease the difference with experimental results. Using a value of 12 instead of 17.6 (with D_h) then gave model predictions in between the experimental values from both thrusters. All experimental values were then within the desired bounds of ±10 %. This is equivalent to scaling Re_t up by a constant factor of 2.15. The results from this adjustment can be seen in Figure 8.11. This is mostly a suggestion for future research. It could be argued though that the change in geometry compared to that used for the empirical relation by Spisz et al. may necessitate changing the fitting constants to some degree.

8.4. Conclusion

Heating tests showed the thruster could be heated to its design temperature of 400 °C, around 250 °C above the temperature that has been reached by the current silicon VLM. Higher temperatures up to (454 ± 6) °C were also possible, but only for a limited time if the pressure sensor was to remain

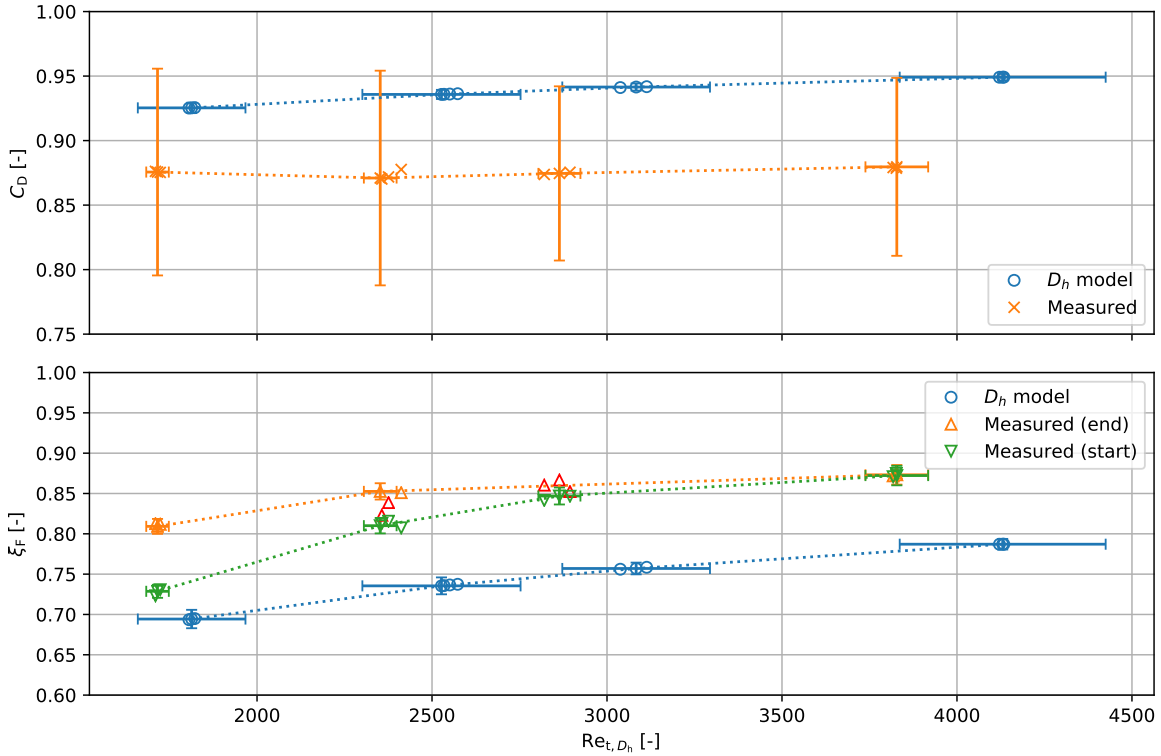

(a) Re_t with D_h as characteristic length.

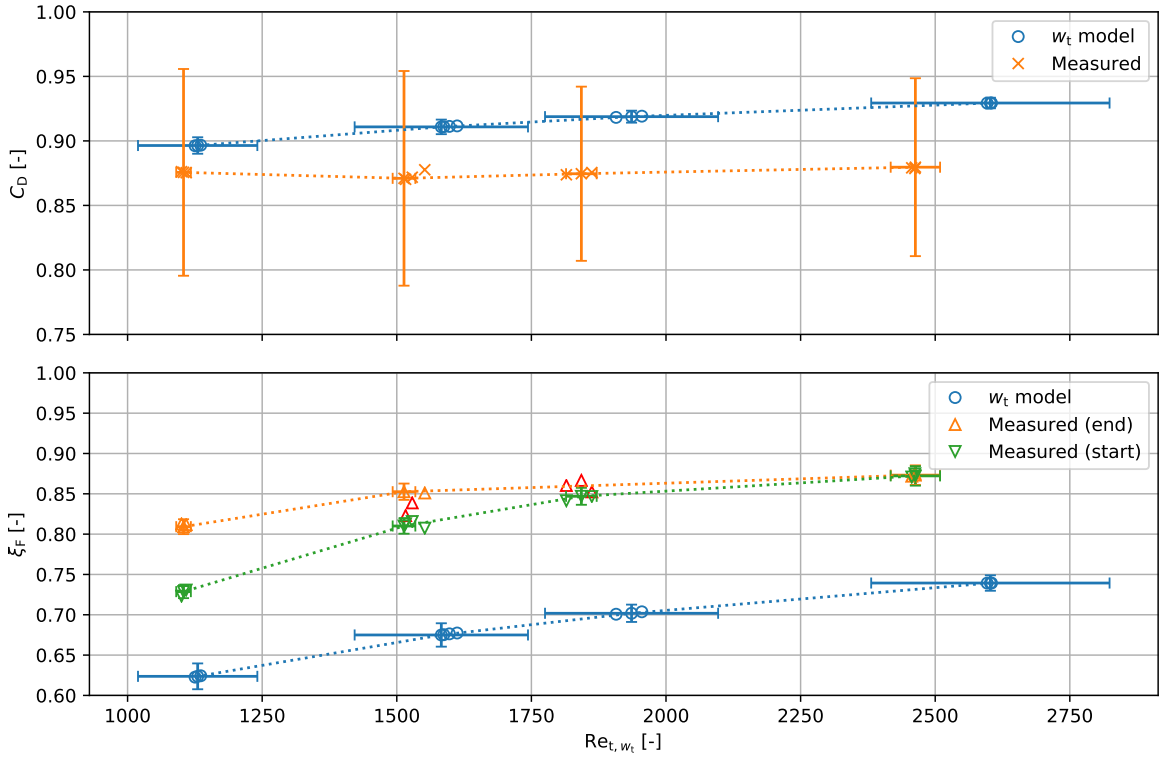

(b) Re_t with w_t as characteristic length.

Figure 8.10: Measured and modelled hot gas discharge factor and specific impulse efficiency. Tests where the pendulum could not reach its distance setpoint after the thrust phase are indicated in red.

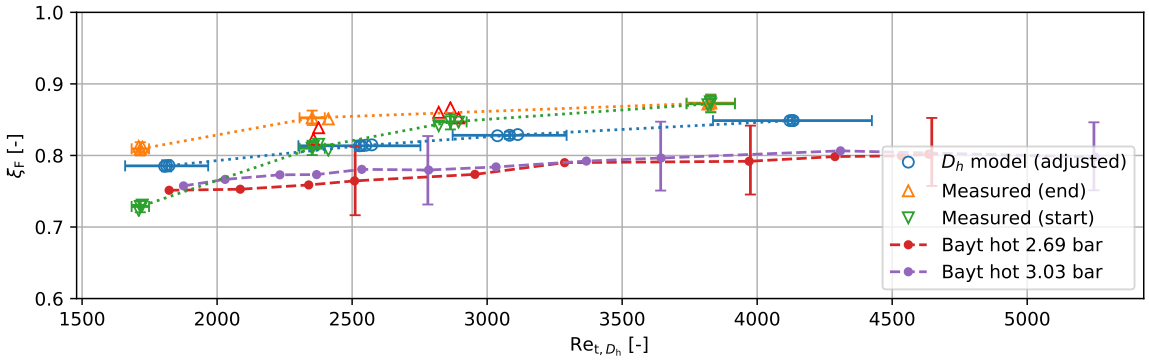

Figure 8.11: Experimental I_{sp} efficiencies for the new and reference thruster, compared with an adjusted thrust coefficient loss model (changing a fitting constant from 17.6 to 12 in equation (4.23) on page 35).

undamaged. Thruster heat loss was then estimated from temperature dynamics. Compared to the model predictions from the detailed design phase, these showed 20 % higher losses at 700 K and 50 % higher losses at 425 K. This changing accuracy, combined with curve fitting parameters for the heat loss, suggested that the modelled radiative heat losses were around 10 % too high and conductive losses were 2 to 3 times too low. This was hypothesized to be primarily because conduction through the heater electrical power leads, which are made of good electrical / thermal conductors, were not incorporated into the model. The main source of heat loss at the maximum temperature was still found to be radiation, though with only 64 % of the total instead of the modelled 84 %.

Subsequently hot gas thrust tests were performed in vacuum. Comparing the results to those obtained earlier for cold gas tests, lower thrust and mass flow scaling with pressure was found, which suggested an ~8 % smaller throat area. This was in agreement with the new throat width measurements that were performed after thruster reassembly in the previous chapter. A 2 to 3 % higher discharge factor was found, which could partially be attributed to the leakage flow of 1 % as measured in the previous chapter. The difference may also just be an artefact of the new nozzle throat measurement, as confidence bounds for the new value were fully encapsulated by those from the cold gas tests. I_{sp} efficiency on the other hand was found to be 2 to 3 % lower than before. This could again partially be explained by the leak presence, which leaves 1 to 2 % difference as a possible result of the re-installation process. The effect of pressure stiffening may also have been reduced, as the propellant feed tube was now laid down in a more gradual loop, with lower stiffness. The differences in the data between cold gas and hot gas tests can thus be accounted for. Further reproduction of results will require more testing in the future, which may then also be done at different pressures, lower Reynolds numbers or with different propellants.

A comparison of the thrust test results with the reference thruster data showed differences similar to those found with cold gas testing at low temperatures, though with results from both thrusters converging for higher temperatures. The discharge factors found for the highest temperature were within 1 % of one other, but still with around ± 8 % uncertainty. More accurate throat area and chamber pressure measurements would be needed for higher accuracy measurements of this value in the future. The I_{sp} efficiency was still around (10 ± 6) % higher than that of the reference thruster, over the whole range of throat Reynolds numbers. This is above the threshold of $\geq$90 % that was set for verification. It can thus once again be concluded that the thruster has been verified for thrust production, though now also for temperatures up to 400 °C.

Compared to the model predictions, the experimental values showed the same trends that were also seen with cold gas testing. For lower Reynolds numbers / higher temperatures, the C_D values now started to converge however, especially when using w_t for Re_t. Predictions for I_{sp} efficiency were still too low though, with a difference of 12 to 14 % when using D_h and 15 to 23 % using w_t. Possible ways to provide thrust performance predictions within 10 % of the experimental results for both the new thruster and the reference device were looked into. To this end, the C_D model based on w_t can be used. The I_{sp} efficiency model described can also be used, *if* a fitted constant in the used empirical thrust coefficient loss equation is changed from 17.6 to 12. The model is then within 10 % of all experimental data from both thrusters, and makes better predictions than IRT, which overestimates ξ_F by 10 to 25 %.

8.5. Recommendations

For future projects it may be useful to have the available FLIR thermal camera functioning inside the vacuum chamber. With this, temperature variations over the thruster body, the radiation shield and other components could then be shown. This could give a wealth of information for insulation design, and would allow for testing the hypothesis of the propellant tubes cooling down during firing.

A simple point for improvement is further to move the power feed-through block inside the vacuum chamber to the side opposite the magnetic actuator. This way the heaters can remain on during thruster firing without the possibility of current running through their leads influencing thrust measurements.

Adding a viscous damper as discussed before in section 6.5 may also help shed light on the possible thermal expansion behaviour. As this would allow for faster response with less oscillation, fast dynamic behaviour may then become visible, which would currently be obscured by transients.

On a similar note, if the mentioned hypothesis turns out to be correct, it could be beneficial to look into using a COG independent thrust bench for future experiments. This could be for instance TB-50m, which is a horizontal platform suspended on sheet metal springs. Some adjustments would have to be made to make it fit inside the vacuum chamber though, as well as possibly adding the calibration actuator and distance sensor to it.

The COG shift with temperature could also be alleviated by making a new thruster design with a COG that is independent of propellant tubing expansion. This could be done by for instance having separate structural supports combined with thin propellant tubing incorporating bent sections for low stiffness.

As a further point, the interface with pressure sensor became quite hot during testing, nearly exceeding its temperature limits. For even higher temperature operation, it may then be necessary to allow for (active) cooling of the interface, while also reducing heat input to it from the tubing.

As mentioned, the main heat loss from the thruster was still found to be radiation. Conduction was seen to play a larger role than initially estimated though, which was hypothesized to be the result of several electrical leads for heaters and sensors connected to the thruster body that were neglected for the earlier model. Heat loss contributions from these are thus recommended to be taken into account for future modelling.

Lastly, it is still not entirely clear why one of the heaters broke. A current hypothesis is that this was due to insufficient thermal contact between the heater and copper heat spreader, as the fit was relatively loose. This could then cause the heater to become much hotter than the measured temperature, possible exceeding its safe temperature limits. Better thermal contact between these two components or heater internal temperature estimation through resistance measurement would then be advised.

9 Conclusion

The goal of this project was:

To realize lower production costs and higher temperature operation of the Delft VLM by designing a version using alternative fabrication techniques, creating a prototype, and performing basic functional verification of said prototype

To this end, four main research questions were formulated, which are repeated here, together with their corresponding findings.

1. *How can a micro-resistojet be created using alternative fabrication techniques?*

Based on an earlier literature study, wire-EDM was determined to be the most promising alternative fabrication method for a micro-nozzle at this time. Several primary issues for a thruster design based around wire-EDM were identified and suitable concepts were found for solving these. This included the use of COTS resistive cartridge heaters and a metal foam heat exchanger. A robust detailed design with large margins was then created. Subsequent fabrication of the cold gas system was successful in terms of nozzle geometry accuracy and leakage. Only the throat width was $(18 \pm 13)\,\%$ too large, with the remaining features being within 1 % of their design values, which is on par with or better than the accuracy found for recent silicon thrusters. Upgrading the system for hot gas operation improved nozzle throat size accuracy to $(+9 \pm 7)\,\%$, but also increased the leakage from $<0.01\,\%$ to $1.0\,\%$ of the total nozzle flow. This increased leakage is hypothesized to be due to a combination of nozzle-re-installation and the use of brazing for attaching components. The leak rate was considered acceptable for this project, but will require design changes for a future thruster.

2. *How does the measured thrust performance of the prototype compare to data from the reference thruster design by Bayt?*

Thrust tests with the prototype were performed in vacuum, first at ambient temperature, later at temperatures up to 400 °C. This resulted in throat Reynolds numbers varying from $4.5 \cdot 10^2$ down to $1.7 \cdot 10^2$. The discharge factor at ambient temperature showed a $(-10 \pm 10)\,\%$ difference with reference data at the same throat Reynolds numbers. Values converged with increasing temperatures though, to a difference of $(0 \pm 8)\,\%$ at 400 °C. The specific impulse efficiency of the prototype was consistently higher than that of the reference thruster by around $(10 \pm 6)\,\%$. Thrust and specific impulse were also similar, with ranges of 11.8 to 13 mN and 63 to 88 s for the prototype, compared to 9.4 to 12.3 mN and 58 to 84 s for the reference thruster. A threshold of $\geq 90\,\%$ I_{sp} efficiency of the reference thruster at the same throat Reynolds numbers was set for verification of the prototype. This criterion was met, thus the hot gas thrust functionality of the prototype was verified.

3. *How do the production cost, production time, and high temperature operation of the prototype compare to that of the current VLM?*

The total cost for the project came to €1009, though €480 of this can be attributed to an error due to miscommunication regarding parallel and serial production of the nozzle. Had this mishap not occurred,

the total cost would have only been 6 % over the given budget of €500. This was only possible because CNC machining of several critical components was performed by contacts at no cost. Without this aid, even when reusing the heaters and tools from this project, a new thruster of the same design is then estimated to cost at least €650. Future projects that need a similar amount of machined parts and other components are thus recommended to seek additional funding. The found cost is still an order of magnitude below that of a single wafer / batch of silicon thrusters. When further including the cost of machined interfaces for the silicon thrusters, a similar unit cost is then expected.

With regards to production time, the cold gas thruster fabrication was completed within 1 to 1.5 months. Later upgrading this to the hot gas thruster then took another 2 to 3 weeks. With the knowledge gained here, these processes can be combined and shortened for future projects, so that a total production time (including component lead times) is estimated at 2 to 3 weeks. Lead times for individually fabricated components is only a fraction of this, for instance a day or two for the wire-EDM cutting of the nozzle. For the silicon VLM, roughly a week of full-time clean room work was required per batch (excluding training), with more time needed for e.g. new etching masks in case of a new design.

Furthermore, the thruster was successfully heated and thrust tested up to its design temperature of 400 °C, 250 °C above the temperature that has been reached by the current silicon VLM. Higher temperatures up to (454 ± 6) °C were also possible, but only for a limited time.

In all, 250 °C higher temperature operation can now be achieved, with a similar unit cost as the silicon VLM, and an order of magnitude lower batch cost. Fabrication time for a new thruster is estimated to be similar to that of a silicon VLM batch, though critical components such as the nozzle can be made several times faster. This also means that possible fabrication errors are cheaper and quicker to fix, reducing risk associated with these.

4. *How does the measured thrust performance of the prototype compare to predictions from the analytical model suggested by Makhan?*

Thrust, mass flow and specific impulse predictions of the original model were within 10 % of experimental outcomes for the reference design. This was more accurate than predictions based on IRT alone, which were off by 25 to 30 %. However, experimental data obtained here showed lower values for the discharge coefficient than predicted by around 5 to 10 %. Oppositely, specific impulse efficiency was 10 to 15 % higher than predicted.

To allow for predictions within 10 % of experimental values from both the prototype and reference thruster, the C_D model based on throat width instead of hydraulic diameter can be used. The I_sp efficiency model based on hydraulic diameter can also be used, *if* one of its empirically fitted constants is changed from 17.6 to 12. The model is then within 10 % of all experimental data from both thrusters, and makes better predictions than IRT, which overestimates I_sp efficiency by 10 to 25 %.

Taking into account the answers to the research questions, the goal set out at the start of project is concluded to have been achieved.

10

Recommendations

Many points have been brought up in previous chapters as recommendations for future work. The main items from these are re-iterated here briefly, together with references to where these are discussed in more detail.

For improving thrust testing capabilities, the addition of a viscous damper such as an eddy-current brake would be useful to improve the controller response time and decrease influence of noise and oscillations (section 6.5 and 8.5). A further addition of an electrically controlled pressure regulator just upstream of the thruster would be recommended to counteract pressure stiffening changes of propellant tubes and for easier control of the thrust chamber pressure (section 6.5). To achieve a higher accuracy nozzle discharge factor measurements, the main point to improve at the moment is the accuracy of the nozzle throat area (section 6.5 and 8.5). The use of thermal imaging within the vacuum chamber may also be considered for evaluating insulation and measuring thruster body temperature (section 3.8 and 8.5). A likely next step for the created thruster would be reproduction of the results obtained here, followed by the use of liquid water as propellant, to test its capabilities as a VLM (section 8.5). For this it it would be advised to open up the thruster body, and re-mill the sealing surfaces with chamfered edges for a better metal-metal seal (section 5.14). Removal of the aluminium foil inside the heating chamber is also advised to prevent galvanic corrosion (section 7.12).

For future iterations of this design, there is still a lot of room for improvements and optimization of aspects such as geometry, mass, and heat loss, as the design realized here was quite crude (section 4.9). It would then also be recommended to spend more time designing the metal seal to be more robust for a lower chance of leakage (section 5.14 and 7.12). Joining methods other than gas torch brazing would furthermore be recommended for some of the connections on the thruster body, for instance laser or diffusion welding (section 3.8 and 7.12). Alternative cutting methods for the nozzle profile could also be investigated, for example precision laser or water-jet cutting (section 2.5). Lastly, a method for post-fabrication adjustment of the nozzle throat width should be looked into for smaller and more accurate throat width fabrication (section 3.8 and 5.14).

Bibliography

[1] E. Åkerfeldt. Improving thermal fracture resistance in ceramic microcomponents for spacecraft propulsion. Master's thesis, Uppsala Universitet, 2018.

[2] S. Arestie, E. G. Lightsey, and B. Hudson. Development of a modular, cold gas propulsion system for small satellite applications. *Journal of Small Satellites*, 1(2):63–74, 2012.

[3] K. J. Åstrom and B. Wittenmark. *Computer-controlled systems*. Dover Publications Inc., 2011. ISBN 0486486133.

[4] R. L. Bayt. *Analysis, fabrication and testing of a MEMS-based micropropulsion system*. PhD thesis, MIT, 1999. URL https://dspace.mit.edu/bitstream/handle/1721.1/57601/FDRL_TR-99-1.pdf.

[5] R. L. Bayt and K. S. Breuer. Systems design and performance of hot and cold supersonic microjets. In *39th AIAA Aerospace Sciences Meeting and Exhibit*, page 721, 2001. URL https://arc.aiaa.org/doi/pdf/10.2514/6.2001-721.

[6] I. H. Bell, J. Wronski, S. Quoilin, and V. Lemort. Pure and pseudo-pure fluid thermophysical property evaluation and the open-source thermophysical property library CoolProp. *Industrial & Engineering Chemistry Research*, 53(6):2498–2508, 2014. doi: 10.1021/ie4033999. URL http://pubs.acs.org/doi/abs/10.1021/ie4033999.

[7] J. J. Berton. Divergent thrust loss calculations for convergent-divergent nozzles: extensions to the classical case. Technical report, NASA, 1991. URL https://mdao.grc.nasa.gov/publications/NASA-TM-105176-Diverge.pdf.

[8] R. J. F. Bijster. Design, verification and validation of a micropropulsion thrust stand. Master's thesis, TU Delft, 2014. URL http://resolver.tudelft.nl/uuid:5c3f0eb3-511c-4443-90b2-46eed9a6b184.

[9] A. Bruccoleri, R. Leiter, M. Drela, and P. Lozano. Experimental effects of nozzle geometry on flow efficiency at low reynolds numbers. *Journal of Propulsion and Power*, 28(1):96–105, 2012. doi: 10.2514/1.B34073. URL https://doi.org/10.2514/1.B34073.

[10] V. V. Calmidi and R. L. Mahajan. Forced convection in high porosity metal foams. *Journal of Heat Transfer*, 122(3):557–565, February 2000. ISSN 0022-1481. doi: 10.1115/1.1287793. URL http://dx.doi.org/10.1115/1.1287793.

[11] D. L. J. M. Carroll, R. L. B. Cardin, R. L. Burton, G. F. Benavides, N. Hejmanowski, C. Woodruff, K. Bassett, D. King, J. Laystrom-Woodard, L. Richardson, et al. Propulsion unit for CubeSats (PUC). In *Proceedings of the 62nd JANNAF Propulsion Meeting (7th Spacecraft Propulsion), Nashville, TN, USA*, pages 1–5, 2015.

[12] J. W. Cen and J. L. Xu. Performance evaluation and flow visualization of a MEMS based vaporizing liquid micro-thruster. *Acta Astronautica*, 67(3-4):468–482, 2010.

[13] M. De Athayde Costa e Silva, D. Cordeiro Guerrieri, A. Cervone, and E. K. A. Gill. Topology optimization of heating chamber of vaporizing liquid microthrusters. In *ESA Space Propulsion 2018 Conference, Seville, Spain*, 2018. URL http://resolver.tudelft.nl/uuid:367f2639-cc62-4b55-9036-cd2d3bf119f8.

[14] M. De Athayde Costa e Silva. *MEMS Micropropulsion: design, modeling and control of vaporizing liquid microthrusters*. PhD thesis, TU Delft, 2018. URL http://resolver.tudelft.nl/uuid:57f725e1-b3f3-455c-83ce-9156b2123c88.

[15] M. G. De Giorgi and D. Fontanarosa. A novel quasi-one-dimensional model for performance estimation of a vaporizing liquid microthruster. *Aerospace Science and Technology*, 84:1020 – 1034, 2019. ISSN 1270-9638. doi: 10.1016/j.ast.2018.11.039. URL http://www.sciencedirect.com/science/article/pii/S1270963818320881.

[16] *SM 1540-D, SM 7020-D, SM 3004-D Manual*. Delta Elektronika B.V., January 2. URL https://www.delta-elektronika.nl/upload/MAN_SM700.pdf.

[17] J. Donovan, W. Lord, and P. Sherwood. Fabrication and preliminary testing of a 3kW hydrogen resistojet. In *9th Electric Propulsion Conference*, 1972. doi: 10.2514/6.1972-449. URL https://arc.aiaa.org/doi/abs/10.2514/6.1972-449.

[18] R. A. Ferreira. Development and testing of a water microresistojet. Master's thesis, TU Delft, 2008. URL http://resolver.tudelft.nl/uuid:658ea711-b261-435d-a147-3b827f4766b3.

[19] C. Ganani. Micronozzle performance: a numerical and experimental study. Master's thesis, TU Delft, 2019. URL http://resolver.tudelft.nl/uuid:94162987-534c-4912-ac68-55b26df20585.

[20] Granta Design Limited. CES Edupack, 2018.

[21] C. A. J. Hanselaar. evaporative two-phase micro-flow modelling. Master's thesis, TU Delft, 2016. URL http://resolver.tudelft.nl/uuid:030573d7-42c7-4b3e-802a-5b1b9f98ed38.

[22] R. Hibbeler. *Mechanics of materials, SI edition*. Pearson Education, ninth edition, 2013. ISBN 9789810694364.

[23] D. Hinkley. A novel cold gas propulsion system for nanosatellites and picosatellites. In *Proceedings of the 22nd AIAA/USU Conference Small Satell., Logan, UT: SSC08–VII–7*, 2008.

[24] D. L. Hitt, C. M. Zakrzwski, and M. A. Thomas. MEMS-based satellite micropropulsion via catalyzed hydrogen peroxide decomposition. *Smart Materials and Structures*, 10(6):1163, 2001.

[25] J. Huh and S. Kwon. Design, fabrication and thrust measurement of a micro liquid monopropellant thruster. *Journal of Micromechanics and Microengineering*, 24(10):104001, 2014.

[26] M. Ishibashi and M. Takamoto. Theoretical discharge coefficient of a critical circular-arc nozzle with laminar boundary layer and its verification by measurements using super-accurate nozzles. *Flow Measurement and Instrumentation*, 11(4):305 – 313, 2000. ISSN 0955-5986. doi: 10.1016/S0955-5986(00)00029-7. URL http://www.sciencedirect.com/science/article/pii/S0955598600000297.

[27] E. H. W. Jansen. Improvement and validation of test stand performance for novel micropropulsion systems. Master's thesis, TU Delft, 2016. URL http://resolver.tudelft.nl/uuid:28f0b7fa-1288-4e32-88fd-2e138745714a.

[28] A. N. Johnson, P. I. Espina, G. E. Mattingly, J. D. Wright, and C. L. Merkle. Numerical characterization of the discharge coefficient in critical nozzles. In *NCSL Conference Proceedings, Albuquerque, NM*, pages 407–422, 1998.

[29] H. J. J. Kals, C. Buiting-Csikós, C. A. van Luttervelt, K. A. Moulijn, J. M. Ponsen, and A. H. Streppel. *Industriële productie : het voortbrengen van mechanische producten*. BIM Media B.V., fifth edition, 2012. ISBN 9789039526736.

[30] N. Kazakov. *Diffusion bonding of materials*. Pergamon Press, 1985. URL https://tudelft.on.worldcat.org/oclc/11518747.

[31] Z. Khaji, L. Klintberg, D. Barbade, K. Palmer, and G. Thornell. Endurance and failure of an alumina-based monopropellant microthruster with integrated heater, catalytic bed and temperature sensors. *Journal of Micromechanics and Microengineering*, 27(5):055011, 2017.

[32] I. Krusharev. Micro-thruster development propulsion system for the DelFFi mission. Master's thesis, TU Delft, 2015. URL http://resolver.tudelft.nl/uuid:e60e68fe-d1f6-458b-8a5a-d5036e32fb69.

[33] I. Krusharev, R. Poyck, B. Zandbergen, A. Cervone, and Q. Bellini. Cubesat micro-propulsion systems for extending the capabilities of academic projects. -, 2014.

[34] N. M. Kuluva and G. A. Hosack. Supersonic nozzle discharge coefficients at low Reynolds numbers. *AIAA journal*, 9(9):1876–1879, 1971. URL https://arc.aiaa.org/doi/abs/10.2514/3.6443?journalCode=aiaaj.

[35] A. Kurmanbay. Design, fabrication and characterization of mems based micro heater for vaporizing liquid microthruster. Master's thesis, TU Delft, 2019. URL http://resolver.tudelft.nl/uuid:a9d08ef1-1e95-4a07-b4db-666d51612404.

[36] F. La Torre. *Gas flow in miniaturized nozzles for micro-thrusters*. PhD thesis, TU Delft, 2011. URL http://resolver.tudelft.nl/uuid:176902dc-7234-414c-af5b-87ef11ec6dc1.

[37] H. C. M. Leenders and B. T. C. Zandbergen. Development of a solar thermal thruster system. In *59th International Astronautical Congress: IAC 2008, 29 September-3 October 2008, Glasgow, Scotland*, 2008. URL http://resolver.tudelft.nl/uuid:3af8309c-5feb-41f8-b693-d499eb68b717.

[38] V. Lekholm, A. Persson, K. Palmer, F. Ericson, and G. Thornell. High-temperature zirconia microthruster with an integrated flow sensor. *Journal of Micromechanics and Microengineering*, 23 (5):055004, 2013.

[39] M. C. Louwerse, H. V. Jansen, M. N. W. Groenendijk, and M. C. Elwenspoek. Nozzle fabrication for micropropulsion of a microsatellite. *Journal of micromechanics and microengineering*, 19(4): 045008, 2009.

[40] S. Mahjoob and K. Vafai. A synthesis of fluid and thermal transport models for metal foam heat exchangers. *International Journal of Heat and Mass Transfer*, 51(15):3701 – 3711, 2008. ISSN 0017-9310. doi: 10.1016/j.ijheatmasstransfer.2007.12.012. URL http://www.sciencedirect.com/science/article/pii/S0017931008000197.

[41] R. A. Makhan. Performance of the MEMS vaporizing liquid microthruster using cold nitrogen gas as propellant: an experimental study. Master's thesis, TU Delft, Delft, 2018. URL http://resolver.tudelft.nl/uuid:aaed2594-d414-4c83-967b-0cd94cccd23f.

[42] G. Manzoni and Y. L. Brama. Cubesat micropropulsion characterization in low earth orbit. In *Proceedings of the 29th AIAA/USU Conference Small Satell., Logan, UT: SSC15–IV–5*, 2015.

[43] M. L. Mason, L. E. Putnam, and R. J. Re. The effect of throat contouring on two-dimensional converging-diverging nozzles at static conditions. Technical report, NASA, 1980. URL https://ntrs.nasa.gov/archive/nasa/casi.ntrs.nasa.gov/1980-Mason-Theeffectofthroatcontouringontwo-dimensionalconverging-divergingnozzlesatstatic.pdf.

[44] T. V. Mathew. Design of a MEMS micro-resistojet. Master's thesis, TU Delft, 2011. URL http://resolver.tudelft.nl/uuid:fecce3dd-c613-4a11-860f-7648d8fd42b9.

[45] T. McKechnie and A. Shchetkovskiy. High temperature combustion chambers produced by electroforming. In *Proceedings of Space Propulsion Conference*, 05 2014.

[46] A. Melaika. Design and verification of Delfi-PQ satellite propulsion subsystem. Master's thesis, TU Delft, 2019.

[47] A. Migliaccio, B. T. C. Zandbergen, F. T. Nardini, and M. C. Louwerse. Vacuum testing of a micropropulsion system based on solid propellant cool gas generators. In *61st International Astronautical Congress, Prague, Czech Republic*, 2010.

[48] A. F. Mills. *Basic heat and mass transfer*. PEARSON, 2014. ISBN 9781292042480.

[49] M. J. Mirtich. Resistojet propulsion for large spacecraft systems. Technical report, NASA, 1982.

[50] D. Nakata and K. Kinefuchi. Thermal design and experimental verification of the 3D-printed resistojet. In *2018 Joint Propulsion Conference*, page 4907, 2018.

[51] R. J. Page, W. A. Stoner, and L. Barker. A design study of hydrazine and biowaste resistojets. Technical report, NASA, 1986. URL https://ntrs.nasa.gov/archive/nasa/casi.ntrs.nasa.gov/1986-Page-Adesignstudyofhydrazineandbiowasteresistojets.pdf.

[52] K. Palmer, E. V. Catalan, V. Lekholm, and G. Thornell. Investigation of exhausts from fabricated silicon micronozzles with rectangular and close to rotationally symmetric cross-sections. *Journal of Micromechanics and Microengineering*, 23(10):105001, 2013.

[53] P. H. Pedreira, J. R. Lauretta, and S. D'hers. Planar nozzles for controllable microthrusters. *Journal of Aerospace Engineering*, 30(3):06016007, 2016.

[54] R. M. A. Poyck. Design, manufacturing and characterisation of a water fed CubeSat microresistojet (Dondersteen). Master's thesis, TU Delft, 2014. URL http://resolver.tudelft.nl/uuid:87bc9f46-5f40-4a87-9716-65f7e3ac7c29.

[55] S. Prakash and S. Kumar. Fabrication of microchannels: a review. *Proceedings of the Institution of Mechanical Engineers, Part B: Journal of Engineering Manufacture*, 229(8):1273–1288, 2015.

[56] F. Romei and A. Grubisic. High performance resistojet thruster: STAR status update. In *Space Propulsion Conference 2018*, 05 2018.

[57] K. Rycek. Initial design & preliminary performance characterization of a 1N multipropellant resistojet DUR-1. Master's thesis, TU Delft, 2005.

[58] E. W. Spisz, P. F. Brinich, and J. R. Jack. Thrust coefficients for low-thrust nozzles. Technical report, NASA, 1965.

[59] P. E. P. Stohr. The characterization and design of a CubeSat integrated COTS resistojet thruster. Master's thesis, TU Delft, 2016. URL http://resolver.tudelft.nl/uuid:d612b585-89ba-43ab-8c31-1798e14e0c80.

[60] P. Sturesson, R. Seton, L. Klintberg, G. Thornell, and A. Persson. Effect of resistive and plasma heating on the specific impulse of a ceramic cold gas thruster. *Journal of microelectromechanical systems*, 2019.

[61] S. P. Tang and J. B. Fenn. Experimental determination of the discharge coefficients for critical flow through an axisymmetric nozzle. *AIAA Journal*, 16(1):41–46, 1978.

[62] J. Taylor. *Introduction to error analysis, the study of uncertainties in physical measurements*. University Science Books, 1997. ISBN 0935702423.

[63] *MS5837-30BA ultra small gel filled pressure sensor*. TE connectivity, 2019. URL https://www.te.com/usa-en/product-CAT-BLPS0017.html. Data sheet.

[64] The Lee Company. Electro-fluidic systems handbook. Online product catalog, August 2019. URL https://www.theleeco.com/whats-new/9th-edition-electro-fluidic-systems-handbook/. 9th edition.

[65] R. Tijsterman. Development of a microresistojet. Master's thesis, TU Delft, 2007.

[66] Vacuubrand. vacuum gauge set DCP 3000 + VSP 3000. Online, 2019. URL https://www.vacuubrand.com/us/page936.html.

[67] T. X. Van Wees. characterization and testing of a MEMS-vaporizing liquid microthruster for small satellite propulsion. Master's thesis, TU Delft, 2017. URL http://resolver.tudelft.nl/uuid:33705b93-9450-4fd1-a17c-930fc8b38f17.

[68] H. S. E. Versteeg. Advantages of alternative fabrication techniques for a vaporizing liquid microthruster. Literature Study, July 2019.

[69] T. Yuan and A. Li. Design and fabrication of a mems-based milli-newton level hydrazine thruster. In *45th AIAA/ASME/SAE/ASEE Joint Propulsion Conference & Exhibit*, page 5201, 2009.

[70] B. T. C. Zandbergen. *Thermal rocket propulsion reader*. TU Delft, 2017.

A

Reference thruster performance

For functional verification of the thruster nozzle created for this project, some type of comparison data was needed. Due to the absence of validated thrust models for planar supersonic micro-nozzles, a reference design was chosen for which experimental thrust data was available, namely the hot gas geometry from Bayt [4]. The nozzle of the thruster made here was made similar to this design, so experimental results from both could be compared directly. The data from Bayt was only available in figures and thus had to be extracted from these before it could be used. First the original figures are shown from which the data was taken, followed by an explanation on a pressure thrust correction that was applied, after which the final values that were used are tabulated.

A.1. Original figures

For ease of reference, the figures from which the data was used are reproduced here exactly. Bayt tested their thruster at two different chamber pressures, 2.69 bar (39 psi_a) and 3.03 bar (44 psi_a), from room temperature up to 677 K and 692 K respectively. All experiments were performed in a vacuum chamber at a pressure of $p_\text{a} = 6.66$ Pa (50 mtorr). The resulting discharge coefficient can be seen plotted versus Re_t in Figure A.1, the specific impulse efficiency versus Re_t in Figure A.2, and the I_sp versus thrust in Figure A.3. In this case, Re_t is always calculated using the throat width w_t as characteristic length, not the hydraulic diameter $D_\text{h,t}$. Extraction of data from these figures was performed with Engauge Digitizer[1], a free, open source program for converting graphical plotted data to numerical values in `.csv` or excel table format.

[1] https://markummitchell.github.io/engauge-digitizer/

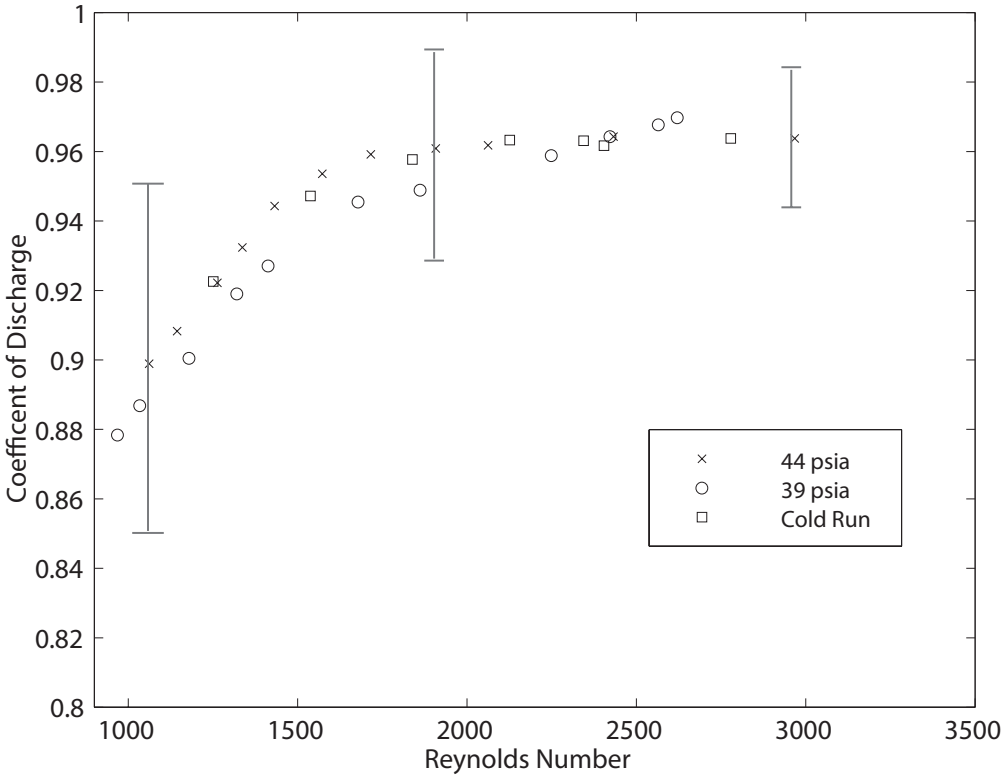

Figure A.1: c_{D} versus $\mathrm{Re_t}$, reproduced from [4, Fig. 6.19]

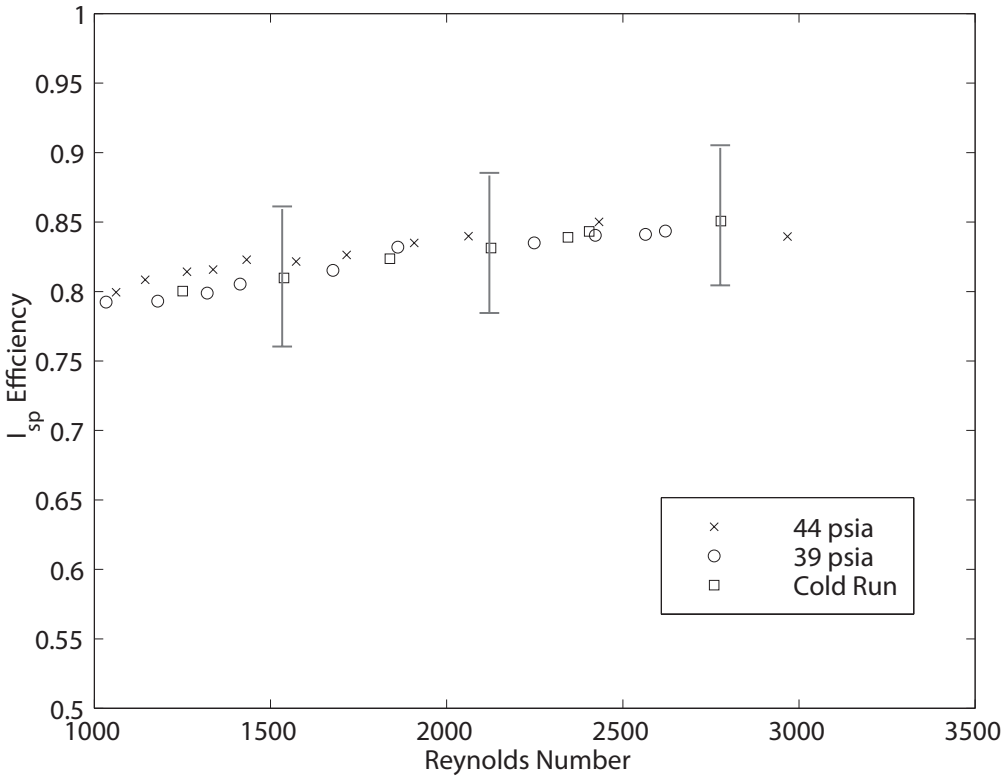

Figure A.2: ξ_{F} (I_{sp} efficiency) versus $\mathrm{Re_t}$, reproduced from [4, Fig. 6.21]

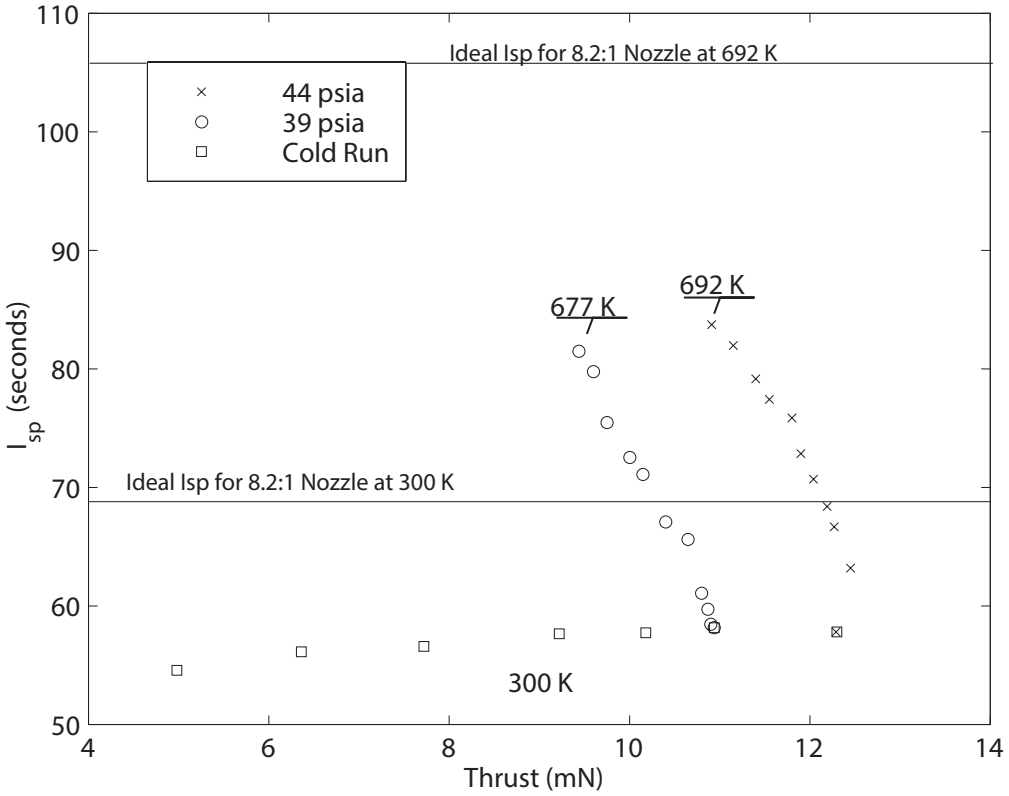

Figure A.3: I_{sp} versus thrust, reproduced from [4, Fig. 6.18]

A.2. Pressure thrust correction

The use of data from the figures in the previous section turned out to be slightly more complicated than first anticipated. The discharge coefficient C_{D} could be used as-is. When replicating the specific impulse efficiencies ξ_{F} though, consistently lower values ($\sim 5\,\%$) were found when starting with reported $I_{\mathrm{sp,exp}}$ from Figure A.3 and using given p_{c}, p_{a}, T_{c}, and geometry to calculate $I_{\mathrm{sp,ideal}}$. Figure A.3 also showed the ideal specific impulse they had calculated for two temperatures, which only lined up with the author's own calculations if pressure thrust was ignored. Incorporating this, their reported values of ξ_{F} could then be replicated exactly.

Due to the high vacuum surroundings and low expansion ratio of the nozzle under consideration ($\epsilon = 8.25$), pressure at the exit plane is actually responsible for around $5\,\%$ of the ideal thrust and specific impulse. For a proper comparison, the results from the reference thruster thus had to be corrected to incorporate this difference. This was done based on the ideal thrust coefficient $C_{\mathrm{F,ideal}}$ and the corresponding characteristic thrust coefficient C_{F}^{0}. As $C_{\mathrm{F,ideal}}$ incorporates both momentum and pressure thrust, while C_{F}° disregards the latter, the full ideal specific impulse $I_{\mathrm{sp,ideal}}$ and the version without pressure thrust I_{sp}° can then be written as follows [70]:

$$I_{\mathrm{sp,ideal}} = \frac{C_{\mathrm{F,ideal}} c^{*}}{g_0} \tag{A.1}$$

$$I_{\mathrm{sp}}^{\circ} = \frac{C_{\mathrm{F}}^{\circ} c^{*}}{g_0} \tag{A.2}$$

Further incorporating this into the ratio of ξ_{F} with pressure thrust, and ξ_{F}° without it gives:

$$\frac{\xi_{\mathrm{F}}}{\xi_{\mathrm{F}}^{\circ}} = \frac{\frac{I_{\mathrm{sp,ideal}}}{I_{\mathrm{sp,exp}}}}{\frac{I_{\mathrm{sp}}^{\circ}}{I_{\mathrm{sp,exp}}}} = \frac{C_{\mathrm{F,ideal}}}{C_{\mathrm{F}}^{\circ}} \tag{A.3}$$

(A.4)

Thus to incorporate the effects of pressure thrust, the original data would have to be multiplied by $C_{\mathrm{F,ideal}}/C_{\mathrm{F}}^{\circ}$. For the both chamber pressures used here, this factor only varied between 0.9513 and 0.9475 from room temperature to 677 K, with an average of 0.9495. The given hot thrust test results of ξ_{F} were multiplied by this average factor to arrive at the values used elsewhere in this report.

A.3. Tabulated values

Here the extracted and pressure-thrust adjusted values are shown in Table A.1 and Table A.2 for $p_{\mathrm{c}} = 2.69\,\mathrm{bar}$ and $p_{\mathrm{c}} = 3.03\,\mathrm{bar}$, respectively. A few points of interest still remain. Firstly, just a select few values were shown with accompanying confidence bounds, these were assumed to be the same for values from different pressures at similar Re_{t}, and interpolated between these points. Confidence bounds for some values such as thrust and I_{sp} were not given and are thus not shown in the tables. Secondly, temperature data was not given besides the maximum and minimum, and is thus not shown in the tables. Next, the first value of ξ_{F} for $p_{\mathrm{c}} = 2.69\,\mathrm{bar}$ (39 $\mathrm{psi_a}$) was just outside of the range shown in Figure A.2 ($\mathrm{Re}_{\mathrm{t}} < 1000$), and is thus left empty in the table. Lastly, in a similar vein to section 4.2 on thrust modelling, both $\mathrm{Re}_{\mathrm{t},w_{\mathrm{t}}}$ and $\mathrm{Re}_{\mathrm{t},D_{\mathrm{h}}}$ are shown. The original data used w_{t}, so that a conversion was needed to arrive at $\mathrm{Re}_{\mathrm{t},D_{\mathrm{h}}}$. With $w_{\mathrm{t}} = 65\,\mu\mathrm{m}$ and $h_{\mathrm{t}} = 491\,\mu\mathrm{m}$, the conversion factor came out to be 1.7662, according to the equation below.

$$\frac{\mathrm{Re}_{\mathrm{t},w_{\mathrm{t}}}}{\mathrm{Re}_{\mathrm{t},D_{\mathrm{h}}}} = \frac{w_{\mathrm{t}}}{D_{\mathrm{h}}} = \frac{w_{\mathrm{t}}}{\frac{2w_{\mathrm{t}}h_{\mathrm{t}}}{w_{\mathrm{t}}+h_{\mathrm{t}}}} = \frac{w_{\mathrm{t}}+h_{\mathrm{t}}}{2h_{\mathrm{t}}} \tag{A.5}$$

$\mathrm{Re}_{\mathrm{t},w_{\mathrm{t}}}$ [-]	$\mathrm{Re}_{\mathrm{t},D_{\mathrm{h}}}$ [-]	T_{c} [K]	C_{D} [%]	ξ_{F} [%]	F_{exp} [N]	$I_{\mathrm{sp,exp}}$ [s]
966	1706	677	87.8 ± 5.2		9.43	81.58
1032	1823	⋮	88.7 ± 5.0	75.1 ± 4.7	9.60	79.80
1178	2081	⋮	90.0 ± 4.6	75.3 ± 4.7	9.75	75.51
1322	2335	⋮	91.9 ± 4.2	75.9 ± 4.8	10.00	72.58
1413	2495	⋮	92.7 ± 4.0	76.4 ± 4.8	10.15	71.12
1675	2959	⋮	94.5 ± 3.4	77.4 ± 4.8	10.40	67.12
1864	3292	⋮	94.9 ± 3.0	79.0 ± 4.8	10.64	65.64
2251	3975	⋮	95.9 ± 2.4	79.2 ± 4.8	10.80	61.05
2421	4275	⋮	96.4 ± 2.2	79.8 ± 4.8	10.87	59.75
2564	4528	⋮	96.8 ± 2.0	79.9 ± 4.8	10.89	58.47
2618	4624	300	97.0 ± 1.9	80.2 ± 4.8	10.95	58.22

Table A.1: Extracted data from Bayt [4], for hot gas thrust testing at $p_{\mathrm{c}} = 2.69\,\mathrm{bar}$ (39 $\mathrm{psi_a}$).

$\mathrm{Re}_{\mathrm{t},w_{\mathrm{t}}}$ [-]	$\mathrm{Re}_{\mathrm{t},D_{\mathrm{h}}}$ [-]	T_{c} [K]	C_{D} [%]	ξ_{F} [%]	F_{exp} [N]	$I_{\mathrm{sp,exp}}$ [s]
1057	1867	692	89.9 ± 5.0	75.7 ± 4.7	10.90	83.77
1139	2012	⋮	90.8 ± 4.8	76.7 ± 4.7	11.15	82.01
1260	2226	⋮	92.2 ± 4.4	77.3 ± 4.7	11.40	79.22
1334	2357	⋮	93.3 ± 4.3	77.3 ± 4.8	11.55	77.50
1438	2539	⋮	94.4 ± 4.0	78.1 ± 4.8	11.80	75.91
1575	2782	⋮	95.4 ± 3.7	78.0 ± 4.8	11.90	72.79
1718	3034	⋮	95.9 ± 3.4	78.4 ± 4.8	12.05	70.65
1908	3369	⋮	96.1 ± 3.0	79.2 ± 4.8	12.19	68.55
2065	3647	⋮	96.2 ± 2.8	79.6 ± 4.8	12.27	66.77
2433	4297	⋮	96.4 ± 2.3	80.6 ± 4.8	12.44	63.26
2968	5241	300	96.3 ± 2.0	79.8 ± 4.8	12.29	57.88

Table A.2: Extracted data from Bayt [4], for hot gas thrust testing at $p_{\mathrm{c}} = 3.03\,\mathrm{bar}$ (44 $\mathrm{psi_a}$).

B

Tabulated test results

To simplify making use of experimental data from this project in future work, test results and derived values from cold and hot gas thruster testing are collected in tables in this appendix. For details on the tests themselves, see Chapter 6 and Chapter 8.

B.1. Accurate calculation of thrust coefficient

Experimental and modelled values for C_F are also shown in this appendix. C_F is normally defined as follows [70]:

$$C_\mathrm{F} = \frac{F}{p_\mathrm{c} A_\mathrm{t}} \tag{B.1}$$

This causes an issue regarding accuracy for the experimental values however, as the confidence bounds for A_t are relatively large. For modelled values calculated from p_c and T_c, the $p_\mathrm{c} A_\mathrm{t}$ term cancels out with one used to calculate F, leaving a value with much smaller confidence bounds. If the same equation is used for experimental values however, this cancelling out does not occur and the uncertainty in A_t becomes dominant. To circumvent this issue, an alternative definition of C_F is used, which is equivalent to the one above for the modelled values. This uses the characteristic velocity c^* [m s^{-1}] and mass flow instead of $p_\mathrm{c} A_\mathrm{t}$ [70]:

$$C_\mathrm{F} = \frac{F}{\dot{m} c^*} = \frac{F}{\dot{m}} \sqrt{\gamma \frac{M}{R T_\mathrm{c}} \left(\frac{2}{\gamma + 1} \right)^{\frac{\gamma+1}{\gamma-1}}} \tag{B.2}$$

Because accurate measurements of F, $\dot{m}$, and $\sqrt{T_\mathrm{c}}$ are all available and the remaining parameters are (nearly) constant, this definition results in values for $C_{\mathrm{F,exp}}$ with much smaller confidence bounds than with the earlier one ($\sim 1\,\%$ instead of $\sim 10\,\%$). The second definition is thus used in this appendix.

B.2. Cold gas thrust testing

For cold gas thrust testing, three sets of three tests were performed, with each set at a slightly higher thrust chamber pressure than the last. The tables in this section also follow this grouping, with the first digit in test names indicating the pressure set and the second digit indicating the specific test within this set in chronological order. For example, TTC-2.3 (Thrust Test Cold) is then the third test of the second thrust chamber pressure set.

Test name	p_c [kPa]	T_c [K]	p_a [Pa]	F_{exp} [mN]	$\dot{m}_{exp}$ [mg s^{-1}]	$I_{sp,exp}$ [s]
TTC-1.1	110.8 ± 5.0	294.0 ± 1.5	170 ± 28	10.430 ± 0.067	16.69 ± 0.12	63.74 ± 0.61
TTC-1.2	110.7 ± 5.0	294.1 ± 1.5	179 ± 28	10.439 ± 0.067	16.69 ± 0.12	63.77 ± 0.61
TTC-1.3	110.7 ± 5.0	294.1 ± 1.5	174 ± 27	10.431 ± 0.067	16.69 ± 0.12	63.74 ± 0.61
TTC-2.1	127.6 ± 5.0	294.2 ± 1.5	246 ± 38	12.165 ± 0.078	19.40 ± 0.14	63.94 ± 0.61
TTC-2.2	127.4 ± 5.0	294.2 ± 1.5	226 ± 35	12.155 ± 0.078	19.40 ± 0.14	63.90 ± 0.61
TTC-2.3	127.3 ± 5.0	294.3 ± 1.5	227 ± 34	12.142 ± 0.078	19.36 ± 0.14	63.95 ± 0.61
TTC-3.1	144.8 ± 5.0	294.3 ± 1.5	222 ± 37	13.959 ± 0.091	22.17 ± 0.16	64.20 ± 0.61
TTC-3.2	144.7 ± 5.0	294.4 ± 1.5	225 ± 38	13.956 ± 0.091	22.13 ± 0.16	64.30 ± 0.62
TTC-3.3	144.5 ± 5.0	294.4 ± 1.5	225 ± 35	13.927 ± 0.090	22.11 ± 0.15	64.22 ± 0.61

Table B.1: Cold gas thrust test results.

Test name	$C_{D,exp}$ [%]	$\xi_{F,exp}$ [%]	Re_{t,exp,D_h} [10^2]	Re_{t,exp,w_t} [10^2]
TTC-1.1	85 ± 10	90.18 ± 1.00	33.69 ± 0.93	22.08 ± 0.25
TTC-1.2	85 ± 10	90.24 ± 1.00	33.69 ± 0.93	22.09 ± 0.25
TTC-1.3	85 ± 10	90.17 ± 1.00	33.68 ± 0.93	22.07 ± 0.25
TTC-2.1	85.7 ± 10.0	90.60 ± 1.00	39.1 ± 1.1	25.66 ± 0.29
TTC-2.2	85.8 ± 10.0	90.47 ± 1.00	39.1 ± 1.1	25.65 ± 0.29
TTC-2.3	85.7 ± 10.0	90.53 ± 1.00	39.1 ± 1.1	25.60 ± 0.29
TTC-3.1	86.3 ± 10.0	90.79 ± 1.00	44.7 ± 1.2	29.32 ± 0.34
TTC-3.2	86.2 ± 10.0	90.94 ± 1.00	44.6 ± 1.2	29.26 ± 0.34
TTC-3.3	86.3 ± 10.0	90.82 ± 1.00	44.6 ± 1.2	29.23 ± 0.33

Table B.2: Cold gas discharge factor and specific impulse efficiency with corresponding throat Reynolds numbers, from experimental data.

Test name	$C_{F,exp}$ [-]	$C_{F,ideal}$ [-]	$C_{F,model,w_t}$ [-]	$C_{F,model,D_h}$ [-]
TTC-1.1	1.450 ± 0.014	1.6074 ± 0.0076	1.173 ± 0.019	1.250 ± 0.011
TTC-1.2	1.450 ± 0.014	1.6069 ± 0.0076	1.173 ± 0.019	1.249 ± 0.011
TTC-1.3	1.449 ± 0.014	1.6072 ± 0.0076	1.173 ± 0.019	1.250 ± 0.011
TTC-2.1	1.454 ± 0.014	1.6046 ± 0.0074	1.198 ± 0.017	1.2694 ± 0.0095
TTC-2.2	1.453 ± 0.014	1.6057 ± 0.0075	1.199 ± 0.017	1.2702 ± 0.0094
TTC-2.3	1.454 ± 0.014	1.6056 ± 0.0075	1.198 ± 0.017	1.2700 ± 0.0094
TTC-3.1	1.459 ± 0.014	1.6073 ± 0.0076	1.223 ± 0.015	1.2906 ± 0.0079
TTC-3.2	1.461 ± 0.015	1.6071 ± 0.0076	1.223 ± 0.015	1.2904 ± 0.0079
TTC-3.3	1.460 ± 0.014	1.6071 ± 0.0076	1.223 ± 0.015	1.2902 ± 0.0079

Table B.3: Cold gas thrust coefficients, from experimental data and model predictions.

Test name	p_c [kPa]	T_c [K]	p_a [Pa]	F_{ideal} [mN]	$\dot{m}_{ideal}$ [mg s^{-1}]	$I_{sp,ideal}$ [s]
TTC-1.1	110.8 ± 5.0	294.0 ± 1.5	170 ± 28	13.6 ± 1.6	19.7 ± 2.3	70.69 ± 0.38
TTC-1.2	110.7 ± 5.0	294.1 ± 1.5	179 ± 28	13.6 ± 1.6	19.6 ± 2.3	70.67 ± 0.38
TTC-1.3	110.7 ± 5.0	294.1 ± 1.5	174 ± 27	13.6 ± 1.6	19.6 ± 2.3	70.69 ± 0.38
TTC-2.1	127.6 ± 5.0	294.2 ± 1.5	246 ± 38	15.7 ± 1.8	22.6 ± 2.6	70.58 ± 0.37
TTC-2.2	127.4 ± 5.0	294.2 ± 1.5	226 ± 35	15.7 ± 1.7	22.6 ± 2.6	70.63 ± 0.38
TTC-2.3	127.3 ± 5.0	294.3 ± 1.5	227 ± 34	15.6 ± 1.7	22.6 ± 2.6	70.63 ± 0.38
TTC-3.1	144.8 ± 5.0	294.3 ± 1.5	222 ± 37	17.8 ± 2.0	25.7 ± 2.9	70.71 ± 0.38
TTC-3.2	144.7 ± 5.0	294.4 ± 1.5	225 ± 38	17.8 ± 2.0	25.7 ± 2.9	70.71 ± 0.38
TTC-3.3	144.5 ± 5.0	294.4 ± 1.5	225 ± 35	17.8 ± 2.0	25.6 ± 2.9	70.71 ± 0.38

Table B.4: Cold gas p_c, T_c and p_a with corresponding calculated thrust, mass flow and specific impulse from IRT.

Test name	F_{model} [mN]	$\dot{m}_{model}$ [mg s^{-1}]	$I_{sp,model}$ [s]	$C_{D,model}$ [%]	$\xi_{F,model}$ [%]	$\mathrm{Re}_{t,model}$ [10^2]
TTC-1.1	10.0 ± 1.3	18.6 ± 2.3	54.97 ± 0.48	94.76 ± 0.36	77.77 ± 0.93	37.6 ± 3.7
TTC-1.2	10.0 ± 1.3	18.6 ± 2.3	54.94 ± 0.49	94.75 ± 0.36	77.75 ± 0.93	37.6 ± 3.7
TTC-1.3	10.0 ± 1.3	18.6 ± 2.3	54.96 ± 0.49	94.75 ± 0.36	77.75 ± 0.93	37.6 ± 3.7
TTC-2.1	11.8 ± 1.5	21.5 ± 2.6	55.83 ± 0.43	95.11 ± 0.33	79.11 ± 0.85	43.5 ± 4.1
TTC-2.2	11.8 ± 1.5	21.5 ± 2.6	55.88 ± 0.42	95.11 ± 0.33	79.11 ± 0.85	43.4 ± 4.1
TTC-2.3	11.8 ± 1.5	21.5 ± 2.6	55.87 ± 0.42	95.10 ± 0.33	79.10 ± 0.85	43.3 ± 4.1
TTC-3.1	13.6 ± 1.7	24.5 ± 2.9	56.78 ± 0.36	95.41 ± 0.31	80.30 ± 0.77	49.4 ± 4.6
TTC-3.2	13.6 ± 1.7	24.5 ± 2.9	56.77 ± 0.36	95.41 ± 0.31	80.29 ± 0.77	49.4 ± 4.6
TTC-3.3	13.6 ± 1.7	24.5 ± 2.9	56.76 ± 0.36	95.40 ± 0.31	80.28 ± 0.78	49.3 ± 4.6
TTC-1.1	9.2 ± 1.3	18.3 ± 2.3	51.60 ± 0.82	92.82 ± 0.62	73.0 ± 1.4	24.2 ± 3.0
TTC-1.2	9.2 ± 1.3	18.2 ± 2.3	51.57 ± 0.82	92.82 ± 0.62	73.0 ± 1.4	24.1 ± 3.0
TTC-1.3	9.2 ± 1.3	18.2 ± 2.3	51.58 ± 0.82	92.82 ± 0.62	73.0 ± 1.4	24.1 ± 3.0
TTC-2.1	10.9 ± 1.5	21.1 ± 2.6	52.69 ± 0.73	93.30 ± 0.57	74.7 ± 1.3	27.9 ± 3.4
TTC-2.2	10.9 ± 1.5	21.1 ± 2.6	52.73 ± 0.73	93.30 ± 0.57	74.6 ± 1.3	27.9 ± 3.4
TTC-2.3	10.9 ± 1.5	21.1 ± 2.6	52.72 ± 0.73	93.29 ± 0.57	74.6 ± 1.3	27.9 ± 3.4
TTC-3.1	12.7 ± 1.7	24.1 ± 2.9	53.82 ± 0.64	93.71 ± 0.53	76.1 ± 1.2	31.8 ± 3.8
TTC-3.2	12.7 ± 1.7	24.1 ± 2.9	53.81 ± 0.65	93.71 ± 0.54	76.1 ± 1.2	31.8 ± 3.8
TTC-3.3	12.7 ± 1.7	24.0 ± 2.9	53.80 ± 0.65	93.70 ± 0.54	76.1 ± 1.2	31.7 ± 3.8

Table B.5: Calculated cold gas thrust performance from geometry, p_c, T_c and p_a. The top half of the table uses Re_t with D_h as characteristic length scale, the bottom half uses w_t as characteristic length.

B.3. Hot gas thrust testing

For hot gas thrust testing, a similar numbering system is used as for the cold gas results, with the exception that the first digit indicates a set of tests with similar *temperatures*. The pressure regulator in the propellant feed system was not adjusted during testing. Interaction between pressure drop over the feed system and decreasing mass flow through the nozzle due to the increased temperatures did however result in tests at higher temperatures also being at increased pressures. There was also an issue with these tests where the thrust bench pendulum had a different equilibrium position at the start and end of each thrust phase, resulting in a different thrust measurement for these two points in time. This difference between start and end was consistent in magnitude between tests and increased for higher temperatures. Based on this and several other indications, it was hypothesized that this was caused by thermal expansion and contraction of the steel thruster propellant tubes, which would shift the pendulum COG. With this in mind, the *end* value was seen as the most indicative of actual

thrust. Both *start* and *end* values are shown here. For several tests the *end* measurement is not entirely accurate, due to the magnetic actuator reaching zero current before the initial equilibrium position could be restored. These are indicated with *red emphasized* test names, and all show a few percent lower thrust than comparable tests.

Test name	p_c [kPa]	T_c [K]	p_a [Pa]	F_{exp} [mN]	$\dot{m}_{exp}$ [mg s^{-1}]	$I_{sp,exp}$ [s]
TTH-1.1	135.6 ± 5.0	305.5 ± 5.8	184 ± 29	11.839 ± 0.076	19.14 ± 0.13	63.07 ± 0.60
TTH-1.2	135.5 ± 5.0	304.8 ± 5.8	203 ± 31	11.847 ± 0.076	19.16 ± 0.13	63.05 ± 0.60
TTH-1.3	135.2 ± 5.0	304.0 ± 5.8	214 ± 33	11.831 ± 0.077	19.12 ± 0.13	63.11 ± 0.60
TTH-2.1	143.1 ± 5.0	393.7 ± 5.8	243 ± 37	12.149 ± 0.078	17.70 ± 0.12	69.98 ± 0.66
TTH-2.2	144.0 ± 5.0	403.1 ± 5.8	219 ± 34	12.326 ± 0.079	17.57 ± 0.12	71.55 ± 0.68
TTH-2.3	143.4 ± 5.0	397.3 ± 5.8	300 ± 45	12.35 ± 0.13	17.64 ± 0.12	71.36 ± 0.91
TTH-3.1	150 ± 10	477.7 ± 5.8	213 ± 33	12.550 ± 0.082	16.81 ± 0.12	76.13 ± 0.73
TTH-3.2	151 ± 10	480.9 ± 5.8	224 ± 34	12.315 ± 0.079	16.76 ± 0.12	74.93 ± 0.71
TTH-3.3	151 ± 10	482.0 ± 5.8	216 ± 33	12.775 ± 0.083	16.76 ± 0.12	77.75 ± 0.75
TTH-3.4	151 ± 10	476.7 ± 5.8	240 ± 36	12.886 ± 0.085	17.04 ± 0.12	77.10 ± 0.74
TTH-4.1	166 ± 10	670.7 ± 5.8	209 ± 32	13.492 ± 0.097	15.61 ± 0.11	88.14 ± 0.89
TTH-4.2	165 ± 10	671.6 ± 5.8	195 ± 30	13.417 ± 0.094	15.55 ± 0.11	87.96 ± 0.87
TTH-4.3	165 ± 10	672.2 ± 5.8	220 ± 34	13.434 ± 0.088	15.51 ± 0.11	88.31 ± 0.85

Table B.6: Hot gas thrust test results, based on end thrust values.

Test name	F_{exp} [mN]	$I_{sp,exp}$ [s]
TTH-1.1	11.825 ± 0.076	62.99 ± 0.60
TTH-1.2	11.834 ± 0.076	62.98 ± 0.60
TTH-1.3	11.823 ± 0.077	63.07 ± 0.60
TTH-2.1	12.066 ± 0.077	69.51 ± 0.66
TTH-2.2	12.055 ± 0.077	69.98 ± 0.66
TTH-2.3	12.064 ± 0.077	69.73 ± 0.66
TTH-3.1	12.204 ± 0.078	74.03 ± 0.70
TTH-3.2	12.164 ± 0.077	74.01 ± 0.70
TTH-3.3	12.138 ± 0.078	73.87 ± 0.70
TTH-3.4	12.225 ± 0.079	73.15 ± 0.70
TTH-4.1	12.144 ± 0.078	79.34 ± 0.75
TTH-4.2	12.082 ± 0.078	79.21 ± 0.75
TTH-4.3	11.954 ± 0.077	78.59 ± 0.75

Table B.7: Hot gas thrust test results, based on start thrust values.

Test name	$C_{\mathrm{D,exp}}$ [%]	$\xi_{\mathrm{F,exp,start}}$ [%]	$\xi_{\mathrm{F,exp,end}}$ [%]	$\mathrm{Re}_{\mathrm{t,exp},D_\mathrm{h}}$ [10^2]	$\mathrm{Re}_{\mathrm{t,exp},w_\mathrm{t}}$ [10^2]	η_{heat} [%]
TTH-1.1	87.9 ± 6.9	87.1 ± 1.2	87.2 ± 1.2	38.18 ± 0.89	24.56 ± 0.46	–
TTH-1.2	88.0 ± 6.9	87.2 ± 1.2	87.3 ± 1.2	38.28 ± 0.90	24.63 ± 0.46	–
TTH-1.3	87.9 ± 6.9	87.5 ± 1.2	87.5 ± 1.2	38.27 ± 0.90	24.62 ± 0.46	–
TTH-2.1	87.5 ± 6.8	84.7 ± 1.1	85.2 ± 1.1	28.94 ± 0.61	18.62 ± 0.29	48
TTH-2.2	87.4 ± 6.7	84.1 ± 1.0	86.0 ± 1.1	28.21 ± 0.59	18.15 ± 0.28	48
TTH-2.3	87.5 ± 6.8	84.7 ± 1.1	86.7 ± 1.3	28.64 ± 0.60	18.43 ± 0.28	48
TTH-3.1	87.2 ± 8.3	81.6 ± 1.0	83.9 ± 1.0	23.76 ± 0.47	15.29 ± 0.21	44
TTH-3.2	87.0 ± 8.3	81.3 ± 1.0	82.3 ± 1.0	23.57 ± 0.47	15.16 ± 0.21	43
TTH-3.3	87.1 ± 8.3	81.01 ± 0.95	85.3 ± 1.0	23.52 ± 0.47	15.13 ± 0.21	43
TTH-3.4	87.8 ± 8.4	80.74 ± 0.96	85.1 ± 1.0	24.12 ± 0.48	15.52 ± 0.22	44
TTH-4.1	87.5 ± 8.0	73.06 ± 0.81	81.18 ± 0.94	17.23 ± 0.32	11.09 ± 0.14	33
TTH-4.2	87.6 ± 8.0	72.87 ± 0.81	80.92 ± 0.92	17.16 ± 0.32	11.04 ± 0.14	33
TTH-4.3	87.6 ± 8.0	72.32 ± 0.80	81.26 ± 0.91	17.10 ± 0.32	11.00 ± 0.14	33

Table B.8: Hot gas discharge factor and specific impulse efficiency with corresponding throat Reynolds numbers and a rough estimate of heating power efficiency, from experimental data.

Test name	$C_{\mathrm{F,exp,start}}$ [-]	$C_{\mathrm{F,exp,end}}$ [-]	$C_{\mathrm{F,ideal}}$ [-]	$C_{\mathrm{F,model},w_\mathrm{t}}$ [-]	$C_{\mathrm{F,model},D_\mathrm{h}}$ [-]
TTH-1.1	1.405 ± 0.019	1.407 ± 0.019	1.6139 ± 0.0050	1.193 ± 0.013	1.2702 ± 0.0085
TTH-1.2	1.407 ± 0.019	1.408 ± 0.019	1.6128 ± 0.0050	1.192 ± 0.013	1.2695 ± 0.0086
TTH-1.3	1.410 ± 0.019	1.411 ± 0.019	1.6122 ± 0.0050	1.192 ± 0.013	1.2690 ± 0.0087
TTH-2.1	1.365 ± 0.016	1.374 ± 0.017	1.6123 ± 0.0051	1.135 ± 0.015	1.2229 ± 0.0096
TTH-2.2	1.358 ± 0.016	1.388 ± 0.017	1.6138 ± 0.0051	1.131 ± 0.015	1.2201 ± 0.0095
TTH-2.3	1.363 ± 0.016	1.395 ± 0.020	1.6094 ± 0.0051	1.130 ± 0.015	1.2183 ± 0.0099
TTH-3.1	1.318 ± 0.015	1.356 ± 0.015	1.6161 ± 0.0052	1.093 ± 0.022	1.190 ± 0.016
TTH-3.2	1.313 ± 0.015	1.330 ± 0.015	1.6156 ± 0.0052	1.091 ± 0.022	1.189 ± 0.016
TTH-3.3	1.309 ± 0.015	1.378 ± 0.016	1.6161 ± 0.0052	1.091 ± 0.022	1.189 ± 0.016
TTH-3.4	1.304 ± 0.015	1.374 ± 0.016	1.6148 ± 0.0052	1.094 ± 0.022	1.191 ± 0.016
TTH-4.1	1.186 ± 0.012	1.318 ± 0.015	1.6237 ± 0.0054	1.014 ± 0.024	1.128 ± 0.017
TTH-4.2	1.184 ± 0.012	1.314 ± 0.014	1.6243 ± 0.0054	1.013 ± 0.024	1.128 ± 0.017
TTH-4.3	1.174 ± 0.012	1.319 ± 0.014	1.6231 ± 0.0054	1.011 ± 0.024	1.126 ± 0.017

Table B.9: Hot gas thrust coefficients, from experimental data and model predictions.

Test name	p_c [kPa]	T_c [K]	p_a [Pa]	F_{ideal} [mN]	$\dot{m}_{ideal}$ [mg s^{-1}]	$I_{sp,ideal}$ [s]
TTH-1.1	135.6 ± 5.0	305.5 ± 5.8	184 ± 29	15.4 ± 1.2	21.8 ± 1.7	72.34 ± 0.73
TTH-1.2	135.5 ± 5.0	304.8 ± 5.8	203 ± 31	15.4 ± 1.2	21.8 ± 1.7	72.21 ± 0.73
TTH-1.3	135.2 ± 5.0	304.0 ± 5.8	214 ± 33	15.4 ± 1.2	21.8 ± 1.7	72.09 ± 0.73
TTH-2.1	143.1 ± 5.0	393.7 ± 5.8	243 ± 37	16.3 ± 1.2	20.2 ± 1.6	82.10 ± 0.67
TTH-2.2	144.0 ± 5.0	403.1 ± 5.8	219 ± 34	16.4 ± 1.2	20.1 ± 1.5	83.17 ± 0.66
TTH-2.3	143.4 ± 5.0	397.3 ± 5.8	300 ± 45	16.3 ± 1.2	20.2 ± 1.6	82.34 ± 0.66
TTH-3.1	150 ± 10	477.7 ± 5.8	213 ± 33	17.2 ± 1.6	19.3 ± 1.8	90.77 ± 0.64
TTH-3.2	151 ± 10	480.9 ± 5.8	224 ± 34	17.2 ± 1.6	19.3 ± 1.8	91.05 ± 0.64
TTH-3.3	151 ± 10	482.0 ± 5.8	216 ± 33	17.2 ± 1.6	19.2 ± 1.8	91.19 ± 0.64
TTH-3.4	151 ± 10	476.7 ± 5.8	240 ± 36	17.3 ± 1.6	19.4 ± 1.8	90.60 ± 0.64
TTH-4.1	166 ± 10	670.7 ± 5.8	209 ± 32	19.0 ± 1.7	17.8 ± 1.6	108.58 ± 0.62
TTH-4.2	165 ± 10	671.6 ± 5.8	195 ± 30	18.9 ± 1.7	17.8 ± 1.6	108.70 ± 0.62
TTH-4.3	165 ± 10	672.2 ± 5.8	220 ± 34	18.9 ± 1.7	17.7 ± 1.6	108.68 ± 0.62

Table B.10: Hot gas p_c, T_c and p_a with corresponding calculated thrust, mass flow and specific impulse from IRT.

Test name	F_{model} [mN]	$\dot{m}_{model}$ [mg s^{-1}]	$I_{sp,model}$ [s]	$C_{D,model}$ [%]	$\xi_{F,model}$ [%]	$Re_{t,model}$ [10^2]
TTH-1.1	11.54 ± 1.00	20.7 ± 1.7	56.93 ± 0.50	94.91 ± 0.25	78.70 ± 0.66	41.2 ± 2.9
TTH-1.2	11.52 ± 1.00	20.7 ± 1.7	56.84 ± 0.51	94.91 ± 0.25	78.71 ± 0.66	41.3 ± 2.9
TTH-1.3	11.49 ± 1.00	20.7 ± 1.7	56.74 ± 0.51	94.92 ± 0.25	78.71 ± 0.66	41.3 ± 2.9
TTH-2.1	11.63 ± 1.00	19.0 ± 1.5	62.27 ± 0.54	94.18 ± 0.28	75.85 ± 0.72	31.1 ± 2.1
TTH-2.2	11.7 ± 1.0	18.9 ± 1.5	62.88 ± 0.54	94.11 ± 0.28	75.61 ± 0.72	30.4 ± 2.1
TTH-2.3	11.6 ± 1.0	19.0 ± 1.5	62.33 ± 0.56	94.15 ± 0.28	75.70 ± 0.73	30.8 ± 2.1
TTH-3.1	11.8 ± 1.3	18.0 ± 1.8	66.86 ± 0.90	93.61 ± 0.35	73.7 ± 1.0	25.5 ± 2.3
TTH-3.2	11.8 ± 1.3	18.0 ± 1.8	66.99 ± 0.90	93.59 ± 0.35	73.6 ± 1.0	25.3 ± 2.3
TTH-3.3	11.8 ± 1.3	18.0 ± 1.8	67.06 ± 0.90	93.58 ± 0.35	73.5 ± 1.0	25.3 ± 2.3
TTH-3.4	11.9 ± 1.3	18.2 ± 1.8	66.81 ± 0.89	93.63 ± 0.35	73.7 ± 1.0	25.7 ± 2.3
TTH-4.1	12.2 ± 1.3	16.5 ± 1.6	75.5 ± 1.1	92.55 ± 0.40	69.5 ± 1.1	18.2 ± 1.5
TTH-4.2	12.2 ± 1.3	16.4 ± 1.6	75.5 ± 1.1	92.54 ± 0.40	69.4 ± 1.1	18.1 ± 1.5
TTH-4.3	12.1 ± 1.3	16.4 ± 1.6	75.4 ± 1.1	92.52 ± 0.40	69.4 ± 1.1	18.1 ± 1.5
TTH-1.1	10.6 ± 1.0	20.2 ± 1.7	53.48 ± 0.62	92.93 ± 0.41	73.93 ± 0.96	26.0 ± 2.2
TTH-1.2	10.6 ± 1.0	20.2 ± 1.7	53.39 ± 0.62	92.94 ± 0.41	73.94 ± 0.96	26.0 ± 2.2
TTH-1.3	10.6 ± 1.0	20.2 ± 1.7	53.30 ± 0.62	92.94 ± 0.41	73.94 ± 0.96	26.0 ± 2.2
TTH-2.1	10.5 ± 1.0	18.6 ± 1.5	57.78 ± 0.76	91.92 ± 0.46	70.4 ± 1.1	19.6 ± 1.6
TTH-2.2	10.6 ± 1.0	18.5 ± 1.5	58.27 ± 0.76	91.82 ± 0.47	70.1 ± 1.1	19.1 ± 1.6
TTH-2.3	10.5 ± 1.0	18.5 ± 1.5	57.79 ± 0.77	91.88 ± 0.46	70.2 ± 1.1	19.4 ± 1.6
TTH-3.1	10.6 ± 1.3	17.6 ± 1.8	61.4 ± 1.2	91.13 ± 0.56	67.6 ± 1.4	16.0 ± 1.6
TTH-3.2	10.6 ± 1.3	17.5 ± 1.8	61.5 ± 1.2	91.10 ± 0.56	67.5 ± 1.5	15.9 ± 1.6
TTH-3.3	10.6 ± 1.3	17.5 ± 1.8	61.5 ± 1.2	91.09 ± 0.56	67.5 ± 1.5	15.8 ± 1.6
TTH-3.4	10.7 ± 1.3	17.7 ± 1.8	61.4 ± 1.2	91.16 ± 0.56	67.7 ± 1.4	16.1 ± 1.6
TTH-4.1	10.6 ± 1.3	16.0 ± 1.6	67.8 ± 1.6	89.67 ± 0.64	62.4 ± 1.6	11.4 ± 1.1
TTH-4.2	10.6 ± 1.3	15.9 ± 1.6	67.8 ± 1.6	89.64 ± 0.64	62.4 ± 1.6	11.3 ± 1.1
TTH-4.3	10.5 ± 1.3	15.9 ± 1.6	67.7 ± 1.6	89.62 ± 0.64	62.3 ± 1.6	11.3 ± 1.1

Table B.11: Calculated hot gas thrust performance from geometry, p_c, T_c and p_a. The top half of the table uses Re_t with D_h as characteristic length scale, the bottom half uses w_t as characteristic length.

C

Test procedures

In this appendix, the procedures are laid out for leak testing, electromagnetic actuator force calibration and thrust testing. Leak-tests are only performed at ambient temperature, while thrust tests can also be performed up to 400 °C. The hot and cold gas thrust tests have separate procedures, as the latter uses additional actuators and sensors.

Components on the nitrogen propellant feed system are regularly referred to throughout this appendix, an image of which can be seen in Figure 5.23 on page 81. An important thing to note is that, once increased, the pressure in the system can only be lowered again by bleeding off excess gas. This can for example be done by opening the top middle line of the feed system board by attaching an open quick-connect fitting to it, or venting the gas through the thruster itself. For a more in-depth look at the other equipment used, see [41, Chapter 4].

Several delta elektronica power supplies are used with voltage or current control from an external source (i.e. an NI DAQ). The manual controls on these then function as *limit* values for current and voltage, though the limit is not shown on the device displays. To be able to use these devices up to their maximum specified outputs, these controls thus have to be increased to their maximum, i.e. rotated clockwise to their physical limit. If either of the manual voltage or current controls is rotated fully counter clockwise, the power supply will not provide any output, regardless of the setpoint from the DAQ.

C.1. Leak testing procedures

In this section, the procedures for performing leak testing of the thruster are laid out. First the steps are given to start up and connect the necessary equipment. Next, leak testing based on mass flow measurement (short duration, large leakage) and pressure dynamics (long duration, small leakage) are both described separately. Following this, the process to safely shut down all equipment afterwards is given.

C.1.1. Leak test preparation

1. Connect the Brooks 2000 sccm mass flow sensor (right) to the breakout board behind the vacuum chamber and plug in its power brick (45 min *warm-up time*) (only for mass-flow based testing).
2. Turn on the E-030-1 and D-030-1 power supplies behind the vacuum chamber.
3. Turn on the clean room computer next to the vacuum chamber, and start LabVIEW after having logged in (the computer is relatively slow to start, other tasks can be completed in parallel).
4. Ensure the tubing leading to the vacuum chamber is connected to the feed system at the specified mass flow sensor.
5. Ensure the valve override switch on the breakout board is set to ON.
6. Connect the thruster to the quick connect tubing for inside the vacuum chamber. Use the MINSTAC torque wrench according to its instructions together with a 5⁄32 inch wrench for tightening the connections.
7. Place the thruster inside the vacuum chamber and plug in the propellant tubing quick connect fitting to the connection in the top rear left of the chamber.

8. Place the NI UBS-8451 and USB-6008 DAQs inside the chamber with the I²C cable interface and plug both into the USB hub on the back wall inside the chamber.
9. Connect the cable from the pressure sensor on the thruster to the I²C interface (colour coded for alignment).
10. Connect the valve electrical pins to the spike and hold driver with a feed-through cable via the 9 pin connector taped to back of the left wall. The wires to use are the black/red pair with blue translucent tape near their end. When looking at the valve with the pins facing towards you, and the direction of flow pointing upwards, the red wire should be on the right.
11. Open the main valve on top of the N_2 cylinder, located behind the feed system board.
12. Make sure the pressure regulator is fully closed by turning it counter-clockwise until a physical stop is reached.
13. Open the high-pressure shut-off valve at the bottom of the feed system board.
14. The high-pressure gauge now indicates the pressure inside the N_2 cylinder. If this is close to zero, the cylinder should be replaced according to the instructions on the board.
15. Slowly adjust the pressure regulator upward to the desired value for the feed-system pressure by carefully rotating it clockwise. The pressure in the feed system (relative to atmospheric) can be read-off on the low-pressure gauge.
16. Open the low-pressure shut-off valve (long red handle) by aligning it with the direction of the tubing.
17. Open the selection valve (small yellow knob) to the rightmost mass flow sensor, again by aligning it with the tubing.
18. Plug the nozzle exit with rubber pieces and a clamp. Use tape to keep the rubber steady during clamp tightening.
19. If tests are to be performed in vacuum, close the chamber door and turn on the vacuum pump, wait roughly 15 min to reach minimum vacuum pressure between 20 and 30 Pa.

C.1.2. Flow rate leak test

1. Open `leak_test.vi` with LabVIEW (see Appendix D for details).
2. Specify the desired test name and folder to save data in, then run the program.
3. Open the valve to the thruster from LabVIEW and allow the mass flow rate to be recorded for at least 30 seconds to obtain a steady state value (initial response will show a mass flow peak to fill the thruster).
4. Close the valve to the thruster from LabVIEW and stop `leak_test.vi`.

C.1.3. Pressure dynamics leak test

1. Open `leak_test_no_mf.vi` with LabVIEW (see Appendix D for details).
2. Specify the desired test name and folder to save data in, then run the program.
3. Open the valve to the thruster from LabVIEW until the thrust chamber pressure remains constant over time.
4. Close the valve to the thruster and record pressure over time for the desired period. For very low leakage flows this can take multiple hours or days, while for relatively severe leaks it may only take minutes or seconds.
5. When sufficient time has passed, stop `leak_test_no_mf.vi`.

C.1.4. Leak test shut-down

1. If tests were performed in vacuum, *first* close the valve between the chamber and the pump (handle left of the door), *then* turn off the pump and open the pressure-equalization port on the front of the chamber to allow air to enter it once more.
2. Open the vacuum chamber door once ambient pressure inside of it has been restored.
3. Close the main valve on top of the N_2 cylinder.
4. Close the high-pressure shut-off valve.
5. Turn the pressure regulator fully counter clockwise, so that it will start at zero outlet pressure for subsequent tests, and gas in the high-pressure line between the cylinder and the regulator is not wasted.
6. Remove the rubber and clamp plug from the nozzle.
7. Bleed the low pressure section of the feed system to ambient conditions by opening the thruster

valve from LabVIEW with the same program as used for performing the test.
8. Close LabVIEW, copy the acquired data to a USB-drive and turn off the computer.
9. Close the low-pressure shut-off and selection valves.
10. Turn off the E-030-1 and D-030-1 power supplies.
11. Unplug the mass flow sensor power brick.
12. Uncouple the propellant quick connect at the back inside the chamber.
13. Uncouple the MINSTAC tubing from the valve (can be done by hand or with the wrenches specified).
14. Disconnect the pressure sensor and valve electrical wiring.
15. Unplug the NI UBS-8451 and USB-6008 DAQs.

C.2. Magnetic actuator force calibration

This section describes the main steps to calibrate the electromagnetic actuator with a scale, for accurate force measurements. The calibration is performed with the same power supply and LabVIEW control as used during thrust testing, to require fewer conversion steps and increase accuracy. The easiest place to connect the actuator to this power supply and perform the calibration is either on the table behind the vacuum chamber, or on the wheeled table in front of it. The LabVIEW program used to apply successive step current increases at a constant rate can be changed to run faster or slower and with larger or smaller steps, though these settings are only available in the block diagram (accompanied by comments). The actuator current data is also measured and recorded as it may not be exactly equal to the demanded value. Taking the raw data from the test to create a calibrated actuator current to force relation is not covered here.

1. Turn on the SM-7020D power supply (60 min *warm up time*).
2. Start the clean room computer next to the vacuum chamber.
3. Remove the actuator coil and magnet arm from the thrust bench.
4. Remove the glass panels around the measuring surface of the Mettler Toledo AG245 scale.
5. Install the actuator coil above the scale as seen in Figure 6.4 on page 93, with the high coil density side facing upwards.
6. Adjust the feet height of the AG245 scale until it is level according to the bubble level attached above its rear right foot.
7. Plug in the power brick of the AG245 scale and turn it on (30 min *warm up time*).
8. Place the magnet arm on the scale and adjust the position of it and the coil, until the arm is centred in the coil and the top of the coil is (7.0 ± 0.1) cm above the top of the magnet arm. Also make sure the coil is level by using a bubble level placed on its top.
9. Connect the actuator coil to the power supply outputs, making sure to route the wiring in a radial direction away from the coil at first and with a wide loop around it further out, to avoid current in these wires influencing the magnetic field inside the coil.
10. Open `actuator_calibration.vi` with LabVIEW (see Appendix D for details).
11. Specify the desired test name and folder to save data in.
12. Have a pen and paper at the ready to record the values shown by the scale, then start `actuator_calibration.vi`.
13. Manually record the corresponding mass/force measurements from the scale as they come up.
14. The default setting of the program will increase the current every 10 s in steps of 0.25 A up to a maximum of 10 A, after which it will loop back to 0 and start over. Stop the program after one cycle.
15. Turn off the SM-7020D power supply.
16. Close LabVIEW, copy the acquired data to a USB-drive and turn off the computer.
17. Turn off the AG245 scale.
18. Remove the actuator parts from the test setup and re-install them on the thrust bench.
19. Centre the magnet arm to the coil and align its end to (7.1 ± 0.1) cm from the high coil density side of the actuator, *while the pendulum is pressed against the distance sensor*. This ensures the middle of the distance sensor range of 0.2 cm coincides with the distance at which calibration was performed.
20. Remove the AG245 scale from the test setup and re-install its glass panels.

C.3. Cold thrust testing

Here the steps to perform thrust testing with cold gas are laid out. This is done in three sections in chronological order: preparation, actual testing, and shut down. The first covers hardware installation and turning on devices, the second describes the tests where actual data is gathered, and the third lays out what must be done after data acquisition has concluded.

C.3.1. Preparation

1. Turn on and/or plug in the components requiring warm-up or start-up time:
   (a) Turn on the SM-7020-D, E-030-1 and D-030-1 power supplies (60 min warm-up time).
   (b) Plug in the power brick for the Brooks 5850S 2000 sccm mass flow sensor (45 min).
   (c) Plug in the power cord for the DT6220/DL6230 distance sensor DAQ (15 min).
   (d) Turn on the clean room computer next to the vacuum chamber, and start LabVIEW (5 min).
2. While the previous devices are warming up, install the thruster on the thrust bench, *outside* of the vacuum chamber:
   (a) Attach the MINSTAC connector end of the seperate vacuum chamber propellant tube to the other end of the valve using the same tools (tube has a quick connect fitting on its other end).
   (b) Clamp the thruster interface to the pendulum vertical beam. Placing the thruster higher up means larger forces can be measured, at the cost of some accuracy.
   (c) Align the thruster axis along the magnet arm by eye (thruster exit faces towards the end of the magnet arm).
   (d) Take length measurements to determine the force conversion factor between the magnetic actuator force and thrust force, see Figure 6.5 on page 95
   (e) Route cables for the p-T sensor, valve and the propellant tubing over the side of the pendulum in the plane perpendicular to the thrust force, starting just above the pivot on the spring-less side in a wide arc downward (to minimize added stiffness), see Figure 8.4 on page 126.
   (f) Secure cables and tubing using small pieces of tape.
   (g) Centre the magnet arm to the coil and align its end to (7.1 ± 0.1) cm from the high coil density side of the actuator, *while the pendulum is pressed against the distance sensor*. This ensures the middle of the distance sensor range of 0.2 cm coincides with the distance at which calibration was performed.
3. Move the thrust bench inside the vacuum chamber, with the magnetic actuator facing to the side:
   (a) Use the installed bubble level on the thrust bench base and the 3 adjustable feet to level the thrust bench.
   (b) Attach the I²C cable from p-T sensor to the NI USB-6008 and NI USB-8451 DAQs through the colour-coded interface cable.
   (c) Plug in the propellant feed tube quick-connect at the rear top-right corner of the vacuum chamber.
   (d) Plug in the two NI DAQs to the USB dock in the vacuum chamber.
   (e) Attach the distance sensor cable to the CS2 sensor on the thrust bench.
   (f) Ensure the power patch-through panel is at the opposite side of the vacuum chamber relative to the magnetic actuator.
   (g) Run the magnetic actuator cables to be primarily perpendicular to the coil length axis at first and in a wide loop later, and plug these into the front two ports on the power patch-through panel (colour coded for $+$ and $-$).
4. Open up the feed system:
   (a) Turn the handle on top of the N_2 cylinder $\sim 180°$ counter clockwise to open its main valve.
   (b) Turn the pressure regulator clockwise until it is fully closed.
   (c) Turn the high-pressure shut-off valve counter-clockwise until it is fully open.
   (d) Check that the cylinder pressure, as indicated on the high-pressure gauge, is still above the desired test pressure, otherwise abort the test and have the N_2 cylinder replaced according to the instructions on the feed system board.

(e) Open the red low-pressure shut-off valve and yellow selection valve toward the mass flow sensor in use, by aligning the handles with the tubing.
(f) Slowly open the pressure regulator valve (clockwise) until the indicator for the downstream pressure has moved ever so slightly, the small gas burst going through can also be heard.

5. Test if all sensors and actuators are working:
   (a) Open `thrust_test_2.vi` with LabVIEW (see Appendix D for details).
   (b) Specify the desired test name and folder to save data in, then run the program.
   (c) Check if all the sensor values being acquired make sense, fix possible issues that come up.
   (d) Check if the PID actuator control and valve switch work.
   (e) Fine-tune the pendulum equilibrium position with counterweights so that it is at roughly 1000 µm.
   (f) Stop `thrust_test_2.vi`.
6. Close the vacuum chamber and the pressure equalization valve on its front, and open the valve between the pump and the chamber.
7. Turn on the vacuum pump and wait for internal pressure to reach $\sim$ 40 Pa.
8. Make sure enough time has passed since turning on the devices in step 1.

C.3.2. Thrust testing at a set pressure

1. Tune the chamber pressure:
   (a) Run `thrust_test_2.vi`.
   (b) Repeat the following until the desired value of p_c is reached to within 50 mbar:
      i. Open the thruster valve to check the resulting chamber pressure during thrust.
      ii. Close the thruster valve.
      iii. If the pressure was too low, open the pressure regulator slightly more (counter clockwise).
      iv. If the pressure was too high, close the pressure regulator slightly more (clockwise) and bleed off the excess gas.
   (c) Stop `thrust_test_2.vi`.
   (d) Allow the vacuum chamber pressure to reach 40 Pa again afterwards.
2. Perform the thrust test:
   (a) Run `thrust_test_2.vi`.
   (b) Turn on PID control to fix the pendulum in a position above its equilibrium point and allow it to settle ($\geq$ 10 s). A corresponding initial current between 0.2 and 0.5 A is recommended to ensure proper damping while leaving enough room for higher force measurements.
   (c) Open the thruster valve.
   (d) Close the thruster valve after 15 s to allow the PID controller to reach a steady state.
   (e) For the same reason, wait another 15 s before turning off the PID controller and stopping `thrust_test_heated.vi`.
   (f) Allow the chamber pressure to go below 40 Pa again before repeating (re-heating can be done simultaneously).

C.3.3. Shutdown

1. Turning off the equipment:
   (a) Close the valve between the chamber and the pump (handle left of the door).
   (b) Turn off the vacuum pump.
   (c) Open the pressure-equalization port on the front of the chamber to allow air to enter.
   (d) Wait for pressure inside chamber to return to ambient, then open the door.
   (e) Close the main valve on top of the N_2 cylinder.
   (f) Close the high-pressure shut-off valve.
   (g) Turn the pressure regulator fully counter clockwise, so that it will start at zero outlet pressure for subsequent tests, and gas in the high-pressure line between the cylinder and the regulator is not wasted.
   (h) Bleed off excess gas in the low-pressure part of the feed system to ambient.

(i) Close the low-pressure shut-off and selection valves.
(j) Turn off the SM-7020-D, E-030-1 and D-030-1 power supplies.
(k) Unplug the power brick for the Brooks 5850S 2000 sccm mass flow sensor.
(l) Close LabVIEW, copy the acquired data to a USB-drive and turn off the computer.

2. Thruster hardware removal:

(a) Uncouple the propellant quick connect at the back inside the chamber.
(b) Unplug the distance sensor cable.
(c) Unplug the USB DAQs from the USB hub.
(d) Unplug the actuator electrical power cables.
(e) Unplug the sensor and valve electrical cables.
(f) Remove the DAQs from the vacuum chamber.
(g) Remove the thrust bench from the vacuum chamber.
(h) Disconnect the thruster from the thrust bench.
(i) Uncouple the MINSTAC tubing from the valve (can be done by hand).

C.4. Hot gas thrust testing

Here the steps to perform thrust testing with hot gas are laid out. This is done in three sections in chronological order: preparation, actual testing, and shut down. The first covers hardware installation and turning on devices, the second describes the tests where actual data is gathered, and the third lays out what must be done after data acquisition has concluded.

C.4.1. Preparation

1. Turn on and/or plug in the components requiring warm-up or start-up time:

(a) Turn on the SM-7020, SM-7020-D, ES-030-10, E-030-1 and D-030-1 power supplies (60 min warm-up time).
(b) Plug in the power brick for the Brooks 5850S 2000 sccm mass flow sensor (45 min).
(c) Plug in the power cord for the DT6220/DL6230 distance sensor DAQ (15 min).
(d) Turn on the clean room computer next to the vacuum chamber, and start LabVIEW (5 min).

2. While the previous devices are warming up, install the thruster on the thrust bench, *outside* of the vacuum chamber:

(a) Attach the MINSTAC connector end of the seperate vacuum chamber propellant tube to the other end of the valve using the same tools (tube has a quick connect fitting on its other end).
(b) Clamp the thruster interface to the pendulum vertical beam (without the radiation shield). Placing the thruster higher up means larger forces can be measured, at the cost of some accuracy.
(c) Align the thruster axis along the magnet arm by eye (thruster exit faces towards the end of the magnet arm).
(d) Take length measurements to determine the force conversion factor between the magnetic actuator force and thrust force, see Figure 6.5 on page 95.
(e) Install the radiation shield (be mindful not to dislodge the thermocouple), and adjust its positioning so it does not touch the thruster body or tubes.
(f) *Fully* insert both heaters into the corresponding holes in the thruster.
(g) Route cables for the p-T sensor, valve, heaters, thermocouple and the propellant tubing over the side of the pendulum in the plane perpendicular to the thrust force, starting just above the pivot on the spring-less side in a wide arc downward (to minimize added stiffness), see Figure 8.4 on page 126.
(h) Secure cables and tubing using small pieces of tape.
(i) Centre the magnet arm to the coil and align its end to (7.1 ± 0.1) cm from the high coil density side of the actuator, *while the pendulum is pressed against the distance sensor*. This ensures the middle of the distance sensor range of 0.2 cm coincides with the distance at which calibration was performed.

3. Move the thrust bench inside the vacuum chamber, with the magnetic actuator facing to the side:

   (a) Use the installed bubble level on the thrust bench base and the 3 adjustable feet to level the thrust bench.
   (b) Attach the I²C cable from p-T sensor to the NI USB-6008 and NI USB-8451 DAQs through the colour-coded interface cable.
   (c) Plug in the propellant feed tube quick-connect at the rear top-right corner of the vacuum chamber.
   (d) Attach the thermocouple plug to a corresponding plug in one of the first two ports of the NI 9211 DAQ.
   (e) Plug in the three NI DAQs to the USB dock in the vacuum chamber.
   (f) Attach the distance sensor cable to the CS2 sensor on the thrust bench.
   (g) Ensure the power patch-through panel is at the opposite side of the vacuum chamber relative to the magnetic actuator.
   (h) Run the magnetic actuator cables to be primarily perpendicular to the coil length axis at first and a in wide loop later, and plug these into the front two ports on the power patch-through panel (colour coded for $+$ and $-$).
   (i) Plug in the heater cables to four of the remaining power patch-through panel ports, matching them up with the ES-030-10 and SM-7020 outputs on the exterior panel.

4. Open up the feed system:
   (a) Turn the handle on top of the N_2 cylinder $\sim 180°$ counter clockwise to open its main valve.
   (b) Turn the pressure regulator clockwise until it is fully closed.
   (c) Turn the high-pressure shut-off valve counter-clockwise until it is fully open.
   (d) Check that the cylinder pressure, as indicated on the high-pressure gauge, is still above the desired test pressure, otherwise abort the test and have the N_2 cylinder replaced according to the instructions on the feed system board.
   (e) Open the red low-pressure shut-off valve and yellow selection valve toward the mass flow sensor in use, by aligning the handles with the tubing.
   (f) Slowly open the pressure regulator valve (clockwise) until the indicator for the downstream pressure has moved ever so slightly, the small gas burst going through can also be heard.
5. Test if all sensors and actuators are working:
   (a) Open `thrust_test_heated.vi` with LabVIEW (see Appendix D for details).
   (b) Specify the desired test name and folder to save data in, then run the program.
   (c) Check if all the sensor values being acquired make sense, fix possible issues that come up.
   (d) Check if the PID actuator control, heaters and valve switch work.
   (e) Fine-tune the pendulum equilibrium position with counterweights so that it is at roughly 1000 µm.
   (f) Stop `thrust_test_heated.vi`.
6. Close the vacuum chamber and the pressure equalization valve on its front, and open the valve between the pump and the chamber.
7. Turn on the vacuum pump and wait for internal pressure to reach ~ 40 Pa.
8. Make sure enough time has passed since turning on the devices in step 1.

C.4.2. Thrust testing at a set pressure

The test described here is for a single initial chamber pressure setting at a specific thruster body temperature. Mass flow for a sonic orifice such as this varies with temperature, which unfortunately also changes the feed system pressure drop and the resulting chamber pressure. The current setup only features a pressure regulator at the very beginning of the feed system. Combined with the use of relatively small diameter tubing and a long tube length overall, this causes the pressure drop from the regulator to the thruster to be in the same order of magnitude as the chamber pressure itself. As a result, if it is desired to have the same p_c at different operating temperatures, the pressure tuning steps below have to be repeated, *at each temperature*. For tests performed during this project, this was not done.

1. Tune the chamber pressure:
   (a) Run `thrust_test_heated.vi`.

   (b) Repeat the following until the desired value of p_c is reached to within 50 mbar:
      i. Open the thruster valve to check the resulting chamber pressure during thrust.
      ii. Close the thruster valve.
      iii. If the pressure was too low, open the pressure regulator slightly more (counter clockwise).
      iv. If the pressure was too high, close the pressure regulator slightly more (clockwise) and bleed off the excess gas.
   (c) Stop `thrust_test_heated.vi`.
   (d) Allow the vacuum chamber pressure to reach 40 Pa again afterwards.
2. Perform the thrust test:
   (a) Run `thrust_test_heated.vi`.
   (b) Heat up thruster to the desired temperature by setting heater power or voltage manually.
   (c) Turn off heaters before thrust test, or set to estimated steady state power value for heating propellant mass flow at this temperature.
   (d) Turn on PID control to fix the pendulum in a position above its equilibrium point and allow it to settle ($\geq$ 10 s). Perform at least one initial thrust test at each temperature to make sure that the equilibrium point can also be reached by the actuator *after* thruster firing has concluded.
   (e) Open the thruster valve.
   (f) Close the thruster valve after 15 s to allow the PID controller to reach a steady state.
   (g) For the same reason, wait another 15 s before turning off the PID controller and stopping `thrust_test_heated.vi`.
   (h) Allow the chamber pressure to go below 40 Pa again before repeating (re-heating can be done simultaneously).

C.4.3. Shutdown

1. Turning off equipment and allowing the thruster to cool:
   (a) Close the valve between the chamber and the pump (handle left of the door).
   (b) Turn off the vacuum pump.
   (c) *Do not* open the pressure equalization valve yet, to avoid oxidation.
   (d) Close the main valve on top of the N_2 cylinder.
   (e) Close the high-pressure shut-off valve.
   (f) Turn the pressure regulator fully counter clockwise, so that it will start at zero outlet pressure for subsequent tests, and gas in the high-pressure line between the cylinder and the regulator is not wasted.
   (g) Bleed off excess gas in the low-pressure part of the feed system to ambient.
   (h) Close the low-pressure shut-off and selection valves.
   (i) Turn off the SM-7020, SM-7020-D, ES-030-10, E-030-1 and D-030-1 power supplies.
   (j) Unplug the power brick for the Brooks 5850S 2000 sccm mass flow sensor.
   (k) Wait for the thruster to cool down to $\leq$ 100 °C to avoid oxidation. Depending on the temperature tested at, doing this overnight may be preferable as especially for lower temperatures this can be very slow. Monitor the initial temperature behaviour from LabVIEW to estimate the time needed.
   (l) Close LabVIEW, copy the acquired data to a USB-drive and turn off the computer.
2. Thruster hardware removal, after the thruster has cooled down sufficiently for safe handling ($\leq$ 40 °C):
   (a) Open the pressure-equalization port on the front of the chamber to allow air to enter.
   (b) Wait for pressure inside chamber to return to ambient, then open the door.
   (c) Uncouple the propellant quick connect at the back inside the chamber.
   (d) Unplug the distance sensor cable.
   (e) Unplug the USB DAQs from the USB hub.
   (f) Unplug the heater and actuator electrical power cables.
   (g) Unplug the sensor and valve electrical cables.
   (h) Remove the DAQs from the vacuum chamber.
   (i) Remove the thrust bench from the vacuum chamber.

(j) Disconnect the thruster from the thrust bench.
(k) Uncouple the MINSTAC tubing from the valve (can be done by hand).
(l) Remove the heaters and heat shield from the thruster.

D

LabVIEW documentation

As mentioned in section 6.1.2, several alterations, simplifications and upgrades were made for the LabVIEW (version 2018) data acquisition programs used in thrust testing and related activities. In this appendix an overview is given of the different files/VIs/programs that were used, and their function. The general structure of the block diagrams of the data acquisition programs is also illustrated, together with examples of what this and the front panel UI looks like. An implementation in Python is also given for parsing the created data files to a consistent format that is easy to work with in Python. Lastly, several recommendations are given with respect to working with LabVIEW in the context of similar MSc thesis projects.

D.1. Files

All the files used can be found on the clean room computer next to the vacuum chamber in the `D:\Huib\` folder, or are otherwise available from the author's thesis supervisor (Zandbergen). Contained within are the `\1_labview_N2_testing\` folder with all the data acquisition programs, and the `\2_test_data\` folder with all the logged data. The latter is user configurable within each LabVIEW program but was kept consistent throughout testing to have all data in the same place.

The data acquisition programs inside `\1_labview_N2_testing\` are listed in Table D.1 with their corresponding functions. Next to these is also the folder `\functions\`, which contains a number of SubVIs (the LabVIEW name for functions) that are used throughout the other programs. These are listed in Table D.2.

D.2. Program structure

All the programs created for this project use the same modular structure. As LabVIEW uses a visual, block diagram-based language, this also means their block diagrams look similar, the generic layout for which is shown in Figure D.1. The main sequence consists of three columns which are executed in order: initialization, data acquisition, and shutdown. The first handles all tasks that only need to be performed once, such as setting up the DAQs. A log file name and path is also constructed here, based on a user specified test name and a main data folder. The start time and date is also recorded from which the file path of the logging data is constructed according to the pattern: `<maindatafolder>\YYYYMMDD<testname>\HHMMSS.tdms`. This ensures a unique name and prevents previous data from accidentally being overwritten, as well as allowing for easy chronological sorting.

The subsequent data acquisition stage consists of three types of (infinite) while loops: a single one for all live-plotting functions, another one for writing all the acquired data to file, and several for data acquisition at different frequencies. Each set of sensors/actuators that run at a different sampling frequency is given its own data acquisition loop, making adding and removing of sensors a relatively simple task. The plotting loop runs at 100 Hz for smooth data viewing, and the file writing loop is executed whenever a queue element with recent data from one of the other loops is available.

The loops are terminated when the "stop" button is pressed by the user, after which the shutdown phase is executed. An example of how this looks in practice can be seen in Figure D.2, which shows the

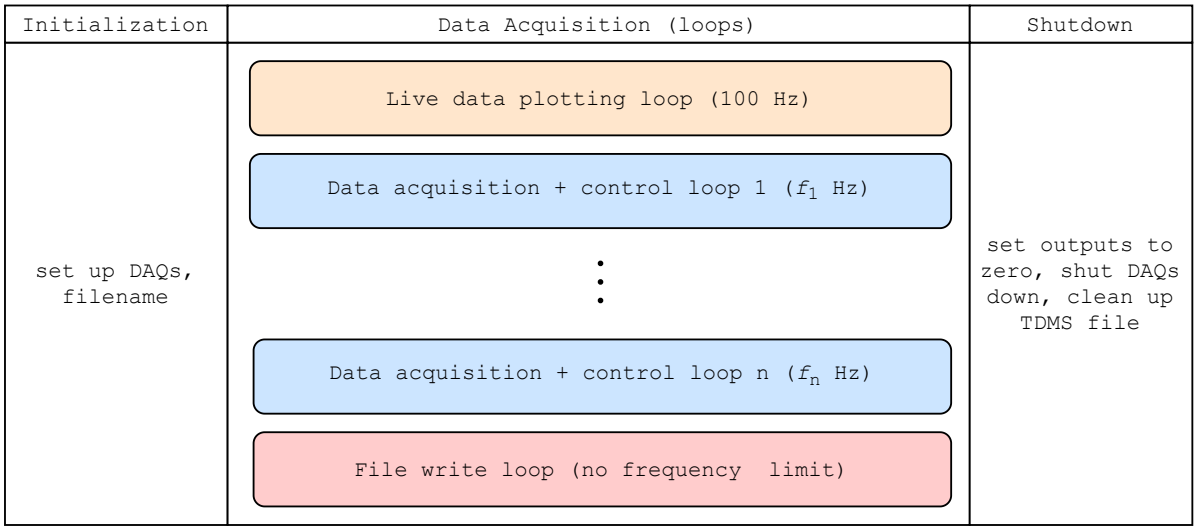

Figure D.1: General structure of the LabVIEW data acquisition programs. Program flow is through the three columns from left to right, each sensor or actuator working at a different frequency is given its own timed while loop in the centre. Data collected in each of these loops is sent to the bottom loop for writing to disk as a `.tdms` file and to the top loop for live plotting.

block diagram for `leak_test.vi`. A further example of an accompanying front panel user interface can be seen in Figure D.3, which is from `thrust_test_heated.vi`, the largest program.

D.3. Python tdms parser

The way the `.tdms` format was used in these programs, some additional information is incorporated besides the raw data. This includes time relative to program start for each group of channels and information on units and the physical quantity of the data encoded in channel names. For easy access to the data, a parser was written to convert the data in the file to a `pandas` data frame in Python, the source code for which is shown below. This also makes use of the external package `nptdms` which handles the actual reading of the binary `.tdms` file format.

```
import re
import numpy as np
from nptdms import TdmsFile
from pandas import DataFrame

def info_from_name(name):
    """
    Gets title, quantity and unit from name (if they are in there)
    Acceptable formats:
    <title> {<quantity>} [<unit>]
    <title> [<unit>]
    <title>
    Args:
        title (string): title string from labview data file
    Returns:
        tuple: containing:
            string: title (full name string of other items not found)
            string: quantity ('?' if not found)
            string: unit ('?' if not found)
    """
    quantity_match = re.search('(?<={).*(?=})', name)
    unit_match = re.search('(?<=\[).*(?=\])', name)
    if quantity_match is None and unit_match is None:
        title = name
    elif quantity_match is None and unit_match is not None:
        title = re.search('^.*(?= \[)', name).group(0)
    else:
        title = re.search('^.*(?= {)', name).group(0)
    quantity = quantity_match.group(0) if quantity_match is not None else '?'
    unit = unit_match.group(0) if unit_match is not None else '?'
```

```
    return title, quantity, unit



def read_tdms(file_path):
    """
    Reads TDMS measurement file from labview data acquisition system in SSE cleanroom
    Format assumes one group per data acquisition frequency, each with at least one
    channel for time [s] and one or more channels for associated data.
    Channel names are formatted according to the format
    specified in info_from_name() for title quantity and unit of the data
    Args:
        file_path (string): path to file to be read (relative or absolute)
    Returns:
        Pandas DataFrame: with rows for each channel and the following columns:
            x_quantity (string): physical quantity on x-axis
            x_unit (string): unit of values on x-axis
            title (string): title given to y quantity of data
            y_unit (string): unit of values on y-axis
            y_quantity (string): physical quantity on y-axis
            x (array): x data
            y (array): y data
    """
    tdms_file = TdmsFile(file_path)
    data = []
    for group in tdms_file.groups():
        channel_indices = []
        group_x_data = None
        group_name = group
        # look for time data first
        for i, channel_obj in enumerate(tdms_file.group_channels(group)):
            channel_name = channel_obj.channel
            if channel_name == 'time':
                group_x_data = channel_obj.data
            else:
                channel_indices += [i] # non-time channel found, save for later use
        # if time data was found in group, loop over non-time channels
        if group_x_data is not None:
            for ind in channel_indices:
                channel_obj = tdms_file.group_channels(group)[ind]
                data += [{}] # add new data element to total list
                data[-1]['x_quantity'] = 'Time' # always assume time in seconds
                data[-1]['x_unit']     = 's'
                title, quantity, unit  = info_from_name(channel_obj.channel)
                data[-1]['title']      = title
                data[-1]['y_quantity'] = quantity
                data[-1]['y_unit']     = unit
                data[-1]['x'] = group_x_data
                data[-1]['y'] = channel_obj.data
        else:
            raise RuntimeError('time channel not found in group')
    data_df = DataFrame(data)
    return DataFrame(data).sort_values(by=['title']).reset_index(drop=True)
```

D.4. Recommendations

For future changes and other work on similar LabVIEW programs, several recommendations are given here.

Firstly it would be advised to make liberal use of comment boxes to indicate the function of specific parts of the block diagram. This should aid in making the code easier to understand for future students, as the small visual nature of LabVIEW can otherwise be quite cryptic.

In a similar vein, keeping the layout of the block diagram tidy is also of great importance. The block diagram language can be simple and intuitive for relatively small programs, but also means it is very easy to create literal spaghetti code from crossing countless numbers of wires. Using SubVIs (with comments) to condense parts of the program that are used more than once and the use of local variables (read and write) to simplify line structures is recommended to keep complexity in check.

As a last point regarding layout and structure, try to keep programs relatively simple. Reading out

Filename	Description
actuator_calibration.vi	Calibration of the magnetic actuator with AG-245 scales.
calibration.vi	Calibration of the pendulum with magnetic actuator (obsolete).
heater_control.vi	Control of the two heaters with temperature and pressure sensors, without thrust measurement.
leak_test.vi	Pressure, temperature and mass flow measurement for leak testing (short duration).
leak_test_no_mf.vi	Pressure and temperature measurement for leak testing, no mass flow for longer duration and reduced data file size.
mfc_voltage.vi	Monitor voltage output of mass flow controller/sensor, used for diagnosing issue with sensor sticking to 50 mV output at end of tests.
pendulum_control.vi	(obsolete, do not use)
pendulum_control_2.vi	2nd iteration of pendulum distance controller, no other measurements (prototype).
thrust_test.vi	Cold thruster testing with distance calibrated force measurement (obsolete).
thrust_test_2.vi	Cold thruster testing with electromagnetic force compensation.
thrust_test_heated.vi	Hot thruster testing with electromagnetic force compensation (adds heater and thermocouples on top of thrust_test_2.vi).

Table D.1: List of LabVIEW VI names used for testing and their descriptions, as found in D:\Huib\1_labview_N2_testing\ on the clean room computer.

DAQs and saving measurements to disk can be done relatively easily with LabVIEW. Making a more complex UI on the other hand with things like state machines and different modes of operation can quickly become complicated, and can make changing the program very cumbersome. Master students only have a limited time to perform their work, so having complex, difficult to figure out programs is both a detriment to the person making them and future students.

Finally, it would be recommended to follow a course on LabVIEW basics, be it online or on campus, to get familiar with the subtleties of the interface and the language. These can also show useful tips to optimize your work-flow that you might not find otherwise. For example the wonderful “context help” window, the “quick drop” menu for placing blocks (ctrl+space), the “navigation window” for easier scrolling (ctrl+shift+N), etc.

Filename	Description
`bool_rise.vi`	Detects a rising edge on a `boolean` signal.
`file_path_creation.vi`	Create a file path to save logged data to based on the date, time, and user specified test name.
`initialize_chart.vi`	Initialize all items in a stacked chart to use zero-order hold display and use waveform names for y-axis label.
`log_channel_element.ctl`	Type definition for output of `to_channel_element.vi`.
`log_queue_element.ctl`	Type definition for output of `to_queue_element.vi`.
`ms5803_05bar_convert.dll`	(not used)
`ms5803_05bar_convert.h`	(not used)
`ms5837_30bar_convert.dll`	Handles digital signal to measurement conversion for `readTP_30bar.vi` [14].
`ms5837_30bar_convert.h`	Header file for `ms5837_30bar_convert.h`.
`pid_controller.vi`	Implementation of PID controller for distance control of the pendulum (see equations (6.1)–(6.5)).
`read_distance.vi`	Pendulum distance sensor read-out.
`readTP_30bar.vi`	MS5837 temperature and pressure sensor read-out [14].
`reset_prom_30bar.vi`	Initialize MS5837 I²C p-T sensor.
`resistance_estimator.vi`	Estimates resistance of heater/resistor based on current and voltage measurements.
`signal_to_time_waveform.vi`	Converts a signal to a specific waveform for time-based plotting of results during testing.
`subvi_Pgauge.vi`	Vacuum chamber pressure sensor read-out.
`to_channel_element.vi`	Combines a single `double` signal with a `string` to create a channel element (data + channel name) for logging to a `.tdms` file.
`to_queue_element.vi`	Combines an array of channel elements with a `string` to create a queue element (channels + group name) to process into a `.tdms` file in the separate logging loop.

Table D.2: List of LabVIEW SubVI names and their descriptions, as found in `D:\Huib\1_labview_N2_testing\functions\` on the clean room computer.

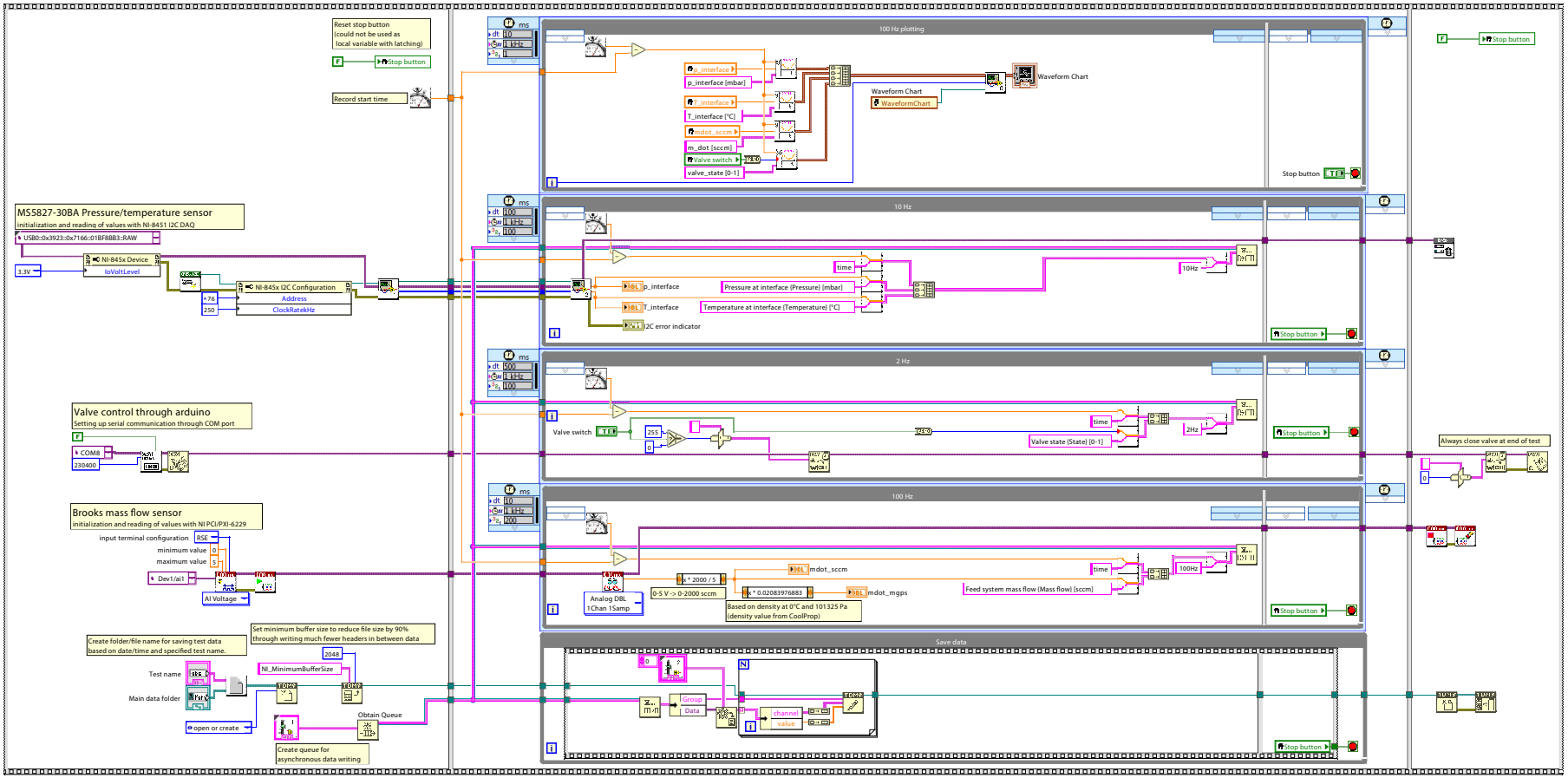

Figure D.2: Example LabVIEW block diagram from `leak_test.vi`.

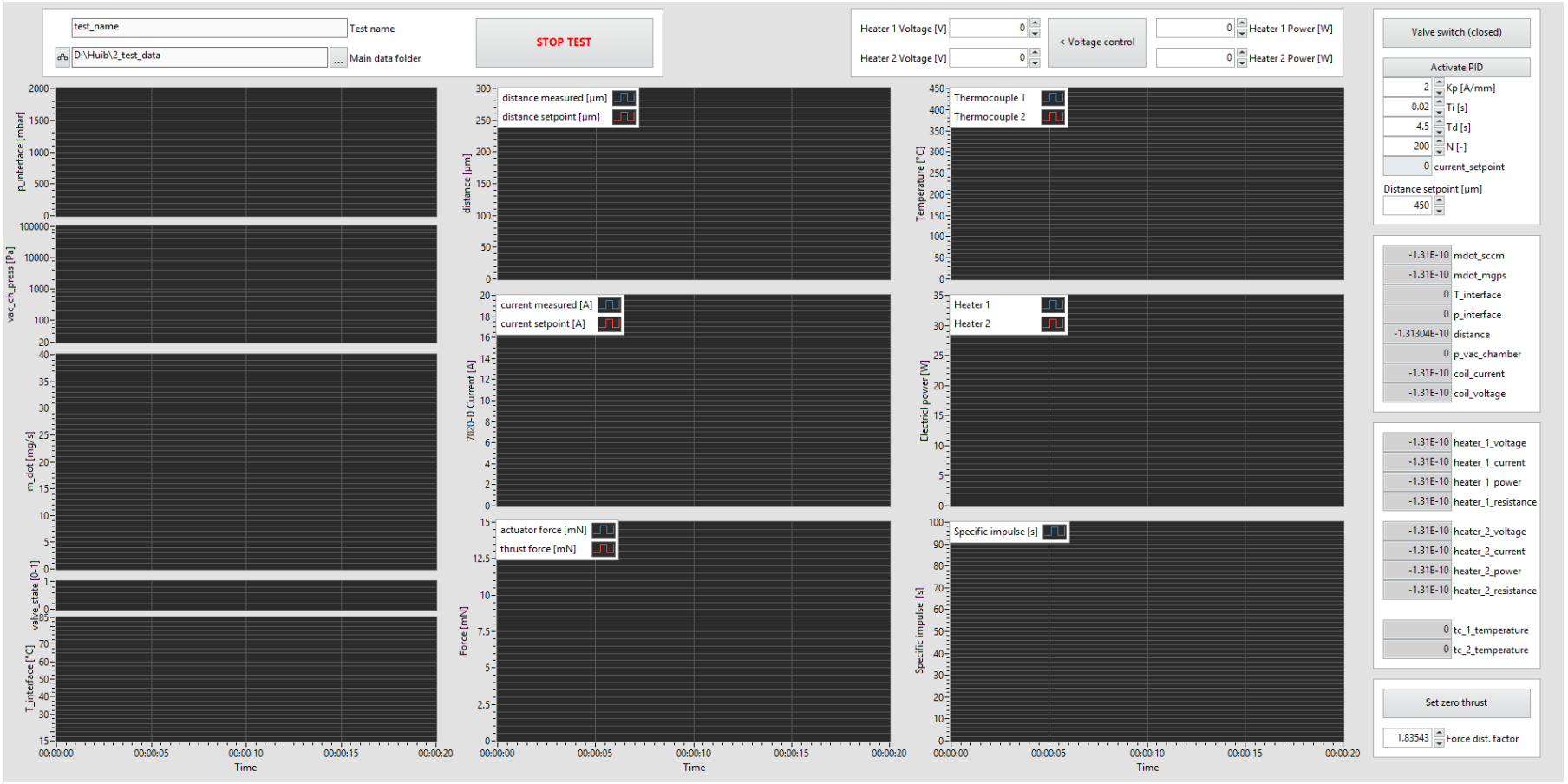

Figure D.3: Example LabVIEW front panel user interface from `thrust_test_heated.vi`.

E

Abstract for Space Propulsion Conference 2020

The main findings from this project were submitted to the 2020 Space Propulsion Conference in Lisbon, the accepted abstract for which can be found below.

Novel manufacturing method for planar hot and cold supersonic micro-thrusters

H. S. E. Versteeg[(1)], **B. T. C Zandbergen**[(2)]

Delft University of Technology, Kluyverweg 1, 2629 HS Delft, The Netherlands, E-mail:
(1) H.S.E.Versteeg@gmail.com
(2) B.T.C.Zandbergen@tudelft.nl

KEYWORDS: Micro-thrusters, micro-resistojet, microjet, vaporizing liquid micro-resistojet, manufacturing, fabrication, nozzle, propulsion

A key element in the development of more capable nano- and pico-satellites is the development of high specific impulse micro-propulsion systems. Such micro-propulsion systems are considered essential to allow for large orbital manoeuvres so that more challenging space missions can be flown.

One such system being developed at Delft University of Technology is a micro-resistojet with a planar supersonic nozzle geometry. This is fabricated out of silicon using Deep Reactive Ion Etching (DRIE); a standard MEMS production method also used by other institutes for similar devices. Unfortunately this has long lead times for new designs and uses highly specialized equipment, which also results in a high total cost. As a result, design iterations and thrust model validation are slow and expensive processes.

As a faster, more accessible alternative, wire Electric Discharge Machining (wire-EDM) has been used here for creating the heater chamber and supersonic nozzle. This process is limited to prismatic geometry, thus leaving two sides of the fluid channel open. These were closed off using machined and polished soft copper sealing surfaces. These copper elements are also used to conduct heat from Commercial Off-The-Shelf (COTS) resistive cartridge heaters through a metal foam heat exchanger to the propellant.

The thruster was tested in a vacuum using nitrogen as propellant at temperatures up to 400 °C, with throat Reynolds numbers varying from 3800 down to 1700. Results showed similar thrust and specific impulse values as reported by others for a comparable DRIE-based micro-thruster, thereby confirming the validity of the novel manufacturing method.

Using the manufacturing method discussed here, experiments with varying nozzle geometries can now be performed with reduced time between iterations, at temperatures up to 400 °C (with potential for extending the range up to 600 °C) , and at considerably lower cost than with DRIE. Future experiments at TU-Delft will initially focus on testing the current prototype with water as propellant to verify its functionality as a Vaporizing Liquid Micro-resistojet (VLM).